

ABSTRACT

Title of Document: DESIGN OF BEAM STEERING
ELECTRONIC CIRCUITS FOR MEDICAL
APPLICATIONS.

Mohammad A A A Safar, Doctor of
Philosophy, 2011

Directed By: Professor, Robert Newcomb, Electrical &
Computer Engineering Department

This thesis deals with the theory and design of a hemispherical antenna array circuit that is capable to operate in the intermediate zones. By doing that, this array can be used in Hyperthermia Treatment for Brain Cancer in which the aim is to noninvasively focus the fields at microwave frequencies to the location of the tumor cells in the brain. Another possible application of the array is to offer an alternative means of sustaining Deep Brain Stimulation other than using the traditional (surgical) approach.

The new noninvasive technique is accomplished by the use of a hemispherical antenna array placed on the human's head. The array uses a new beamforming technique that achieves 3 dimensional beamforming or focusing of the magnetic field of antennas to desired points in the brain to achieve either cell death by temperature rise (Hyperthermia Application) or to cause brain stimulation and hopefully alleviate the affects of Parkinson's Disease (Deep Brain Stimulation).

The main obstacle in this design was that the far field approximation that is usually used when designing antenna arrays does not apply in this case since the hemispherical array is in close proximity to where the magnetic field is desired to be focused. The antenna array problem is approached as a boundary-valued problem with the human head being modeled as a three layered hemisphere. The exact expressions for electromagnetic fields are derived. Health issues such as electric field exposure and specific absorption rate (SAR) are considered.

After developing the main antenna and beamforming theory, a neural network is designed to accomplish the beamforming technique used. The radio-frequency (RF) transmitter was designed to transmit the fields at a frequency of 1.8 GHz.

The antenna array can also be used as a receiver. The antenna and beamforming theory is presented. A new reception technique is shown which enables the array to receive multiple magnetic field sources from within the hemispherical surface. The receiver is designed to operate at 500 kHz with the RF receiver circuit designed to receive any signal from within the hemispherical surface at a frequency of 500 kHz.

DESIGN OF BEAM STEERING ELECTRONIC CIRCUITS FOR MEDICAL
APPLICATIONS.

By

Mohammad A A A Safar.

Dissertation submitted to the Faculty of the Graduate School of the
University of Maryland, College Park, in partial fulfillment
of the requirements for the degree of
Doctor of Philosophy
2011

Advisory Committee:
Professor Robert Newcomb, Chair
Professor Neil Goldsman
Professor Martin Peckerar
Professor John Melngailis
Associate Professor Paulo Bedaque

© Copyright by
Mohammad A A A Safar
2011

Dedication

I dedicate this dissertation to my wife Abrar Jeraq who supported me throughout my graduate studies in the University of Maryland, College Park. For 5 years she put hold all of her academic and career ambitions to take on the exhausting challenge of standing by my side day in and day out with no second thoughts. She always believed in my ability to get the Ph. D Degree even at times when I doubted myself. She was able to provide for me and my two daughters a suitable loving environment in which I was able to study and conduct research while she took care of my daughters.

This dissertation is also a dedication to my two daughters Shahad and Dalal. They and my wife had to endure the fact of living overseas for a considerable period of time away from family and friends. This dissertation is a symbol of love and appreciation to their patience and sacrifice.

Acknowledgements

I would like to take this opportunity to thank Prof. R. Newcomb from the Electrical and Computer Engineering Department in the University of Maryland, College Park for giving me the opportunity to work with him in a very interesting field that combines different electrical engineering disciplines. I wouldn't be able to write this dissertation without Prof. Newcomb's constant support and advice. His ability to point me to the right direction and the right way of thinking has helped me a lot in my research.

When I first arrived at UMD and worked with Prof. Newcomb I was, and still, amazed by his research achievements in many different areas of engineering. His knowledge in microelectronic circuits, neural networks and medical devices helped me in my dissertation. Beside his academic achievements, he is easy going and working with him was my honor.

I am very grateful that I had the privilege of studying and building my research skills in the University of Maryland, College Park which is considered one of the top universities in the field of engineering.

Table of Contents

Dedication	ii
Acknowledgements	iii
Table of Contents	iv
List of Tables	vi
List of Figures	vii
Chapter 1: Introduction	1
1.1 Basic Ideas	1
1.2 Research Motivation	2
1.3 Dissertation Outline	6
1.4 List of Contributions	8
Chapter 2: Literature Review	10
2.1 Traditional Antenna Arrays	10
2.1.1 Main Concepts	10
2.1.2 Beam Steering	15
2.1.3 Direction of Arrival Estimation (DOA)	19
2.2 Transcutaneous Power and Data Transmission via Inductive Link	23
2.2.1 Principle of Operation	24
2.2.2 RFID/IMD Circuit Model	26
2.2.3 Inductive Link Design	29
2.2.4 Available Coupling-Insensitive Transcutaneous Links Techniques	35
2.3 RF Phase Shifters	36
2.4 Hyperthermia Cancer Therapy	41
2.5 Deep Brain Stimulation (DBS)	43
Chapter 3: Antenna Array Theory & Beamforming Techniques for the Intermediate Zone	48
3.1 Antenna Array System	48
3.2 Theoretical Analysis of the Array as a Transmitter	51
3.2.1 Problem Statement	51
3.2.2 Loop Current Construction	55
3.2.3 Boundary Valued Problem	57
3.2.4 TM Waves	59
3.2.5 TE Waves	61
3.2.6 Applying Boundary Conditions	62
3.2.7 Fields Inside the Brain	68
3.2.8 Exterior & Intermediate Fields	70
3.3 Beamforming Techniques for Transmission	73
3.3.1 Phase Control Technique	73
3.3.2 Orthogonality Technique	81
3.3.2.1 Both TE & TM Modes Present	83
3.3.2.2 TE Modes Present	87
3.3.2.3 Ability to Transmit to Multiple Points	100
3.4 Theoretical Analysis of the Array as a Receiver	103

3.4.1 Antenna Array Receivers	103
3.4.2 Boundary Valued Problem in the Receiving Case.....	103
3.5 Beamforming Technique for Reception.....	108
3.5.1 Determining g_i	109
3.5.2 Multiple Reception.....	117
3.6 Power and Safety Considerations	118
3.7 Reflection & Transmission Issues	126
3.8 Other RFID/IMD Applications	135
Chapter 4: Neural Networks	136
4.1 Introduction.....	136
4.2 Learning Algorithms	138
4.3 Neural Network for Beamforming	139
Chapter 5: RF Electronics	156
5.1 RF Front-End	156
5.2 RF Transmitter Circuit Components.....	158
5.2.1 Phase Shifter Design	158
5.2.1.1 Theory of the Phase Shifter.....	158
5.2.1.2 PSPICE Simulation Results	166
5.2.2 Antenna Element Impedance	169
5.2.3 Power Amplifier (PA).....	172
5.2.3.1 PA Theory.....	172
5.2.3.2 PSPICE Simulation.....	176
5.2.4 RF Amplitude Amplifiers	178
5.3 RF Receiver Circuit Components	182
5.3.1 Low Noise Amplifier (LNA)	182
5.3.2 RF Adder.....	187
Chapter 6: Conclusion & Future Work	192
6.1 Conclusion	192
6.2 Future Work	194
Appendix A.....	196
Appendix B.....	200
Appendix C	204
Appendix D.....	208
Appendix E	211
Appendix F.....	214
Bibliography.....	216

List of Tables

3.1 Relative Permittivity & Conductivity of the Four Regions of Operation [35]	54
3.2 Relative Permittivity & Conductivity of the Four Regions of Operation at 500kHz [45]	113
3.3 Density & Conductivity of the Skin (1), Skull (2) & Brain (3) at 1.8GHz [35]	119
4.1 Mean Square Error (MSE) versus the Number of Epochs for Each Neural Network	144

List of Figures

2.1 Geometry of an Antenna Array with N Identical and Parallel Elements ([4] <i>Fig 1.1, p.2</i>)	13
2.2 Typical Array Configuration ([5] <i>Fig. 19.1.1, p.772</i>)	16
2.3 Three Element Array (a) located on the positive x-axis; (b) located on the x-axis; and (c) located on both the x-axis and the y-axis ([5] <i>Example. 19.3.2 & 19.3.3, pp.774 & 776</i>)	17
2.4 A Typical Antenna Array Receiver Structure ([11] <i>Fig. 3, pp. 423</i>)	20
2.5 DOA of Two Sources Using the Conventional Beamformer ([11] <i>Fig. 5, pp. 424</i>)	23
2.6. A Typical Near-Field power/communication mechanism for RFID/IMD tags ([16] <i>Fig 3, p.28</i>)	25
2.7 RFID/IMD Circuit Model ([19] <i>Fig 1, p.801</i>)	26
2.8. Class E Amplifier ([18] <i>Fig 15.9, p.505</i>)	27
2.9 Typical Rectifier	28
2.10 Full-Wave CMOS Rectifier ([19] <i>Fig 3, p.803</i>)	28
2.11 Equivalent Circuit for Inductive Link Power Transfer ([20] <i>Fig 1, p.72</i>)	29
2.12 Ideal Coil Configuration for the Tx and Rx Coils ([20] <i>Fig 2, p.73</i>)	31

2.13 Lateral Misalignment Configuration for the Tx and Rx Coils	
([20] <i>Fig 3, p.73</i>)	32
2.14 Angular Misalignment Configuration for the Tx and Rx Coils	
([20] <i>Fig 4, p.73</i>)	33
2.15 Plot of Power Gain across the Inductive Link for a number of Tx, Rx Combinations, in the Lateral Misalignment Case ([20] <i>Fig 5, p.74</i>)	34
2.16 Plot of Power Gain across the Inductive Link for a number of Tx, Rx Combinations, in the Angular Misalignment Case ([20] <i>Fig 6, p.74</i>)	34
2.17 The High-Pass Filter Phase Shifter ([24] <i>Fig. 2, pp. 2174</i>)	37
2.18 Tunable Active Inductor with a Feedback Resistance ([24] <i>Fig. 3, pp. 2174</i>)	37
2.19 Schematic of the Phase shifter ([25] <i>Fig. 4, pp. 300</i>)	38
2.20 Block diagram of the phase shifter ([28] <i>Fig.12, p.2667</i>)	39
2.21 Baseband VGA ([1] <i>Fig.8, p.2665</i>)	40
2.22 Showing the Location of the Small Antenna Sources ([62], <i>Fig. 1(a), pp. 2</i>)	42
2.23 Heating Characteristics at 4 Different Resonant Frequencies	
([63], <i>Fig. 6, pp. 3066</i>)	42
2.24 Heating Spot at Different Distances ([63], <i>Fig. 8, pp.3067</i>)	43

2.25 (a) Implanted Deep Brain Stimulators ([2] Fig 3, p.15). (b) Deep Brain Stimulator Apparatus ([2] Fig 4, p.25)	45
2.26 Cross sectional view of the human head with showing the location of the thalamus (<i>in red</i>) [34]	46
3.1 A simple model of a human's head as seen from the front. There are four regions denoted by (0), (1), (2) and (3) which represent free space, skin, skull and brain respectively. The radius of the brain is a , b denotes the radius from the center of the brain to the outer part of the skull and c denotes that to the skin where the antenna elements are going to be placed	54
3.2 (a) The loop current designed. The center of the loop is located at the point (c, θ_i, φ_i) . The loop carries the current I_i . (b) Loop Antennas Placed on the Human head	56
3.3 Magnetic Field Intensity of the Antenna Array without Phase Correction	76
3.4 Magnetic Field Intensity for the Antenna Array for $\theta_i=0$ & $\varphi_i=0$	77
3.5 Magnetic Field Intensity for the Antenna Array for $\theta_i=\pi/2$ & $\varphi_i=0$	77
3.6 Magnetic Field Intensity for the Antenna Array for $\theta_i=\pi/4$ & $\varphi_i=\pi/4$	78
3.7 Magnetic Field Intensity for the Antenna Array for $\theta_i=\pi/3$ & $\varphi_i=\pi$	78
3.8 Magnetic Field Intensity for the Antenna Array for $\theta_i=\pi/2$ & $\varphi_i=\pi/2$	79
3.9 Magnetic Field Intensity for the Antenna Array for $\theta_i=\pi/6$ & $\varphi_i=3\pi/2$	79

3.10 H-field (θ -component) for the Antenna Array for $r_o=2cm$, $\theta_o=0$ & $\varphi_o=0$	91
3.11 H-field (φ -component) for the Antenna Array for $r_o=2cm$, $\theta_o=0$ & $\varphi_o=0$	91
3.12 H-field (θ -component) for the Antenna Array for $r_o=2cm$, $\theta_o=\pi/4$ & $\varphi_o=\pi$	92
3.13 H-field (φ -component) for the Antenna Array for $r_o=2cm$, $\theta_o=\pi/4$ & $\varphi_o=\pi$	92
3.14 H-field (θ -component) for the Antenna Array for $r_o=2cm$, $\theta_o=\pi/4$ & $\varphi_o=\pi/2$	93
3.15 H-field (φ -component) for the Antenna Array for $r_o=2cm$, $\theta_o=\pi/4$ & $\varphi_o=\pi/2$	93
3.16 H-field (θ -component) for the Antenna Array for $r_o=2cm$, $\theta_o=\pi/4$ & $\varphi_o=3\pi/2$	94
3.17 H-field (φ -component) for the Antenna Array for $r_o=2cm$, $\theta_o=\pi/4$ & $\varphi_o=3\pi/2$	94
3.18 H-field (θ -component) for the Antenna Array for $r_o=2cm$, $\theta_o=\pi/2$ & $\varphi_o=0$	95
3.19 H-field (φ -component) for the Antenna Array for $r_o=2cm$, $\theta_o=\pi/2$ & $\varphi_o=0$	95
3.20 H-field (θ -component) for the Antenna Array for $r_o=2cm$, $\theta_o=\pi/3$ & $\varphi_o=\pi/2$	96
3.21 H-field (φ -component) for the Antenna Array for $r_o=2cm$, $\theta_o=\pi/3$ & $\varphi_o=\pi/2$	96
3.22 Normalized H-Field versus radial distance for $r_o=0.5cm$, $\theta_o=\pi/2$ & $\varphi_o=0$	97
3.23 Normalized H-Field versus radial distance for $r_o=1cm$, $\theta_o=\pi/2$ & $\varphi_o=0$	97
3.24 Normalized H-Field versus radial distance for $r_o=2cm$, $\theta_o=\pi/2$ & $\varphi_o=0$	98
3.25 Normalized H-Field versus radial distance for $r_o=4cm$, $\theta_o=\pi/2$ & $\varphi_o=0$	98
3.26 H-Field for the Antenna Array for $r_o=1cm$, $\theta_o=\pi/4$ & $\varphi_o=\pi$	99

3.27 H-Field for the Antenna Array for $r_o=0.5cm$, $\theta_o=\pi/2$ & $\varphi_o=0$	99
3.28 H-field (θ -component) for the Antenna Array for $(\pi/4,\pi)$ and $(\pi/2,0)$	
for $r_o=5cm$	102
3.29 H-field (φ -component) for the Antenna Array for $(\pi/4,\pi)$ and $(\pi/2,0)$	
for $r_o=5cm$	102
3.30 $I_{out}(\theta,\varphi)$ for $\theta_s=0$ & $\varphi_s=0$	113
3.31 $I_{out}(\theta,\varphi)$ for $\theta_s=\pi/4$ & $\varphi_s=0$	114
3.32 $I_{out}(\theta,\varphi)$ for $\theta_s=\pi/4$ & $\varphi_s=0$	114
3.33 $I_{out}(\theta,\varphi)$ for $\theta_s=\pi/4$ & $\varphi_s=\pi$	115
3.34 $I_{out}(\theta,\varphi)$ for $\theta_s=\pi/4$ & $\varphi_s=\pi/2$	115
3.35 $I_{out}(\theta,\varphi)$ for $\theta_s=\pi/2$ & $\varphi_s=\pi/4$	116
3.36 $I_{out}(\theta,\varphi)$ for $\theta_s=\pi/4$ & $\varphi_s=3\pi/2$	116
3.37 $I_{out}(\theta,\varphi)$ for $\theta_{s1}=\pi/4$ & $\varphi_{s1}=3\pi/2$ and $\theta_{s2}=\pi/4$ & $\varphi_{s2}=\pi/2$	117
3.38 $I_{out}(\theta,\varphi)$ for $\theta_{s1}=\pi/4$ & $\varphi_{s1}=\pi$ and $\theta_{s2}=0$ & $\varphi_{s2}=0$	118
3.39 Magnitude of Electric Field on the Skin for $\theta_o=0$ & $\varphi_o=0$	120
3.40 SAR of the Skin for $\theta_o=0$ & $\varphi_o=0$	120
3.41 Magnitude of Electric Field on the Skin for $\theta_o=\pi/4$ & $\varphi_o=\pi$	121

3.42 SAR of the Skin for $\theta_o=\pi/4$ & $\varphi_o=\pi$	121
3.43 Magnitude of Electric Field on the Skin for $\theta_o=\pi/4$ & $\varphi_o=\pi/2$	122
3.44 SAR of the Skin for $\theta_o=\pi/4$ & $\varphi_o=\pi/2$	122
3.45 Magnitude of Electric Field on the Skin for $\theta_o=\pi/4$ & $\varphi_o=3\pi/2$	123
3.46 SAR of the Skin for $\theta_o=\pi/4$ & $\varphi_o=3\pi/2$	123
3.47 Magnitude of Electric Field on the Skin for $\theta_o=\pi/2$ & $\varphi_o=0$	124
3.48 SAR of the Skin for $\theta_o=\pi/2$ & $\varphi_o=0$	124
3.49 Magnitude of Electric Field on the Skin for $\theta_o=2\pi/3$ & $\varphi_o=\pi$	125
3.50 SAR of the Skin for $\theta_o=2\pi/3$ & $\varphi_o=\pi$	125
3.51 Γ_{21} for the skin-skull interface for $\theta_o=\pi/4$ & $\varphi_o=\pi$	129
3.52 T_{12} for the skin-skull interface for $\theta_o=\pi/4$ & $\varphi_o=\pi$	129
3.53 Γ_{32} for the skull-brain interface for $\theta_o=\pi/4$ & $\varphi_o=\pi$	130
3.54 T_{23} for the skull-brain interface for $\theta_o=\pi/4$ & $\varphi_o=\pi$	130
3.55 Γ_{21} for the skin-skull interface for $\theta_o=\pi/2$ & $\varphi_o=0$	131
3.56 T_{12} for the skin-skull interface for $\theta_o=\pi/2$ & $\varphi_o=0$	131
3.57 Γ_{32} for the skull-brain interface for $\theta_o=\pi/2$ & $\varphi_o=0$	132
3.58 T_{23} for the skull-brain interface for $\theta_o=\pi/2$ & $\varphi_o=0$	132

3.59 Γ_{21} for the skin-skull interface for $\theta_o = \pi/4$ & $\varphi_o = 3\pi/2$	133
3.60 T_{12} for the skin-skull interface for $\theta_o = \pi/4$ & $\varphi_o = 3\pi/2$	133
3.61 Γ_{32} for the skull-brain interface for $\theta_o = \pi/4$ & $\varphi_o = 3\pi/2$	134
3.62 T_{23} for the skull-brain interface for $\theta_o = \pi/4$ & $\varphi_o = 3\pi/2$	134
4.1 A scalar product neuron ([50] Fig. 1, pp. 24)	137
4.2 Multi-layers networks ([50] Fig. 2, pp. 24)	138
4.3 The Neural Network Used for Beamforming ([51] pp. 3-6)	142
4.4 Tan-sigmoid transfer function used in the hidden layer ([51] pp. 3-4)	142
4.5 Detailed interconnections for each layer. Note that here the <i>logsig</i> neuron is shown but in the thesis the <i>tansig</i> and the <i>purelin</i> neurons are used instead. This figure is only shown to illustrate what actually goes ([51] pp. 3-5)	143
4.6 Linear transfer function used in the output layer ([51] pp. 3-4)	143
4.7 MSE versus Epochs for Network 1	144
4.8 MSE versus Epochs for Network 2	145
4.9 MSE versus Epochs for Network 3	145
4.10 MSE versus Epochs for Network 4	146
4.11 Comparison of $Re\{I_{opt}\}$ for the first 15 elements between the neural network and the exact output for $\theta_o = \pi/6$ & $\varphi_o = 2\pi$	147

4.12 Comparison of $Re\{I_{opt}\}$ for the other 27 elements between the neural network and the exact output for $\theta_o=\pi/6$ & $\varphi_o=2\pi$	147
4.13 Comparison of $Im\{I_{opt}\}$ for the first 15 elements between the neural network and the exact output for $\theta_o=\pi/6$ & $\varphi_o=2\pi$	148
4.14 Comparison of $Im\{I_{opt}\}$ for the other 27 elements between the neural network and the exact output for $\theta_o=\pi/6$ & $\varphi_o=2\pi$	148
4.15 Comparison of $Re\{I_{opt}\}$ for the first 15 elements between the neural network and the exact output for $\theta_o=\pi/2$ & $\varphi_o=2\pi$	149
4.16 Comparison of $Re\{I_{opt}\}$ for the other 27 elements between the neural network and the exact output for $\theta_o=\pi/2$ & $\varphi_o=2\pi$	149
4.17 Comparison of $Im\{I_{opt}\}$ for the first 15 elements between the neural network and the exact output for $\theta_o=\pi/2$ & $\varphi_o=2\pi$	150
4.18 Comparison of $Im\{I_{opt}\}$ for the other 27 elements between the neural network and the exact output for $\theta_o=\pi/2$ & $\varphi_o=2\pi$	150
4.19 Comparison of $Re\{I_{opt}\}$ for the first 15 elements between the neural network and the exact output for $\theta_o=0$ & $\varphi_o=0$	151

4.20 Comparison of $Re\{I_{opt}\}$ for the other 27 elements between the neural network and the exact output for $\theta_o=0$ & $\varphi_o=0$	151
4.21 Comparison of $Im\{I_{opt}\}$ for the first 15 elements between the neural network and the exact output for $\theta_o=0$ & $\varphi_o=0$	152
4.22 Comparison of $Im\{I_{opt}\}$ for the other 27 elements between the neural network and the exact output for $\theta_o=0$ & $\varphi_o=0$	152
4.23 Comparison of $Re\{I_{opt}\}$ for the first 15 elements between the neural network and the exact output for $\theta_o=5\pi/6$ & $\varphi_o=2\pi$	153
4.24 Comparison of $Re\{I_{opt}\}$ for the other 27 elements between the neural network and the exact output for $\theta_o=5\pi/6$ & $\varphi_o=2\pi$	153
4.25 Comparison of $Im\{I_{opt}\}$ for the first 15 elements between the neural network and the exact output for $\theta_o=5\pi/6$ & $\varphi_o=2\pi$	154
4.26 Comparison of $Im\{I_{opt}\}$ for the other 27 elements between the neural network and the exact output for $\theta_o=5\pi/6$ & $\varphi_o=2\pi$	154
5.1 A typical RF antenna array transmitter	157
5.2 A typical RF antenna array receiver	157
5.3 RC Circuit to be used for the All-Pass Filter	159

5.4 Circuit Topology for the First Order All-Pass Filter	160
5.5 The two differential-to-single ended amplifiers to realize the voltage differences needed	164
5.6 Voltage Gain versus Frequency for v_{o1}	166
5.7 Voltage Gain versus Frequency for v_{o2}	167
5.8 Phase Response versus Frequency for v_{o1} & v_{o2}	168
5.9 (a) Symbolic representation of an antenna element & (b) Circuit model representation of an antenna element with inductive reactance	169
5.10 Class E Power Amplifier (PA)	173
5.11 Position of R	174
5.12 (a) The simplified circuit, (b) The same circuit with the transformation of the RL series connection to an RL parallel connection	175
5.13 V_{DS} time response of the PA	176
5.14 I_{DS} time response of the PA	177
5.15 The normalized drain voltage and current time responses	178
5.16 Tuned RF amplifier	179
5.17 Frequency response of the output voltage for several values of V_c	181
5.18 LNA circuit	182

5.19 Small signal model of M1	184
5.20 Frequency response of LNA	187
5.22 RF adder capable of adding 5 RF signals	188
5.23 Adder structure to combine all 42 signals	189
5.24 Voltage time response, output versus input	191
D.1 Circuit topology for the phase shifter given in Chapter 5	208
D.2 Small signal model of the phase shifter (excluding the difference circuits)	209
D.3 Simplified small signal circuit model	209
E.1 RF tuned amplitude amplifier	211
E.2 Small signal model of the RF amplitude at resonance	212
F.1 Series to Parallel Transformation	214

Chapter 1: Introduction

1.1 Basic Ideas

The topic of radio-frequency (RF) circuits for antenna arrays is very important because of its endless applications in the field of communication. Antenna array circuits provide the ability of any transceiver to send or receive a signal or multiple signals to or from specific points of interest. This means that antenna arrays possess the ability of directivity and are capable of improving the signal-to-noise (SNR) ratio of the signal.

Designing an antenna array circuit incorporates the knowledge of different engineering disciplines. An array consists of a number of antenna elements distributed on some kind of a geometric surface area such as linear, cylindrical or spherical geometries. The design of each element and determining what kind of electromagnetic field it will generate requires the knowledge of antenna and electromagnetic theory. When considering the transmitter or receiver circuits, this requires the knowledge of RF electronics and the sub circuits that make up the transceiver. Finally, the main purpose of the array is to concentrate or direct its total power or field towards a specific direction (known as beam steering or beamforming), and this requires the design of an algorithm or technique to carry out this task and this is considered as signal processing for beamforming.

As it will be explained in Chapter 2, most of the literature on antenna array theory is based on what is known as the far field approximation. This approximation simply means that the point of observation or the target where the beam is directed to is far away from the array. This assumption dramatically simplifies the antenna theory. The difficulty usually rises from the shape of the antenna element used and the geometric distribution of the elements.

1.2 Research Motivation

In this thesis it is desired to make use of an antenna array in medical applications where the observation point can be anywhere. The observation point can be right under the array (i.e. near field) or somewhere in between the far and the near field zones known as the intermediate zone [1]. The present day array theory and related circuits will not be sufficient to handle this task because of the far field approximation. The aim of this thesis is to design an antenna array circuit that is capable of transmitting and receiving signals in the intermediate zone.

The main attraction of this new array theory is in the design of a hemispherical antenna array for controlling the magnetic field pattern inside the hemispherical surface. A possible application of this array would be when considering that the array can be placed on top of a human's head. This array can be used in Hyperthermia Cancer Treatment for brain cancer. The array may also serve as a possible alternative in treating patients that suffer from Parkinson's Disease.

In hyperthermia applications, the antenna array can be used to cause a noninvasive field focusing areas in the brain with cancer tumors. This focusing of the total field

will cause an increase in cell temperature at the desired point in the brain (i.e. tumor location) and will result in killing the cancer cells.

The array may also offer [61] a noninvasive approach in causing magnetic stimulation in the specific area of the brain as needed. Noninvasive in the sense that this method can help avoid the need of surgery to place the deep brain stimulator apparatus. By negating the need for deep brain stimulators, the patient does not need to change the battery of the stimulator every 2 to 7 years or worry about being in close proximity to devices that emit magnetic fields, which cause malfunction in currently used stimulators [2].

Since the array is capable of transmitting in a desired point in the brain to stimulate that part then the reciprocal should be possible. Many medical applications involve the reception of brain waves, by applying some stimulant, using some kind of an array placed on the top of the patient's head. Stimulants can test to see how the brain will react to anything like specific sounds, visual images, smell etc. The antenna array can be a valuable tool in indentifying the exact point in the brain that will react to such stimulants.

Another interesting application of the array is its possible use in radio-frequency identification (RFID) and implemental microelectronic devices (IMD). These are two major categories of devices where a reader and a tag (usually embedded in the body) communicate wirelessly with over a short distance through loosely coupled coils. RFID systems are used in applications such as access control, transportation, traceability and wireless sensing [16]. On the other hand, IMDs are used in medical

devices for both diagnosis and treatment of a wide variety of conditions such as pacemakers, retinal implants, cochlear implants, deep brain stimulators, spinal cord stimulators and brain-machine interfaces.

Many design issues affect the performance of RFID and IMD. These are: (1) power transmitted by reader; (2) coupling efficiency; (3) power dissipation; (4) reader sensitivity; (5) resonator circuit quality factor (Q); and (6) data modulation and demodulation.

In the literature the key factor is optimizing the power transmission and this is done by having an efficient and robust inductive link. Efficient in the sense that the inductors used for the link are designed with minimal parasitic resistance and optimum geometric shape. To have a robust link means that it must be insensitive to power level fluctuations. One of the factors that cause power level fluctuations is coil misalignment. The misalignments can take several forms and they are: link coils moving away or closer to each other and coils of the link shift laterally or angularly which means that, for near zone RFID/IMD, the secondary coil in the link will not be exposed to the optimum magnetic field flux lines. In the literature the problem of misalignment is partially solved by using power control units. This approach does not solve the problem of lateral and angular misalignments.

To overcome the problem of misalignments in an inductive link, and hence increase the power transfer efficiency, an antenna array will be used but of course with a geometrical layout that best fits the situation given. The antenna array will be

used to focus the magnetic field flux lines to the direction of optimum reception of the secondary coil. The array will form an electronically beam steered RFID system.

As mentioned before, the task of building an antenna array circuit requires the integration of many components. After setting the antenna theory and finding the proper expressions for the electromagnetic fields it is evident that regular beam steering algorithms are unsatisfactory for the intermediate zone since in this zone there is no decoupling between the radial and angular components of fields. The angular dependence alone makes up what is known as the *array factor* and in the intermediate zone the radial and angular components are meshed together so the concept of array factor no longer exists. This issue is addressed in this thesis and a satisfactory solution is reached.

When considering the RF front end circuit for the transceiver an important component is the phase shifter. The phase shifter is the RF component responsible in causing a controlled phase change in the RF signal before transmitting it or after receiving it. The phase shifters in the literature (see Chapter 2) have many drawbacks. To cause a phase shift many phase shifters use inductors or capacitors. The problem with inductors is that they are hard to integrate on chip and still maintain a high quality factor. Another issue is that inductors consume a large area on the chip itself so it would be beneficial to eliminate the need of using inductors when designing phase shifters. Other phase shifters are Gilbert Cell like circuits ([26] & [27]) and ones that cause a phase shift by making use of the trigonometric identity (explained in Chapter 2). Unfortunately these circuits are complicated and large to design and also they require complicated schemes for phase control. These issues have lead to the

design of new kind of phase shifters that are based on all-pass filter topology. The new phase shifter requires no inductors, it is very compact (relative to other designs) and the phase control is analog and achieved with ease.

1.3 Dissertation Outline

The dissertation is divided in the following manner: Chapter 1 contains the *Introduction* with motivation to the main ideas presented for research; Chapter 2 deals with the *Literature Review* that is the basis on which the new theory and design is built; Chapter 3 deals with the *Antenna Array Theory and Beamforming Techniques* used for transmission and reception; Chapter 4 deals with the theory and application of the *Neural Network* which is used to execute the beamforming techniques; Chapter 5 deals with the *RF Electronics* designed and simulated using PSPICE; and finally Chapter 6 contains the *Conclusion & Future Work* of the theory and techniques presented throughout the thesis.

In Chapter 2 will include the literature review. The literature will cover many topics. Beginning with the papers on RFID and IMD circuits, the literature will be presented showing the basic mechanism of these kinds of circuits. After that the problem with the misalignment between the RFID reader and tag will be addressed. The process of Hyperthermia Therapy for brain cancer will be discussed. Another medical device which is the *Deep Brain Stimulator* (DBS) will be explained. The function of the device and its drawbacks will be shown and an indication to the possible solution will be addressed. Finally, the RF components of the antenna array will be shown. The RF circuits will be for transmission and reception.

Chapter 3 deals with the main theory of the entire thesis. This is the theoretical study of the antenna array in the intermediate zone. This antenna array will have a hemispherical geometry since it will be placed on the top of the human head. It deals with the design of the antenna elements and their geometrical distribution. The equations for the electromagnetic fields will be derived with no approximation. After getting the form of the fields, a new beamforming technique will be presented that will allow the array to direct the main beam towards the direction of interest regardless of the distance between it and the array. The beamforming technique followed will allow the transmission and reception in multiple directions. Since the array will be possibly used in a medical application, health issues such as field exposure will be taken into account. Finally, it will be shown how the antenna array can be incorporated in IMD applications where there is a loosely coupled inductive link between the reader and the tag. The tag can be embedded inside a human's body and the reader will be formed by an array of antennas. Since, for a tag inside the body, there is no control over it when it is bent or twisted from within. This will cause a misalignment as mentioned earlier. The antenna array can be used here to direct the beam to the direction that is going to maximize the power transfer efficiency of the inductive link.

A neural network will be presented in Chapter 4, for use in offering real time beamforming for the antenna array. The main idea of the neural network will be discussed and the minimization algorithm that the network uses to reach its desired function will be explained.

The RF electronics will be presented in Chapter 5. Chapter 5 is the chapter where circuit theory will be presented. Since a transmitter and a receiver will be designed, the chapter will discuss the theory and design of the following components: power amplifier (PA), low noise amplifier (LNA), phase shifter, RF adders and RF amplifiers. The role of each component will be explained theoretically and its circuit designed and simulated using PSPICE.

1.4 List of Contributions

The contributions of this thesis can be summed in the following points:

- 1- Design of a hemispherical antenna array that is capable to direct the electromagnetic fields in the intermediate zone (where no approximations are applicable).
 - a. A new beamforming technique developed which makes use of the orthogonality property of the TE and TM modes of the electromagnetic fields. This technique enables the use of this antenna array in application where the point of interest is in close proximity to the array.
 - b. The antenna array is capable of targeting the magnetic field in multiple directions as desired.
 - c. The antenna array was considered at a frequency of 1.8GHz
- 2- The hemispherical antenna array can also be used as a receiver of magnetic field sources from within the hemispherical surface.

- a. A new beamforming technique for reception is developed using the TE and TM modes orthogonality property.
 - b. The beamforming technique enables the antenna array to receive and distinguish multiple signals from multiple points from within the brain.
- 3- An RF transmitter and receiver are designed and simulated in PSPICE. The circuits used standard power amplifiers, low noise amplifiers and RF amplitude amplifiers. The contribution of this thesis is in the design of a new RF phase shifter which is based on the all-pass filter topology. Another RF component designed is an RF adder.
- 4- A neural network is designed and simulated in MATLAB that is capable of approximating the function of the beamforming technique.

Chapter 2: Literature Review

2.1 Traditional Antenna Arrays

2.1.1 Main Concepts

The work done on antenna arrays is extensive in the literature, but most of the work assumes either the near zone or the far zone approximation. It turns out that for most applications these approximations are enough and there is no need to deal with the complications of solving the electromagnetic fields in its most general form. There are three main zones of operation, static, intermediate and radiation. In [1] these zones of operation are defines as follows:

$$d \ll r \ll \lambda ; \text{Near (static) zone}$$

$$d \ll r \approx \lambda ; \text{Intermediate (induction) zone}$$

$$d \ll \lambda \ll r ; \text{Far (radiation) zone}$$

Where d , is the largest dimension of the antenna element, r is the distance from the observation point to the origin of the antenna element and λ is the wavelength of the frequency of operation. Most of the studies in the literature deal with the static and radiation zones. Antenna arrays are usually used for far field zones, since the designer has the ability to change the phase (electronically) of each element in the array such that the main beam of each element is directed to a desired direction (note that also the shape of the antenna plays an important role in beam directivity). The ability rises

from the exponential term that survives in the expressions of the electromagnetic fields. The theory starts from considering Maxwell's equations [3, pp: 15].

$$\nabla \times \vec{E} = -i\omega\vec{B} \quad (2.1a)$$

$$\nabla \times \vec{H} = i\omega\vec{D} + \vec{J} \quad (2.1b)$$

$$\nabla \cdot \vec{D} = \rho \quad (2.1c)$$

$$\nabla \cdot \vec{B} = 0 \quad (2.1d)$$

Where E is the electric field, H is the magnetic field intensity, $B=\mu H$, $D=\epsilon E$, i is the complex quantity $\sqrt{-1}$, ρ is the charge density, ϵ is the permittivity, μ is the permeability, J is the current density and ω is the frequency in rad/s. By introducing a new variable called the *vector potential* which is given by:

$$\vec{B} = \nabla \times \vec{A} \quad (2.2)$$

By working through the equations an expression for the vector potential can be reached [3]:

$$\vec{A}(\vec{r}) = \int_V \frac{\mu_0 \vec{J}(\vec{r}') dV'}{4\pi |\vec{r} - \vec{r}'|} e^{-jk_0|\vec{r} - \vec{r}'|} \quad (2.3)$$

This is the general equation for the vector potential for an arbitrary current distribution. The terms in (2.3) V represents the volume of the arbitrary current, \vec{r} is the radial vector that points from the origin of the current to the point of observation, \vec{r}' is the radial vector that points from the origin to the current distribution and k_0 is

the wavenumber in vacuum. Now by applying the far field approximation that assumes that the point of observation is far away from the current distribution and takes the following form:

$$|\vec{r} - \vec{r}'| \approx r - \hat{r} \cdot \vec{r}' \quad (2.4)$$

Where \hat{r} is the radial unit vector. With the far field assumption, equation (2.3) simplifies to the standard vector potential equation which is used in antenna arrays.

$$\vec{A}(\vec{r}) = \frac{\mu_0 e^{-jk_0 r}}{4\pi r} \int_V \vec{J}(\vec{r}') e^{jk_0 \hat{r} \cdot \vec{r}'} dV' \quad (2.5)$$

It is clear from (2.5) how the far field approximation greatly simplifies the task of making an antenna array. From equation (2.5) the expression for the electric field (E-field) is given by the following equation.

$$\vec{E}(\vec{r}) = \frac{jk_0 Z_0 e^{-jk_0 r}}{4\pi r} \vec{f}(\theta, \varphi) \quad (2.6)$$

Where $\vec{f}(\theta, \varphi)$, which is the integral in (2.5), describes the angular dependence of the radiation distribution in space and the term $e^{-jk_0 r} / 4\pi r$ describes the outward-propagating spherical wave function. The far field approximation enables the decoupling between angular dependence and the travelling spherical wave function.

A typical antenna array for N elements is shown in Fig. 2.1 where the expression for the E-field is similar to that shown in (2.6). The total electric field due to N elements is given by [4]:

$$\vec{E}_{Total}(\vec{r}) = \sum_{i=1}^N \vec{E}_i(\vec{r}) \quad (2.7)$$

(2.7) simply states the total field is simply the summation of the fields for N antenna elements. The total magnetic field intensity is given by the following equation.

$$\vec{H}_{Total}(\vec{r}) = \frac{1}{Z_0} \hat{r} \times \vec{E}_{Total}(\vec{r}) \quad (2.8)$$

Where $Z_0 = \sqrt{(\mu_0/\epsilon_0)}$ is called the *intrinsic impedance*. The total angular dependence factor or the *pattern function* is given by the following equation.

$$\vec{f}_{Total}(\theta, \phi) = \sum_{i=1}^N I_i \vec{f}_i(\theta, \phi) \quad (2.9)$$

Where I_i is the current of the i th antenna element and $f_i(\theta, \phi)$ is the same as that given in (2.6).

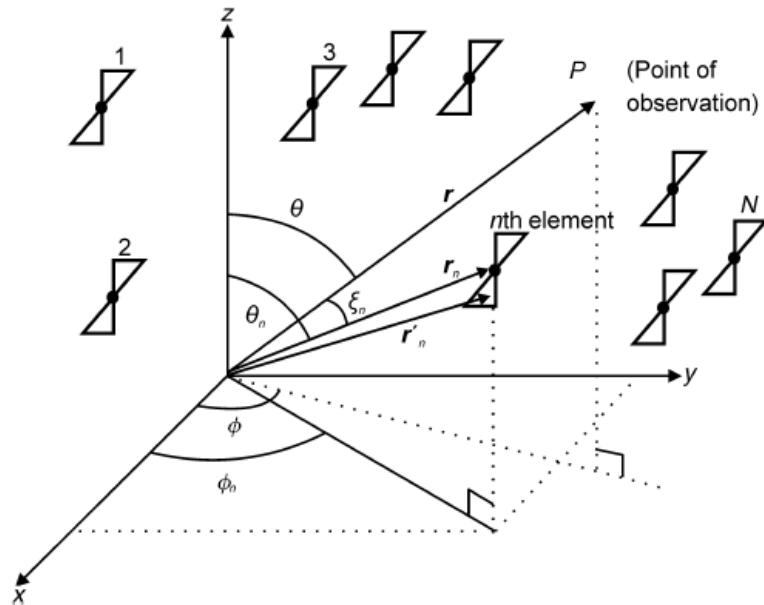


Fig 2.1. Geometry of an Antenna Array with N Identical and Parallel Elements ([4] Fig 1.1, p.2).

By considering the geometry of the array presented in Fig. 2.1, the E-field will take the following form.

$$\bar{E}(\bar{r}) = \frac{jk_0 Z_0 e^{-jk_0 r}}{4\pi r} \bar{f}(\theta, \varphi) \sum_{i=1}^N I_i e^{jk_0 r_i \cos(\xi_i)} \quad (2.10)$$

Where $\cos(\xi_i) = \sin(\theta)\sin(\theta_i)\cos(\varphi - \varphi_i) + \cos(\theta)\cos(\theta_i)$ and the angle ξ_i denotes the solid angle (shown in Fig. 2.1) between r and r_n . Note that the last term in equation (2.10) is called the *array factor* and it is given by the following equation.

$$AF(\theta, \varphi) = \sum_{i=1}^N I_i e^{jk_0 r_i \cos(\xi_i)} \quad (2.11)$$

Equation (2.11) is for a general antenna array. The array factor can be modified to fit the desired geometry of the array.

The *average radiated power* through a closed surface S of an antenna is given by the following equation [4]:

$$P_r = \frac{1}{2} \oiint_S \Re[\bar{E} \times \bar{H}^*] \cdot d\bar{s} \quad (2.12)$$

Where $\Re[\bar{E} \times \bar{H}^*]$ is the *Poynting Vector* and \Re represents the real part. Note that the total power of the antenna array is just the addition of the radiated power of the individual elements. The *radiation intensity*, which is defined as the power radiated per unit solid angle in a specific direction, is given by [4] (far field):

$$U(\theta, \varphi) = \frac{1}{2} \frac{r^2}{Z_0} |\bar{E}|^2 = \frac{1}{2} Z_0 r^2 |\bar{H}|^2 \quad (2.13)$$

Note that the total power radiated can be expressed in terms of the intensity by [4]:

$$P_r = \oiint_{\Omega} U(\theta, \varphi) d\Omega = \int_{\theta=0}^{\pi} \int_{\varphi=0}^{2\pi} U(\theta, \varphi) \sin \theta d\varphi d\theta \quad (2.14)$$

To calculate the *directivity* of the antenna, which is the ratio between the radiation intensity in a specific direction over the average radiated intensity, the following equation can be used.

$$D = \frac{U|_{(\theta_o, \varphi_o)}}{U_{average}} = \frac{U|_{(\theta_o, \varphi_o)}}{P_r} \quad (2.15)$$

Where the direction given by (θ_o, φ_o) is the simply the direction of interest.

Almost all of the entire antenna array theory in the literature is based upon the previous derivations. Note that all the equations presented assume that the fields have $e^{j\omega t}$ time dependence. To retrieve the physical fields simply multiply the fields by the factor $e^{j\omega t}$ and take the real part.

2.1.2 Beam Steering

Once the expressions for the electromagnetic field are established it is now time to show how beam steering is achieved. In the far field, the angular dependence is decoupled from the travelling wave function and so it can be dealt with independently. Depending on the application it is possible to direct the main beam of the array in two directions which are best described by the elevation angle θ and the azimuthal angle φ . Arrays where the elements are placed in a linear straight line have the ability to direct the beam with one degree of freedom (i.e. either θ or φ). To

achieve two degrees of freedom the geometrical distribution of the antennas should be in 2 or 3 dimension. Typical array configurations are shown in Fig. 2.2.

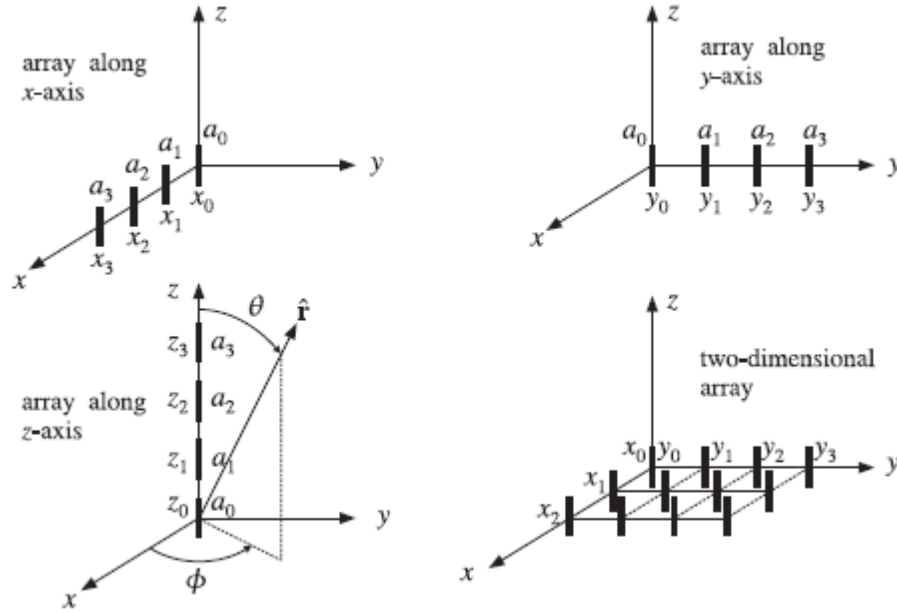


Fig. 2.2. Typical Array Configurations ([5] Fig. 19.1.1, p.772).

To explain how the beamforming process works the array configuration must be determined first (the configuration should be chosen to best fit the application). By determining the configuration the array factor can then be derived. From Fig. 2.3, three examples are given and for each the array factor is derived using the general equation (2.11). In the figure, (a) is an antenna array located on the positive x-axis, (b) is an antenna array located on either side of the origin and (c) shows an antenna array located on the non-negative portions of both the x-axis and the y-axis. The following set of equations show the array factor for the arrays given in Fig. 2.3 assuming that all elements are equally spaced and have the same currents [5].

$$AF_{(a)}(\varphi) = 1 + e^{jkd \cos \varphi} + e^{j2kd \cos \varphi} \quad (2.16)$$

$$AF_{(b)}(\varphi) = e^{-jkd \cos \varphi} + 1 + e^{jkd \cos \varphi} \quad (2.17)$$

$$AF_{(c)}(\theta, \varphi) = 1 + e^{jkd \sin \theta \cos \varphi} + e^{jkd \sin \theta \sin \varphi} \quad (2.18)$$

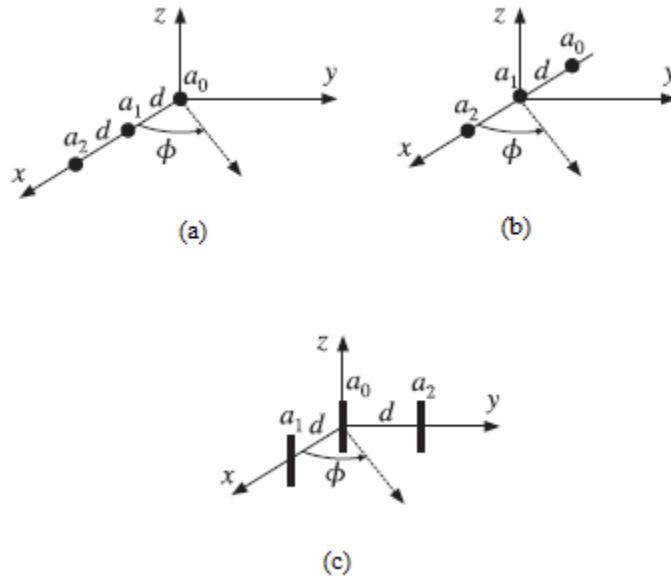


Fig. 2.3. Three Element Array (a) located on the positive x-axis; (b) located on the x-axis; and (c) located on both the x-axis and the y-axis ([5] *Example. 19.3.2 & 19.3.3, pp.774 & 776*).

The equations show the array factor that corresponds to Fig. 2.3 (a), (b) and (c) respectively. Note that the distance between each consecutive element is d . It is clear that equation (2.18) shows an array that has an array factor that is a function of both θ and φ . This means that the array of Fig. 2.3(c) is capable of directing its beams in all directions in the 3-dimensional space. The gain or the directivity of the antenna array is directly proportional to the square of the magnitude of the array factor.

Allowing the array elements to have different magnitudes, the array factor for equation (2.16) becomes:

$$AF(\varphi) = I_1 + I_2 e^{jkd \cos \varphi} + I_3 e^{j2kd \cos \varphi} \quad (2.19)$$

Considering the square of the magnitude of the array factor, the following equation can be written.

$$|AF(\varphi)|^2 = |I_1 + I_2 e^{jkd \cos \varphi} + I_3 e^{j2kd \cos \varphi}|^2 \quad (2.20)$$

To beam steer the antenna towards a specific angle φ_o , then the currents I_1 to I_3 should be set such that the square of the array factor is maximized. To maximize (2.20) for a certain angle φ_o set $|I_1|=|I_2|=|I_3|=1$ then set the phase of the currents should be changed to achieve the following equation.

$$|AF(\varphi)|^2 = |1 + e^{-jkd \cos \varphi_o} e^{jkd \cos \varphi} + e^{-j2kd \cos \varphi_o} e^{j2kd \cos \varphi}|^2 \quad (2.21)$$

By setting the currents as shown in (2.21), it is guaranteed that the square of the array factor would be maximum when $\varphi = \varphi_o$ since only at this angle the phases from all the elements will add up constructively to yield the maximum result which is 9. The maximum array factor gain that can be achieved from an array of with 3 elements with unity current magnitudes is 9. Of course higher gains can be reached if the magnitudes of the individual currents are increased. This process of changing the phase to maximize the array factor is called *electronic beam steering* and it is the aim of antenna arrays.

2.1.3 Direction of Arrival Estimation (DOA)

In the previous subsection, beam steering in the transmission case was discussed. Here beam steering in the reception case is introduced. There are many techniques for reception beam steering found in the literature [6]-[15]. The basic idea is to come up with an algorithm that will detect from where the signal is coming. This is usually done by first defining or calculating a real property of the signal that will be maximum in the direction where the signal is coming from and all what the designer have to do is try to scan for this maximum using some kind of an optimization scheme. According to [11], the algorithms for DOA estimation fall into the following 3 categories:

- 1- Spectral-based algorithm
 - a. Conventional beamformer
 - b. Capon's beamformer
- 2- Subspace-based methods
 - a. Multiple signal classification (MUSIC) method
 - b. Extension to MUSIC algorithm
- 3- Parametric methods
 - a. Deterministic Maximum likelihood method
 - b. Stochastic maximum likelihood method

Before looking at some of the techniques, the general build up of the theory is done in the following manner beginning with Fig. 2.4. The figure shows the basic receiver structure, there are 5 elements separated on a line by an equal distance d and the

signal is incident from an angle θ . When the antennas feed through their signals to the array circuit, each signal is updated by using a weight vector (w_i) to give the element output vector $x^V(t)$ which is given in (2.22) [11].

$$x^V(t) = a^V(\theta)s(t) \quad (2.22)$$

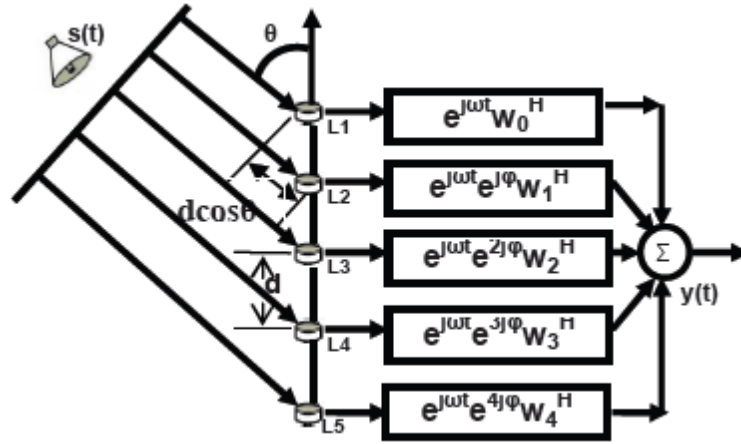


Fig. 2.4. A Typical Antenna Array Receiver Structure ([11] Fig. 3, pp. 423)

Where V denotes a column vector, $s(t)=exp(j\omega t)$ is the incoming normalized wave and $a^V(\theta)$ is the steering vector and it is given by [11]:

$$a^V(\theta) = \begin{bmatrix} 1 \\ e^{j\phi} \\ e^{j2\phi} \\ \cdot \\ \cdot \\ e^{j(L-1)\phi} \end{bmatrix} \quad (2.23)$$

Where the phase delay between the elements $\phi = -(d/\lambda)\cos\theta$ (λ wavelength of incoming signal) and L is the total number of elements in the array. If the receiver receives M signals from M DOA's $\theta_1, \dots, \theta_M$ then the output vector takes the form:

$$x^V(t) = A(\theta)s^V(t) = \begin{bmatrix} a^V(\theta_1) & a^V(\theta_2) & \dots & a^V(\theta_M) \end{bmatrix} \begin{bmatrix} s_1(t) \\ s_2(t) \\ \vdots \\ s_M(t) \end{bmatrix} \quad (2.24)$$

Finally, in the presence of additive noise, $n(t)$, the final form of the output vector is given by equation (2.25) [11].

$$x^V(t) = A(\theta)s^V(t) + n^V(t) \quad (2.25)$$

The idea of the DOA algorithm is to steer the array to all directions and for each direction calculate the output power. The directions with the highest power output will give the DOA estimates. The array response is formed and steered by forming a linear combination of the linear combination of the receiver's outputs.

$$y(t) = w^H x^V(t) \quad (2.26)$$

Where w is the weight vector multiplied to cancel the phase delay between the elements and H denotes the Hermitian of w . The output power is for each time sample is then calculated as follows [11]:

$$P(w) = \frac{1}{N} \sum_{t=1}^N |y(t)|^2 = w^H R w \quad (2.27)$$

Where N denotes the number of time samples taken, R is the *autocorrelation matrix* and is given by [11]:

$$R = \frac{1}{N} \sum_{t=1}^N w^H x^V(t) x^{VH}(t) w \quad (2.28)$$

After coming up with the equations it is now possible to use the methods stated at the beginning of this subsection. Looking at the first method would be sufficient since all the methods use similar concepts in which to transform the problem into a optimization problem and find the optimum weight vector w that will give the maximum power output at the DOA.

The conventional technique works by expressing the total power by using the following statement and then finding the weights that will optimize this statement.

$$\max_w E \{ w^H x^V(t) x^{VH}(t) w \} \quad (2.29)$$

Where E is the expected value and the maximization is done by maximization the expected value by adjusting the weight vector w . For this optimization to hold the following optimum weight vector is derived [11].

$$w_{opt} = \frac{a^V(\theta)}{\sqrt{a^{VH}(\theta)a^V(\theta)}} \quad (2.30)$$

From this equation the power function versus the angle of incidence θ is derived as [11]:

$$P_{opt} = \frac{a^{VH}(\theta)Ra(\theta)}{a^{VH}(\theta)a(\theta)} \quad (2.31)$$

In [11] a MATLAB simulation for an antenna array is done. The receiver receives two signals one at 45° and the other at 135° from the axis of the array. The power optimization scheme is done and the output power versus angle (2.31) is plotted in

Fig. 2.5. Note that the test done in [11] was to see will if the array can successfully receive two signals.

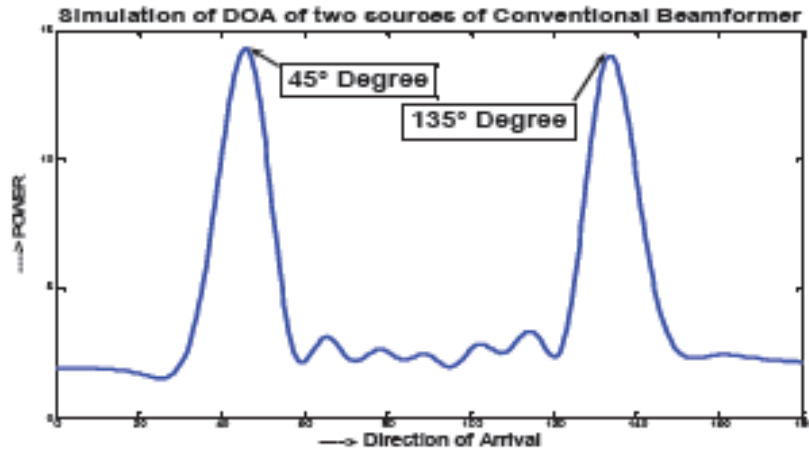


Fig. 2.5. DOA of Two Sources Using the Conventional Beamformer ([11] Fig. 5, pp. 424).

2.2 Transcutaneous Power and Data Transmission via Inductive Link

Transcutaneous power/data transmission via inductive link is the method in which near field passive *Radio Frequency Identification (RFID) Systems* and *Implantable Microelectronic Devices (IMD)* transfer power and data from the reader/source to the tag/implant. Although RFID systems also use far field *electromagnetic (EM) wave capture*, this dissertation focuses on the near field method.

RFID systems are used in applications such as access control, transportation, traceability and wireless sensing. On the other hand, IMDs are used in medical devices for both diagnosis and treatment of a wide variety of conditions such as

pacemakers, retinal implants, cochlear implants, deep brain stimulators, spinal cord stimulators and brain-machine interfaces.

Many design issues affect the performance of RFID and IMD. Among these are: (1) power transmitted by reader; (2) coupling efficiency; (3) power dissipation; (4) reader sensitivity; (5) resonator circuit quality factor (Q); and (6) data modulation.

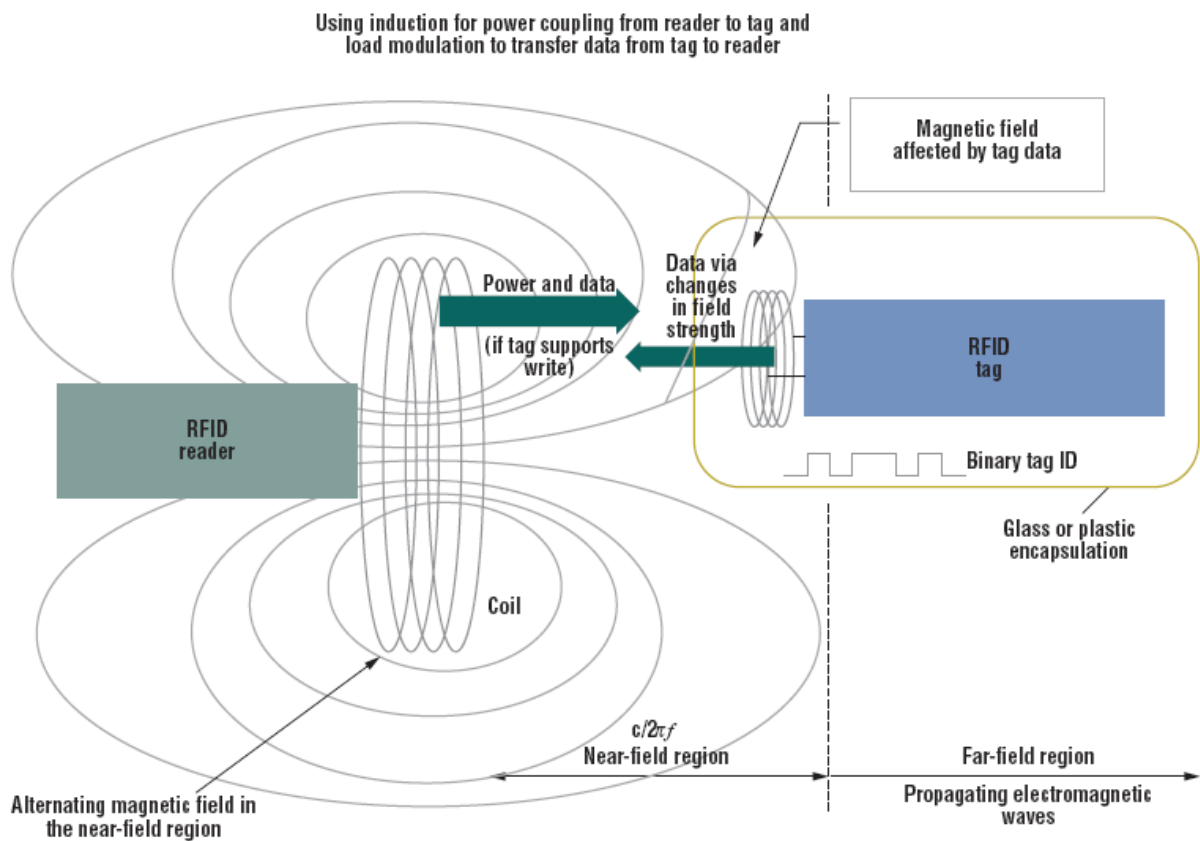
2.2.1 Principle of Operation

A near field RFID and IMD system, operating usually at frequencies less than 100 MHz, uses Faraday's principle of magnetic induction to couple between the reader and tag. In the case of an IMD system the reader is the external source and the tag is the implant. The reader passes a large alternating current through its transmitting coil antenna, resulting in an alternating magnetic field that in turn will induce an alternating voltage across the tag's receiving coil located in the near field. This voltage is then rectified and stored in a capacitor to act as the tag's voltage source. Fig. 2.6 (which is on the next page) shows the basic block diagram for a RFID and IMD.

Tags use the concept of *load modulation* to send back data to the reader. This is done by varying the impedance of the tag (by varying resistance or capacitance) which will cause a fluctuation in the current flow in the tag's coil. This fluctuation will generate a magnetic field that opposes the original field of the reader and, therefore, will be sensed by the reader as an induced voltage fluctuation.

The current limitations of the magnetic induction technique are: (1) the range for effective magnetic induction is approximated by $c/2\pi f$, as stated in [16], where c is the

speed of light and f is the frequency of operation. It is clear that as the frequency of operation increases, the range of the RFID/IMD is reduced. (2) The magnetic field drops off at a factor of $1/r^3$ [16], where r is the distance between the reader and tag. (3) In IMDs, coupling efficiency needs close attention since a layer of skin separates the reader from the tag. (4) It is stated in [17] that the magnetic field in the near zone is spatially static, meaning that it cannot be electronically focused or directed towards



a specific area (like in antenna arrays).

Fig. 2.6. A Typical Near-Field power/communication mechanism for RFID/IMD tags ([16] Fig 3,

p.28).

2.2.2 RFID/IMD Circuit Model

Figure 2.7 shows the basic circuit model for a transcutaneous power/data transmission system. The system consists of a power amplifier, an inductive link, rectifier and back telemetry, and the load. Note that in Fig. 2.7 the transponder is the tag or the receiver.

Since power efficiency is a critical factor in an IMD, the power amplifier used in transcutaneous systems is the *Class E Amplifier*. Theoretically, class E amplifiers have zero power dissipation because of their switching mechanism. The amplifier uses a high order reactive network that provides enough degrees of freedom to shape the switch voltage to both zero value and zero slope at switch turn on, thus reducing switch loss.

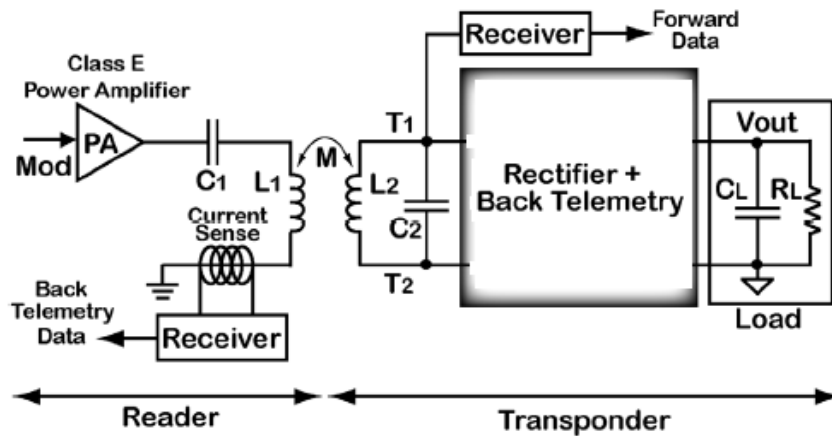


Fig 2.7. RFID/IMD Circuit Model ([19] Fig 1, p.801).

Figure 2.8 shows a typical class E amplifier. The big fat inductor *BFL* is used to provide a DC path to the supply and approximates an open circuit at RF (i.e an RF choke). The shunt capacitor C_1 is conveniently positioned to absorb device output capacitance. The inductor L and capacitor C_2 make up the primary resonator with the

resistance R representing the inductors series resistance. The design equations for a class E amplifier are given in [18] as:

$$L = \frac{QR}{\omega_o} \quad (2.32)$$

$$C_1 = \frac{1}{\omega_o R \left(\frac{\pi^2}{4} + 1 \right) \frac{\pi}{2}} \quad (2.33)$$

$$C_2 = C_1 \frac{5.447}{Q} \left(\frac{2.42}{Q - 2.08} \right) \quad (2.34)$$

Where Q is the inductor's quality factor and ω_o is the operating frequency. Note that the inductor L is also part of the inductive link since it represents L_1 in Fig. 2.7.

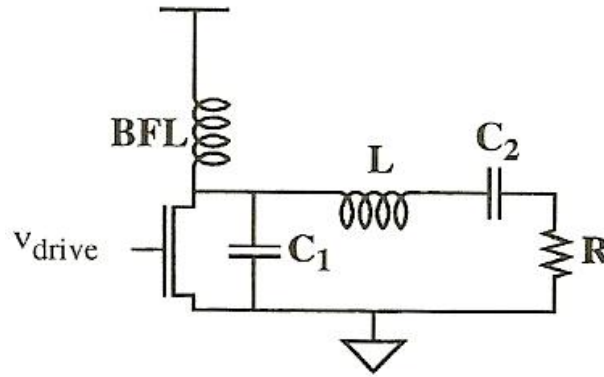


Fig 2.8. Class E Amplifier ([18] Fig 15.9, p.505).

Note that in Fig. 2.8, the voltage v_{drive} is the input signal of the PA.

Going back to Fig. 2.7, L_1 and L_2 represent the loosely coupled inductive link with a mutual inductance of M . The main function of the link is to transfer maximum

power from the amplifier to the transponder via magnetic induction. This will be explained in later sections.

The rectifier circuit (a rectifier is a circuit that extracts a DC signal from an AC one) can range in complexity from a simple diode and capacitor network, shown in Fig. 2.9, to a full wave CMOS rectifier, shown in Fig. 2.10 [19] where the input to the rectifier is across the terminals of L_2 (i.e. T1 & T2). Like any rectifier, the aim is to convert an AC voltage to DC and store it in a capacitor.

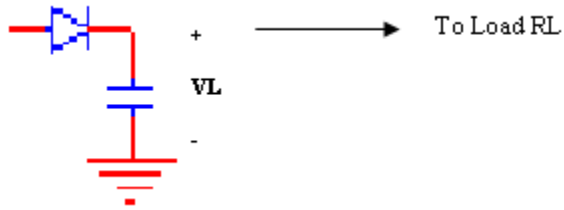


Fig. 2.9. Typical Rectifier.

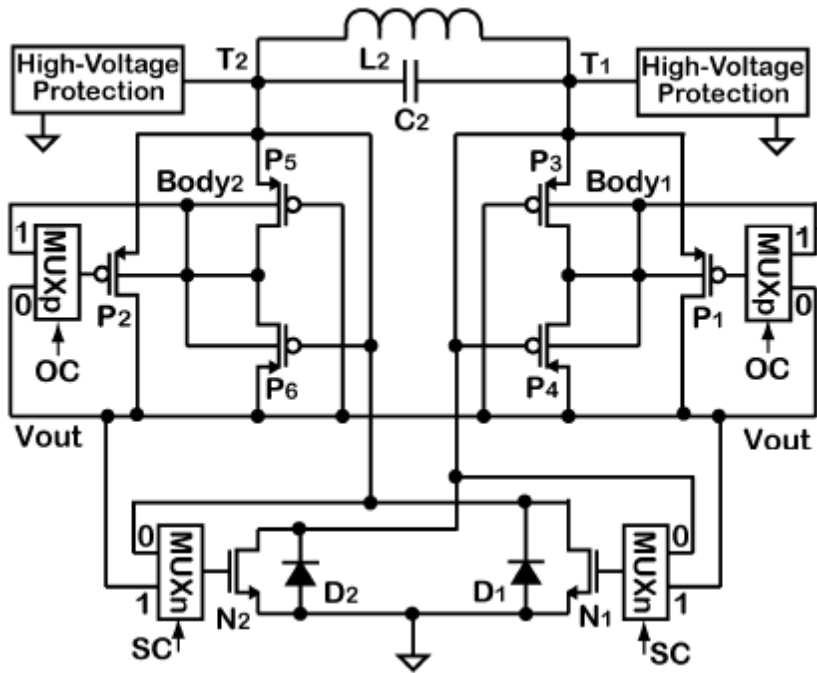


Fig. 2.10. Full-Wave CMOS Rectifier ([19] Fig 3, p.803).

The back telemetry in the tag is achieved by load modulation. The modulation is achieved by varying the reflected impedance seen by L_I . Impedance variation is achieved through resistive and capacitive means.

2.2.3 Inductive Link Design

As mentioned earlier, the inductive link is an essential component in optimizing the power transfer efficiency from the reader to the transponder. In [20] an optimum inductor coil structure is considered and an analytical model is presented. From the analysis an expression for the power transfer efficiency is derived that shows what factors are most effective.

Based on the model, lateral and angular misalignment issues are studied to show to what extreme these issues affect the power transfer efficiency. The equivalent model used in [20] for power transfer efficiency derivation is shown in Fig. 2.11.

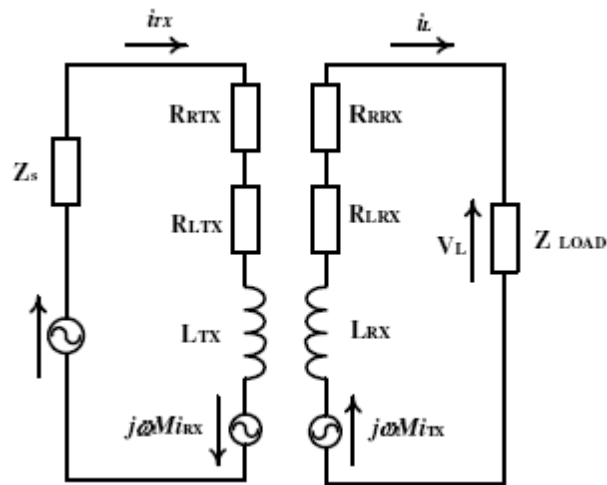


Fig. 2.11. Equivalent Circuit for Inductive Link Power Transfer ([20] Fig 1, p.72).

From the figure, Z_s represents the pure capacitive impedance that will resonate with the transmitter's inductance L_{TX} (which corresponds to L_I). The transmitter (Tx) is excited by a sinusoidal current $I_{Tx} = I_o e^{j\omega t}$. In [20] the circuit is analyzed to relate the magnetic intensity H with the power transfer efficiency ratio P_{RX}/P_{TX} . P_{TX} and P_{RX} are the Tx and Rx powers respectively, where Rx is the receiver. Following the derivation in [20], the following relationship can be realized:

$$\frac{P_{RX}}{P_{TX}} = \frac{\mu_0^2 A_{RX}^2 \omega^2 H^2}{16\pi^2 R_{TX} R_{RX}} \quad (2.35)$$

Where μ_o is the permeability of free space, A_{Rx} is the area occupied by the Rx coil, $R_{Tx} = R_{RTx} + R_{LTX}$ is the total Tx resistance and $R_{Rx} = R_{RRx} + R_{LRx}$ is the total Rx resistance.

It is clearly seen how important it is to increase the magnetic intensity and this leads [20] to the study of different geometric structures (circular coils and solenoids). Another important aspect is to study how lateral and angular misalignments affect the magnitude of the magnetic intensity and, hence, the power transfer efficiency. [20] studies three cases of coil alignment: (1) ideal coil configuration for the Tx and Rx coils; (2) lateral misalignment configuration for the Tx and Rx; and (3) angular misalignment configuration for the Tx and Rx.

Figures 2.12, 2.13 and 2.14 show the three coil cases considered. From these figures the magnetic field intensity between the coils is derived by using the Biot-Savart law and is found in [20] to be:

$$H_{Fig.2.13} = \frac{a^2 \pi}{(a^2 + D^2)^{3/2}} \quad (2.36)$$

$$H_{Fig.2.13} = \frac{a\sqrt{2m}}{(2a\Delta)^{3/2}} \left[\Delta K(m) + \frac{(am - (2-m)\Delta)E(m)}{2-2m} \right] \quad (2.37)$$

$$H_{Fig.2.14} = \frac{a^2 \pi \cos \gamma}{(a^2 + D^2)^{3/2}} \quad (2.38)$$

Where a is the radius of the Tx coil, D is the separation between the Tx and Rx coils, Δ is the lateral displacement, K & E are the complete elliptic integrals of the first and second kind, $m = 4a\Delta/[(a + \Delta)^2 + D^2]$ is the modulus and γ is the angle of tilt..

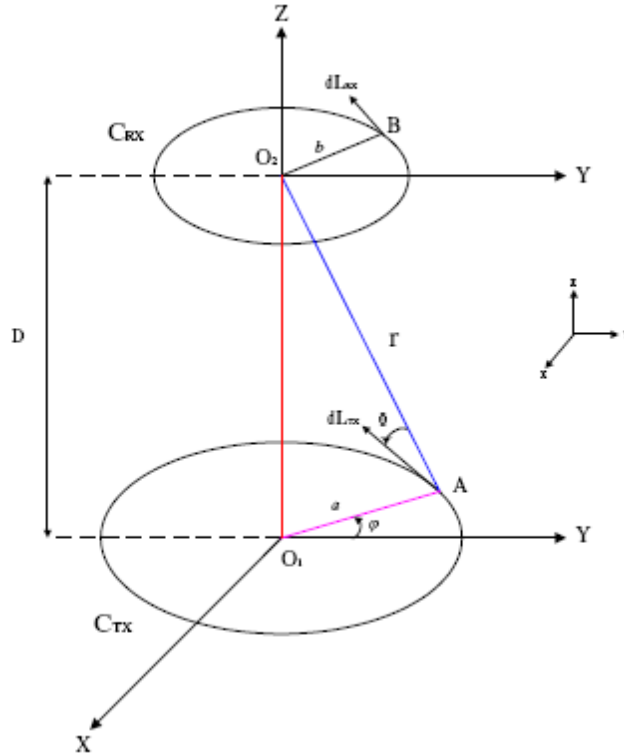


Fig. 2.12. Ideal Coil Configuration for the Tx and Rx Coils ([20] Fig 2, p.73).

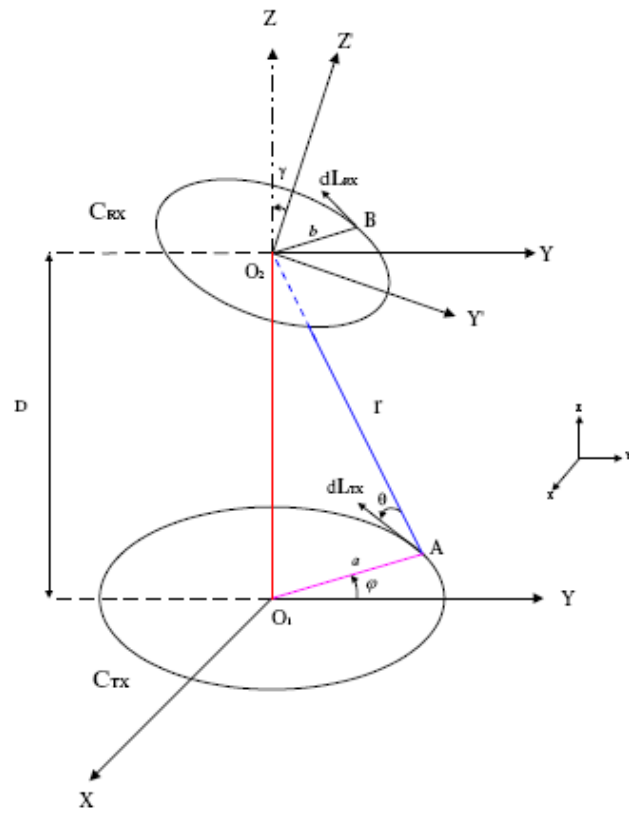


Fig. 2.14. Angular Misalignment Configuration for the Tx and Rx Coils ([20] Fig 4, p.73).

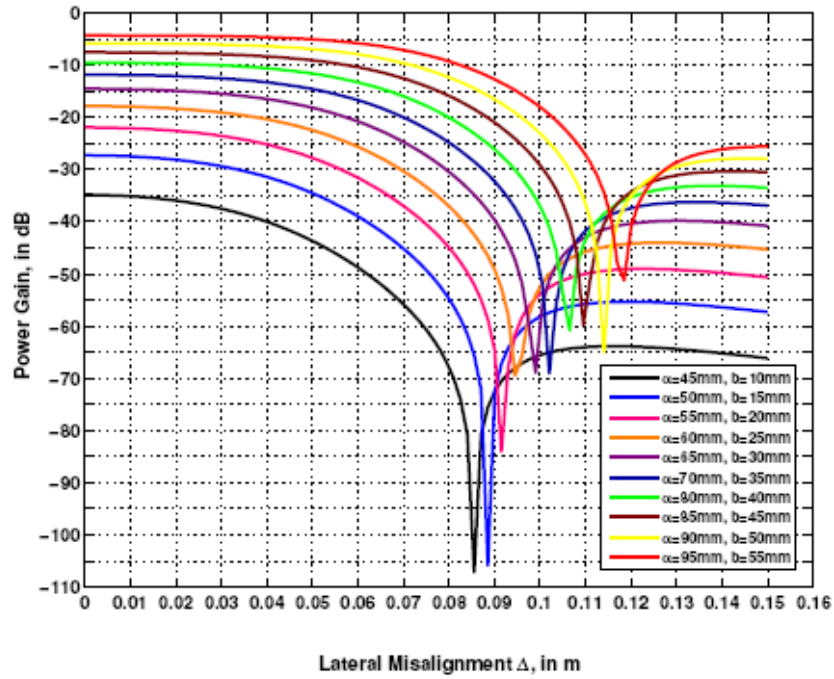


Fig. 2.15. Plot of Power Gain across the Inductive Link for a number of Tx, Rx Combinations, in the Lateral Misalignment Case ([20] Fig 5, p.74).

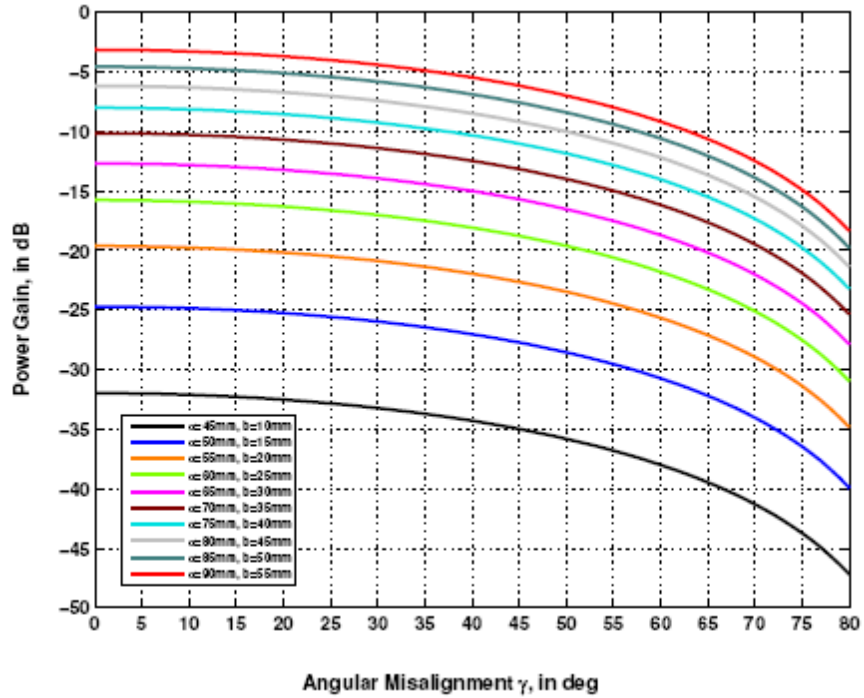


Fig. 2.16. Plot of Power Gain across the Inductive Link for a number of Tx, Rx Combinations, in the Angular Misalignment Case ([20] Fig 6, p.74).

2.2.4 Available Coupling-Insensitive Transcutaneous Links Techniques

Energy transfer is the bottle neck in RF links. This is why it is very important to study the issues that affect RF links. Bad geometrical alignment, like the cases discussed in [20], have a great impact on the power transfer efficiency. In [21] a coupling-insensitive transcutaneous link was designed. The idea was to have a self oscillating class E amplifier with a tapped primary inductance. Coupling variations cause an offset in the operating frequency, and in turn the operating frequency seeks the absolute transmission efficiency maximum. The down side of this technique is that it is more suited for relatively high coupling and no study was made on the efficiency losses due to the rectifier circuit.

A feedback approach used in [22] adds a geometric insight to the design of RF power links. A design approach was used to find a way to select an efficiency-maximizing load for an expected mean separation between the primary and secondary coils.

Another approach used in [23] focused on using a closed loop control for the class E amplifier with a power control unit. The methodology used was to stabilize the induced DC voltage in the secondary circuit by determining a compensating function in the feedback control loop. A derivative circuit was then realized that will compare two voltage levels, sensed by the a current sensor in the feedback loop of the class E amplifier, using this current the power control unit will drive the gate of the class E amplifier to adjust the power level. As a result the induced DC voltage (i.e. after

rectification) is kept at the desired level that will guarantee proper operation of the implanted circuitry.

2.3 RF Phase Shifters

The component that distinguishes the RF circuitry of the antenna array from any other RF circuit is the phase shifter. Phase shifters are essential building blocks in the design of antenna array transceivers. In the transmitter case, they provide the necessary phase shift for each RF signal in each antenna element to achieve electronic beamforming. In the receiver case they provide the necessary weight alteration (with the addition of voltage controlled gain amplifiers) to allow for the beamforming methods discussed earlier. There are many types of phase shifter topologies in the literature. In [24] the phase shifter in Fig. 2.17 is realized by utilizing a high pass filter topology where the phase shift is achieved by varying a tunable element. In this case two varactors and an active inductor are used for phase adjusting in which a phase shift range of 96° is achieved (from 14° to 110°) at 4 GHz (phase shifters at this frequency range are investigated since the desired antenna array transmitter is designed to operate in the gigahertz range). The active inductor is designed using a *gyrator-C* topology and is shown in Fig. 2.18. The main idea in this circuit is that the value of the active inductance is a function of the feedback resistance R_f . Thus, by controlling R_f it is possible to control the value of the inductance L (2.39) which in turn will enable the control of the phase φ [24].

$$L \approx \frac{2}{g_{m1,2}g_{m4}} \left[C_{gs4} \left(1 + \frac{R_f}{r_o} \right) + C_o \right] \quad (2.39)$$

$$\Phi = \frac{3\pi}{2} - \tan^{-1} \frac{2\omega CZ_o(1 - \omega^2 LC)}{1 - \omega^2 C(2L + CZ_o^2)} \quad (2.40)$$

Where $g_{m1,2}$ & g_{m4} are the transconductances of transistors M1, M2 and M4, respectively (Fig. 2.18), r_o is the output resistance seen by the differential pair, C_{gs4} is the gate-to-source capacitance of M4, C is the capacitance of the varactor (voltage control is applied to vary the value of C) shown in Fig. 2.17 and Z_o is the load impedance assumed to be connected to the output of the phase shifter.

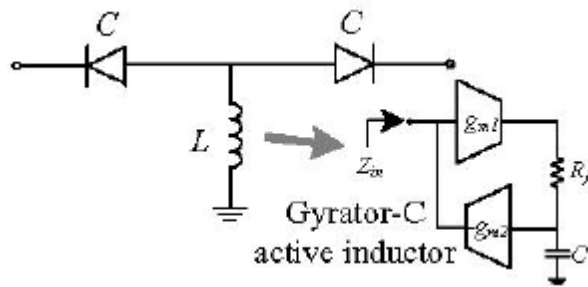


Fig. 2.17. The High-Pass Filter Phase Shifter ([24] Fig. 2, pp. 2174).

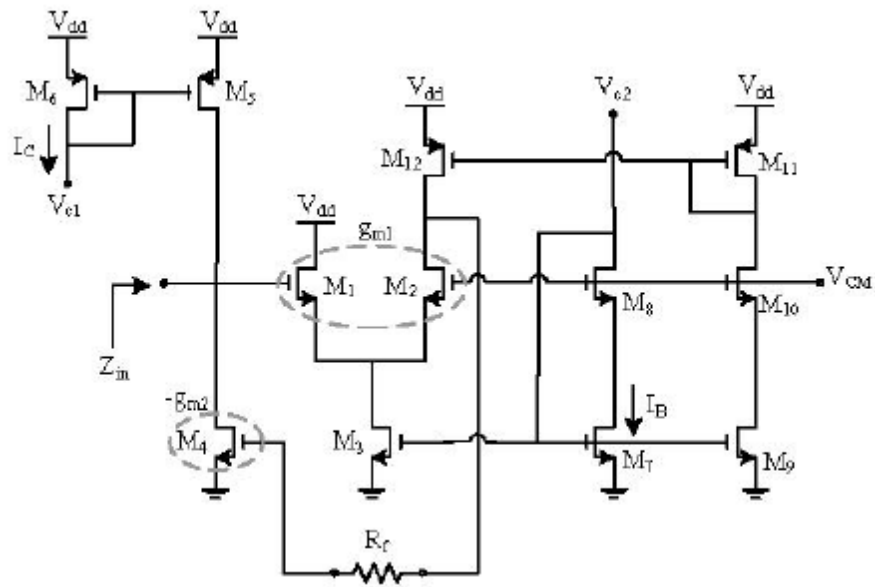


Fig. 2.18. Tunable Active Inductor with a Feedback Resistance ([24] Fig. 3, pp. 2174).

Reference [25] uses two common source transistors with a capacitor to the gate of one transistor and an inductor connected to each gate of the other to form a combination of highpass-lowpass amplifiers (Fig. 2.19). Phase shifting is achieved by varying the bias voltage (V_{GS}) of the transistors. The inductor is implemented using bondwire interconnects. The phase range achieved is 400° .

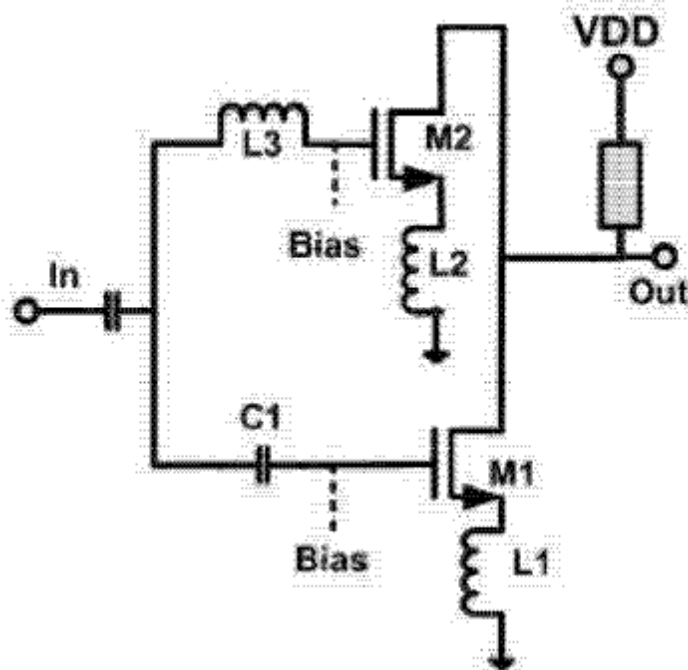


Fig. 2.19. Schematic of the Phase shifter ([25] Fig. 4, pp. 300).

The phase shifters in [26] and [27] perform phase shifting using similar methods. They both use a two Gilbert-cell type VGAs (*variable gain amplifiers*) where the gains are controlled by using *digital to analog converters* (DACs). The phase shifting of the signal is achieved by adding the signal to a 90° phase shifted replica of it (I & Q components) with proper gains in the current domain. [28] a phase rotator which follows the same concept as [26] and [27]. Fig. 2.20 shows the architecture of the

phase rotator. Phase shifting is accomplished in the current domain (i.e. the signal is a current). The rotator takes the I and Q components of the downconverted signal (signal is downconverted with a local oscillator of frequency ω_{LO2}) LO_2 as an input and applies a different gain (A_I and A_Q) independently to each of them using two digitally controlled *variable gain amplifiers (VGA)*. By adding the two VGA outputs in the current domain, the desired phase (ϕ_{out}) and amplitude (A_{out}) can be interpolated in the Cartesian coordinates of the I and Q outputs.

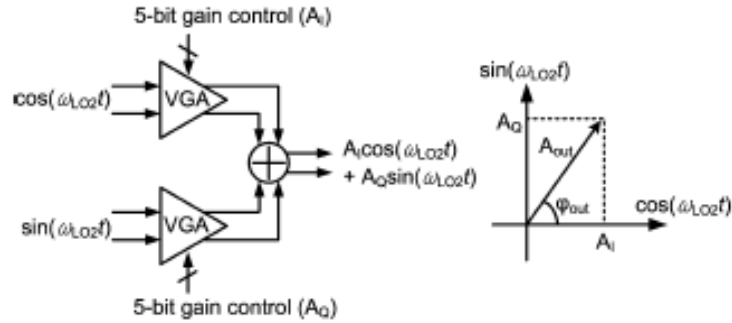


Fig. 2.20. Block diagram of the phase shifter ([28] Fig.12, p.2667).

The analysis of the above circuit can be done by assuming an input current signal $I_I(t)=\cos(\omega_{LO2}t)$ and its 90° phase shifted copy $I_Q(t)=\sin(\omega_{LO2}t)$ each amplified using the VGA's (current wise) with gains A_I and A_Q respectively. The output current $I_{out}(t)$ is given by [28]:

$$I_{out}(t) = A_I \cos(\omega_{LO2}t) + A_Q \sin(\omega_{LO2}t) \quad (2.41)$$

Now if we consider the gain amplitudes $A_I=A\cos(\phi)$ and $A_Q=A\sin(\phi)$, where ϕ is the desired phase shift, then equation (2.41) becomes:

$$\begin{aligned}
I_{out}(t) &= A \cos(\varphi) \cos(\omega_{LO_2}t) + A \sin(\varphi) \sin(\omega_{LO_2}t) \\
I_{out}(t) &= A [\cos(\varphi) \cos(\omega_{LO_2}t) + \sin(\varphi) \sin(\omega_{LO_2}t)] \\
I_{out}(t) &= A \cos(\omega_{LO_2}t - \varphi)
\end{aligned}
\tag{2.42}$$

In this way the desired phase shift is achieved.

The desired gains are controlled by the VGA shown in Fig. 2.21. The VGA combines five transconductance amplifiers in the current domain with digitally switched bias voltages. TA₁ and TA₂, TA₃ and TA₄ are two sets of identical pairs of transconductance amplifiers that constitute current-commutating cells by digital switches (SW₁ and SW₂). Each transconductance amplifier has a differential common-source topology with resistive degeneration. Since the output port is configured with open drains, the output signals from each array element can be easily combined in the current domain using a passive network which imposes little additional impact on the nonlinearity performance.

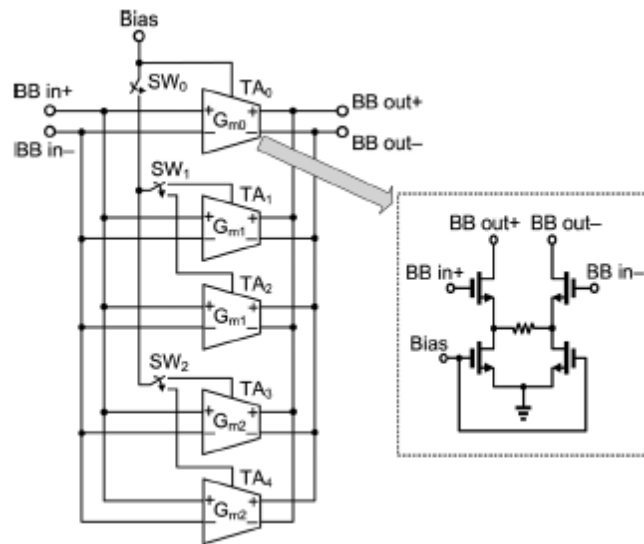


Fig. 2.21. Baseband VGA ([1] Fig.8, p.2665).

In [29] the phase shifter is designed by using a ring oscillator with phase-locked loop architecture to achieve phase shifting in the gigahertz range. In [30] a phase shifter is devised by using an all-pass filter topology in which a regular all-pass filter is achieved and then the phase is adjusted through the use of an analog voltage signal.

2.4 Hyperthermia Cancer Therapy

Hyperthermia is a clinical application used in oncology in which a temperature elevation in cancerous tissue is produced to induce cell death or make the cells more susceptible to radiation therapy or chemotherapy [62]. One method of inducing hyperthermia noninvasively is by focusing microwave energy at the tumor site. This is done in many different ways such as adaptive microwave phased-array techniques. In [62] a microwave phased-array system is used that utilizes 134 small antennas positioned around the head as shown in Fig. 2.22. The frequency of operation used is 1-GHz and in the paper a time-multiplexing beamforming technique is used. The aim of time multiplexing is to focus the microwave energy to the desired location while minimizing the exposure of healthy tissue.

In [63] and [64] a different kind of hyperthermia technique is used in which the human head is placed inside a cylindrical cavity like the one shown in Fig. 2.23. As seen in the figure, inside the cavity the head is positioned between two electrodes that radiate at different resonant frequencies. For each resonant frequency the heating point in the brain is controlled as shown in Fig. 2.24. So the control of the heating location in the brain is accomplished by varying the resonant frequency of the electrodes and the spot size of the heating is controlled by the separation distance between the head

and the electrodes. Figure 2.25 shows how the heating concentration changes by changing the separation distance.

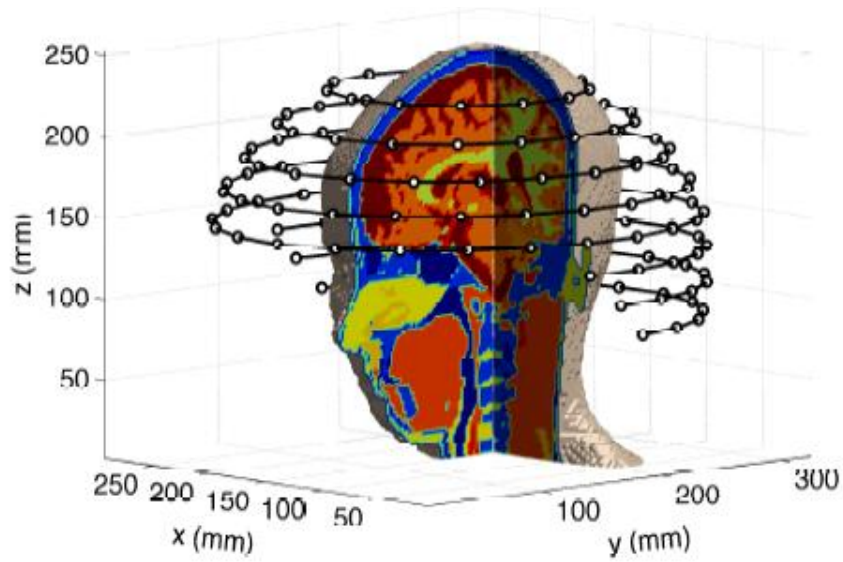


Fig. 2.22. Showing the Location of the Small Antenna Sources ([62], Fig. 1(a), pp. 2).

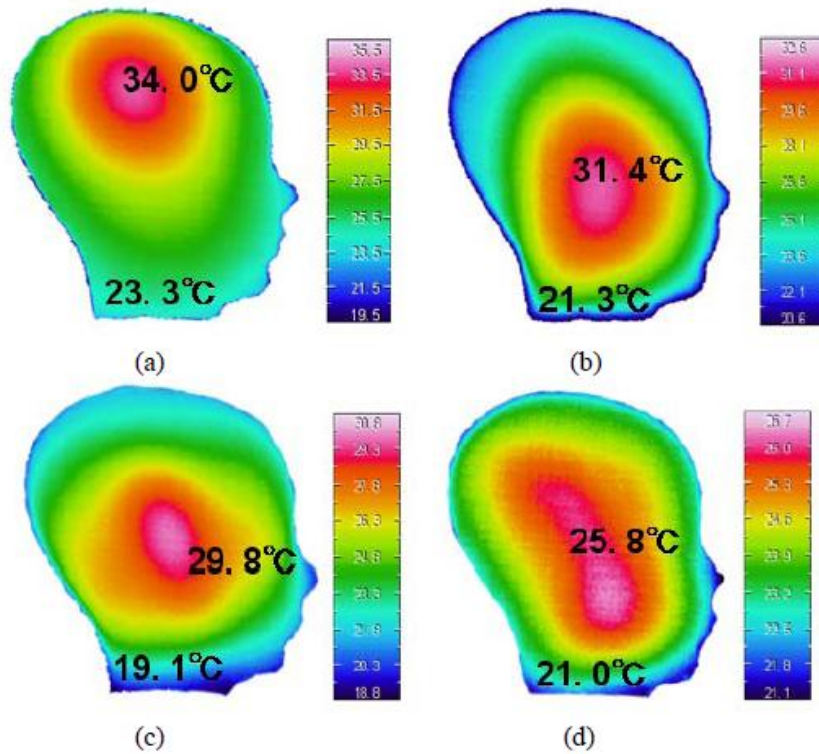


Fig. 2.23. Heating Characteristics at 4 Different Resonant Frequencies ([63], Fig. 6, pp. 3066).

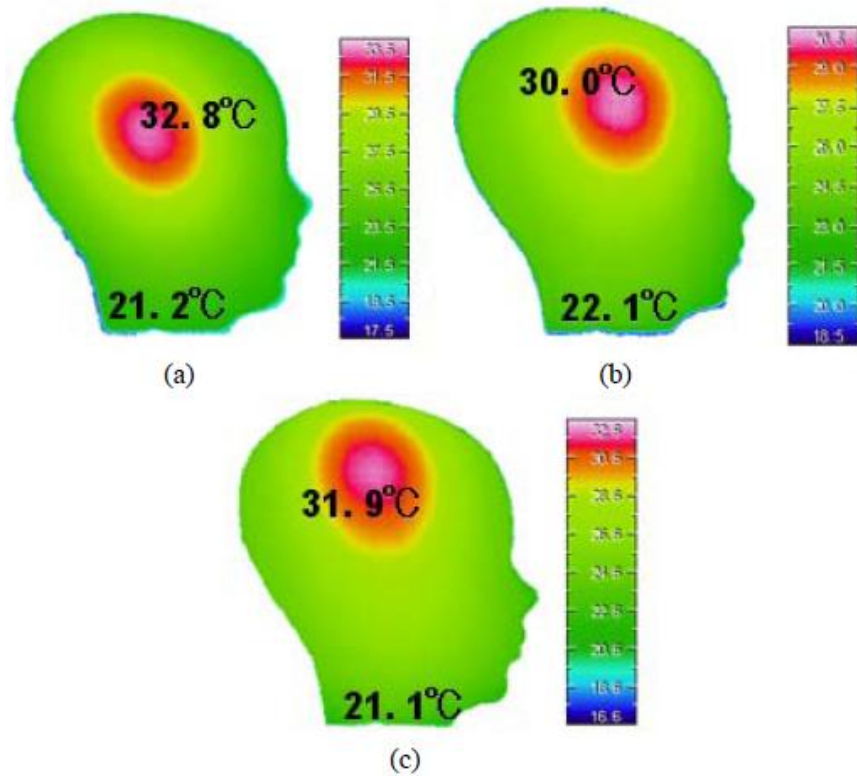


Fig. 2.24. Heating Spot at Different Distances ([63], Fig. 8, pp.3067).

In [65] another example of phased-array is given, but in this case the beamforming is done by putting testing LED sensors that give an indication of where the fields are focused before applying the device to human subjects.

2.5 Deep Brain Stimulation (DBS)

Deep brain stimulation is a surgical treatment which involves the implantation of a medical device called the *brain pacemaker*. This pacemaker (Fig. 2.25) consists of an implanted pulse generator (IPG), connecting lead and electrodes placed on brain sites where electric impulses must be applied for the treatment [2]. This method is used to treat patients with movement disorder such as *chronic pain*, *Parkinson's Disease*, *tremors* and *dystonia*. The stimulator's battery must be changed every 2-7 years

[2]. This means that another surgery is necessary. Furthermore, the device is very sensitive to external magnetic fields, so any device in the proximity of the stimulator that generates a magnetic field may cause the stimulator to shut down without the patient knowing about it.

The IPG is a device that sends electric pulses in a form a voltage. According to the literature [31]-[33], the amplitude of the voltage used can vary from 1 V to 10 V and the frequency of operation can vary from 50 Hz to 10 kHz. The electrode's placement depends on the kind of disorder the patient has. For non-Parkinsonian essential tremor the electrodes are placed in the *ventrointermedial nucleus (VIM)* of the *thalamus* while for dystonia and symptoms associated with Parkinson's disease (rigidity, bradykinesia/akinesia and tremor), the lead may be placed in either the *globus pallidus* or *subthalamic nucleus*. The thalamus [34] (shown in Fig. 2.26) is a midline paired symmetrical structure within the brains. It is located almost in the middle of the brain between the cerebral cortex and midbrain, both in terms of location and neurological connections. Its function includes relaying sensation, spatial sense and motor signals to the cerebral cortex, along with the regulation of consciousness, sleep and alertness. This is why for most movement disorder symptoms the electrodes are targeted to the thalamus.

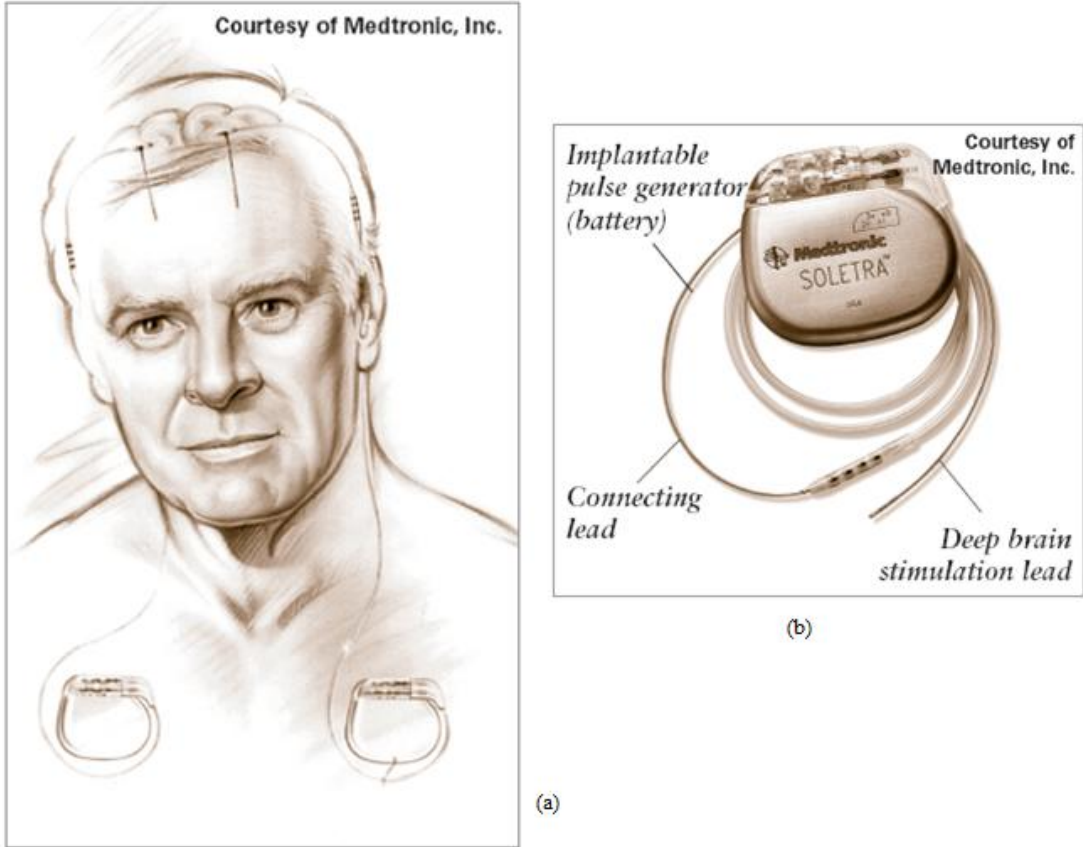


Fig. 2.25 (a) Implanted Deep Brain Stimulators ([2] Fig 3, p.15). (b) Deep Brain Stimulator Apparatus ([2] Fig 4, p.25).

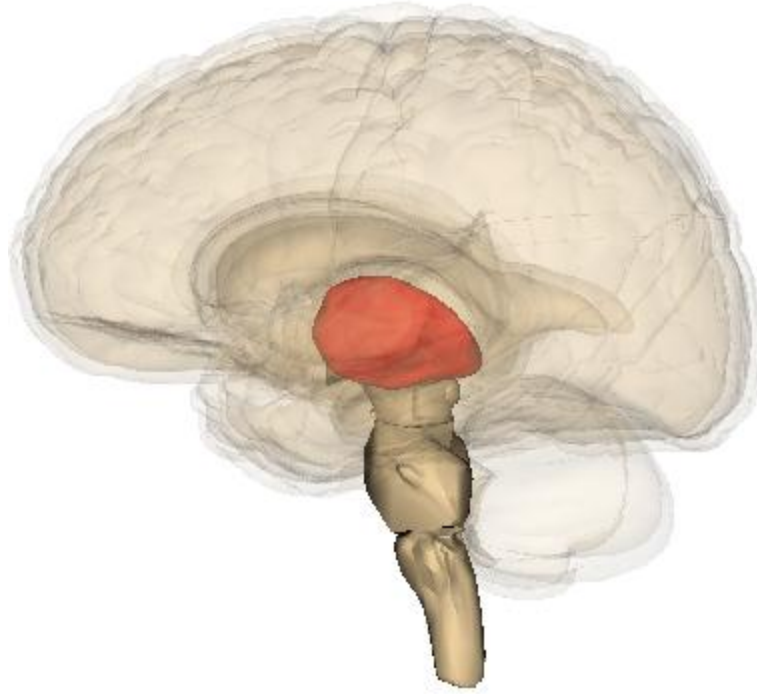


Fig. 2.26. Cross sectional view of the human head with showing the location of the thalamus (*in red*) [34].

The frequency of deep brain stimulation (DBS) is a very essential factor in the treatment of the tremors. According to [33] the stimulations are categorized by *low frequency stimulation (LFS)* (1-14 Hz) and *high frequency stimulation (HFS)* (40-300 Hz). Of course there are other approaches that go beyond 300 Hz. Both LFS and HFS excite the *axons* of the *neurons*, but the two methods differ in the postsynaptic responses. At low frequencies inhibitory and excitatory postsynaptic potentials are evoked while at high frequencies the pathological excitation of the subthalamic nucleus (STN) neurons is silenced. This is a strong indication that the higher the frequency the better postsynaptic response results. Silencing the pathological and spontaneous activity improves the signal-to-noise ratio of the postsynaptic signal.

So far the principles and the reasons for using DBS were given, but no explanation was given on how to insert the electrodes in the first place. The way this is done (as given in [31]) is by the use of *sensory evoked potential (SEP)*. An *evoked potential* is a potential response by the neurons in the brain when a specific kind of stimulant is applied. When a stimulant is applied, specific neurons are excited and produce potentials in response to that stimulant. The location of the evoked potential is detected and the electrode is placed at that point. SEP allows the identification of the brain sites where the electrodes must be placed.

Chapter 3: Antenna Array Theory & Beamforming Techniques for the Intermediate Zone

3.1 Antenna Array System

An antenna array is a system that consists of a number of antenna elements spaced in a particular geometry (linear, planar, spherical or cylindrical). This spacing between the elements creates a phase difference when the array is transmitting or receiving a signal. This phase difference can be utilized to create a constructive interference between the elements in a particular direction or point in space while causing a destructive interference in all other directions. Thus the array is capable of electronically steering the beam of the overall antennas to receive or transmit a signal to/from a particular direction or point in space.

The benefits of electronic steering are high signal directivity, interference rejection, signal-to-noise ratio (SNR) improvement and fast scanning response. Furthermore, the gain achieved by an array is much larger than that of a single element system. If the gain (in dB) of a single element system is G_{single} , then the total gain of an N -element array system (in dB) is given by [28]:

$$G_{Array} = G_{Single} + 20 \log_{10} N \text{ (dB)} \quad (3.1)$$

Antenna array systems consist of many components such as the antenna elements, radio-frequency (RF) components and the beamforming circuit or network. The antenna elements can take many forms or shapes and are designed in the best interest

of the designer. The RF components consist of the low noise amplifier (LNA), power amplifier (PA), RF adders and phase shifters. The RF components will be discussed in greater detail in Chapter 5. The beamforming technique or algorithm is accomplished by the beamforming circuit or network. In this case the beamforming is carried out by a neural network which will be discussed in Chapter 4.

In this chapter the antenna array theory and new beamforming technique for the intermediate zone will be discussed. As mentioned in Chapter 2, the usual antenna array theory is based on the far field approximation where the observation point is far away from the array which in turn simplifies the equation of the vector potential and allows designers to use the standard approach when it comes to phase shifting. In this case the observation point can be from anywhere underneath the array or far from the array and therefore no approximation can be made to simplify the antenna theory and a different approach must be followed.

Before starting the theory of the antenna array and new beamforming technique for the intermediate zone an outline of the steps taken in the chapter are going to be given in point form.

- 1- Expressing the antenna array problem as a boundary valued problem where the human head is modeled as a three layered hemisphere (each layer having its own relative permittivity and permeability values).
 - a. Constructing the antenna element.
 - b. Give the general form for the electromagnetic fields in all regions.

- c. Applying boundary conditions to solve for the electromagnetic fields (note that the antenna elements are introduced in the boundary conditions).
- 2- The new beamforming technique is introduced. It is based on the orthogonality of the electromagnetic fields. Two different scenarios are discussed.
 - a. The general case where both the transverse electric (TE) and transverse magnetic (TM) modes of the electromagnetic fields are present.
 - b. The final case is the case studied extensively in the dissertation where only the TE modes are considered. For this scenario two conditions are examined.
 - i. Beamforming in one desired direction.
 - ii. Beamforming in multiple directions.
- 3- Another beamforming technique is introduced for the case where the antenna array is used as a receiver. Two scenarios are studied.
 - a. Receiving from one source.
 - b. Receiving from multiple sources with the ability of distinguishing between the sources.
- 4- In the transmission case, safety issues are addressed when using the array for DBS.
 - a. Electric field exposure is calculated.

- b. Specific absorption rate (SAR) (which is a safety measure) is calculated and kept within international standards.
- 5- Reflection considerations are taken into account to understand how the fields behave in all the layers.
 - a. Transmission measurements from one layer to the other are calculated.
 - b. Reflections measurements from one layer to the prior are calculated.
- 6- The antenna array was designed for the general case (@1.8GHz) where the fields are in the intermediate zone and no approximations are applicable.
- 7- Considering how the antenna array can be used in other RFID systems where there is a reader and tag system. The reader in this case is made up of an antenna array.
 - a. The array geometry is the geometry that best fits the application at hand.
 - b. The reader in this case has the ability to direct its transmitted power to any direction of interest.
 - c. Misalignments issues due to the tag can be alleviated by this antenna array set up since the array can direct the power towards the coil of the tag to optimize the power transfer efficiency.

3.2 Theoretical Analysis of the Array as a Transmitter

3.2.1 Problem Statement

The problem in hand is the design of a hemispherical antenna array which will be placed on a human's head. The point of observation is anywhere in the brain which

makes the antenna problem quite difficult since, as mentioned previously, the point of observation is no longer in the far zone. The analysis must be carried out with no approximation to the form of the field.

The design of the hemispherical array was done by solving an electromagnetic boundary valued problem in which the human head was modeled as a three layered hemisphere like the one shown in Fig. 3.1. The antenna elements are of course fixed onto a helmet which is in turn placed on the head but in the analysis it is assumed that the antennas are placed right above the head to reduce the number of layers and hence simplify the analysis. It is seen from the figure that there are four regions marked as (0), (1), (2) and (3). Region (0) is the outside of the head (i.e. free space), while region (1) is the skin, region (2) is the skull and finally region (3) in the brain [35]. The antennas are going to be placed on top of the skin surface and they will cover a hemispherical surface of radius c .

Since the human head is spherical, it is therefore obvious that the boundary value problem will be solved by utilizing the spherical coordinate system. According to [36], any electromagnetic problem with spherical symmetry can be solved using the electric vector potential F_r and the magnetic vector potential A_r in spherical coordinates. Any electromagnetic wave can be decomposed into two orthogonal sets of functions which are the *transverse electric (TE)* and the *transverse magnetic (TM)* waves. The TE waves are represented by F_r while the TM waves are represented by A_r . Both vector potentials are solutions to the Helmholtz equation given by equation (3.2) [36]. The general solution to both vectors is identical, but what differs is how they are used to form the electric and magnetic fields. A linear combination between

the curl of one vector with the double curl of the other are used to construct the fields as discussed later.

$$(\nabla^2 + k^2)\left(\frac{F_r}{r}\right) = 0 \quad (3.2a)$$

$$(\nabla^2 + k^2)\left(\frac{A_r}{r}\right) = 0 \quad (3.2b)$$

where ∇^2 is the Laplacian operator, r is the radial distance from the origin expressed in spherical coordinates and k is the wavenumber. Since the head is divided into three layers, which are the skin, skull and brain, there will be four regions of operation (free space, skin, skull and brain) with four different values of k . According to [37], the electric properties of the human skin, skull and brain are a function of the frequency of the applied electromagnetic wave. Specifying the frequency of operation is essential for determining the values of the relative permeability and electric conductivity for each layer. The relationship between the wavenumber k and the prior quantities is given by equation (3.3).

$$k = \omega \sqrt{\mu_0 \varepsilon_0 \left(\varepsilon_r + \frac{j \sigma_r}{\omega \varepsilon_0} \right)} \quad (3.3)$$

where ω is the operating frequency, μ_0 is the permeability of free space, ε_0 is the permittivity of free space, ε_r is the relative permittivity of the region (free space, skull or brain) and σ_r the electric conductivity of the region. It is clear from (3.3) that there will be four values for k denoted as k_0 (free space), k_1 (skin), k_2 (skull) and k_3 (brain). The values of the relative permittivities and conductivities are given in Table. 3.1.

Since there are four values of k , equations (3.2a) and (3.2b) must be solved for four different regions each, which will result in eight equations for F_r and A_r in total.

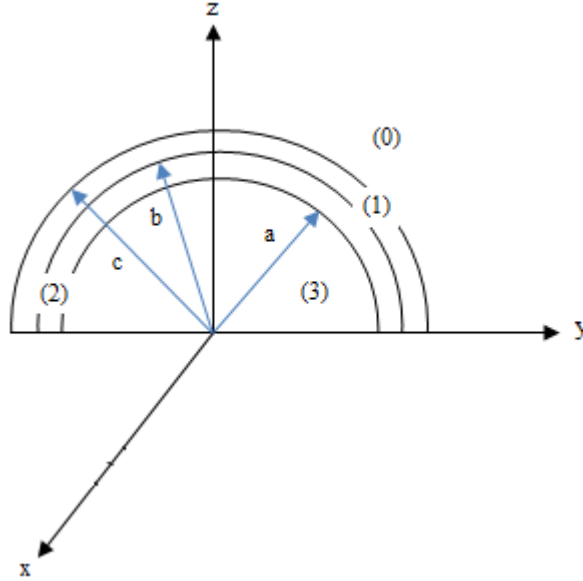


Fig. 3.1. A simple model of a human's head as seen from the front. There are four regions denoted by (0), (1), (2) and (3) which represent free space, skin, skull and brain respectively. The radius of the brain is a , b denotes the radius from the center of the brain to the outer part of the skull and c denotes that to the skin where the antenna elements are going to be placed.

TABLE 3.1

Relative Permittivity & Conductivity of the Four Regions of Operation [35].

	ϵ_r	σ (S/m)
Region (0)	1	0
Region (1)	38.87	1.88
Region (2)	19.34	0.59
Region (3)	51.8	1.5

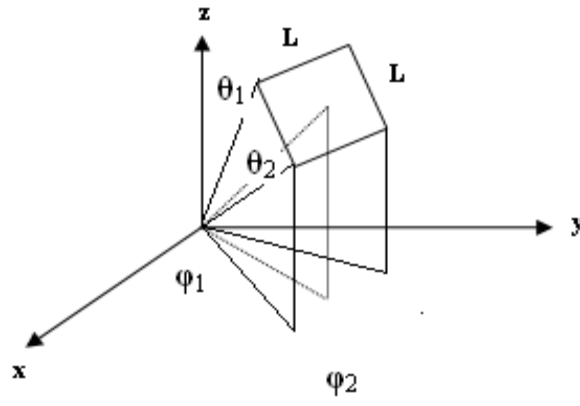
3.2.2 Loop Current Construction

Before solving the boundary valued problem (BVP), it is important to know how to include the antenna elements in the problem. The antennas are assumed to be loops of current placed on the surface of the skin. As demonstrated in [38]-[42], the loop current will be included in the boundary condition of the magnetic field intensity (H) which will be discussed in complete detail in Subsection 3.2.3. As in [38], the loop current is described in terms of spherical coordinates and the same is done here for the loop current shown in Fig. 3.2. Figure 3.2(a) shows the model of the loop current that is used in the design for each element in the array. Figure 3.2(b) shows how the all the antenna elements are placed on top of the human head.

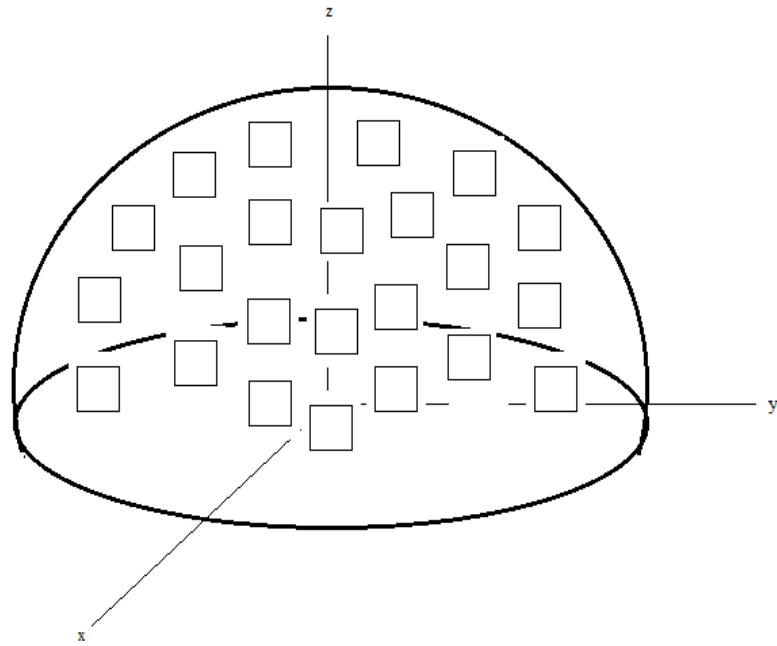
As it can be seen from Fig. 3.2(a), the element is a loop antenna centered about the point designated by the elevation angle θ_i and the azimuthal angle φ_i . The loop can be thought of as a segment of the surface of a sphere extending from φ_1 to φ_2 in the azimuthal direction and from θ_1 to θ_2 in the elevation direction. The loop has equal arc lengths (L) in both directions where the arc length is given by equation (3.4).

$$L = c\Delta\theta = c\Delta\varphi \quad (3.4)$$

where c is the radius of the spherical surface on which the antenna is placed on top, $\Delta\theta = \theta_2 - \theta_1$ and $\Delta\varphi = \varphi_2 - \varphi_1$. The loop carries a current I_i . Following the same argument used in [5], the expression for the current density (\vec{J}_i) for a loop current shown Fig. 3.2 is given by equation (3.5).



(a)



(b)

Fig. 3.2. (a) The loop current designed. The center of the loop is located at the point (c, θ_i, φ_i) . The loop carries the current I_i . (b) Loop Antennas Placed on the Human head.

$$\begin{aligned} \vec{J}_i(r, \theta, \varphi) = & \frac{I_i}{cL} \delta(r-c) [\hat{\theta} \delta(\theta - \theta_i) \{ \delta(\varphi - \varphi_i + \frac{\Delta\varphi}{2}) - \delta(\varphi - \varphi_i - \frac{\Delta\varphi}{2}) \} \\ & + \hat{\varphi} \delta(\varphi - \varphi_i) \{ \delta(\theta - \theta_i - \frac{\Delta\theta}{2}) - \delta(\theta - \theta_i + \frac{\Delta\theta}{2}) \}] \end{aligned} \quad (3.5)$$

where \vec{J}_i denotes the vector current density for the i th antenna element, $\hat{\theta}$ is the unit vector in the elevation angle direction, $\hat{\varphi}$ is the unit vector in the azimuthal angle

direction and I_i is the current applied. The current density is expressed in terms of delta functions that denote where the current is present. Here the current I_i is assumed to be constant to simplify the derivation. The above equation can be simplified by simply noting that the current density can only exist on the spherical surface of radius c , and therefore the simplified version of (3.5) where $\delta(r-c)$ is dropped and is given by (3.6). Note that θ_i and φ_i denote the position of the center of the i th antenna element on the spherical surface of radius c .

$$\begin{aligned} \vec{J}_i(\theta, \varphi) = & \frac{I_i}{cL} [\hat{\theta}\delta(\theta - \theta_i) \{ \delta(\varphi - \varphi_i + \frac{\Delta\varphi}{2}) - \delta(\varphi - \varphi_i - \frac{\Delta\varphi}{2}) \} \\ & + \hat{\varphi}\delta(\varphi - \varphi_i) \{ \delta(\theta - \theta_i - \frac{\Delta\theta}{2}) - \delta(\theta - \theta_i + \frac{\Delta\theta}{2}) \}] \end{aligned} \quad (3.6)$$

The frequency of operation is very important in determining the number of elements, the spacing between the elements and the size of L . The frequency of operation is 1.8 GHz which corresponds to a free space wavelength ($\lambda=c_s/f$) of 16.7cm (where c_s is the speed of light). For acceptable phase relationship between the antenna elements, the distance between the centers of each element to the next is set to be $\lambda/4$ which is equal to 4.17 cm. With this in mind the total number of possible elements is equal to 42 distributed on the surface of a hemisphere of radius c . Note that a frequency of 1.8 GHz is chosen to allow for the design of an antenna array with the elements being separated from each with a distance of $\lambda/4$, this will allow for constructive interference between the elements.

3.2.3 Boundary Valued Problem

As mentioned in Subsection 3.2.1, equations (3.2a) and (3.2b) will be solved for three regions and the solution of the Helmholtz equation in spherical coordinates is

given by equations (3.7) and (3.8) as seen from [36].

$$A_r = \sum_{l=0}^{\infty} \sum_{m=-l}^l \begin{pmatrix} a_{lm} H_l^{(2)}(k_0 r) \\ b_{lm} H_l^{(1)}(k_1 r) + c_{lm} H_l^{(2)}(k_1 r) \\ d_{lm} H_l^{(1)}(k_2 r) + e_{lm} H_l^{(2)}(k_2 r) \\ f_{lm} J_l(k_3 r) \end{pmatrix} Y_{lm}(\theta, \varphi) \quad (3.7)$$

$$F_r = \sum_{l=0}^{\infty} \sum_{m=-l}^l \begin{pmatrix} A_{lm} H_l^{(2)}(k_0 r) \\ B_{lm} H_l^{(1)}(k_1 r) + C_{lm} H_l^{(2)}(k_1 r) \\ D_{lm} H_l^{(1)}(k_2 r) + E_{lm} H_l^{(2)}(k_2 r) \\ F_{lm} J_l(k_3 r) \end{pmatrix} Y_{lm}(\theta, \varphi) \quad (3.8)$$

where $J_l(x) = x j_l(x)$ in which $j_l(x)$ is the spherical Bessel function [36], $H_l^{(1,2)}(x) = x h_l^{(1,2)}$ in which $h_l^{(1,2)}$ is the spherical Hankel function of the first and second kind [36], $Y_{lm}(\theta, \varphi)$ is the spherical harmonic [36] and the coefficients a_{lm} to f_{lm} and A_{lm} to F_{lm} are going to be determined after applying the boundary conditions. Note that when solving for all the coefficients, the solution for the electromagnetic waves is for one antenna element.

The electric field (E) and the magnetic field intensity (H) are determined from equations (3.7) and (3.8) by using equation (3.9) as shown in [36].

$$E_{\theta} = \frac{-1}{r \sin \theta} \frac{\partial F_r}{\partial \varphi} + \frac{1}{j \omega \epsilon r} \frac{\partial^2 A_r}{\partial r \partial \theta} \quad (3.9a)$$

$$E_{\varphi} = \frac{1}{r} \frac{\partial F_r}{\partial \theta} + \frac{1}{j \omega \epsilon r \sin \theta} \frac{\partial^2 A_r}{\partial r \partial \varphi} \quad (3.9b)$$

$$H_{\theta} = \frac{1}{r \sin \theta} \frac{\partial A_r}{\partial \varphi} + \frac{1}{j \omega \mu r} \frac{\partial^2 F_r}{\partial r \partial \theta} \quad (3.9c)$$

$$H_\varphi = \frac{-1}{r} \frac{\partial A_r}{\partial \theta} + \frac{1}{j\omega\mu r \sin \theta} \frac{\partial^2 F_r}{\partial r \partial \varphi} \quad (3.9d)$$

where ε is the permittivity, μ is the permeability, $j = \sqrt{-1}$, $\omega = 2\pi f$ is the frequency of operation in rad/s. Now by applying equations (3.7) and (3.8) into (3.9) one can get the E-field and the H-field in the three regions of operation. The derivation will be separated for the TM and TE waves respectively to make matters simple. Note that the radial components for the E-field and H-field are not considered since no boundary conditions are going to be imposed in the radial direction like in [38].

3.2.4 TM Waves

The TM waves can be derived by applying equation (3.7) into (3.9). The E-field and the H-field expressions are shown in equation (3.10).

$$\begin{aligned} \bar{E}_0 &= \hat{\theta} \frac{1}{j\omega\varepsilon_0 r} \sum_{l=1}^{\infty} \sum_{m=-l}^l a_{lm} H_l^{(2)}(k_0 r) \frac{\partial Y_{lm}(\theta, \varphi)}{\partial \theta} \\ &+ \hat{\varphi} \frac{1}{\omega\varepsilon_0 r \sin \theta} \sum_{l=1}^{\infty} \sum_{m=-l}^l m a_{lm} H_l^{(2)}(k_0 r) Y_{lm}(\theta, \varphi) \end{aligned} \quad (3.10a)$$

$$\begin{aligned} \bar{E}_1 &= \hat{\theta} \frac{1}{j\omega\varepsilon_1 r} \sum_{l=1}^{\infty} \sum_{m=-l}^l \{b_{lm} H_l^{(1)}(k_1 r) + c_{lm} H_l^{(2)}(k_1 r)\} \frac{\partial Y_{lm}(\theta, \varphi)}{\partial \theta} \\ &+ \hat{\varphi} \frac{1}{\omega\varepsilon_1 r \sin \theta} \sum_{l=1}^{\infty} \sum_{m=-l}^l m \{b_{lm} H_l^{(1)}(k_1 r) + c_{lm} H_l^{(2)}(k_1 r)\} Y_{lm}(\theta, \varphi) \end{aligned} \quad (3.10b)$$

$$\begin{aligned} \bar{E}_2 &= \hat{\theta} \frac{1}{j\omega\varepsilon_2 r} \sum_{l=1}^{\infty} \sum_{m=-l}^l \{d_{lm} H_l^{(1)}(k_2 r) + e_{lm} H_l^{(2)}(k_2 r)\} \frac{\partial Y_{lm}(\theta, \varphi)}{\partial \theta} \\ &+ \hat{\varphi} \frac{1}{\omega\varepsilon_2 r \sin \theta} \sum_{l=1}^{\infty} \sum_{m=-l}^l m \{d_{lm} H_l^{(1)}(k_2 r) + e_{lm} H_l^{(2)}(k_2 r)\} Y_{lm}(\theta, \varphi) \end{aligned} \quad (3.10c)$$

$$\begin{aligned}\bar{E}_3 &= \hat{\theta} \frac{1}{j\omega\varepsilon_3 r} \sum_{l=1}^{\infty} \sum_{m=-l}^l f_{lm} J_l'(k_3 r) \frac{\partial Y_{lm}(\theta, \varphi)}{\partial \theta} \\ &+ \hat{\phi} \frac{1}{\omega\varepsilon_3 r \sin \theta} \sum_{l=1}^{\infty} \sum_{m=-l}^l m f_{lm} J_l'(k_3 r) Y_{lm}(\theta, \varphi)\end{aligned}\quad (3.10d)$$

$$\begin{aligned}\bar{H}_0 &= \hat{\theta} \frac{j}{r \sin \theta} \sum_{l=1}^{\infty} \sum_{m=-l}^l m a_{lm} H_l^{(2)}(k_0 r) Y_{lm}(\theta, \varphi) \\ &- \hat{\phi} \frac{1}{r} \sum_{l=1}^{\infty} \sum_{m=-l}^l a_{lm} H_l^{(2)}(k_0 r) \frac{\partial Y_{lm}(\theta, \varphi)}{\partial \theta}\end{aligned}\quad (3.10e)$$

$$\begin{aligned}\bar{H}_1 &= \hat{\theta} \frac{j}{r \sin \theta} \sum_{l=1}^{\infty} \sum_{m=-l}^l m \{b_{lm} H_l^{(1)}(k_1 r) + c_{lm} H_l^{(2)}(k_1 r)\} Y_{lm}(\theta, \varphi) \\ &- \hat{\phi} \frac{1}{r} \sum_{l=1}^{\infty} \sum_{m=-l}^l \{c_{lm} H_l^{(1)}(k_1 r) + c_{lm} H_l^{(2)}(k_1 r)\} \frac{\partial Y_{lm}(\theta, \varphi)}{\partial \theta}\end{aligned}\quad (3.10f)$$

$$\begin{aligned}\bar{H}_2 &= \hat{\theta} \frac{j}{r \sin \theta} \sum_{l=1}^{\infty} \sum_{m=-l}^l m \{d_{lm} H_l^{(1)}(k_2 r) + e_{lm} H_l^{(2)}(k_2 r)\} Y_{lm}(\theta, \varphi) \\ &- \hat{\phi} \frac{1}{r} \sum_{l=1}^{\infty} \sum_{m=-l}^l \{d_{lm} H_l^{(1)}(k_2 r) + e_{lm} H_l^{(2)}(k_2 r)\} \frac{\partial Y_{lm}(\theta, \varphi)}{\partial \theta}\end{aligned}\quad (3.10g)$$

$$\begin{aligned}\bar{H}_3 &= \hat{\theta} \frac{j}{r \sin \theta} \sum_{l=1}^{\infty} \sum_{m=-l}^l m f_{lm} J_l(k_3 r) Y_{lm}(\theta, \varphi) \\ &- \hat{\phi} \frac{1}{r} \sum_{l=1}^{\infty} \sum_{m=-l}^l f_{lm} J_l(k_3 r) \frac{\partial Y_{lm}(\theta, \varphi)}{\partial \theta}\end{aligned}\quad (3.10h)$$

Note that all the equations start with $l=1$ instead from starting of zero because the spherical harmonics were either differentiated with respect to θ or φ . Also the subscripts 0, 1, 2 & 3 represent the layers 0 to 3.

3.2.5 TE Waves

Similar to the TM waves, the TE waves can be determined by applying equation (3.8) in (3.9). The resulting expressions for the E-field and H-field are shown in equation (3.11).

$$\begin{aligned}\bar{E}_0 &= -\hat{\theta} \frac{j}{r \sin \theta} \sum_{l=1}^{\infty} \sum_{m=-l}^l m A_{lm} H_l^{(2)}(k_0 r) Y_{lm}(\theta, \varphi) \\ &+ \hat{\phi} \frac{1}{r} \sum_{l=1}^{\infty} \sum_{m=-l}^l A_{lm} H_l^{(2)}(k_0 r) \frac{\partial Y_{lm}(\theta, \varphi)}{\partial \theta}\end{aligned}\quad (3.11a)$$

$$\begin{aligned}\bar{E}_1 &= -\hat{\theta} \frac{j}{r \sin \theta} \sum_{l=1}^{\infty} \sum_{m=-l}^l m \{B_{lm} H_l^{(1)}(k_1 r) + C_{lm} H_l^{(2)}(k_1 r)\} Y_{lm}(\theta, \varphi) \\ &+ \hat{\phi} \frac{1}{r} \sum_{l=1}^{\infty} \sum_{m=-l}^l \{B_{lm} H_l^{(1)}(k_1 r) + C_{lm} H_l^{(2)}(k_1 r)\} \frac{\partial Y_{lm}(\theta, \varphi)}{\partial \theta}\end{aligned}\quad (3.11b)$$

$$\begin{aligned}\bar{E}_2 &= -\hat{\theta} \frac{j}{r \sin \theta} \sum_{l=1}^{\infty} \sum_{m=-l}^l m \{D_{lm} H_l^{(1)}(k_2 r) + E_{lm} H_l^{(2)}(k_2 r)\} Y_{lm}(\theta, \varphi) \\ &+ \hat{\phi} \frac{1}{r} \sum_{l=1}^{\infty} \sum_{m=-l}^l \{D_{lm} H_l^{(1)}(k_2 r) + E_{lm} H_l^{(2)}(k_2 r)\} \frac{\partial Y_{lm}(\theta, \varphi)}{\partial \theta}\end{aligned}\quad (3.11c)$$

$$\begin{aligned}\bar{E}_3 &= -\hat{\theta} \frac{j}{r \sin \theta} \sum_{l=1}^{\infty} \sum_{m=-l}^l m F_{lm} J_l(k_3 r) Y_{lm}(\theta, \varphi) \\ &+ \hat{\phi} \frac{1}{r} \sum_{l=1}^{\infty} \sum_{m=-l}^l F_{lm} J_l(k_3 r) \frac{\partial Y_{lm}(\theta, \varphi)}{\partial \theta}\end{aligned}\quad (3.11d)$$

$$\begin{aligned}\bar{H}_0 &= \hat{\theta} \frac{1}{j \omega \mu_0 r} \sum_{l=1}^{\infty} \sum_{m=-l}^l A_{lm} H_l^{(2)}(k_0 r) \frac{\partial Y_{lm}(\theta, \varphi)}{\partial \theta} \\ &+ \hat{\phi} \frac{1}{\omega \mu_0 r \sin \theta} \sum_{l=1}^{\infty} \sum_{m=-l}^l m A_{lm} H_l^{(2)}(k_0 r) Y_{lm}(\theta, \varphi)\end{aligned}\quad (3.11e)$$

$$\begin{aligned}\bar{H}_1 &= \hat{\theta} \frac{1}{j\omega\mu_0 r} \sum_{l=1}^{\infty} \sum_{m=-l}^l \{B_{lm} H_l^{(1)}(k_1 r) + B_{lm} H_l^{(2)}(k_1 r)\} \frac{\partial Y_{lm}(\theta, \varphi)}{\partial \theta} \\ &+ \hat{\varphi} \frac{1}{\omega\mu_0 r \sin \theta} \sum_{l=1}^{\infty} \sum_{m=-l}^l m \{B_{lm} H_l^{(1)}(k_1 r) + C_{lm} H_l^{(2)}(k_1 r)\} Y_{lm}(\theta, \varphi)\end{aligned}\quad (3.11f)$$

$$\begin{aligned}\bar{H}_2 &= \hat{\theta} \frac{1}{j\omega\mu_0 r} \sum_{l=1}^{\infty} \sum_{m=-l}^l \{D_{lm} H_l^{(1)}(k_2 r) + E_{lm} H_l^{(2)}(k_2 r)\} \frac{\partial Y_{lm}(\theta, \varphi)}{\partial \theta} \\ &+ \hat{\varphi} \frac{1}{\omega\mu_0 r \sin \theta} \sum_{l=1}^{\infty} \sum_{m=-l}^l m \{D_{lm} H_l^{(1)}(k_2 r) + E_{lm} H_l^{(2)}(k_2 r)\} Y_{lm}(\theta, \varphi)\end{aligned}\quad (3.11g)$$

$$\begin{aligned}\bar{H}_3 &= \hat{\theta} \frac{1}{j\omega\mu_0 r} \sum_{l=1}^{\infty} \sum_{m=-l}^l F_{lm} J_l'(k_3 r) \frac{\partial Y_{lm}(\theta, \varphi)}{\partial \theta} \\ &+ \hat{\varphi} \frac{1}{\omega\mu_0 r \sin \theta} \sum_{l=1}^{\infty} \sum_{m=-l}^l m F_{lm} J_l'(k_3 r) Y_{lm}(\theta, \varphi)\end{aligned}\quad (3.11h)$$

Note that the total E-field and H-field is simply the summation of the TE and TM components.

3.2.6 Applying Boundary Conditions

There are six boundary conditions, two at $r=c$ (air-skin interface), two at $r=b$ (skin-skull interface) and two at $r=a$ (skull-brain interface). Beginning with the boundary condition of the E-field, the following statements can be made according to [26].

$$\hat{r} \times (\vec{E}_1 - \vec{E}_0) = 0 \quad \text{for } r=c \quad (3.12)$$

$$\hat{r} \times (\vec{E}_2 - \vec{E}_1) = 0 \quad \text{for } r=b \quad (3.13)$$

$$\hat{r} \times (\vec{E}_3 - \vec{E}_2) = 0 \quad \text{for } r=a \quad (3.14)$$

where \hat{r} is simply the unit vector in the radial direction. Equations (3.12), (3.13) and (3.14) indicate that the E-field is continuous in the tangential directions (i.e. tangential to the surface of a sphere). By using equations (3.10a), (3.10b), (3.11a), (3.11b) and (3.12), the following equation can be written at $r=c$.

$$\begin{aligned}
& \frac{-j}{c \sin \theta} \sum_{l=1}^{\infty} \sum_{m=-l}^l m \{ B_{lm} H_l^{(1)}(k_1 c) + C_{lm} H_l^{(2)}(k_1 c) \} Y_{lm}(\theta, \varphi) \\
& + \frac{1}{j \omega \epsilon_1 c} \sum_{l=1}^{\infty} \sum_{m=-l}^l \{ b_{lm} H_l^{(1)}(k_1 c) + c_{lm} H_l^{(2)}(k_1 c) \} \frac{\partial Y_{lm}(\theta, \varphi)}{\partial \theta} \\
& = \frac{-j}{c \sin \theta} \sum_{l=1}^{\infty} \sum_{m=-l}^l m A_{lm} H_l^{(2)}(k_0 c) Y_{lm}(\theta, \varphi) \\
& + \frac{1}{j \omega \epsilon_0 c} \sum_{l=1}^{\infty} \sum_{m=-l}^l a_{lm} H_l^{(2)}(k_0 c) \frac{\partial Y_{lm}(\theta, \varphi)}{\partial \theta}
\end{aligned} \tag{3.15}$$

Note that the above equation is obtained when considering the θ -component of the E-field at $r=c$. Since the unit vectors θ and φ are orthogonal another equation can be written when considering the φ -component of the E-field.

$$\begin{aligned}
& \frac{1}{c} \sum_{l=1}^{\infty} \sum_{m=-l}^l \{ B_{lm} H_l^{(1)}(k_1 c) + C_{lm} H_l^{(2)}(k_1 c) \} \frac{\partial Y_{lm}(\theta, \varphi)}{\partial \theta} \\
& + \frac{1}{\omega \epsilon_1 c \sin \theta} \sum_{l=1}^{\infty} \sum_{m=-l}^l m \{ b_{lm} H_l^{(1)}(k_1 c) + c_{lm} H_l^{(2)}(k_1 c) \} Y_{lm}(\theta, \varphi) \\
& = \frac{1}{c} \sum_{l=1}^{\infty} \sum_{m=-l}^l A_{lm} H_l^{(2)}(k_0 c) \frac{\partial Y_{lm}(\theta, \varphi)}{\partial \theta} \\
& + \frac{1}{\omega \epsilon_0 c \sin \theta} \sum_{l=1}^{\infty} \sum_{m=-l}^l m a_{lm} H_l^{(2)}(k_0 c) Y_{lm}(\theta, \varphi)
\end{aligned} \tag{3.16}$$

To extract the coefficients the orthogonality principle for the TE and TM waves must be applied and for this to happen in a simplified manner, one can join equations (3.15) and (3.16) in a vector form which is more compact and easier to manipulate

[43]. Note that the two equations were written to illustrate what happens when considering the scalar form of the fields.

$$\begin{aligned}
& -\sum_{l=1}^{\infty} \sum_{m=-l}^l \{B_{lm}H_l^{(1)}(k_1c) + C_{lm}H_l^{(2)}(k_1c)\} \bar{r} \times \nabla Y_{lm}(\theta, \varphi) + \\
& \frac{1}{j\omega\epsilon_1} \sum_{l=1}^{\infty} \sum_{m=-l}^l \nabla \times \left[\frac{1}{r} \{b_{lm}H_l^{(1)}(k_1r) + c_{lm}H_l^{(2)}(k_1r)\} \bar{r} \times \nabla Y_{lm}(\theta, \varphi) \right] \Big|_{r=c} \\
& = -\sum_{l=1}^{\infty} \sum_{m=-l}^l A_{lm}H_l^{(2)}(k_0c) \bar{r} \times \nabla Y_{lm}(\theta, \varphi) + \\
& \frac{1}{j\omega\epsilon_0} \sum_{l=1}^{\infty} \sum_{m=-l}^l \nabla \times \left[\frac{1}{r} a_{lm}H_l^{(2)}(k_0r) \bar{r} \times \nabla Y_{lm}(\theta, \varphi) \right] \Big|_{r=c}
\end{aligned} \tag{3.17}$$

Now by using the orthogonality property of the TE and TM modes as shown in equation (3.18) (taken from [43]), it is possible to solve equation (3.17) for some value of l and m .

$$\begin{aligned}
& \int_0^{2\pi} d\varphi \int_0^{\pi} \sin\theta d\theta [\bar{r} \times \nabla Y_{l'm}^*(\theta, \varphi)] \cdot [\bar{r} \times \nabla Y_{lm}(\theta, \varphi)] = l(l+1)\delta_{l'l} \delta_{m'm} \\
& [\bar{r} \times \nabla Y_{lm}^*(\theta, \varphi)] \cdot \nabla \times [g_l(kr) \bar{r} \times \nabla Y_{lm}(\theta, \varphi)] = 0
\end{aligned} \tag{3.18}$$

where; $\delta_{ij} = \begin{cases} 1; i = j \\ 0; i \neq j \end{cases}$

Here $g_l(kr)$ represents one of the Bessel or Hankel functions and the superscript $*$ denotes the complex conjugate. By taking the dot product of the term $\bar{r} \times \nabla Y_{lm}^*(\theta, \varphi)$ with both sides of equation (3.17) and integrating over the surface of a sphere, one can make use of equation (3.18) to yield the following equations (Appendix A).

$$B_{lm}H_l^{(1)}(k_1c) + C_{lm}H_l^{(2)}(k_1c) = A_{lm}H_l^{(2)}(k_0c) \tag{3.19}$$

To extract the other set of coefficients (i.e. a_{lm} , b_{lm} & c_{lm}), the curl is applied to both sides of (3.17) which has an effect over the TE and TM modes as described in (3.20) [43].

$$\begin{aligned} g_l(kr)\bar{r} \times \nabla Y_{lm}(\theta, \varphi) &\rightarrow \nabla \times [g_l(kr)\bar{r} \times \nabla Y_{lm}(\theta, \varphi)]|_{r=c} \\ \nabla \times [g_l(kr)\bar{r} \times \nabla Y_{lm}(\theta, \varphi)] &\rightarrow \nabla \times \nabla \times [g_l(kr)\bar{r} \times \nabla Y_{lm}(\theta, \varphi)]|_{r=c} \end{aligned} \quad (3.20)$$

Note that (3.20) is true for any value of r , but in this case $r=c$. The latter statement in (3.20) can be simplified using the following property shown in (3.21).

$$\nabla \times \left\{ \nabla \times [g_l(kr)\hat{r} \times \nabla Y_{lm}(\theta, \varphi)]|_{r=c} \right\} |_{r=c} = -\frac{1}{c^2 k} [G_l'(kc)\bar{r} \times \nabla Y_{lm}(\theta, \varphi)] \quad (3.21)$$

Where $G_l(kr)=kr g_l(kr)$. After applying the curl, the dot product of the term $\bar{r} \times \nabla Y_{lm}^*(\theta, \varphi)$ with equation (3.17) can now be applied. By integrating over the surface of a sphere one can get the following equation (Appendix A).

$$\frac{\varepsilon_1}{\varepsilon_0} a_{lm} H_l^{(2)}(k_0 c) = b_{lm} H_l^{(1)}(k_1 c) + c_{lm} H_l^{(2)}(k_1 c) \quad (3.22)$$

Similarly, by using the second (at $r=b$) and third (at $r=a$) boundary conditions, expressed by equations (3.13) and (3.14), respectively, and using equations (3.18) and (3.21), the following equations can be obtained.

$$D_{lm} H_l^{(1)}(k_2 b) + E_{lm} H_l^{(2)}(k_2 b) = B_{lm} H_l^{(1)}(k_1 b) + C_{lm} H_l^{(2)}(k_1 b) \quad (3.23)$$

$$\frac{\varepsilon_2}{\varepsilon_1} [b_{lm} H_l^{(1)}(k_1 b) + c_{lm} H_l^{(2)}(k_1 b)] = d_{lm} H_l^{(1)}(k_2 b) + e_{lm} H_l^{(2)}(k_2 b) \quad (3.24)$$

$$F_{lm}J_l(k_3a) = D_{lm}H_l^{(1)}(k_2a) + E_{lm}H_l^{(2)}(k_2a) \quad (3.25)$$

$$\frac{\varepsilon_3}{\varepsilon_2} \left[d_{lm}H_l^{(1)}(k_1a) + e_{lm}H_l^{(2)}(k_1a) \right] = f_{lm}J_l'(k_3a) \quad (3.26)$$

Looking at the boundary conditions for the H-field, the following equations can be written according to [36] for $r=c$, $r=b$ and $r=a$ respectively.

$$\hat{r} \times (\vec{H}_1 - \vec{H}_0) = \hat{\theta}J_\theta(\theta, \phi) + \hat{\phi}J_\phi(\theta, \phi) \quad \text{for } r=c \quad (3.27)$$

$$\hat{r} \times (\vec{H}_2 - \vec{H}_1) = 0 \quad \text{for } r=b \quad (3.28)$$

$$\hat{r} \times (\vec{H}_3 - \vec{H}_2) = 0 \quad \text{for } r=a \quad (3.29)$$

By applying the boundary condition in equation (3.27) to (3.10e), (3.10f), (3.11e) and (3.11f) the following equations can be obtained.

$$\begin{aligned} & \hat{r} \times \left\{ - \sum_{l=1}^{\infty} \sum_{m=-l}^l \{ b_{lm}H_l^{(1)}(k_1c) + c_{lm}H_l^{(2)}(k_1c) \} \vec{r} \times \nabla Y_{lm}(\theta, \phi) - \right. \\ & \left. \frac{1}{j\omega\mu_0} \sum_{l=1}^{\infty} \sum_{m=-l}^l \nabla \times \left[\frac{1}{r} \{ B_{lm}H_l^{(1)}(k_1r) + C_{lm}H_l^{(2)}(k_1r) \} \vec{r} \times \nabla Y_{lm}(\theta, \phi) \right] \Big|_{r=c} \right. \\ & \left. + \sum_{l=1}^{\infty} \sum_{m=-l}^l a_{lm}H_l^{(2)}(k_0c) \vec{r} \times \nabla Y_{lm}(\theta, \phi) + \right. \\ & \left. \frac{1}{j\omega\mu_0} \sum_{l=1}^{\infty} \sum_{m=-l}^l \nabla \times \left[\frac{1}{r} A_{lm}H_l^{(2)}(k_0r) \vec{r} \times \nabla Y_{lm}(\theta, \phi) \right] \Big|_{r=c} \right\} = \vec{J}_i(\theta, \phi) \end{aligned} \quad (3.30)$$

Where the current density is defined in equation (3.5) (remember that all the derivation are done for one antenna element). By applying the same methods as

before for extracting the coefficients, one can obtain the following equation by applying (3.18) on (3.30).

$$a_{lm}H_l^{(2)}(k_0c) - b_{lm}H_l^{(1)}(k_1c) - c_{lm}H_l^{(2)}(k_1c) = \frac{J_{TM}}{l(l+1)} \quad (3.31)$$

Where J_{TM} is surface integral of the TM component of the current density and is given by the following equation (Appendix B).

$$J_{TM} = \int_{\theta} \int_{\varphi} [\bar{r} \times \nabla Y_{lm}^*(\theta, \varphi)] \cdot \bar{J}_i(\theta, \varphi) \sin \theta d\theta d\varphi$$

$$J_{TM} = \frac{I_i}{cL} \left[\frac{\partial Y_{lm}^*\left(\theta_i + \frac{\Delta\theta}{2}, \varphi_i\right)}{\partial \theta} \sin\left(\theta_i + \frac{\Delta\theta}{2}\right) - \frac{\partial Y_{lm}^*\left(\theta_i - \frac{\Delta\theta}{2}, \varphi_i\right)}{\partial \theta} \sin\left(\theta_i - \frac{\Delta\theta}{2}\right) \right. \\ \left. - 2mY_{lm}^*(\theta_i, \varphi_i) \sin\left(\frac{m\Delta\varphi}{2}\right) \right] \quad (3.32)$$

Equation (3.32) is obtained by using equation (3.5). By taking the curl of equation (3.30) and applying the same method applied earlier, the following equation can be derived.

$$A_{lm}H_l^{(2)}(k_0c) - B_{lm}H_l^{(1)}(k_1c) - C_{lm}H_l^{(2)}(k_1c) = -\frac{j\omega\mu_0cJ_{TE}}{l(l+1)} \quad (3.33)$$

Where J_{TE} is surface integral of the TE component of the current density and is given by the following equation (Appendix B).

$$J_{TE} = \int_{\theta} \int_{\varphi} [\bar{r} \times \nabla Y_{lm}^*(\theta, \varphi)] \cdot [\nabla \times \bar{J}_i(\theta, \varphi)] \sin \theta d\theta d\varphi$$

$$J_{TE} = \frac{I_i}{c^2L} \left[jm(Y_{lm}^*\left(\theta_i - \frac{\Delta\theta}{2}, \varphi_i\right) - Y_{lm}^*\left(\theta_i + \frac{\Delta\theta}{2}, \varphi_i\right)) + j2 \sin \theta_i \frac{\partial Y_{lm}^*(\theta_i, \varphi_i)}{\partial \theta} \sin\left(\frac{m\Delta\varphi}{2}\right) \right] \quad (3.34)$$

Finally, looking at the last two boundary conditions at $r=b$ and $r=a$ in equations (3.28) and (3.29) the following equations can be written.

$$B_{lm}H_l^{(1)}(k_1b) + C_{lm}H_l^{(2)}(k_1b) = D_{lm}H_l^{(1)}(k_2b) + E_{lm}H_l^{(2)}(k_2b) \quad (3.35)$$

$$b_{lm}H_l^{(1)}(k_1b) + c_{lm}H_l^{(2)}(k_1b) = d_{lm}H_l^{(1)}(k_2b) + e_{lm}H_l^{(2)}(k_2b) \quad (3.36)$$

$$D_{lm}H_l^{(1)}(k_2a) + E_{lm}H_l^{(2)}(k_2a) = F_{lm}J_l'(k_3a) \quad (3.37)$$

$$d_{lm}H_l^{(1)}(k_2a) + e_{lm}H_l^{(2)}(k_2a) = f_{lm}J_l(k_3a) \quad (3.38)$$

3.2.7 Fields Inside the Brain

Since the interest is to focus the H-field inside the brain (i.e. in region (3)), equations (3.19), (3.22), (3.23), (3.24), (3.25), (3.26), (3.31), (3.33), (3.35), (3.36), (3.37) and (3.38) must be solved to get the coefficients f_{lm} and F_{lm} . Working through the equations one can get the following expressions.

$$f_{lm} = \frac{\varepsilon_1}{\varepsilon_0} \frac{J_{TM}H_l^{(2)}(k_0c)}{\Delta_l l(l+1)J_l(k_3a)} \left[\alpha_l H_l^{(1)}(k_2a) + H_l^{(2)}(k_2a) \right] \quad (3.39a)$$

$$\alpha_l = \frac{H_l^{(2)}(k_2a)J_l'(k_3a) - \frac{\varepsilon_3}{\varepsilon_2} H_l^{(2)}(k_2a)J_l(k_3a)}{\frac{\varepsilon_3}{\varepsilon_2} H_l^{(1)}(k_2a)J_l(k_3a) - H_l^{(1)}(k_2a)J_l'(k_3a)} \quad (3.39b)$$

$$\Delta_l = \xi_l \left[H_l^{(1)}(k_1 c) H_l^{(2)}(k_0 c) - \frac{\varepsilon_1}{\varepsilon_0} H_l^{(1)}(k_1 c) H_l^{(2)}(k_0 c) \right] + \frac{1}{H_l^{(2)}(k_1 b)} \left[\alpha_l H_l^{(1)}(k_2 b) + H_l^{(2)}(k_2 b) - \xi_l H_l^{(1)}(k_1 b) \right]^* \quad (3.39c)$$

$$\left[H_l^{(2)}(k_1 c) H_l^{(2)}(k_0 c) - \frac{\varepsilon_1}{\varepsilon_0} H_l^{(2)}(k_1 c) H_l^{(2)}(k_0 c) \right]$$

$$\xi_l = \frac{\left[\alpha_l H_l^{(1)}(k_2 b) + H_l^{(2)}(k_2 b) \right] H_l^{(2)}(k_1 b) - \frac{\varepsilon_2}{\varepsilon_1} \left[\alpha_l H_l^{(1)}(k_2 b) + H_l^{(2)}(k_2 b) \right] H_l^{(2)}(k_1 b)}{\frac{\varepsilon_2}{\varepsilon_1} \left[H_l^{(1)}(k_1 b) H_l^{(2)}(k_1 b) - H_l^{(1)}(k_1 b) H_l^{(2)}(k_1 b) \right]} \quad (3.39d)$$

Similarly, for the TE modes:

$$F_{lm} = \frac{j\omega\mu_0 c J_{TE} H_l^{(2)}(k_0 c)}{\chi_l l(l+1)} \left[\frac{\gamma_l H_l^{(1)}(k_2 a) + H_l^{(2)}(k_2 a)}{J_l(k_3 a)} \right] \quad (3.40a)$$

$$\gamma_l = \frac{H_l^{(2)}(k_2 a) J_l(k_3 a) - H_l^{(2)}(k_2 a) J_l'(k_3 a)}{H_l^{(1)}(k_2 a) J_l'(k_3 a) - H_l^{(1)}(k_2 a) J_l(k_3 a)} \quad (3.40b)$$

$$\chi_l = \tau_l \left[H_l^{(1)}(k_1 c) H_l^{(2)}(k_0 c) - H_l^{(1)}(k_1 c) H_l^{(2)}(k_0 c) \right] + \frac{1}{H_l^{(2)}(k_1 b)} \left[\gamma_l H_l^{(1)}(k_2 b) + H_l^{(2)}(k_2 b) - \tau_l H_l^{(1)}(k_1 b) \right]^* \quad (3.40c)$$

$$\left[H_l^{(2)}(k_1 c) H_l^{(2)}(k_0 c) - H_l^{(2)}(k_1 c) H_l^{(2)}(k_0 c) \right]$$

$$\tau_l = \frac{\left[\gamma_l H_l^{(1)}(k_2 b) + H_l^{(2)}(k_2 b) \right] H_l^{(2)}(k_1 b) - \left[\gamma_l H_l^{(1)}(k_2 b) + H_l^{(2)}(k_2 b) \right] H_l^{(2)}(k_1 b)}{\left[H_l^{(1)}(k_1 b) H_l^{(2)}(k_1 b) - H_l^{(1)}(k_1 b) H_l^{(2)}(k_1 b) \right]} \quad (3.40d)$$

By finding f_{lm} and F_{lm} it is possible to write the H-field in region (3) and it is given by the following equation.

$$\begin{aligned} \bar{H}_3 = & \hat{\theta} \left[\frac{1}{j\omega\mu_0 r} \sum_{l=1}^{\infty} \sum_{m=-l}^l F_{lm} J_l'(k_3 r) \frac{\partial Y_{lm}(\theta, \varphi)}{\partial \theta} + \frac{j}{r \sin \theta} \sum_{l=1}^{\infty} \sum_{m=-l}^l m f_{lm} J_l(k_3 r) Y_{lm}(\theta, \varphi) \right] \\ & + \hat{\varphi} \left[\frac{1}{\omega\mu_0 r \sin \theta} \sum_{l=1}^{\infty} \sum_{m=-l}^l m F_{lm} J_l'(k_3 r) Y_{lm}(\theta, \varphi) - \frac{1}{r} \sum_{l=1}^{\infty} \sum_{m=-l}^l f_{lm} J_l(k_3 r) \frac{\partial Y_{lm}(\theta, \varphi)}{\partial \theta} \right] \end{aligned} \quad (3.41)$$

As mentioned earlier, equation (3.41) represents the H-field of one antenna element. It will be shown how the H-field for all elements interact to focus the magnitude of the total field at the desired point (P). The point P is defined by $(r_o, \theta_o, \varphi_o)$ which are spherical coordinates of the desired point in region (3).

3.2.8 Exterior & Intermediate Fields

Determining f_{lm} and F_{lm} is very important for determining the nature of the fields inside the brain, but from a design standpoint it is also important to know what happens to the field in all the other regions. It is important to know how much field exposure the human head experiences when the antenna array is placed on the patient's head. To determine this one has to solve for a_{lm} and A_{lm} which are the coefficients of the fields in region (0). After determining the fields in region (0) the designer can address the health and safety issues of the array.

The intermediate fields (region (1) & region (2)) are also extremely important because they will give an indication of how much of the field intensity actually penetrates through to region (3) and how much will be reflected back to region (0). By addressing these issues, it might be possible to account for this when considering

the beamforming algorithm which will allow for the optimum amount of fields penetrating all surfaces. The intermediate fields are determined by deriving the coefficients b_{lm} , c_{lm} , d_{lm} , e_{lm} , B_{lm} , C_{lm} , D_{lm} and E_{lm} . By solving the results of the boundary conditions seen in (3.22), (3.24), (3.26), (3.31), (3.36) and (3.38) the following equations can be derived for the TM modes.

$$c_{lm} = f_{lm} \frac{J_l(k_3 a)}{H_l^{(2)}(k_1 b)} \left[\frac{\alpha_l H_l^{(1)}(k_2 b) + H_l^{(2)}(k_2 b) - \xi_l H_l^{(1)}(k_1 b)}{\alpha_l H_l^{(1)}(k_2 a) + H_l^{(2)}(k_2 a)} \right] \quad (3.42)$$

$$b_{lm} = f_{lm} \frac{\xi_l J_l(k_3 a)}{\alpha_l H_l^{(1)}(k_2 a) + H_l^{(2)}(k_2 a)} \quad (3.43)$$

$$e_{lm} = f_{lm} \frac{J_l(k_3 a)}{\alpha_l H_l^{(1)}(k_2 a) + H_l^{(2)}(k_2 a)} \quad (3.44)$$

$$d_{lm} = f_{lm} \frac{\alpha_l J_l(k_3 a)}{\alpha_l H_l^{(1)}(k_2 a) + H_l^{(2)}(k_2 a)} \quad (3.45)$$

$$a_{lm} = \frac{\varepsilon_0}{\varepsilon_1} \frac{f_{lm}}{H_l^{(2)}(k_0 c)} \left\{ H_l^{(1)}(k_1 c) \left[\frac{\xi_l J_l(k_3 a)}{\alpha_l H_l^{(1)}(k_2 a) + H_l^{(2)}(k_2 a)} \right] + H_l^{(2)}(k_1 c) \left[\frac{J_l(k_3 a)}{H_l^{(2)}(k_1 b)} \left[\frac{\alpha_l H_l^{(1)}(k_2 b) + H_l^{(2)}(k_2 b) - \xi_l H_l^{(1)}(k_1 b)}{\alpha_l H_l^{(1)}(k_2 a) + H_l^{(2)}(k_2 a)} \right] \right] \right\} \quad (3.46)$$

Similarly, by using equations (3.19), (3.23), (3.25), (3.33), (3.35) and (3.37) one can derive the coefficients for the TE modes.

$$E_{lm} = F_{lm} \frac{J_l(k_3 a)}{\gamma_l H_l^{(1)}(k_2 a) + H_l^{(2)}(k_2 a)} \quad (3.47)$$

$$D_{lm} = \gamma_l F_{lm} \frac{J_l(k_3 a)}{\gamma_l H_l^{(1)}(k_2 a) + H_l^{(2)}(k_2 a)} \quad (3.48)$$

$$B_{lm} = \tau_l F_{lm} \frac{J_l(k_3 a)}{\gamma_l H_l^{(1)}(k_2 a) + H_l^{(2)}(k_2 a)} \quad (3.49)$$

$$C_{lm} = F_{lm} \frac{J_l(k_3 a)}{H_l^{(2)}(k_1 b)} \left[\frac{\gamma_l H_l^{(1)}(k_2 b) + H_l^{(2)}(k_2 b) - \tau_l H_l^{(1)}(k_1 b)}{\gamma_l H_l^{(1)}(k_2 a) + H_l^{(2)}(k_2 a)} \right] \quad (3.50)$$

$$A_{lm} = \frac{F_{lm}}{H_l^{(2)}(k_0 c)} \left\{ H_l^{(1)}(k_1 c) \left[\frac{\tau_l J_l(k_3 a)}{\gamma_l H_l^{(1)}(k_2 a) + H_l^{(2)}(k_2 a)} \right] + \right. \\ \left. H_l^{(2)}(k_1 c) \left[\frac{J_l(k_3 a)}{H_l^{(2)}(k_1 b)} \left[\frac{\gamma_l H_l^{(1)}(k_2 b) + H_l^{(2)}(k_2 b) - \tau_l H_l^{(1)}(k_1 b)}{\gamma_l H_l^{(1)}(k_2 a) + H_l^{(2)}(k_2 a)} \right] \right] \right\} \quad (3.51)$$

Note that the coefficients of equations (3.42)-(3.51) are all given in terms of the f_{lm} and F_{lm} which are the coefficients of the TM and TE modes in region (3) respectively.

Next calculation of the power exposure of the human head to the fields the electric and magnetic fields in region (0) will be considered. After calculating the power produced by the array it will be determined what are the safe power levels for this kind of an application. Power and SNR calculations will be shown in greater detail in later sections.

The coefficients of the in between layers c_{lm} , e_{lm} , C_{lm} and E_{lm} represent the fields that are penetrating to regions (2) and (3) while b_{lm} , d_{lm} , B_{lm} and D_{lm} represent the fields that reflected back to regions (0) and (1). It is possible to calculate the transmission and reflection coefficients to determine the efficiency of the array.

3.3 Beamforming Techniques for Transmission

3.3.1 Phase Control Technique

The aim of the antenna array is to focus the magnitude of the total H-field to the point $P(r_o, \theta_o, \varphi_o)$ by adjusting the phase of each element in the manner that there will give constructive interference in the specific point of interest P and destructive in all other points. The expression that must be phase corrected is the following.

$$\begin{aligned}
 \vec{H}_{3T} &= H_{3\theta}(r, \theta, \varphi) + H_{3\varphi}(r, \theta, \varphi) \\
 &= \frac{1}{j\omega\mu_0 r} \sum_{l=1}^{\infty} \sum_{m=-l}^l F_{lm} J'_l(k_3 r) \frac{\partial Y_{lm}(\theta, \varphi)}{\partial \theta} + \frac{j}{r \sin \theta} \sum_{l=1}^{\infty} \sum_{m=-l}^l m f_{lm} J_l(k_3 r) Y_{lm}(\theta, \varphi) \\
 &+ \frac{1}{\omega\mu_0 r \sin \theta} \sum_{l=1}^{\infty} \sum_{m=-l}^l m F_{lm} J'_l(k_3 r) Y_{lm}(\theta, \varphi) - \frac{1}{r} \sum_{l=1}^{\infty} \sum_{m=-l}^l f_{lm} J_l(k_3 r) \frac{\partial Y_{lm}(\theta, \varphi)}{\partial \theta}
 \end{aligned} \tag{3.52}$$

Here it is clear that the expression being corrected is simply the addition of the θ and φ components of the H-field in equation (3.41) and naming it as the total field for a single antenna element \vec{H}_{3T} . The total H-field for the entire antenna array is given by summing over all current elements as given in equation (3.53).

$$\begin{aligned}
 \vec{H}_{3T} &= \sum_{i=1}^{N=42} \left[\frac{1}{j\omega\mu_0 r} \sum_{l=1}^{\infty} \sum_{m=-l}^l F_{lmi} J'_l(k_3 r) \frac{\partial Y_{lm}(\theta, \varphi)}{\partial \theta} + \frac{j}{r \sin \theta} \sum_{l=1}^{\infty} \sum_{m=-l}^l m f_{lmi} J_l(k_3 r) Y_{lm}(\theta, \varphi) \right. \\
 &+ \left. \frac{1}{\omega\mu_0 r \sin \theta} \sum_{l=1}^{\infty} \sum_{m=-l}^l m F_{lmi} J'_l(k_3 r) Y_{lm}(\theta, \varphi) - \frac{1}{r} \sum_{l=1}^{\infty} \sum_{m=-l}^l f_{lmi} J_l(k_3 r) \frac{\partial Y_{lm}(\theta, \varphi)}{\partial \theta} \right]
 \end{aligned} \tag{3.53}$$

Another summation has been added that describes the sum over all 42 antenna elements and the integer i is added to F_{lm} and f_{lm} to indicate that these coefficients differ from element to element. The difference is embedded in the fact that θ_i and φ_i for each element is different; this will yield different current values and hence different coefficients.

Usually what happens in antenna arrays is that the E-field or the H-field is expressed as a spherical travelling wave multiplied by a constant exponential function that contains the angular dependence of the fields. This is almost always the case since the interest is in the far fields where the expressions simplify a lot. In the far field case it is enough to make a phase shift by simply changing the phase of the antenna current since it is clear how much phase shift is needed to direct the fields to a specific point. In our case, however, the radial and angular dependence cannot be separated because they both are included in four different double sums as shown in (3.52).

What is done here is that for a specific point of interest $P(r_o, \theta_o, \varphi_o)$ equation (3.52) is pre-calculated (electronically) for all 42 elements. This means that for a desired point P equation (3.52) becomes:

$$\begin{aligned} \bar{H}_o = & \frac{1}{j\omega\mu_0 r_o} \sum_{l=1}^{\infty} \sum_{m=-l}^l F_{lm} J_l'(k_3 r_o) \frac{\partial Y_{lm}(\theta_o, \varphi_o)}{\partial \theta} + \frac{j}{r_o \sin \theta_o} \sum_{l=1}^{\infty} \sum_{m=-l}^l m f_{lm} J_l(k_3 r_o) Y_{lm}(\theta_o, \varphi_o) \\ & + \frac{1}{\omega\mu_0 r_o \sin \theta_o} \sum_{l=1}^{\infty} \sum_{m=-l}^l m F_{lm} J_l'(k_3 r_o) Y_{lm}(\theta_o, \varphi_o) - \frac{1}{r_o} \sum_{l=1}^{\infty} \sum_{m=-l}^l f_{lm} J_l(k_3 r_o) \frac{\partial Y_{lm}(\theta_o, \varphi_o)}{\partial \theta} \end{aligned} \quad (3.54)$$

When (3.54) is calculated, the result is simply a complex number that has a real and imaginary part. Afterwards, the phase of this complex number must be determined as follows.

$$\begin{aligned} \vec{H}_o &= R + jX \\ \Phi_o &= \begin{cases} \tan^{-1}\left(\frac{X}{R}\right) \rightarrow R \geq 0; X \geq 0 \\ -\tan^{-1}\left(\frac{|X|}{R}\right) \rightarrow R \geq 0; X \leq 0 \\ \pi - \tan^{-1}\left(\frac{X}{|R|}\right) \rightarrow R \leq 0; X \geq 0 \\ \pi + \tan^{-1}\left(\frac{|X|}{|R|}\right) \rightarrow R \leq 0; X \leq 0 \end{cases} \end{aligned} \quad (3.55)$$

where R and X are the real and imaginary parts of the H_o at point $P(r_o, \theta_o, \varphi_o)$ respectively and Φ_o is the phase. In order to focus the H-field of all the antenna elements on P , the phase due to the current I_i at each antenna element must be set to:

$$\Phi_i = -\Phi_o \quad (3.56)$$

In this way the total phase corrected H-field is given by the following equation.

$$\begin{aligned} \vec{H}_{3Tcorrected} &= \sum_{i=1}^{N=42} e^{j\Phi_i} \left[\frac{1}{j\omega\mu_0 r} \sum_{l=1}^{\infty} \sum_{m=-l}^l F_{lmi} J'_l(k_3 r) \frac{\partial Y_{lm}(\theta, \varphi)}{\partial \theta} + \frac{j}{r \sin \theta} \sum_{l=1}^{\infty} \sum_{m=-l}^l m f_{lmi} J_l(k_3 r) Y_{lm}(\theta, \varphi) \right. \\ &+ \left. \frac{1}{\omega\mu_0 r \sin \theta} \sum_{l=1}^{\infty} \sum_{m=-l}^l m F_{lmi} J'_l(k_3 r) Y_{lm}(\theta, \varphi) - \frac{1}{r} \sum_{l=1}^{\infty} \sum_{m=-l}^l f_{lmi} J_l(k_3 r) \frac{\partial Y_{lm}(\theta, \varphi)}{\partial \theta} \right] \end{aligned} \quad (3.57)$$

It is clear from the above analysis that the only alteration needed to control $H_{3Tcorrected}$ is in the phase of the currents of the antenna elements. Also, only the phase in the

point of interest is corrected while all other points in space are not considered. This will lead in some deficiencies in the total beam.

Simulations were performed using MATLAB on 42 elements distributed around a hemisphere of radius $c=9.5\text{ cm}$ where each element carries a current with magnitude of 1 mA (i.e. all current have the same magnitude). The frequency of operation was 1.8 GHz and an antenna spacing of $\lambda/4$, only 42 antennas could fit on the hemisphere with each element having an arc length of 4 cm. In all the equations it is clear that the summation over l is from 1 to ∞ , but obviously this cannot be achieved in the simulation. When calculating the H-field only the first 7 terms were taken into account such that l goes from 1 to 7. The radial distance of the point of signal concentration was chosen as r_o was set to 5cm (i.e. almost in the center of the brain). Two kinds of simulations were done; (1) the first simulation was for equation (3.53) in which the H-field was plotted without any phase correction, and (2) the second kind was performed on equation (3.57) for 6 different set of angles (θ_o, ϕ_o) . The angles that were chosen were $(0,0)$, $(\pi/2,0)$, $(\pi/4,\pi/4)$, $(\pi/3,\pi)$, $(\pi/2,\pi/2)$ and $(\pi/6,3\pi/2)$.

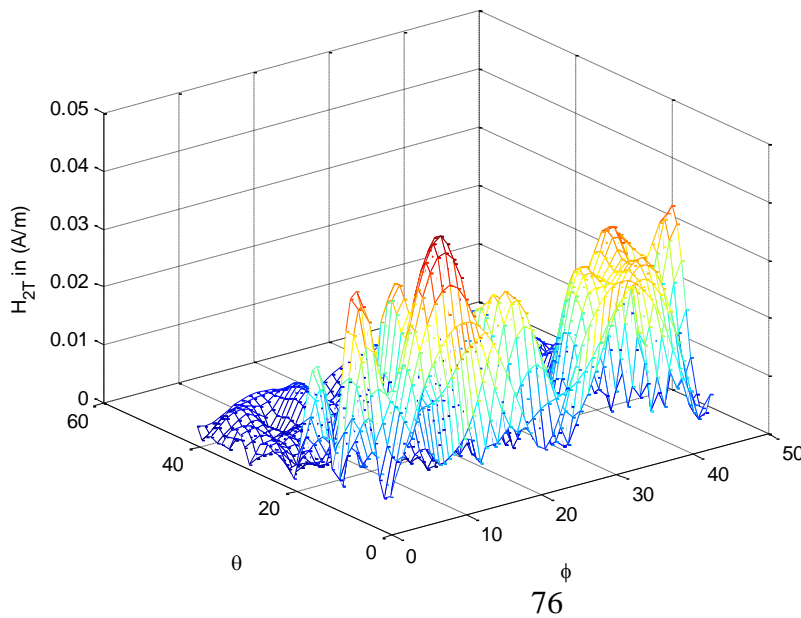


Fig. 3.3. Magnetic Field Intensity of the Antenna Array without Phase Correction.

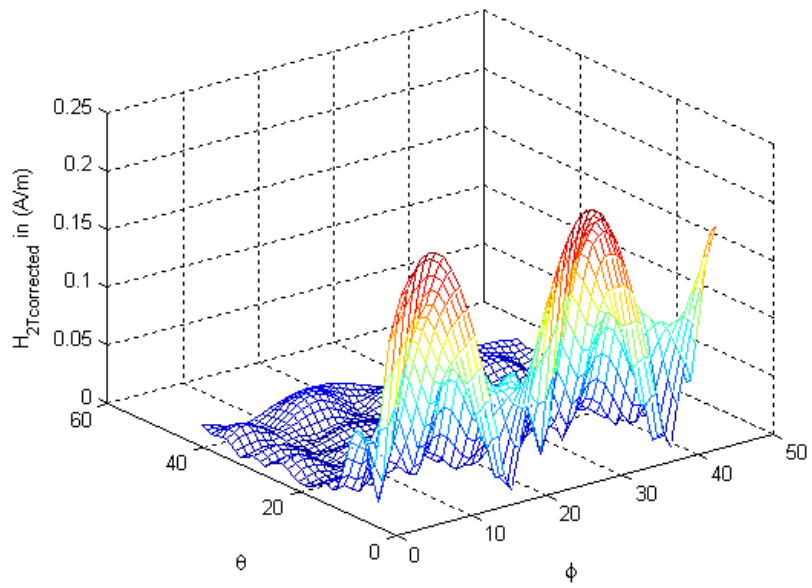


Fig. 3.4. Magnetic Field Intensity for the Antenna Array for $\theta_i=0$ & $\phi_i=0$.

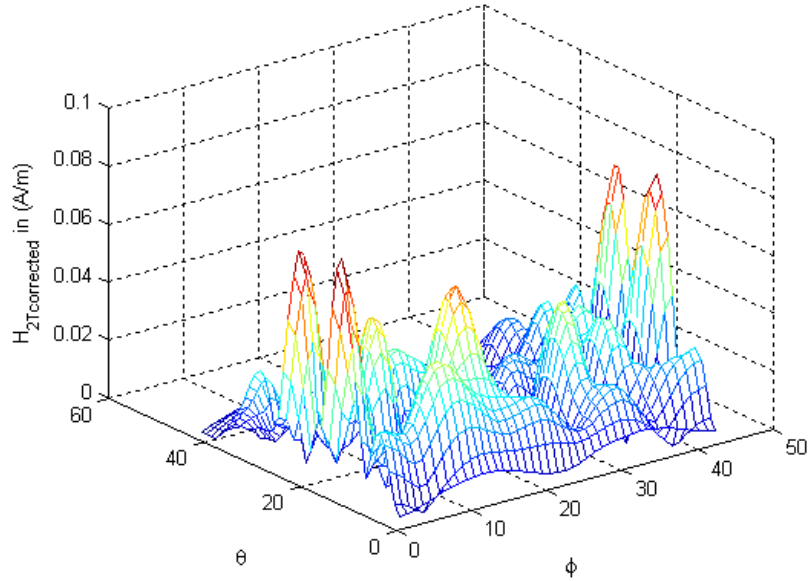


Fig. 3.5. Magnetic Field Intensity for the Antenna Array for $\theta_i=\pi/2$ & $\phi_i=0$.

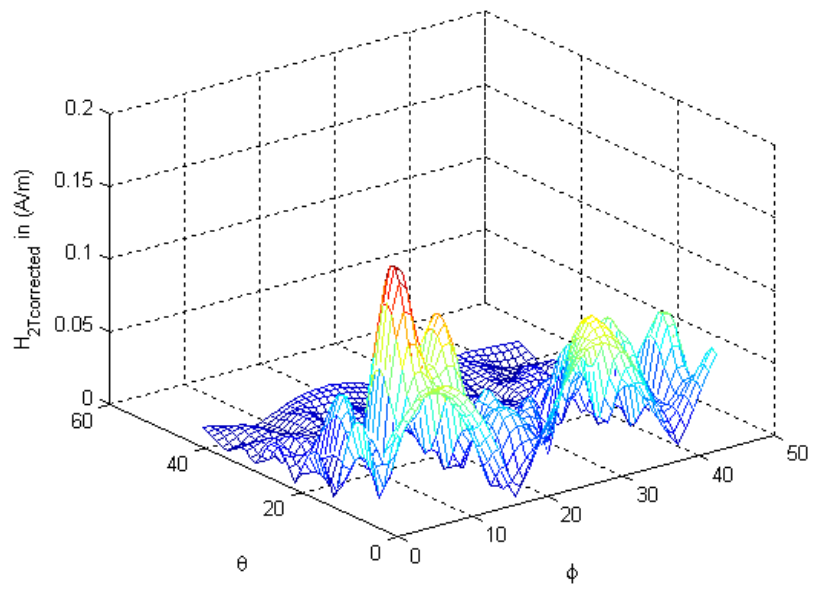


Fig. 3.6. Magnetic Field Intensity for the Antenna Array for $\theta_i = \pi/4$ & $\phi_i = \pi/4$.

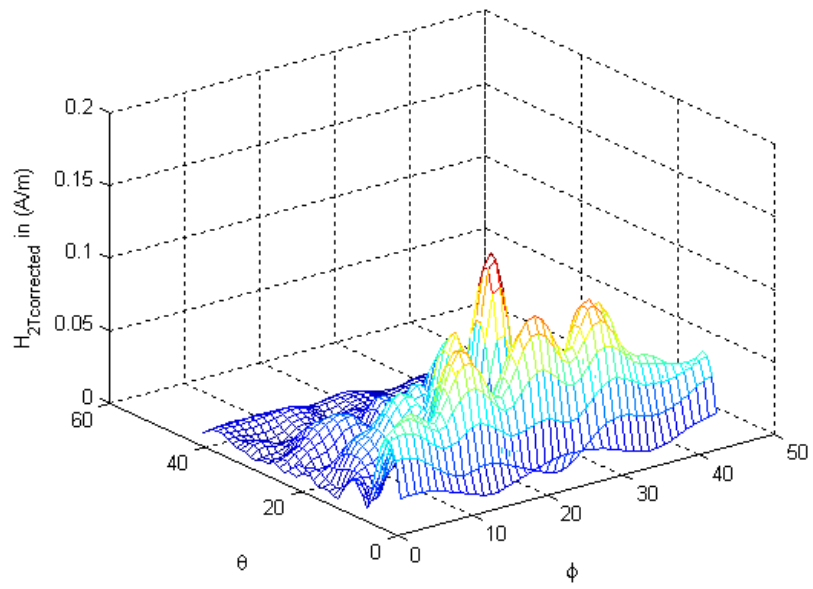


Fig. 3.7. Magnetic Field Intensity for the Antenna Array for $\theta_i = \pi/3$ & $\phi_i = \pi$.

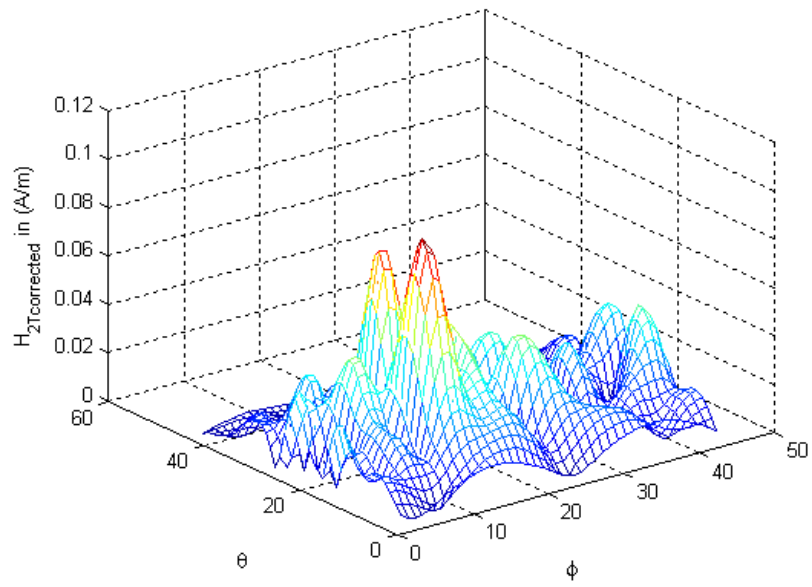


Fig. 3.8. Magnetic Field Intensity for the Antenna Array for $\theta_i=\pi/2$ & $\phi_i=\pi/2$.

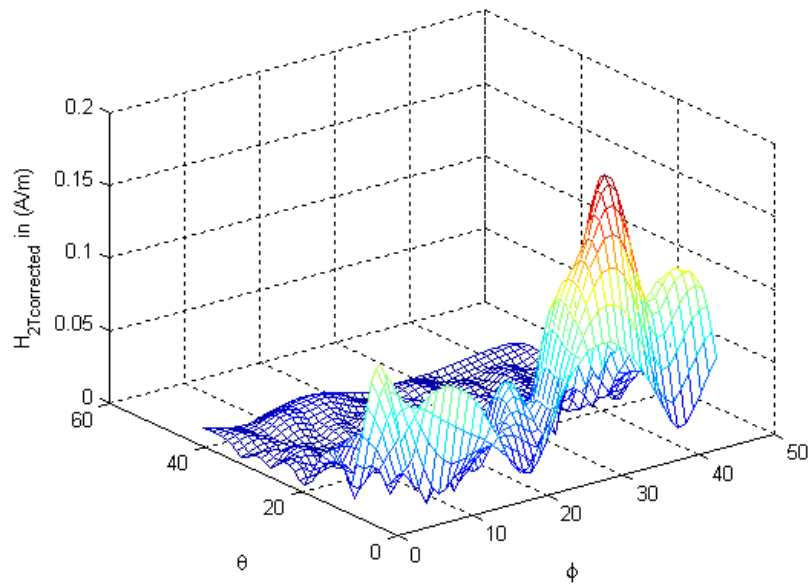


Fig. 3.9. Magnetic Field Intensity for the Antenna Array for $\theta_i=\pi/6$ & $\phi_i=3\pi/2$.

Before discussing the figures it is important to note that in the plots θ runs from 0 to π and φ runs from 0 to 2π . In the simulation the intervals 0 to π and 0 to 2π were both divided up into 42 points, hence, the reason why the figures show the θ and φ axes running from 0 to 42. That is, for the θ -axis each point represents $\pi/42$ radians while for the φ -axis each point represents $2\pi/42$ radians.

Figure 3.3 shows the H-field of the antenna array without any phase correction, it is clear that the field is scattered throughout the region with no desirable directivity whatsoever. Looking at Fig. 3.4 the phase correction scheme was used to direct the beam to the angles $(0,0)$ and it works but with some errors. The direction $(0,0)$ implies that the maximum magnetic field should be situated at the two corners $(0,0)$ and $(0,40)$, but unfortunately there is an extra peak in the middle of the plot which means that there is some field wasted in a direction which is not desirable. This occurred because the technique used only maximized the peak. As mentioned before, the technique only takes care of the phase in the direction of interest leaving all the other directions to chance which means that there will be other directions to which the array will radiate. Similarly; for all the other 5 figures it is clear that the ability to focus the magnitude of the H-field to a desired angle is present but with similar deficiencies. This is why another technique, present in the next subsection, was developed to solve the problem of unwanted radiation directions.

The good thing about the technique so far discussed is that it is very simple and straightforward and should be useful for applications that do not need high signal directivity. In this case not only high directivity is needed, but also accuracy in transmitting to the point or direction desired and only there. It is unknown what is

going to happen, for example to brain cells, when the fields are directed to places other than the one desired.

3.3.2 Orthogonality Technique

In the technique of this subsection the issues and concerns addressed in the previous subsection are addressed and a solution presented. Once again the magnetic field (H-field) for each antenna element in region (3) is considered with the objective of constructing a beam with a regular beampattern focused to a specific point $(r_o, \theta_o, \varphi_o)$. In [44] a beamforming technique was used to direct sound to a certain direction of interest using the orthogonality property of spherical harmonics. Here a similar approach is followed, but since the aim is to direct the H-field which is a vector (not a scalar like sound) it is necessary to find the right orthogonal basis functions which are vectors to be begin with. The natural choice is to use the orthogonality property of the TE and TM modes. Recall from the previous technique that the function of interest was equation (3.52) and this equation assumed that the total magnetic field resulting from one antenna element in region (3) is simply the sum of the elevation component (θ) and the azimuthal (φ) of the magnetic field. In this subsection's technique this assumption is unnecessary since with the right vector basis function it is possible to adjust the beampattern for all magnetic field components individually.

Considering a compact representation of the H-field, this representation of the equation will reveal how to use the TE and TM components for beamforming.

$$\begin{aligned}
\vec{H}_3 &= -k_3 \sum_{l=1}^{\infty} \sum_{m=-l}^l f_{lm} j_l(k_3 r) \vec{r} \times \nabla Y_{lm}(\theta, \varphi) \\
&- j \sqrt{\frac{\epsilon_3}{\mu_0}} \sum_{l=1}^{\infty} \sum_{m=-l}^l F_{lm} \nabla \times [j_l(k_3 r) \vec{r} \times \nabla Y_{lm}(\theta, \varphi)]
\end{aligned} \tag{3.58}$$

Recall that the term $j_l(k_3 r) \vec{r} \times \nabla Y_{lm}(\theta, \varphi)$ represents the TM modes and the term $\nabla \times [j_l(k_3 r) \vec{r} \times \nabla Y_{lm}(\theta, \varphi)]$ represents the TE modes. According to the basic electromagnetic theory that any function within a spherical surface can be expressed as an infinite sum of the TE and the TM terms mentioned earlier. This fact is the key in finding a beamforming technique that will enable the array to focus the beam to a single point in region (3). The best known function that has this point like behavior is the delta function.

The desired magnetic field pattern is a delta function in the point of interest $(r_o, \theta_o, \varphi_o)$, like the one shown in equation (3.59). By using the orthogonality property of the TE and TM modes, it is possible to express (3.59) in terms of the orthogonal modes as shown in equation (3.60).

$$\vec{H}_{Desired} = \delta(r - r_o) \delta(\theta - \theta_o) \delta(\varphi - \varphi_o) (\hat{\theta} + \hat{\varphi}) \tag{3.59}$$

$$\begin{aligned}
\vec{H}_{Desired} &= -k_3 \sum_{l=1}^{\infty} \sum_{m=-l}^l \Lambda_{lm} j_l(k_3 r) \vec{r} \times \nabla Y_{lm}(\theta, \varphi) \\
&- j \sqrt{\frac{\epsilon_3}{\mu_0}} \sum_{l=1}^{\infty} \sum_{m=-l}^l \Xi_{lm} \nabla \times [j_l(k_3 r) \vec{r} \times \nabla Y_{lm}(\theta, \varphi)]
\end{aligned} \tag{3.60}$$

One can equate (3.59) and (3.60) and then solve for Λ_{lm} and Ξ_{lm} by applying the orthogonality principle of both the spherical Bessel function $j_l(k_3 r)$ and the spherical harmonics vector $\vec{r} \times \nabla Y_{lm}(\theta, \varphi)$ to get the following equations. The orthogonality

principle equations are stated in equation (3.18), for the spherical harmonics, and (3.61) for the spherical Bessel [1].

$$\int_{r=0}^{\infty} r^2 j_l(kr) j_l(k'r) dr = \frac{\pi}{2k^2} \delta(k - k') \quad (3.61)$$

By making use of (3.18) and (3.61) the desired H-field can be constructed in three dimensions. By using the orthogonality property of the TE and TM modes in the entire spherical space, the coefficients A_{lm} and Ξ_{lm} can be expressed as (3.62) and (3.63) respectively (Appendix C).

$$\Lambda_{lm} = \frac{-2r_o J_l(k_3 r_o)}{\pi l(l+1)} \left[\sin \theta_o \frac{\partial Y_{lm}^*(\theta_o, \varphi_o)}{\partial \theta} + jm Y_{lm}^*(\theta_o, \varphi_o) \right] \quad (3.62)$$

$$\Xi_{lm} = \frac{2r_o \sqrt{\mu_o} (2l+1)}{j\sqrt{\epsilon_3} \pi k_3 l(l+1)^2} J_{l-1}(k_3 r_o) \left[\sin \theta_o \frac{\partial Y_{lm}^*(\theta_o, \varphi_o)}{\partial \theta} - jm Y_{lm}^*(\theta_o, \varphi_o) \right] \quad (3.63)$$

3.3.2.1 Both TE & TM Modes Present

In the case where both modes are present with comparable magnitudes it is necessary to consider how to beamform both modes. This is possible by considering the following scenario. Instead of having a signal current loop like the one shown in Fig 3.2 another smaller loop can be placed within the one so far discussed such as to have two different loops with two independent current sources that can be controlled to beamform both modes.

The beamforming technique can be considered as a minimization problem where the following error functions can be defined.

$$E_a = \left\| f_{lm}^a I_a + f_{lm}^b I_b - \Lambda_{lm}^V \right\|^2 \quad (3.64)$$

$$E_b = \left\| F_{lm}^a I_a + F_{lm}^b I_b - \Xi_{lm}^V \right\|^2 \quad (3.65)$$

Where f_{lm}^a and f_{lm}^b are two matrices representing all the terms of the coefficient f_{lm} for loops a and b respectively, F_{lm}^a and F_{lm}^b are two matrices representing all the terms of the coefficient F_{lm} for loops a and b respectively, I_a and I_b are the currents for loop a and b respectively and Λ_{lm}^V and Ξ_{lm}^V are two vectors representing all the terms of the desired coefficients Λ_{lm} and Ξ_{lm} respectively. The above matrices and vectors have the following form.

$$f_{lm}^{a,b} = \begin{bmatrix} f_{1,-1}(\theta_1, \varphi_1) & f_{1,-1}(\theta_2, \varphi_2) & \cdot & \cdot & \cdot & f_{1,-1}(\theta_N, \varphi_N) \\ f_{1,0}(\theta_1, \varphi_1) & f_{1,0}(\theta_2, \varphi_2) & \cdot & \cdot & \cdot & f_{1,0}(\theta_N, \varphi_N) \\ f_{1,1}(\theta_1, \varphi_1) & f_{1,1}(\theta_2, \varphi_2) & \cdot & \cdot & \cdot & f_{1,1}(\theta_N, \varphi_N) \\ \cdot & \cdot & \cdot & \cdot & \cdot & \cdot \\ \cdot & \cdot & \cdot & \cdot & \cdot & \cdot \\ f_{M,M}(\theta_1, \varphi_1) & f_{M,M}(\theta_2, \varphi_2) & \cdot & \cdot & \cdot & f_{M,M}(\theta_N, \varphi_N) \end{bmatrix} \quad (3.66)$$

$$F_{lm}^{a,b} = \begin{bmatrix} F_{1,-1}(\theta_1, \varphi_1) & F_{1,-1}(\theta_2, \varphi_2) & \cdot & \cdot & \cdot & F_{1,-1}(\theta_N, \varphi_N) \\ F_{1,0}(\theta_1, \varphi_1) & F_{1,0}(\theta_2, \varphi_2) & \cdot & \cdot & \cdot & F_{1,0}(\theta_N, \varphi_N) \\ F_{1,1}(\theta_1, \varphi_1) & F_{1,1}(\theta_2, \varphi_2) & \cdot & \cdot & \cdot & F_{1,1}(\theta_N, \varphi_N) \\ \cdot & \cdot & \cdot & \cdot & \cdot & \cdot \\ \cdot & \cdot & \cdot & \cdot & \cdot & \cdot \\ F_{M,M}(\theta_1, \varphi_1) & F_{M,M}(\theta_2, \varphi_2) & \cdot & \cdot & \cdot & F_{M,M}(\theta_N, \varphi_N) \end{bmatrix} \quad (3.67)$$

$$\Lambda_{lm}^V = \begin{bmatrix} \Lambda_{1,-1}(r_o, \theta_o, \varphi_o) \\ \Lambda_{1,0}(r_o, \theta_o, \varphi_o) \\ \Lambda_{1,1}(r_o, \theta_o, \varphi_o) \\ \cdot \\ \cdot \\ \Lambda_{M,M}(r_o, \theta_o, \varphi_o) \end{bmatrix} \quad (3.68)$$

$$\Xi_{lm}^V = \begin{bmatrix} \Xi_{1,-1}(r_o, \theta_o, \varphi_o) \\ \Xi_{1,0}(r_o, \theta_o, \varphi_o) \\ \Xi_{1,1}(r_o, \theta_o, \varphi_o) \\ \cdot \\ \cdot \\ \Xi_{M,M}(r_o, \theta_o, \varphi_o) \end{bmatrix} \quad (3.69)$$

Here (θ_i, φ_i) represent the position of the i th antenna element, N is the final antenna element which is 42 for our example, M represents the largest value of l of the spherical harmonic, the Bessel and Hankel functions and in this case $M=7$ and the superscript V indicates a vector. To find the optimal current values $I_{a,opt}$ and $I_{b,opt}$ one has to minimize the above two errors simultaneously and this is done by solving the following equation.

$$\frac{\partial E_a}{\partial I_a} + \frac{\partial E_a}{\partial I_b} = 0 \quad (3.70)$$

$$\frac{\partial E_b}{\partial I_a} + \frac{\partial E_b}{\partial I_b} = 0 \quad (3.71)$$

By solving the two equations the following simultaneous equations are derived.

$$\begin{aligned} XI_a + YI_b &= \Omega^H \Lambda_{lm}^V \\ WI_a + ZI_b &= Q^H \Xi_{lm}^V \end{aligned} \quad (3.72)$$

Where X, Y, W, Z, Ω and Q are matrices given by the following equations.

$$\begin{aligned} X &= (f_{lm}^{aH} f_{lm}^a + f_{lm}^{aH} f_{lm}^b)^H \\ Y &= (f_{lm}^{bH} f_{lm}^a + f_{lm}^{bH} f_{lm}^b)^H \\ W &= (F_{lm}^{aH} F_{lm}^a + F_{lm}^{aH} F_{lm}^b)^H \\ Z &= (F_{lm}^{bH} F_{lm}^a + F_{lm}^{bH} F_{lm}^b)^H \\ \Omega &= f_{lm}^a + f_{lm}^b \\ Q &= F_{lm}^a + F_{lm}^b \end{aligned} \quad (3.73)$$

Note that the superscript H represents the complex conjugate transpose of a matrix.

Equation (3.72) can be put into the following compact matrix form.

$$\begin{bmatrix} X & Y \\ W & Z \end{bmatrix} \begin{bmatrix} I_a \\ I_b \end{bmatrix} = \begin{bmatrix} \Omega^H \Lambda_{lm}^V \\ Q^H \Xi_{lm}^V \end{bmatrix} \quad (3.74)$$

The solution to the above matrix equation is:

$$\begin{bmatrix} I_{a,opt} \\ I_{b,opt} \end{bmatrix} = \begin{bmatrix} X & Y \\ W & Z \end{bmatrix}^{-1} \begin{bmatrix} \Omega^H \Lambda_{lm}^V \\ Q^H \Xi_{lm}^V \end{bmatrix} \quad (3.75)$$

By solving equation (3.75) the optimal current values will be obtained. Note that both $I_{a,opt}$ and $I_{b,opt}$ are $N \times 1$ column vectors. After obtaining the currents the beamformed H-field will take the following form.

$$\begin{aligned}
\vec{H}_{Total} = & \sum_{i=1}^N I_{ai} \left\{ -k_3 \sum_{l=1}^{\infty} \sum_{m=-l}^l f_{lmai} j_l(k_3 r) \vec{r} \times \nabla Y_{lm}(\theta, \varphi) \right. \\
& \left. - j \sqrt{\frac{\epsilon_3}{\mu_0}} \sum_{l=1}^{\infty} \sum_{m=-l}^l F_{lmai} \nabla \times [j_l(k_3 r) \vec{r} \times \nabla Y_{lm}(\theta, \varphi)] \right\} + \\
& \sum_{i=1}^N I_{bi} \left\{ -k_3 \sum_{l=1}^{\infty} \sum_{m=-l}^l f_{lmbi} j_l(k_3 r) \vec{r} \times \nabla Y_{lm}(\theta, \varphi) \right. \\
& \left. - j \sqrt{\frac{\epsilon_3}{\mu_0}} \sum_{l=1}^{\infty} \sum_{m=-l}^l F_{lmbi} \nabla \times [j_l(k_3 r) \vec{r} \times \nabla Y_{lm}(\theta, \varphi)] \right\}
\end{aligned} \tag{3.76}$$

Where I_{ai} and I_{bi} are the currents of the coincided loop currents for the i th antenna element, F_{lmai} and f_{lmai} are the coefficients for the i th antenna element that consists of two coincided loops and.

In theory the above currents should direct the H-field to the desired point $(r_o, \theta_o, \varphi_o)$ in a delta function manner as designed for.

3.3.2.2 TE Modes Present

From observations into the nature of the TE and TM modes of equation (3.58) it was to conclude that the magnitude of the TE modes is much larger than that of the TM modes. This means that it is sufficient to beamform the TE modes only.

By comparing (3.58) and (3.60) it is clear that the beamforming technique is achieved by mapping F_{lm} (coefficients of the present TE mode) to the desired coefficient Ξ_{lm} . Since these coefficients are embedded in the double sum, this mapping cannot be achieved for each antenna element individually but rather by considering the entire array as a system of linear equations.

Recall that F_{lm} (3.40a) is a function of J_{TE} (3.34) which in turn is a function of the angular position (θ_i, φ_i) of the i -th antenna element so that $F_{lm} = F_{lm}(\theta_i, \varphi_i)$. From equation (3.62) it is clear that $\Xi_{lm} = \Xi_{lm}(r_o, \theta_o, \varphi_o)$ and so the mapping would be possible by considering the following minimization statement (minimization over D).

$$\arg \min_I \left\| F_{lm}^{Mx} I - \Xi_{lm}^V \right\|^2 \quad (3.82)$$

Where:

$$F_{lm}^{Mx} = \begin{bmatrix} F_{1,-1}(\theta_1, \varphi_1) & F_{1,-1}(\theta_2, \varphi_2) & \cdot & \cdot & \cdot & F_{1,-1}(\theta_N, \varphi_N) \\ F_{1,0}(\theta_1, \varphi_1) & F_{1,0}(\theta_2, \varphi_2) & \cdot & \cdot & \cdot & F_{1,0}(\theta_N, \varphi_N) \\ F_{1,1}(\theta_1, \varphi_1) & F_{1,1}(\theta_2, \varphi_2) & \cdot & \cdot & \cdot & F_{1,1}(\theta_N, \varphi_N) \\ \cdot & \cdot & \cdot & \cdot & \cdot & \cdot \\ \cdot & \cdot & \cdot & \cdot & \cdot & \cdot \\ F_{M,M}(\theta_1, \varphi_1) & F_{M,M}(\theta_2, \varphi_2) & \cdot & \cdot & \cdot & F_{M,M}(\theta_N, \varphi_N) \end{bmatrix} \quad (3.83)$$

$$\Xi_{lm}^V = \begin{bmatrix} \Xi_{1,-1}(r_o, \theta_o, \varphi_o) \\ \Xi_{1,0}(r_o, \theta_o, \varphi_o) \\ \Xi_{1,1}(r_o, \theta_o, \varphi_o) \\ \cdot \\ \cdot \\ \Xi_{M,M}(r_o, \theta_o, \varphi_o) \end{bmatrix} \quad (3.84)$$

$$I = \begin{bmatrix} I_1 \\ I_2 \\ I_3 \\ \cdot \\ \cdot \\ I_N \end{bmatrix} \quad (3.85)$$

Where the superscript V indicates a column vector (to distinguish Ξ_{lm} the coefficient from Ξ_{lm}^V the vector) and the superscript Mx denotes a matrix (again to distinguish

F_{lm} the coefficient from $F_{lm}^{M \times N}$ the matrix). The minimization of (3.82) with respect to the current vector I will yield the following optimal current values for all N antenna elements.

$$I_{opt} = (F_{lm}^{M \times H} F_{lm}^{M \times N})^{-1} F_{lm}^{M \times H} \Xi_{lm}^V \quad (3.86)$$

The matrix $K_{lm}^{M \times N}$ is an $O \times N$ matrix that contains the TE coefficients K_{lm} for all N antenna elements. O represents the total number of terms included from the infinite double sum. The following equation describes O .

$$O = \sum_{l=1}^M (2l + 1) \quad (3.87)$$

Where l is the first index in the spherical harmonics and M is the maximum value of l desired to be reached and in this case $M=7$; thus $O=63$. By solving the minimization problem of equation (3.82) one can get the optimum current vector I_{opt} (3.86) that will ensure that the magnetic field will have a delta-like behavior in the desired point $(r_o, \theta_o, \varphi_o)$.

After determining the optimal set of currents I_{opt} , the total H-field H_{Total} can be expressed as in equation (3.88).

$$\begin{aligned} \vec{H}_{Total} = \sum_{i=1}^N I_i \left\{ -k_3 \sum_{l=1}^{\infty} \sum_{m=-l}^l f_{lmi} j_l(k_3 r) \vec{r} \times \nabla Y_{lm}(\theta, \varphi) \right. \\ \left. - j \sqrt{\frac{\epsilon_3}{\mu_0}} \sum_{l=1}^{\infty} \sum_{m=-l}^l F_{lmi} \nabla \times [j_l(k_3 r) \vec{r} \times \nabla Y_{lm}(\theta, \varphi)] \right\} \quad (3.88) \end{aligned}$$

The theory presented in this subsection was simulated in MATLAB (like the simulations shown in the previous subsection of this chapter). As mentioned earlier 42 elements were used in the simulation. Each element has a dimension of $L=2cm$ and since the frequency of operation is 1.8GHz then the spacing between the centers of the elements is $\lambda/4 \approx 4cm$. For an operating frequency of 1.8GHz the electromagnetic properties of the human head in region 0-3 are given in Table 3.1. The simulations in Figures 3.10-3.21 show how the magnitudes of both components of the H-field in (3.88) vary with the angular parameters θ and φ for a fixed radial distance $r_o=2cm$. Figures 3.22-3.25 show how the normalized H-field vary with the radial parameter r for a fixed angular direction θ_o and φ_o . Figure 3.26 and Fig. 3.27 show the three dimensional field concentration on the human head. All kind of plots will show how the beamforming technique achieves 3 dimensional beam focusing to the desired point given by $(r_o, \theta_o, \varphi_o)$.

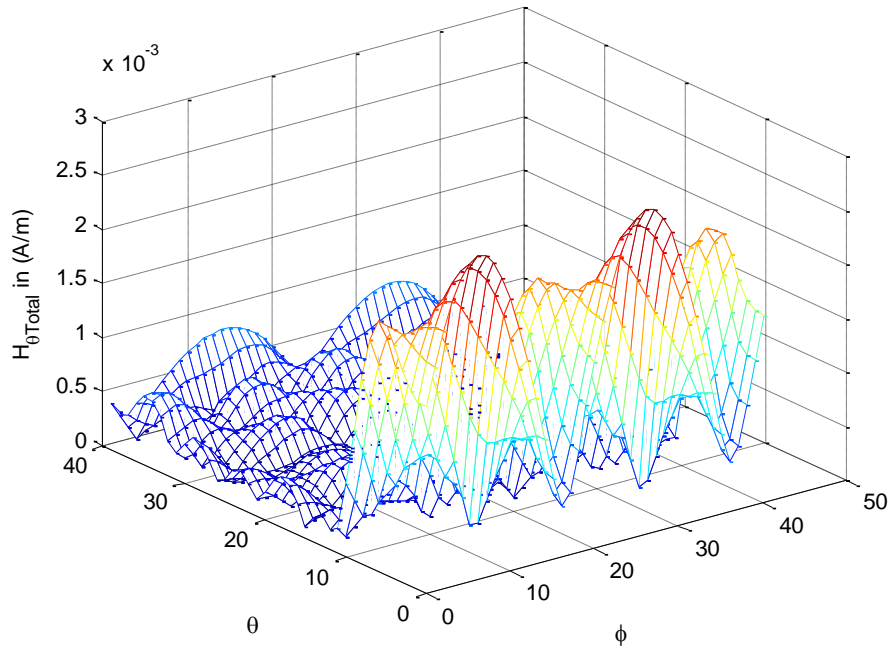


Fig. 3.10. H-field (θ -component) for the Antenna Array for $r_o=2\text{cm}$, $\theta_o=0$ & $\phi_o=0$.

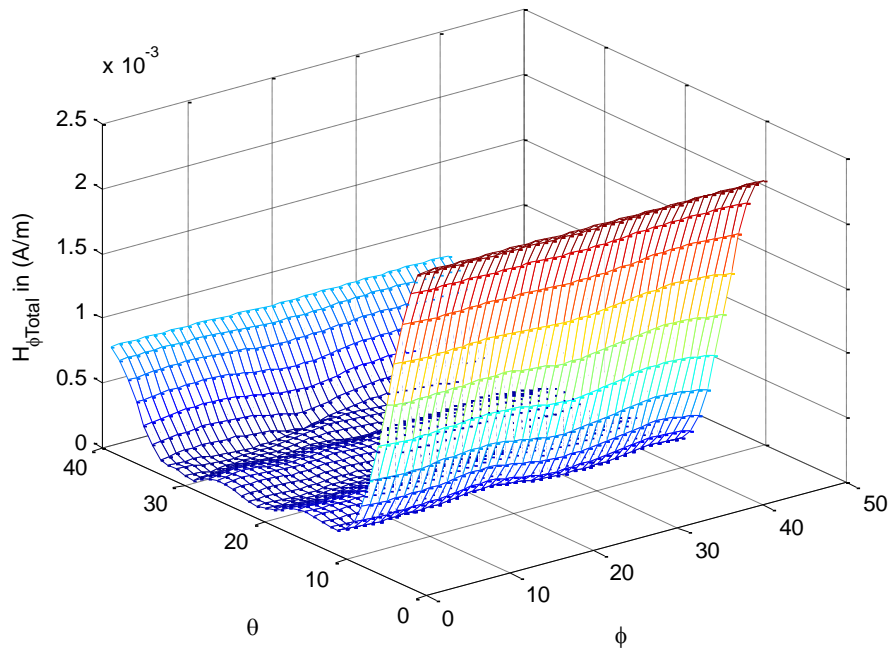


Fig. 3.11. H-field (ϕ -component) for the Antenna Array for $r_o=2\text{cm}$, $\theta_o=0$ & $\phi_o=0$.

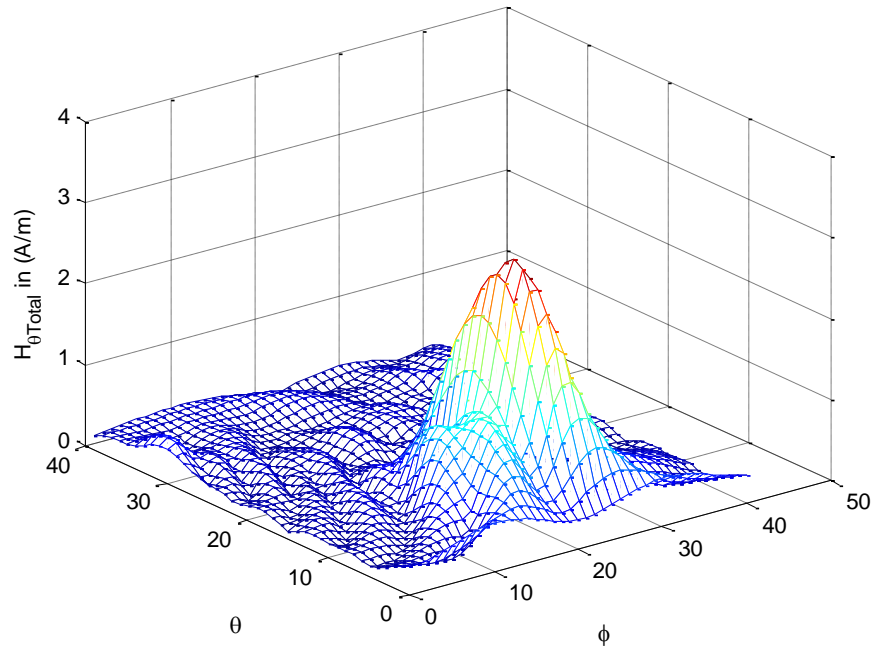


Fig. 3.12. H-field (θ -component) for the Antenna Array for $r_o=2\text{cm}$, $\theta_o=\pi/4$ & $\phi_o=\pi$.

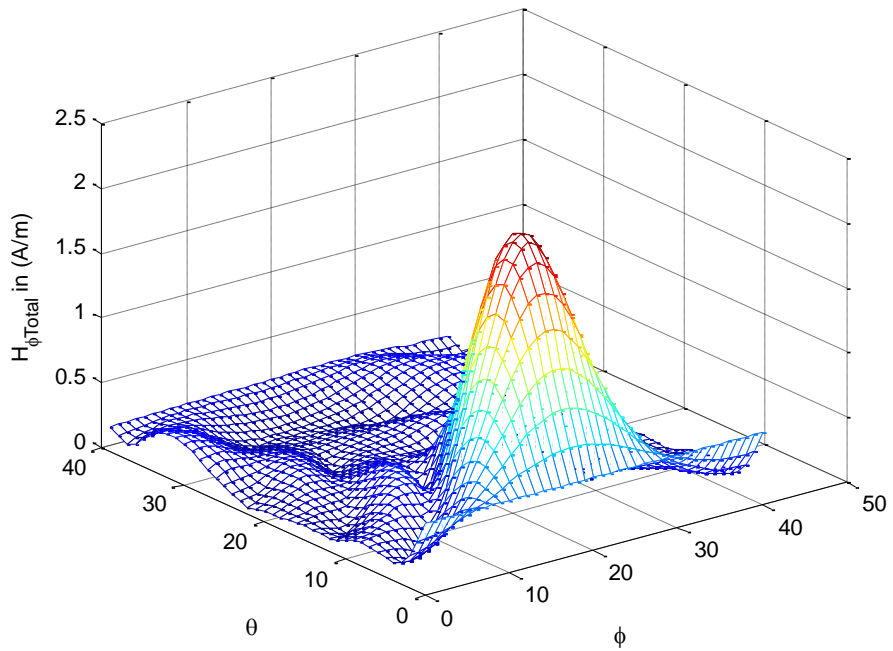


Fig. 3.13. H-field (ϕ -component) for the Antenna Array for $r_o=2\text{cm}$, $\theta_o=\pi/4$ & $\phi_o=\pi$.

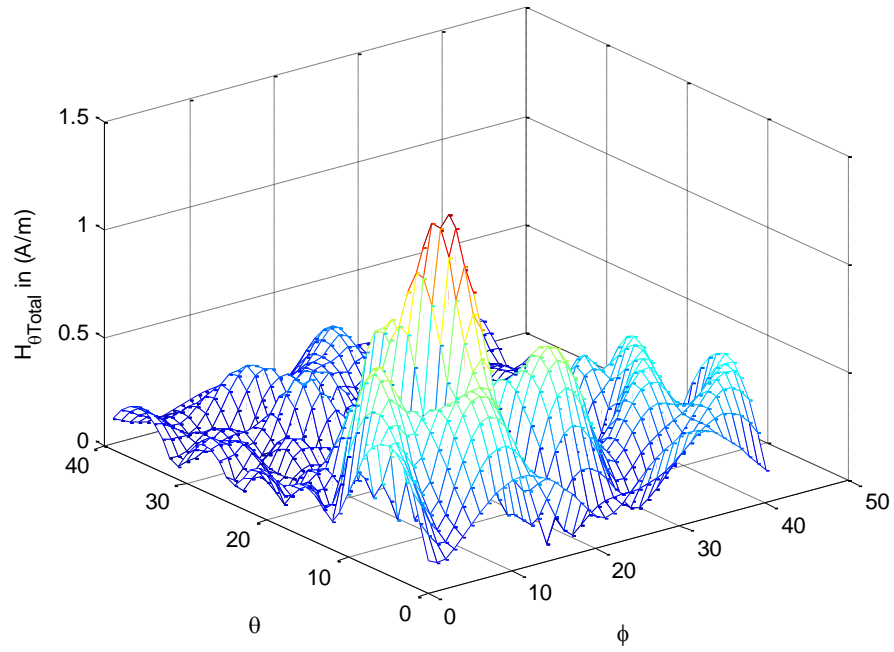


Fig. 3.14. H-field (θ -component) for the Antenna Array for $r_o=2\text{cm}$, $\theta_o=\pi/4$ & $\phi_o=\pi/2$.

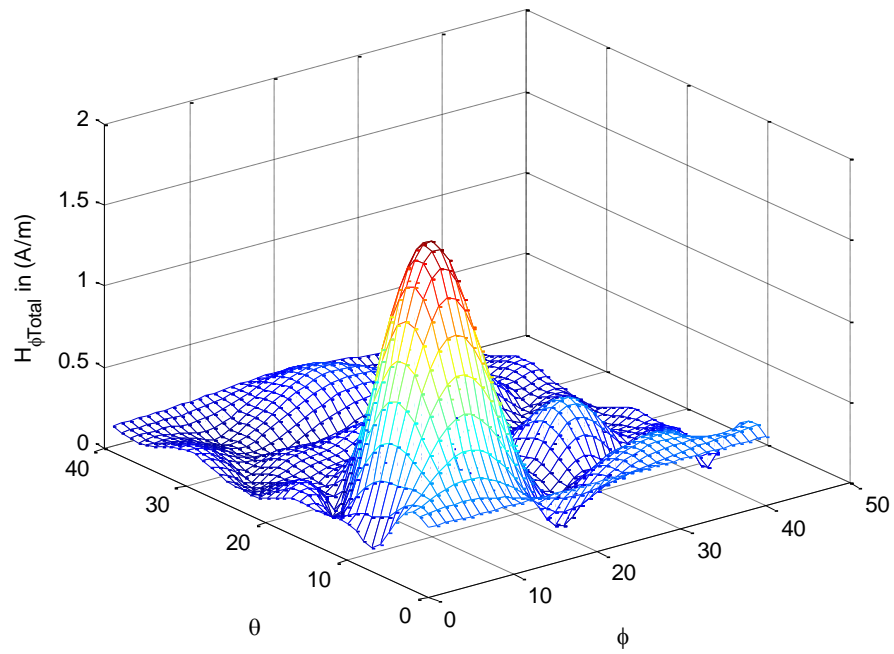


Fig. 3.15. H-field (ϕ -component) for the Antenna Array for $r_o=2\text{cm}$, $\theta_o=\pi/4$ & $\phi_o=\pi/2$.

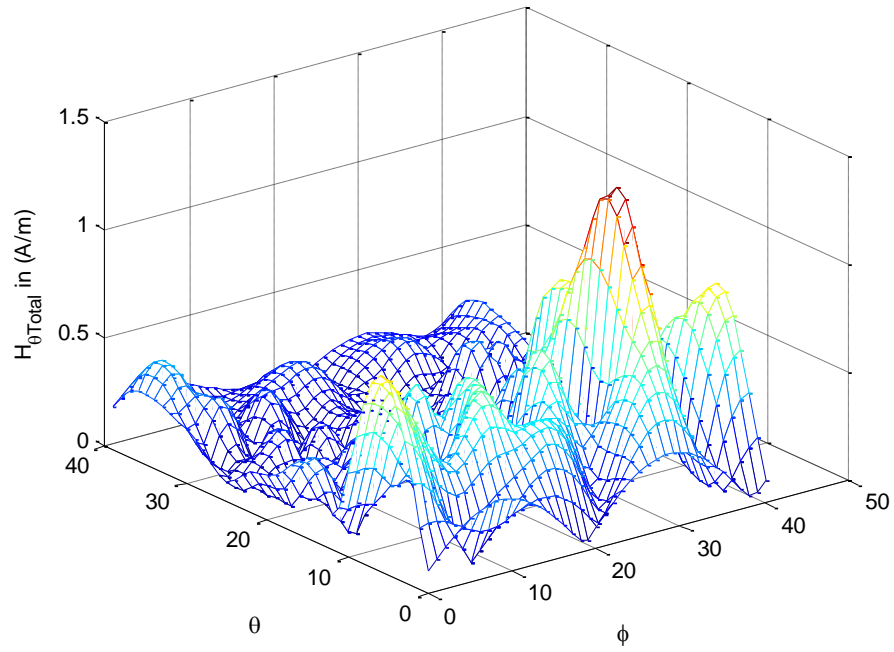


Fig. 3.16. H-field (θ -component) for the Antenna Array for $r_o=2\text{cm}$, $\theta_o=\pi/4$ & $\phi_o=3\pi/2$.

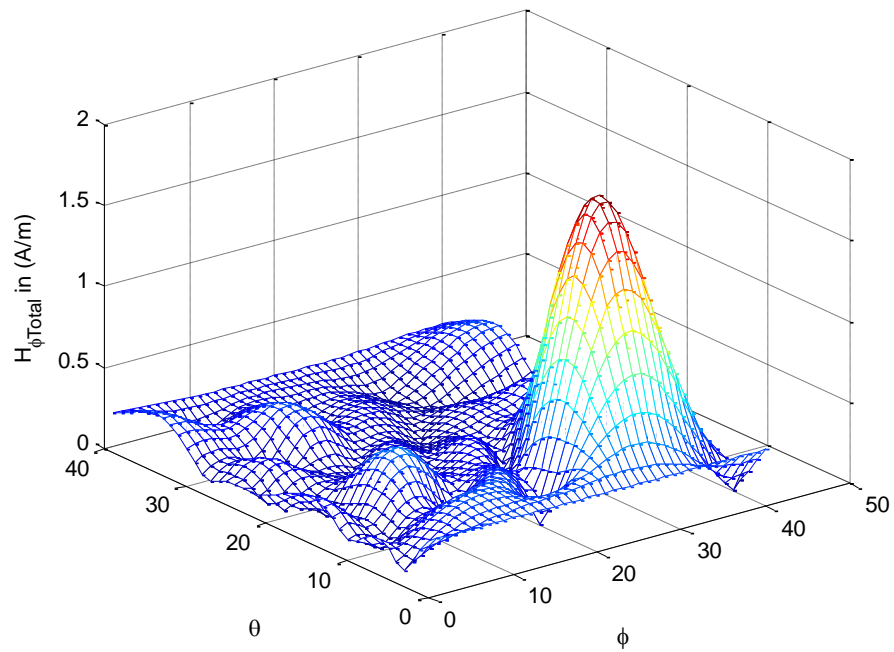


Fig. 3.17. H-field (ϕ -component) for the Antenna Array for $r_o=2\text{cm}$, $\theta_o=\pi/4$ & $\phi_o=3\pi/2$.

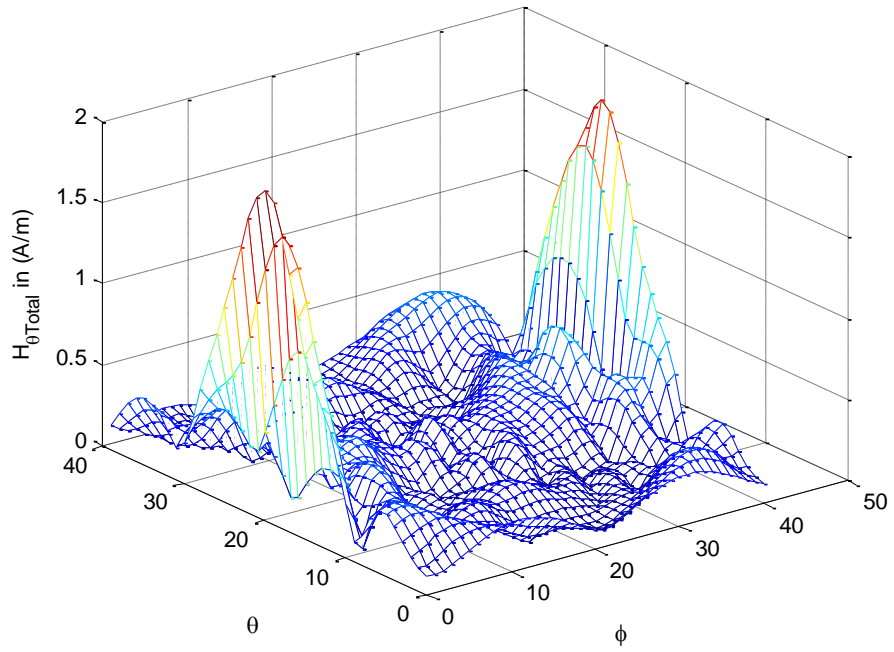


Fig. 3.18. H-field (θ -component) for the Antenna Array for $r_o=2\text{cm}$, $\theta_o=\pi/2$ & $\phi_o=0$.

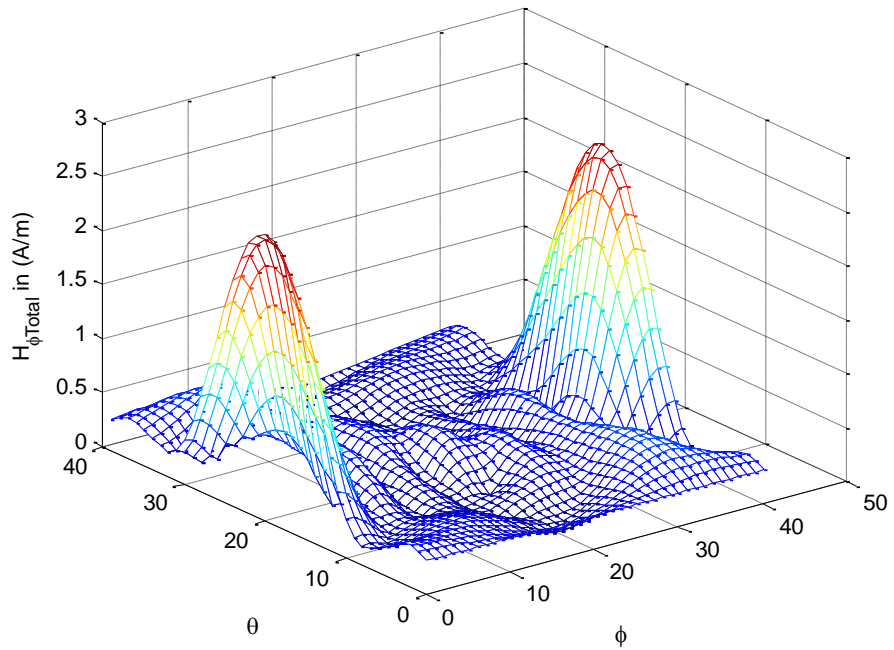


Fig. 3.19. H-field (ϕ -component) for the Antenna Array for $r_o=2\text{cm}$, $\theta_o=\pi/2$ & $\phi_o=0$.

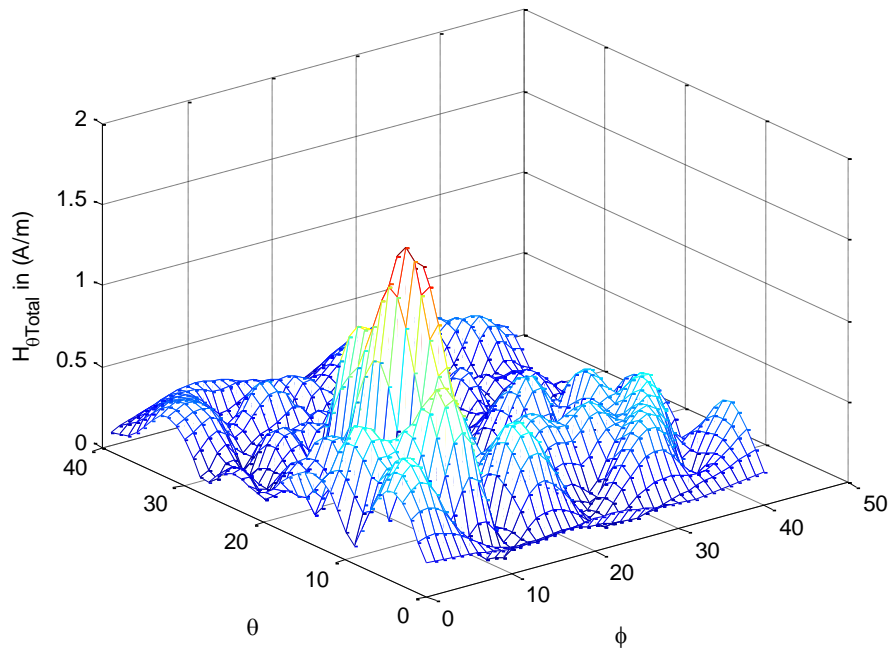


Fig. 3.20. H-field (θ -component) for the Antenna Array for $r_o=2\text{cm}$, $\theta_o=\pi/3$ & $\phi_o=\pi/2$.

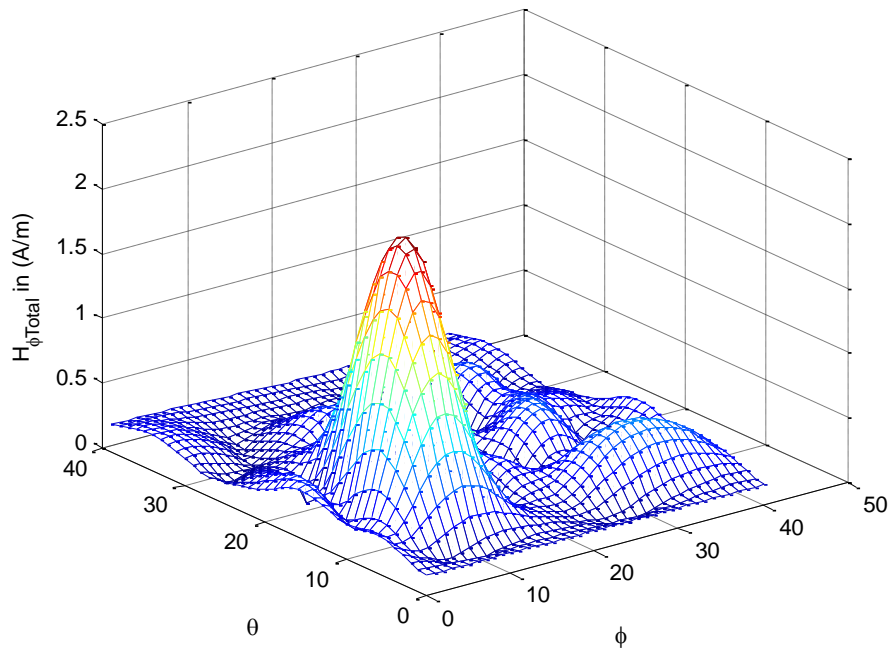


Fig. 3.21. H-field (ϕ -component) for the Antenna Array for $r_o=2\text{cm}$, $\theta_o=\pi/3$ & $\phi_o=\pi/2$.

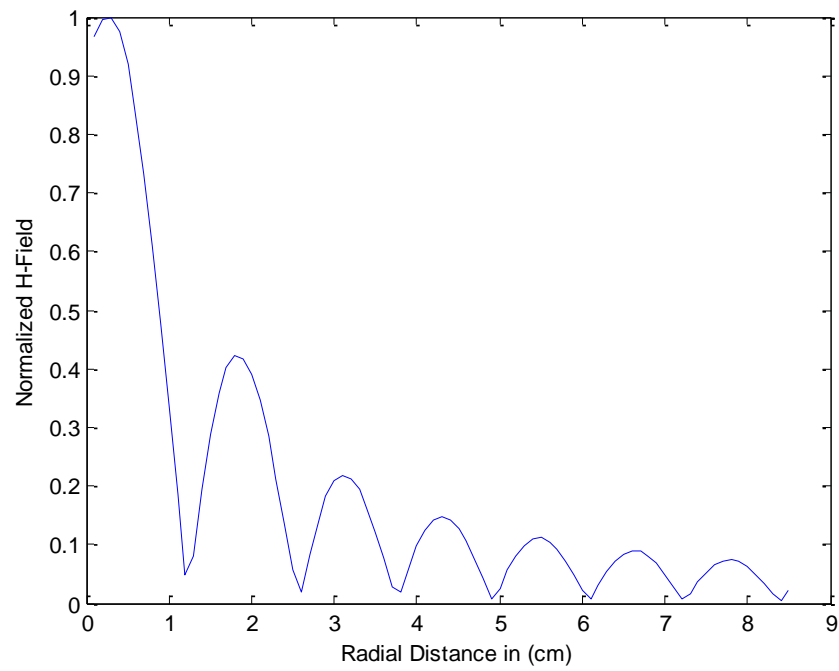


Fig. 3.22. Normalized H-Field versus radial distance for $r_o=0.5\text{cm}$, $\theta_o=\pi/2$ & $\phi_o=0$.

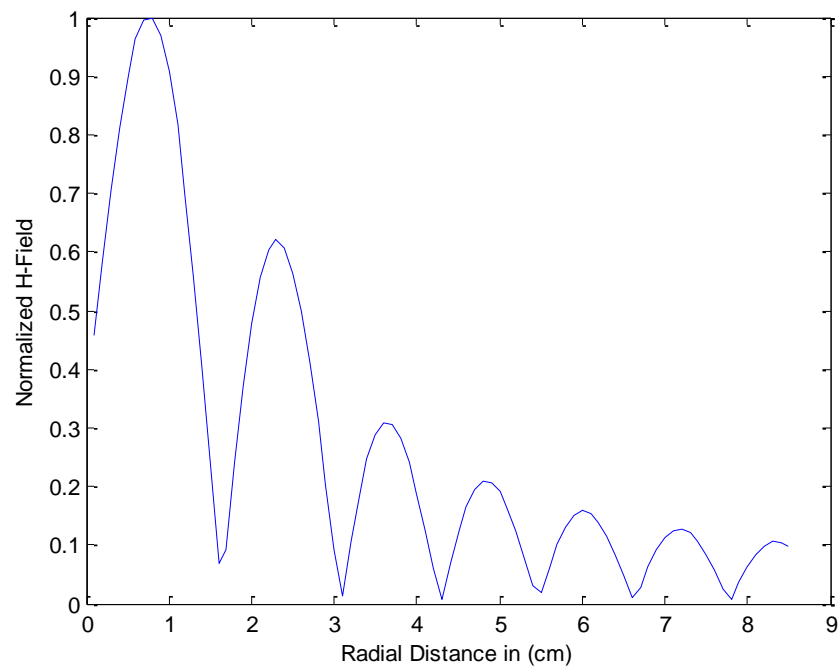


Fig. 3.23. Normalized H-Field versus radial distance for $r_o=1\text{cm}$, $\theta_o=\pi/2$ & $\phi_o=0$.

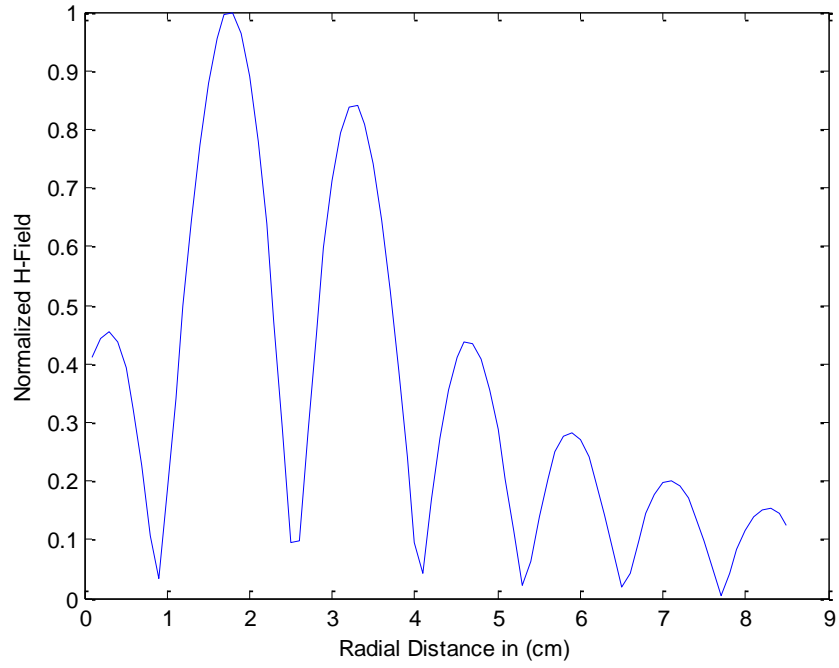


Fig. 3.24. Normalized H-Field versus radial distance for $r_o=2\text{cm}$, $\theta_o=\pi/2$ & $\varphi_o=0$.

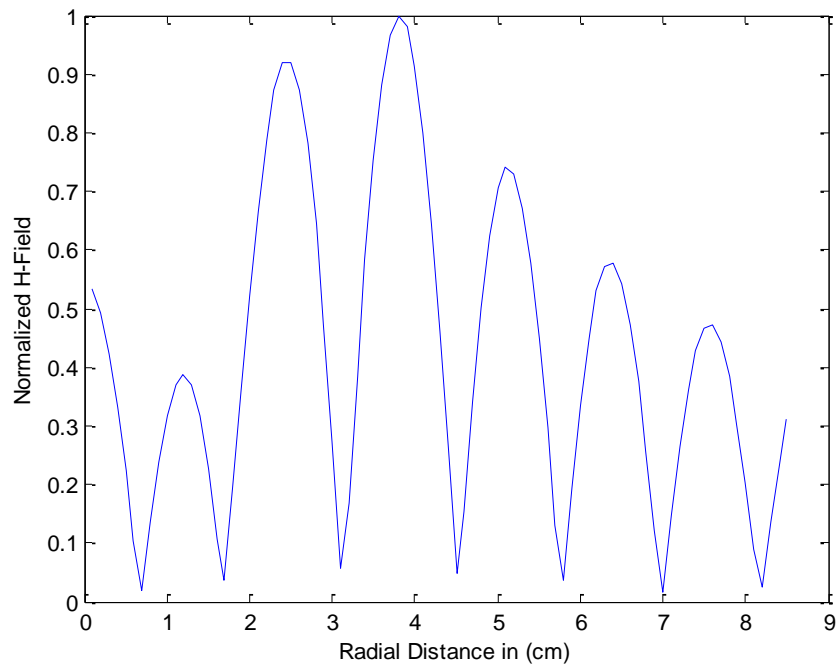


Fig. 3.25. Normalized H-Field versus radial distance for $r_o=4\text{cm}$, $\theta_o=\pi/2$ & $\varphi_o=0$.

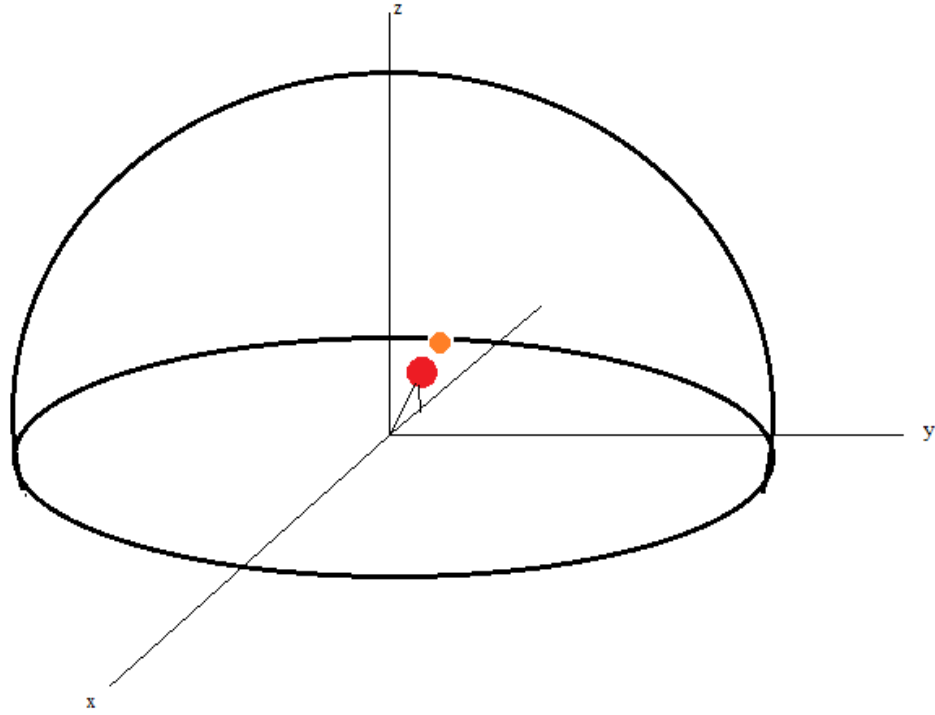


Fig. 3.26. H-Field for the Antenna Array for $r_o = 1\text{cm}$, $\theta_o = \pi/4$ & $\phi_o = \pi$. Note that the red dot indicates high intensity while the orange dot is for a low intensity.

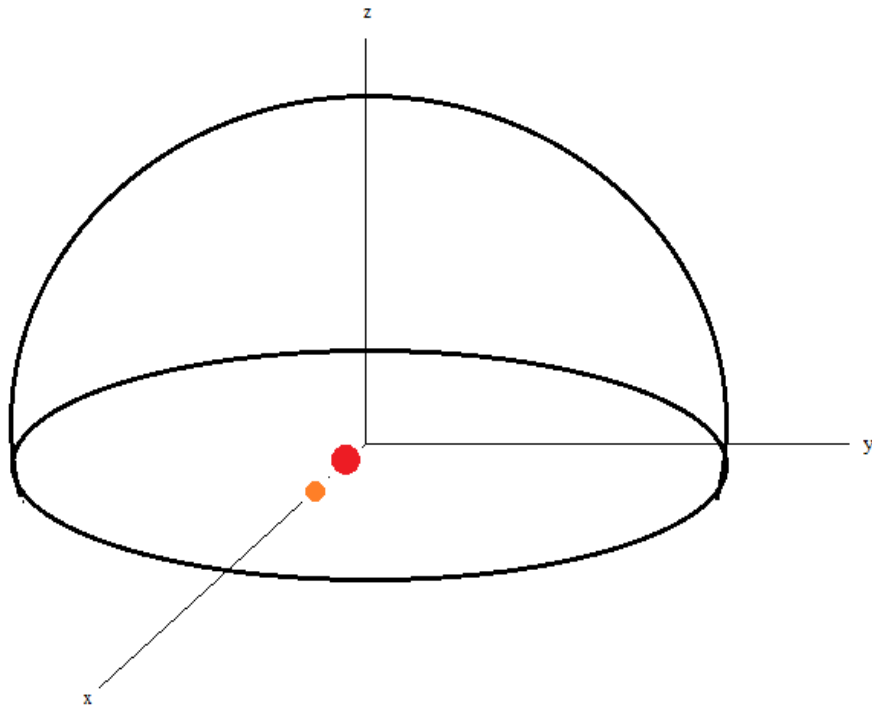


Fig. 3.27. H-Field for the Antenna Array for $r_o = 0.5\text{cm}$, $\theta_o = \pi/2$ & $\phi_o = 0$. Note that the red dot indicates high intensity while the orange dot is for a low intensity.

It is clear from the simulations for this orthogonal beamforming technique that it is successful in constructing a delta-like H-field in region (3) for every point as desired. The advantage in this technique over the one presented in Subsection 3.3.1 is that the designer has total control on both the θ -component and the φ -component of the H-field. Also, it is guaranteed in most cases that the H-field is concentrated only in the desired direction. The weakness of this technique is seen by looking at Fig 3.10 and Fig. 3.11. Although the array was able to direct the beam in the direction $(0,0)$ but unfortunately the magnitude of the H-field is almost zero.

Another remark that must be made is that the magnitude of the H-field in the desired direction is always almost equal to 1 because the desired function that was intended to be mapped or constructed was given in (3.59) which was a delta function with magnitude of 1. For real applications the intensity of the field would be adjusted to the magnitude needed, but of course with the expense of changing the magnitude of the currents in the antenna elements.

3.3.2.3 Ability to Transmit to Multiple Points

The orthogonality technique applied in the last subsection can be easily modified to allow the transmission to multiple points of interest without losing the delta-like behavior of the H-field. For example, if the designer was interested to direct the field to two direction $(r_{o1}, \theta_{o1}, \varphi_{o1})$ and $(r_{o2}, \theta_{o2}, \varphi_{o2})$ then equation (3.59) gets modified to the following equation.

$$\begin{aligned}\bar{H}_{Desired} &= \delta(r - r_{o1})\delta(\theta - \theta_{o1})\delta(\varphi - \varphi_{o1})\left(\hat{\theta} + \hat{\varphi}\right) \\ &+ \delta(r - r_{o2})\delta(\theta - \theta_{o2})\delta(\varphi - \varphi_{o2})\left(\hat{\theta} + \hat{\varphi}\right)\end{aligned}\quad (3.89)$$

The desired coefficients of the TE modes Ξ_{lm} will simply be the superposition of those in equation (3.63) for two sets of directions as shown in the following equation.

$$\begin{aligned}\Xi_{lm}^{multiple} &= \frac{2r_{o1}\sqrt{\mu_o}(2l+1)}{j\sqrt{\epsilon_3}\pi k_3 l(l+1)^2} J_{l-1}(k_3 r_{o1}) \left[\sin\theta_{o1} \frac{\partial Y_{lm}^*(\theta_{o1}, \varphi_{o1})}{\partial \theta} - jmY_{lm}^*(\theta_{o1}, \varphi_{o1}) \right] + \\ &\frac{2r_{o2}\sqrt{\mu_o}(2l+1)}{j\sqrt{\epsilon_3}\pi k_3 l(l+1)^2} J_{l-1}(k_3 r_{o2}) \left[\sin\theta_{o2} \frac{\partial Y_{lm}^*(\theta_{o2}, \varphi_{o2})}{\partial \theta} - jmY_{lm}^*(\theta_{o2}, \varphi_{o2}) \right]\end{aligned}\quad (3.90)$$

The minimization equation is similar to that presented in (3.82) with the only difference being the column vector Ξ_{lm}^V , where in this case it will take the form shown in the following equation.

$$\Xi_{lm}^V = \begin{bmatrix} \Xi_{1,-1}^{multiple}(r_{o1}, \theta_{o1}, \varphi_{o1}, r_{o2}, \theta_{o2}, \varphi_{o2}) \\ \Xi_{1,0}^{multiple}(r_{o1}, \theta_{o1}, \varphi_{o1}, r_{o2}, \theta_{o2}, \varphi_{o2}) \\ \Xi_{1,1}^{multiple}(r_{o1}, \theta_{o1}, \varphi_{o1}, r_{o2}, \theta_{o2}, \varphi_{o2}) \\ \cdot \\ \cdot \\ \Xi_{M,M}^{multiple}(r_{o1}, \theta_{o1}, \varphi_{o1}, r_{o2}, \theta_{o2}, \varphi_{o2}) \end{bmatrix}\quad (3.91)$$

The solution to this problem is given in (3.86). Fig. 3.28 and Fig. 3.29 show the components of the H-field when directed in two directions simultaneously at an equal radial distance of $r_o=5cm$. The directions used in this simulation were chosen to be $(\pi/4, \pi)$ and $(\pi/2, 0)$. It is clear from the figures that the beamforming technique used was successful in directing the beam of the H-field in those specific directions.

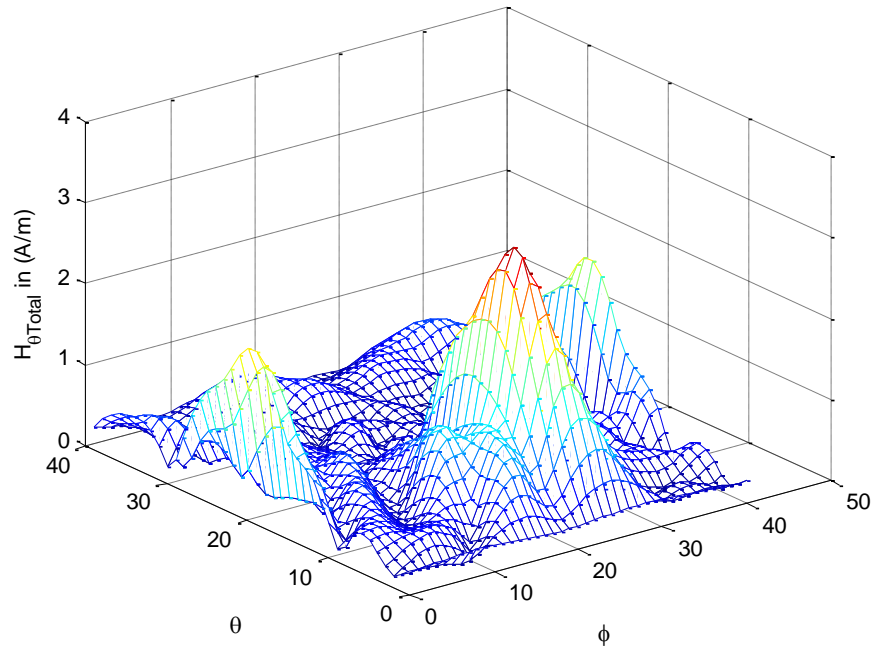


Fig. 3.28. H-field (θ -component) for the Antenna Array for $(\pi/4, \pi)$ and $(\pi/2, 0)$ for $r_o=5cm$.

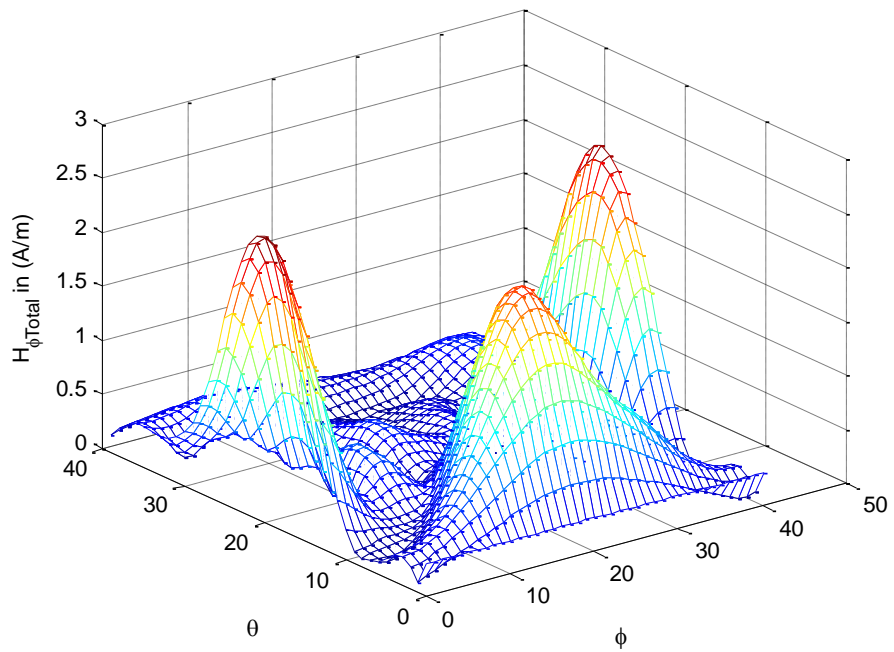


Fig. 3.29. H-field (ϕ -component) for the Antenna Array for $(\pi/4, \pi)$ and $(\pi/2, 0)$ for $r_o=5cm$.

3.4 Theoretical Analysis of the Array as a Receiver

3.4.1 Antenna Array Receivers

One of the powerful functions of an antenna array is its ability to receive a signal while suppressing the noise that comes with the desired signal. This comes from the fact that the incoming signal is received at every antenna element and by applying the proper phase shifting algorithm the signals from each element can be added coherently to enhance the strength of the desired signal while suppressing the noise level. This will result in a better SNR. In the literature there are a lot of techniques to enhance the SNR and properly scan the surroundings to determine the origin of the incoming signal and then direct the array's beam to that desired origin [6]-[15].

3.4.2 Boundary Valued Problem in the Receiving Case

Before considering the type of beamforming strategy that best fits the situation, it is important to derive the expression of the signal that will be received by each antenna element first. Of course in this case the signal will be defined by the induced current density on each antenna element from the magnetic field intensity source coming, for example from within the brain. The derivation of the current is done by making use of the equations already derived for the transmitter case. In the transmitter case $\vec{J}_i(\theta, \varphi)$ from each antenna element was the source and the objective was to find the coefficients of the fields in all three regions. In the receiving case the problem is backwards, the fields inside region (3) are known and the same boundary conditions

apply to find all the coefficients. After finding all the coefficients the current density for each antenna element is found.

The derivation starts with the assumption that there is a localized (i.e. assumed as a delta function) radiating magnetic field in region (3) at a distance r_s coming from the direction (θ_s, φ_s) (the subscript s denotes source) . Since the H-field is localized it can be described by the following equation which was used previously.

$$\vec{H}_s = \hat{\theta} H_o \delta(\theta - \theta_s) \delta(\varphi - \varphi_s) + \hat{\phi} H_o \delta(\theta - \theta_s) \delta(\varphi - \varphi_s) \quad (3.92)$$

Where H_o represents the magnitude of the H-field. To include the above H-field in the boundary-valued problem it must be represented as an infinite sum of the TE modes, thus:

$$\vec{H}_s = -j \sqrt{\frac{\epsilon_3}{\mu_0}} \sum_{l=1}^{\infty} \sum_{m=-l}^l F_{lm}^R \nabla \times [j_l(k_3 r) \vec{r} \times \nabla Y_{lm}(\theta, \varphi)]|_{r=r_s} \quad (3.93)$$

To avoid any mix up in the coefficients for the transmission and reception case a superscript R is added to the coefficients of the TE modes in regions (0) to (3). By equating (3.92) and (3.93) and applying the orthogonality property (3.18), F_{lm}^R is given by the following equation.

$$F_{lm}^R = \frac{k_3 r_s \sqrt{\mu_0} / J_l'(k_3 r_s)}{j \sqrt{\epsilon_3} l(l+1)} \left[\sin \theta_s \frac{\partial Y_{lm}^*(\theta_s, \varphi_s)}{\partial \theta} - jm Y_{lm}^*(\theta_s, \varphi_s) \right] \quad (3.94)$$

Beginning with the field in region (3) as the source, one can use the boundary conditions presented in (3.12), (3.13), (3.14), (3.27), (3.28) and (3.29) the following relationships between the coefficients of the TE mode (in reception) can be stated.

$$B_{lm}^R H_l^{(1)}(k_1 c) + C_{lm}^R H_l^{(2)}(k_1 c) = A_{lm}^R H_l^{(2)}(k_0 c) \quad (3.95)$$

$$D_{lm}^R H_l^{(1)}(k_2 b) + E_{lm}^R H_l^{(2)}(k_2 b) = B_{lm}^R H_l^{(1)}(k_1 b) + C_{lm}^R H_l^{(2)}(k_1 b) \quad (3.96)$$

$$F_{lm}^R J_l(k_3 a) = D_{lm}^R H_l^{(1)}(k_2 a) + E_{lm}^R H_l^{(2)}(k_2 a) \quad (3.97)$$

$$B_{lm}^R H_l^{(1)}(k_1 b) + C_{lm}^R H_l^{(2)}(k_1 b) = D_{lm}^R H_l^{(1)}(k_2 b) + E_{lm}^R H_l^{(2)}(k_2 b) \quad (3.98)$$

$$D_{lm}^R H_l^{(1)}(k_2 a) + E_{lm}^R H_l^{(2)}(k_2 a) = F_{lm}^R J_l'(k_3 a) \quad (3.99)$$

By solving the above equations, the following coefficients are obtained.

$$E_{lm}^R = F_{lm}^R \frac{J_l(k_3 a)}{\gamma_l H_l^{(1)}(k_2 a) + H_l^{(2)}(k_2 a)} \quad (3.100)$$

$$D_{lm}^R = \gamma_l F_{lm}^R \frac{J_l(k_3 a)}{\gamma_l H_l^{(1)}(k_2 a) + H_l^{(2)}(k_2 a)} \quad (3.101)$$

$$B_{lm}^R = \tau_l F_{lm}^R \frac{J_l(k_3 a)}{\gamma_l H_l^{(1)}(k_2 a) + H_l^{(2)}(k_2 a)} \quad (3.102)$$

$$C_{lm}^R = F_{lm}^R \frac{J_l(k_3 a)}{H_l^{(2)}(k_1 b)} \left[\frac{\gamma_l H_l^{(1)}(k_2 b) + H_l^{(2)}(k_2 b) - \tau_l H_l^{(1)}(k_1 b)}{\gamma_l H_l^{(1)}(k_2 a) + H_l^{(2)}(k_2 a)} \right] \quad (3.103)$$

$$\begin{aligned}
A_{lm}^R &= \frac{F_{lm}^R}{H_l^{(2)}(k_0c)} \left\{ H_l^{(1)}(k_1c) \left[\frac{\tau_l J_l(k_3a)}{\gamma_l H_l^{(1)}(k_2a) + H_l^{(2)}(k_2a)} \right] + \right. \\
& \left. H_l^{(2)}(k_1c) \left[\frac{J_l(k_3a)}{H_l^{(2)}(k_1b)} \left[\frac{\gamma_l H_l^{(1)}(k_2b) + H_l^{(2)}(k_2b) - \tau_l H_l^{(1)}(k_1b)}{\gamma_l H_l^{(1)}(k_2a) + H_l^{(2)}(k_2a)} \right] \right] \right\} \quad (3.104)
\end{aligned}$$

By using equation (3.27), the induced current density at the i th antenna element can be expressed as:

$$\bar{J}_i(\theta, \varphi) = \hat{r} \times \left\{ \begin{aligned} & \eta_0 \sum_{l=1}^{\infty} \sum_{m=-l}^l \nabla \times \left[\frac{1}{r} A_{lm}^R h_l^{(2)}(k_0r) \bar{r} \times \nabla Y_{lm}(\theta, \varphi) \right] \Big|_{r=c} \\ & - \eta_1 \sum_{l=1}^{\infty} \sum_{m=-l}^l \nabla \times \left[\frac{1}{r} \{ B_{lm}^R h_l^{(1)}(k_1r) + C_{lm}^R h_l^{(2)}(k_1r) \} \bar{r} \times \nabla Y_{lm}(\theta, \varphi) \right] \Big|_{r=c} \end{aligned} \right\} \quad (3.105)$$

At the i th antenna element the induced current density is at the point given by the angles (θ_i, φ_i) . Equation (3.105) simplifies to following.

$$\begin{aligned}
\bar{J}_i(\theta_i, \varphi_i) &= \sum_{l=1}^{\infty} \sum_{m=-l}^l \left(\frac{A_{lm}^R}{k_0c} \eta_0 H_l^{(2)}(k_0c) - \frac{B_{lm}^R}{k_1c} \eta_1 H_l^{(1)}(k_1c) - \frac{C_{lm}^R}{k_1c} \eta_1 H_l^{(2)}(k_1c) \right) * \\
& \left[\hat{\varphi} \frac{\partial Y_{lm}(\theta_i, \varphi_i)}{\partial \theta} + \hat{\theta} \frac{jm}{\sin \theta_i} Y_{lm}(\theta_i, \varphi_i) \right] \quad (3.106)
\end{aligned}$$

By finding the induced current density in the i th antenna element we have found the induced current which gives the received signal. Before doing that the relationship between the current and the current density is assumed to be of the following form.

$$\bar{J}_i(\theta_i, \varphi_i) = \frac{1}{L} \left(I_{\theta} \hat{\theta} + I_{\varphi} \hat{\varphi} \right) \quad (3.107)$$

For this the induced current components are therefore given by the following equations.

$$I_{\theta} = L \bar{J}_i(\theta_i, \varphi_i) \cdot \hat{\theta} = L \sum_{l=1}^{\infty} \sum_{m=-l}^l \left(\frac{A_{lm}^R}{k_0 c} \eta_0 H_l^{(2)}(k_0 c) - \frac{B_{lm}^R}{k_1 c} \eta_1 H_l^{(1)}(k_1 c) - \frac{C_{lm}^R}{k_1 c} \eta_1 H_l^{(2)}(k_1 c) \right) * \frac{jm}{\sin \theta_i} Y_{lm}(\theta_i, \varphi_i) \quad (3.108)$$

$$I_{\varphi} = L \bar{J}_i(\theta_i, \varphi_i) \cdot \hat{\varphi} = L \sum_{l=1}^{\infty} \sum_{m=-l}^l \left(\frac{A_{lm}^R}{k_0 c} \eta_0 H_l^{(2)}(k_0 c) - \frac{B_{lm}^R}{k_1 c} \eta_1 H_l^{(1)}(k_1 c) - \frac{C_{lm}^R}{k_1 c} \eta_1 H_l^{(2)}(k_1 c) \right) * \frac{\partial Y_{lm}(\theta_i, \varphi_i)}{\partial \theta} \quad (3.109)$$

Where L represents the antenna dimension and $\eta_{(0,1,2,3)}$ represents the admittance of the regions (0,1,2,3) respectively and the symbol * is just a multiplication sign (not the complex conjugate). η_i is given by the following equation.

$$\eta_i = \sqrt{\frac{\epsilon_i}{\mu_i}} \quad ; i=0,1, 2 \text{ or } 3 \quad (3.110)$$

Before going any further it is better to slightly simplify (3.108) and (3.109) using the fact that A_{lm}^R , B_{lm}^R and C_{lm}^R are all functions of the known coefficient F_{lm}^R . The expression for the currents will then become:

$$I_{\theta} = L \sum_{l=1}^{\infty} \sum_{m=-l}^l F_{lm}^R \Psi_l \frac{jm}{\sin \theta_i} Y_{lm}(\theta_i, \varphi_i) \quad (3.111)$$

where:

$$\begin{aligned}
\Psi_l = & \frac{\eta_0}{k_0 c} \frac{H_l^{(2)}(k_0 c)}{H_l^{(2)}(k_0 c)} \left\{ H_l^{(1)}(k_1 c) \left[\frac{\tau_l J_l(k_3 a)}{\gamma_l H_l^{(1)}(k_2 a) + H_l^{(2)}(k_2 a)} \right] + \right. \\
& H_l^{(2)}(k_1 c) \left[\frac{J_l(k_3 a)}{H_l^{(2)}(k_1 b)} \left[\frac{\gamma_l H_l^{(1)}(k_2 b) + H_l^{(2)}(k_2 b) - \tau_l H_l^{(1)}(k_1 b)}{\gamma_l H_l^{(1)}(k_2 a) + H_l^{(2)}(k_2 a)} \right] \right] \left. \right\} \\
& - \frac{\eta_l}{k_1 c} \frac{\tau_l J_l(k_3 a) H_l^{(1)}(k_1 c)}{\gamma_l H_l^{(1)}(k_2 a) + H_l^{(2)}(k_2 a)} \\
& - \frac{\eta_l}{k_1 c} \frac{J_l(k_3 a) H_l^{(2)}(k_1 c)}{H_l^{(2)}(k_1 b)} \left[\frac{\gamma_l H_l^{(1)}(k_2 b) + H_l^{(2)}(k_2 b) - \tau_l H_l^{(1)}(k_1 b)}{\gamma_l H_l^{(1)}(k_2 a) + H_l^{(2)}(k_2 a)} \right]
\end{aligned} \tag{3.112}$$

$$I_\varphi = L \sum_{l=1}^{\infty} \sum_{m=-l}^l F_{lm}^R \Psi_l \frac{\partial Y_{lm}(\theta_i, \varphi_i)}{\partial \theta} \tag{3.113}$$

3.5 Beamforming Technique for Reception

After obtaining the received current signal equation in the previous section it is now possible to consider the beamforming technique that will allow the array to efficiently scan the environment. By proper scanning the array will determine the source from which the source H-field originated.

The technique used here differs from that used in [44] or the usual techniques followed in [6]-[15]. The new technique is actually somewhere in between the two methods. The idea behind the technique remains the same as that used in the transmission case, i.e. using the orthogonality principle of the TE modes.

To begin the analysis the received input current at the i th antenna element is of the following term [6]-[15].

$$I_i = I_{\theta_i} + n_i \quad (3.114)$$

Where I_{θ_i} is given by equation (3.108) and n_i is a zero mean white Gaussian noise with variance σ_n^2 [10]. Each signal I_i will be multiplied by a weight factor (i.e. magnitude and phase) g_i and then all the signals from all the elements are added up to produce one output current I_{out} given by equation (3.115).

$$I_{out} = \sum_{i=1}^N I_i g_i = \sum_{i=1}^N (I_{\theta_i} g_i + n_i g_i) \quad (3.115)$$

The weight factors are responsible for applying the orthogonality property to estimate the direction of arrival (denoted as DOA). The following process is used to determine the weight factors.

3.5.1 Determining g_i

The weight factors are determined by considering (3.115) in a matrix form like the one shown in (3.116).

$$I_{out} = FSg^V + Ng^V \quad (3.116)$$

Where:

$$F = \begin{bmatrix} F_{1,-1}^R(\theta_s, \varphi_s) & F_{1,0}^R(\theta_s, \varphi_s) & F_{1,1}^R(\theta_s, \varphi_s) & \cdot & \cdot & F_{M,M}^R(\theta_s, \varphi_s) \end{bmatrix} \quad (3.117)$$

$$g^V = \begin{bmatrix} g_1 \\ g_2 \\ g_3 \\ \vdots \\ g_N \end{bmatrix} \quad (3.118)$$

$$S = \begin{bmatrix} \Psi_1 \frac{-j}{\sin \theta_1} Y_{1,-1}(\theta_1, \varphi_1) & \Psi_1 \frac{-j}{\sin \theta_2} Y_{1,-1}(\theta_2, \varphi_2) & \cdot & \cdot & \cdot & \Psi_1 \frac{-j}{\sin \theta_N} Y_{1,-1}(\theta_N, \varphi_N) \\ 0 & 0 & \cdot & \cdot & \cdot & 0 \\ \Psi_1 \frac{j}{\sin \theta_1} Y_{1,1}(\theta_1, \varphi_1) & \Psi_1 \frac{j}{\sin \theta_2} Y_{1,1}(\theta_2, \varphi_2) & \cdot & \cdot & \cdot & \Psi_1 \frac{j}{\sin \theta_N} Y_{1,1}(\theta_N, \varphi_N) \\ \cdot & \cdot & \cdot & \cdot & \cdot & \cdot \\ \cdot & \cdot & \cdot & \cdot & \cdot & \cdot \\ \Psi_M \frac{jM}{\sin \theta_1} Y_{M,M}(\theta_1, \varphi_1) & \Psi_M \frac{jM}{\sin \theta_2} Y_{M,M}(\theta_2, \varphi_2) & \cdot & \cdot & \cdot & \Psi_M \frac{jM}{\sin \theta_N} Y_{M,M}(\theta_N, \varphi_N) \end{bmatrix} \quad (3.119)$$

$$N = [n_1 \quad n_2 \quad n_3 \quad \cdot \quad \cdot \quad n_N] \quad (3.120)$$

F is a vector that contains the information about the source signal, S is a matrix that contains the terms of the double sum present in (3.111), g^V is a column vector that contains the adjustable weights and N is a row vector that contains the noise for each antenna element.

The aim in this problem is to use the vector g^V to transfer the matrix S into the following vector.

$$S_{Desired} = \begin{bmatrix} \frac{-j}{\sin \theta} Y_{1,-1}(\theta, \varphi) \\ 0 \\ \frac{j}{\sin \theta} Y_{1,1}(\theta, \varphi) \\ \cdot \\ \cdot \\ \frac{jM}{\sin \theta} Y_{M,M}(\theta, \varphi) \end{bmatrix} \quad (3.121)$$

Reducing the matrix from S to the vector $S_{Desired}$ enables the use of the orthogonality principle. When considering the product between F and $S_{Desired}$ the output current becomes:

$$I_{out} = FS_{Desired} + Ng^V = I_{\theta} = \sum_{l=1}^{M=7} \sum_{m=-l}^l F_{lm}^R \frac{jm}{\sin \theta} Y_{lm}(\theta, \varphi) + \sum_{i=1}^N n_i g_i \quad (3.122)$$

$$I_{out} \approx \delta(\theta - \theta_s) \delta(\varphi - \varphi_s) + \sum_{i=1}^N n_i g_i$$

It is clear from (3.122) that the resulting current is desired to be a delta-like form in the control angles (θ, φ) with some added noise. The scanning process is done in the sense that the control angles (θ, φ) are going to be varied from 0 to π for θ and from 0 to 2π for φ . For each control angle set (θ, φ) I_{out} is calculated by first finding the optimal set of weight factors g^V . When the calculation is done for all the angle sets, plotting $I_{out}(\theta, \varphi)$ will show that the output will have its maximum value at (θ_s, φ_s) which is the aim of the array. In this way by using some kind of a maximum seeking

circuit and after that determining at which control angle set this maximum was found, the direction of arrival is made possible.

To transform S to $S_{Desired}$ the following problem must be solved for each control angle set.

$$\arg \min_g \left\| Sg^V - S_{Desired} \right\|^2 \quad (3.123)$$

$$g_{opt}^V = (S^H S)^{-1} S^H S_{Desired} \quad (3.124)$$

Before going on to the simulation, the frequency of operation must be fixed. As it was shown in the literature review, the brain waves that are going to be received come as a result of having evoked potentials. These evoked potentials vary in amplitude and frequency. They can range from a couple of hertz up to 500 kHz in frequency. The antenna array for reception should be designed for those frequencies. In the dissertation, the array will be designed to receive signals at 500 kHz. Putting this in mind Table 3.2 should be used for the values of the permittivities and conductivities of the human head at 500 kHz. Also, as it will be shown in Chapter 5, the receiver should be designed at 500 kHz.

TABLE 3.2

Relative Permittivity & Conductivity of the Four Regions of Operation at 500 kHz
[45].

	ϵ_r	σ (S/m)
Region (0)	1	0
Region (1)	38.87	1.88
Region (2)	19.34	0.59
Region (3)	51.8	1.5

With these specifications in mind, Fig. 3.30 to Fig. 3.36 show the normalized output current I_{out} as a function of the control angles.

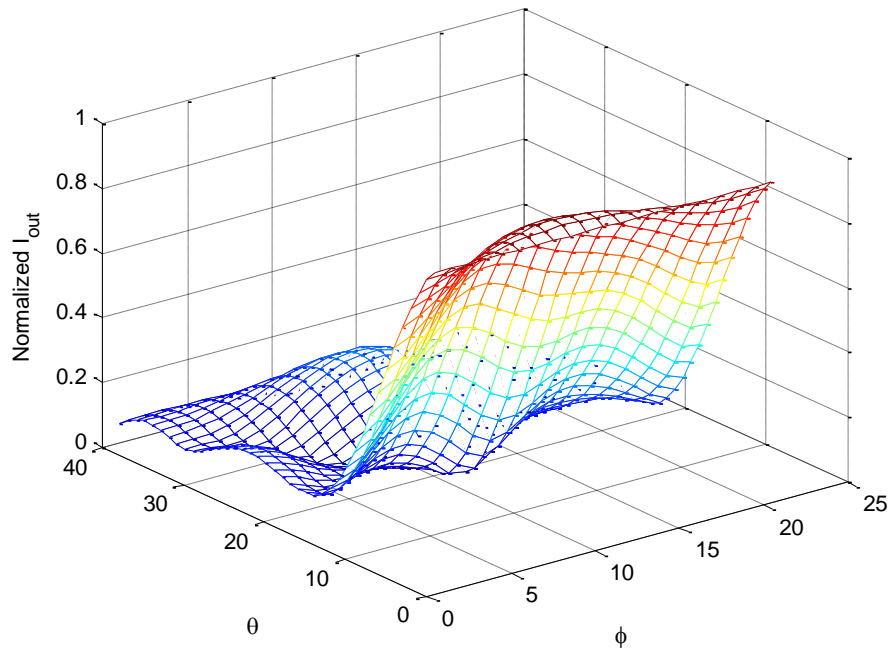


Fig. 3.30. $I_{out}(\theta, \phi)$ for $\theta_s=0$ & $\phi_s=0$.

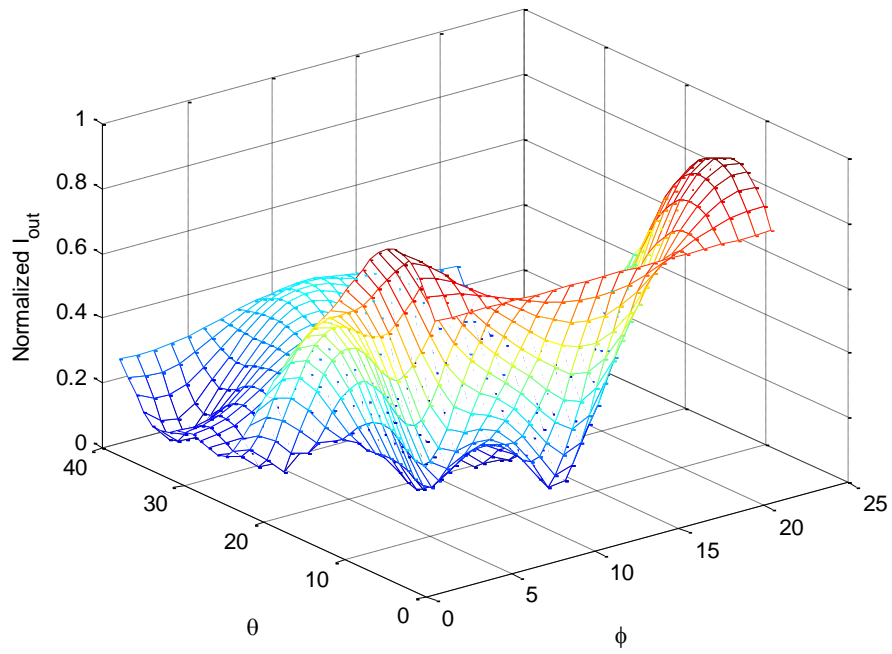


Fig. 3.31. $I_{out}(\theta, \phi)$ for $\theta_s = \pi/4$ & $\phi_s = 0$.

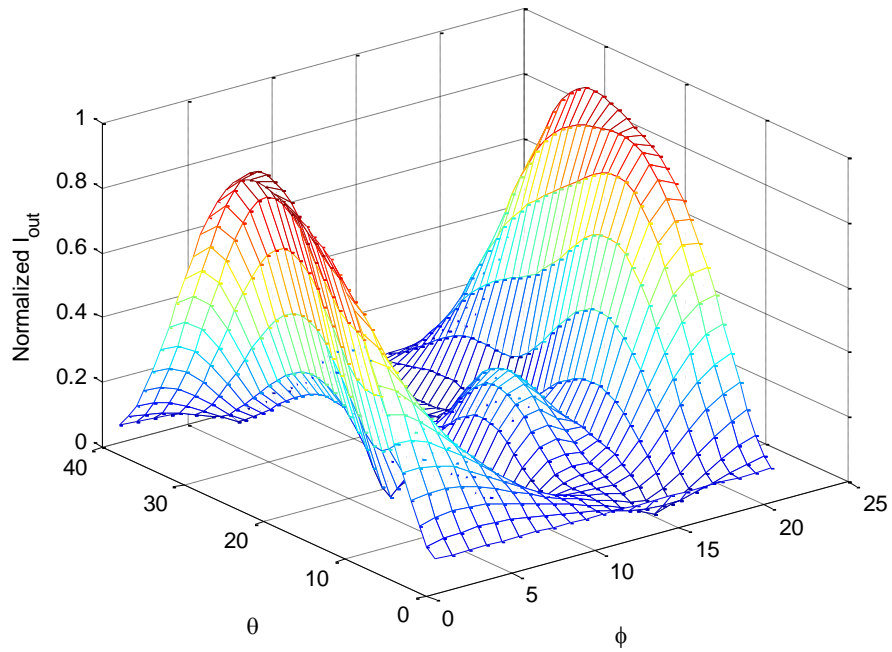


Fig. 3.32. $I_{out}(\theta, \phi)$ for $\theta_s = \pi/2$ & $\phi_s = 0$.

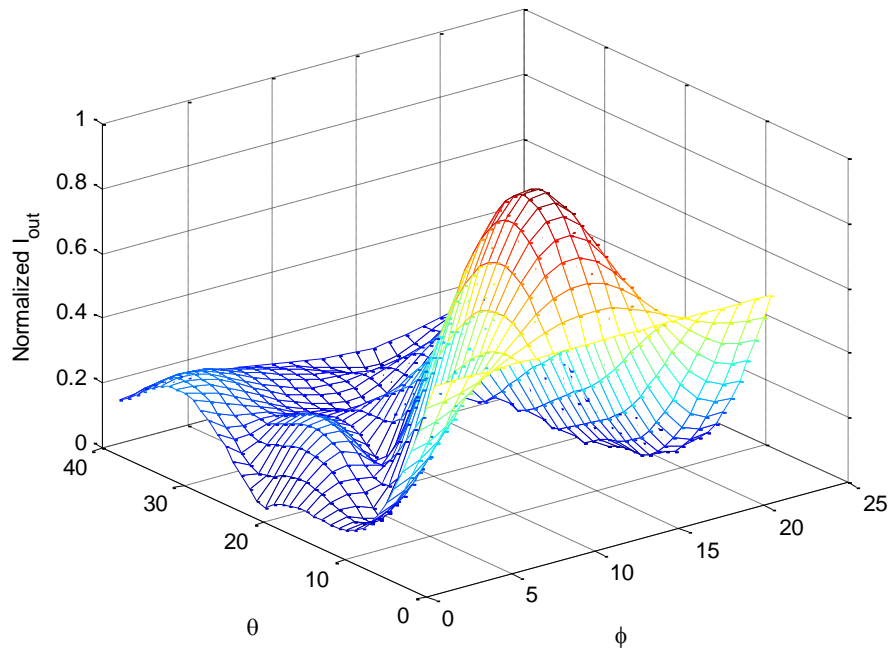


Fig. 3.33. $I_{out}(\theta, \phi)$ for $\theta_s = \pi/4$ & $\phi_s = \pi$.

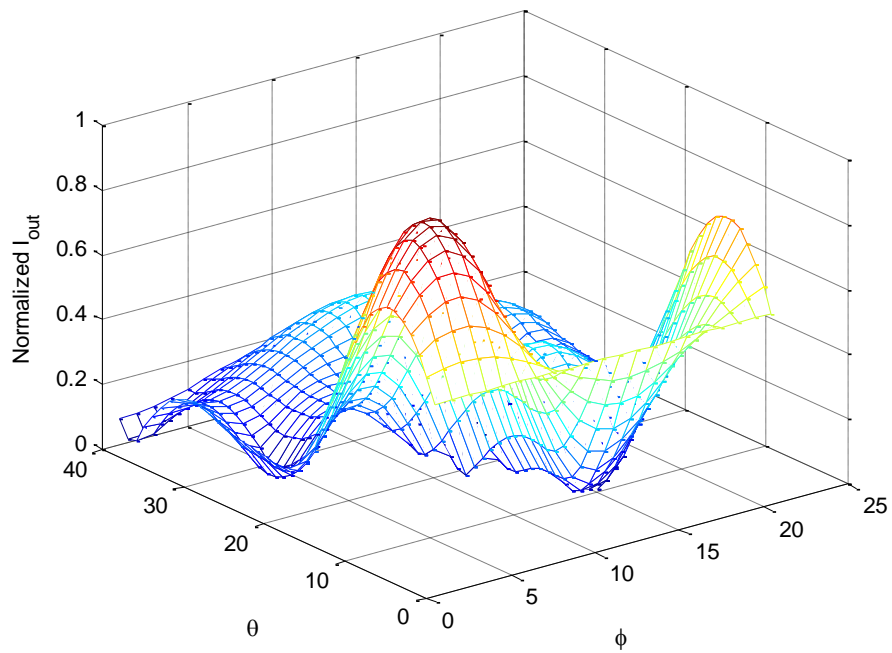


Fig. 3.34. $I_{out}(\theta, \phi)$ for $\theta_s = \pi/4$ & $\phi_s = \pi/2$.

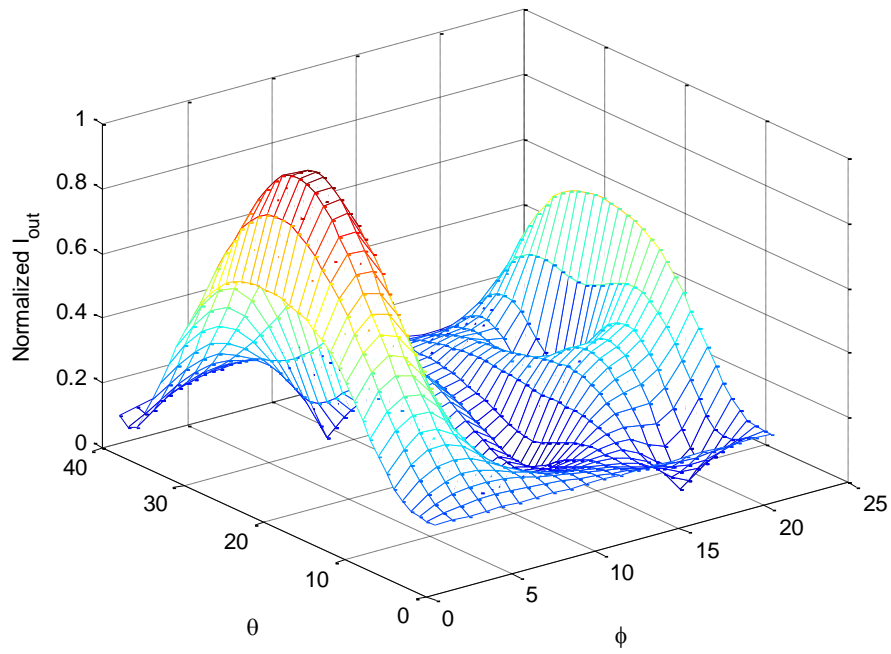


Fig. 3.35. $I_{out}(\theta, \phi)$ for $\theta_s = \pi/2$ & $\phi_s = \pi/4$.

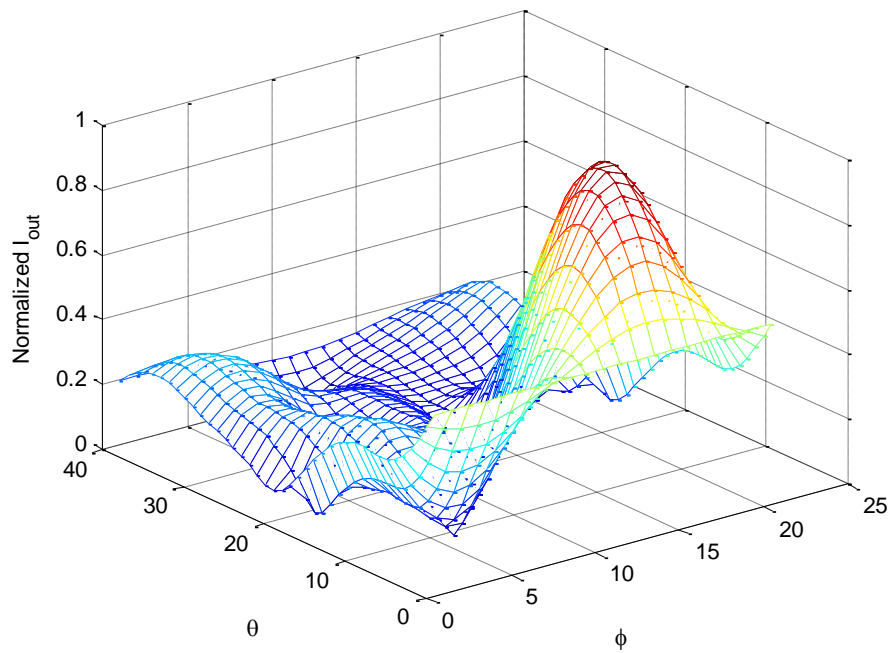


Fig. 3.36. $I_{out}(\theta, \phi)$ for $\theta_s = \pi/4$ & $\phi_s = 3\pi/2$.

As seen from the simulations, the beamforming technique is successful. The maximum value of I_{out} always lies at the position that corresponds to the source field. Any maximum seeking circuit can be used to detect the position of the maximum.

3.5.2 Multiple Reception

The beamforming technique can be easily extended to detect sources from multiple locations within the brain. For example, if there were two or more sources then values for the gains are still given by (3.124).

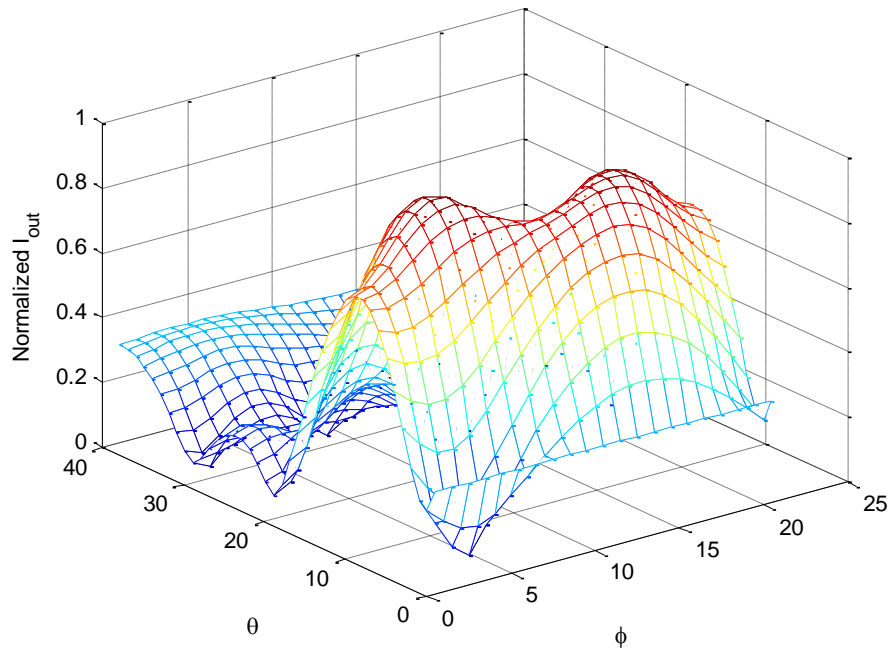


Fig. 3.37. $I_{out}(\theta, \phi)$ for $\theta_{s1}=\pi/4$ & $\phi_{s1}=3\pi/2$ and $\theta_{s2}=\pi/4$ & $\phi_{s2}=\pi/2$.

As it can be seen from Fig. 3.37 in the example of two sources the algorithm gives two peaks which correspond to the location of the sources.

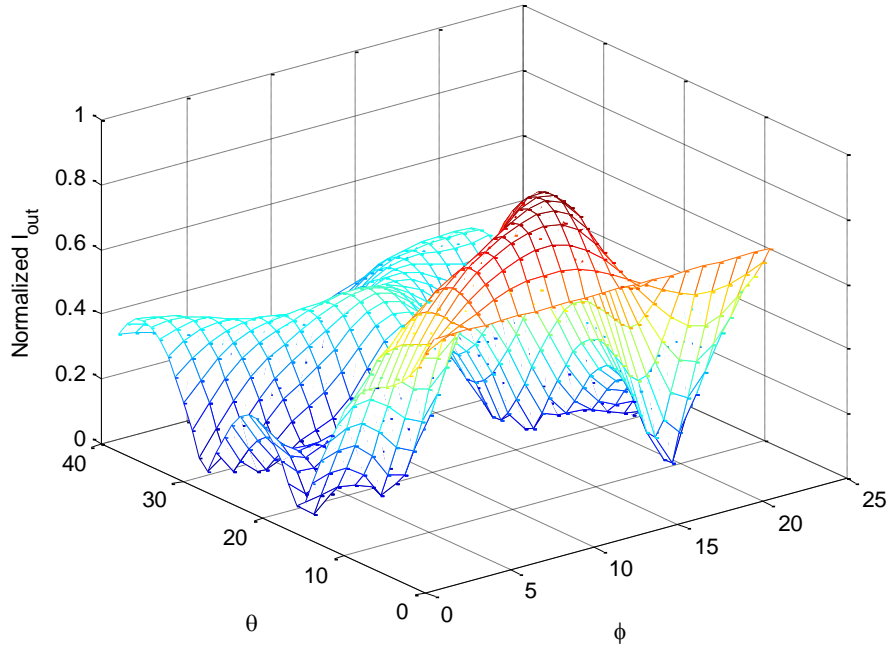


Fig. 3.38. $I_{out}(\theta, \phi)$ for $\theta_{s1}=\pi/4$ & $\phi_{s1}=\pi$ and $\theta_{s2}=0$ & $\phi_{s2}=0$.

3.6 Power and Safety Considerations

When designing a medical device, one of the main priorities is the safety and power considerations. In the transmission mode, the antenna array will transmit electromagnetic radiations to the brain, so it is necessary to investigate the intensity of the fields that are being absorbed by the brain to determine if the device is safe or not. As shown in [35] and [45]-[47], the way to measure the amounts of radiation or fields exposed on the human head is by the use of the *specific absorption rate (SAR)*. The SAR is a measure of how much electric field is present within a certain layer and it is given by the following equation [46].

$$SAR_i = \frac{\sigma_i |E_i|^2}{2\rho_i} \quad (3.125)$$

Where σ_i , $|E_i|$ and ρ_i are the i th layer's conductivity, total electric field and density, respectively. Table 3.3 (taken from [35]), shows the values of the different conductivities and densities for all the layers.

TABLE 3.3

Density & Conductivity of the Skin (1), Skull (2) & Brain (3) at 1.8 GHz [35].

	ρ (kg/m ³)	σ (S/m)
Region (1)	1080	1.88
Region (2)	1180	0.59
Region (3)	1050	1.5

The calculation of the SAR in this thesis will be different than that used in the references, since in [46] for instance, the SAR is calculated with respect to the distance between the RF device and the layers that make up the human head. In the case of the antenna array the situation is quite more complicated since there are 42 sources of RF radiation each radiating in a spherical sense. As seen from [46] the most important value of the SAR is the one at the surface of the skin since it will have the maximum value. By plotting the SAR versus θ and φ for a fixed radial distance, it is possible to detect the whereabouts of the maximum SAR values and see if these values exceed the international standard which is 2 W/kg. The plots for the SAR will be made when the antenna array is used to focus the H-field in a specific direction (θ_o, φ_o) for a radial distance $r_o=5cm$ as was done before.

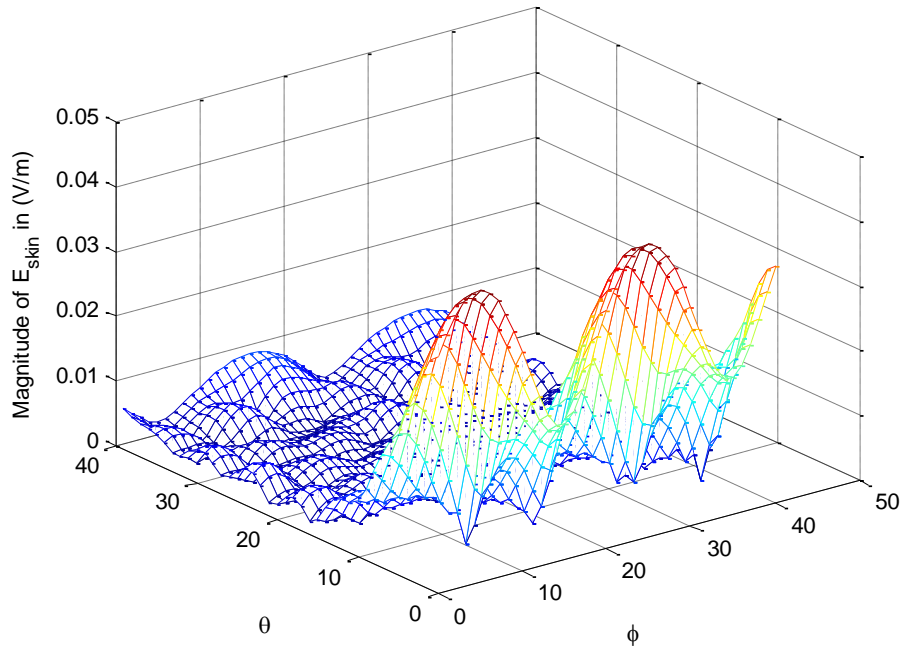


Fig. 3.39. Magnitude of Electric Field on the Skin for $\theta_o=0$ & $\phi_o=0$.

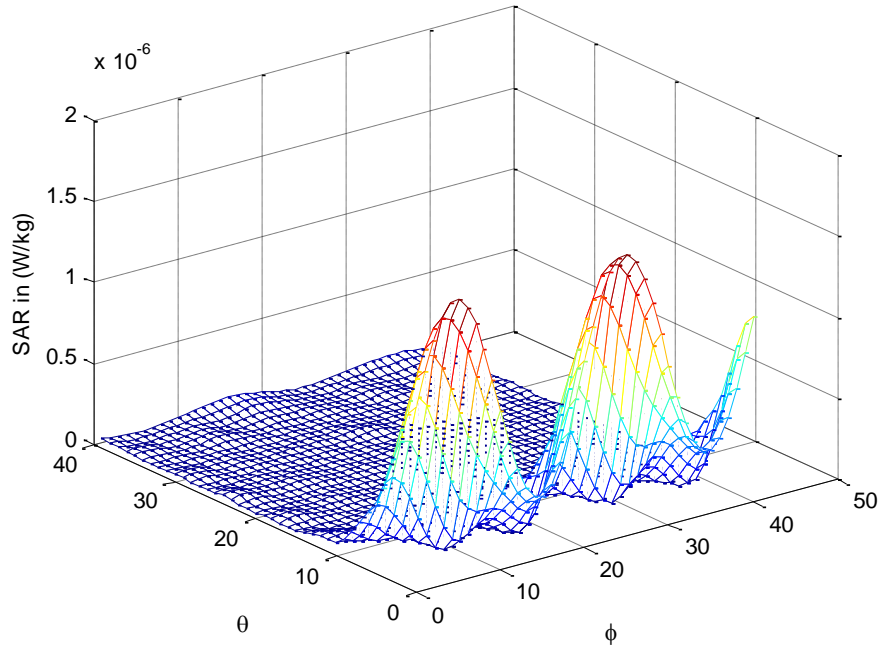


Fig. 3.40. SAR of the Skin for $\theta_o=0$ & $\phi_o=0$.

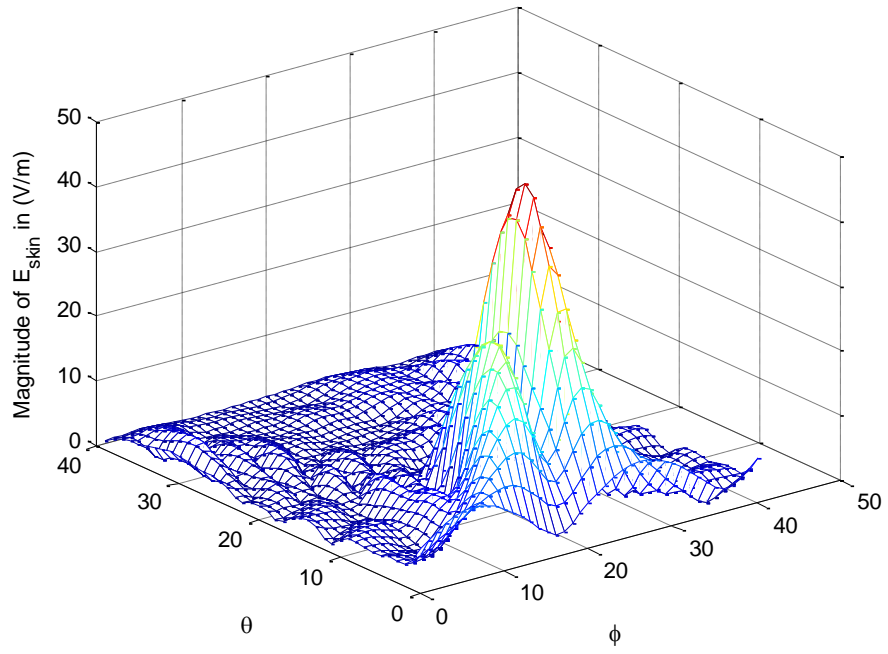


Fig. 3.41. Magnitude of Electric Field on the Skin for $\theta_o = \pi/4$ & $\phi_o = \pi$.

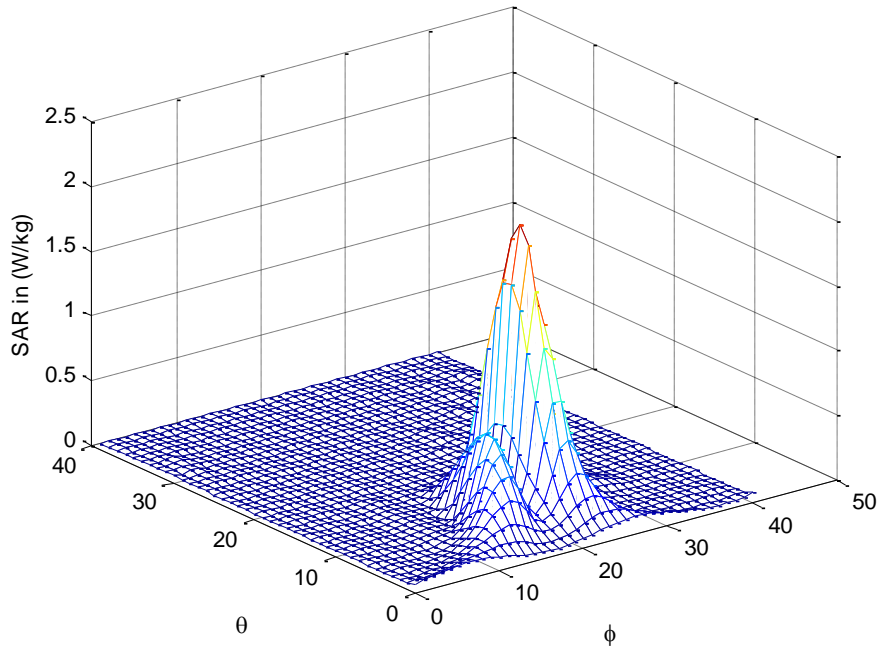


Fig. 3.42. SAR of the Skin for $\theta_o = \pi/4$ & $\phi_o = \pi$.

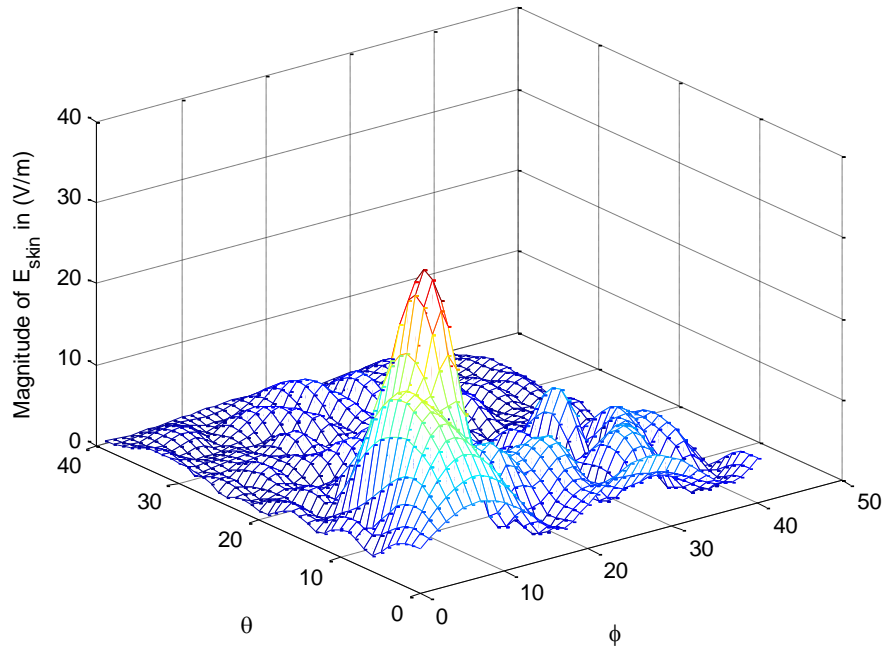


Fig. 3.43. Magnitude of Electric Field on the Skin for $\theta_o=\pi/4$ & $\phi_o=\pi/2$.

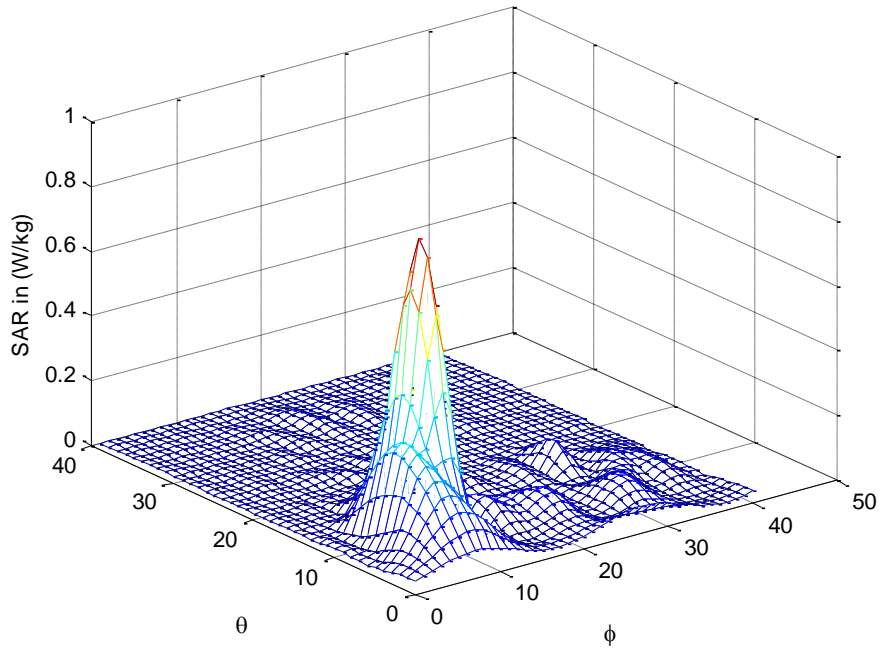


Fig. 3.44. SAR of the Skin for $\theta_o=\pi/4$ & $\phi_o=\pi/2$.

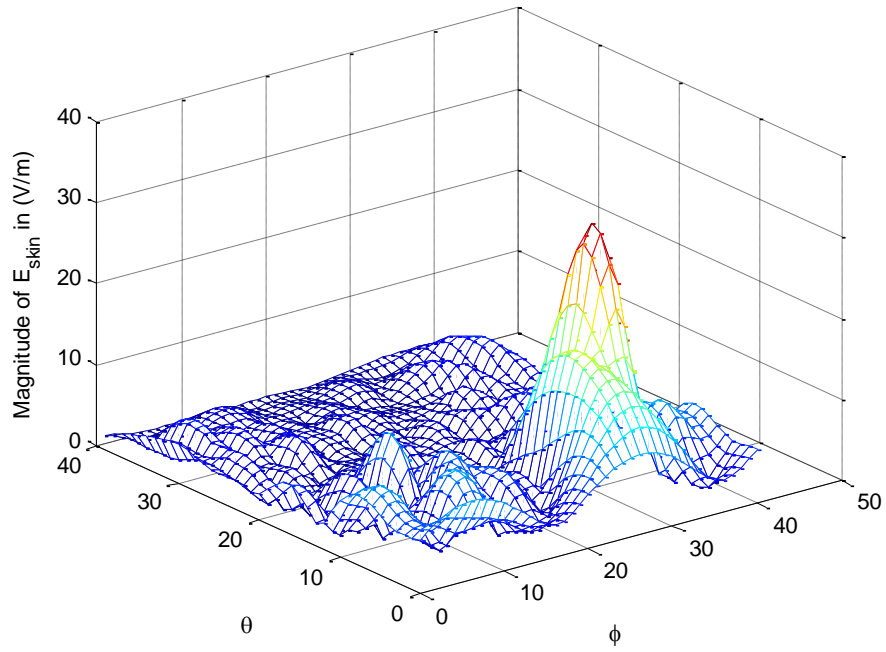


Fig. 3.45. Magnitude of Electric Field on the Skin for $\theta_o = \pi/4$ & $\phi_o = 3\pi/2$.

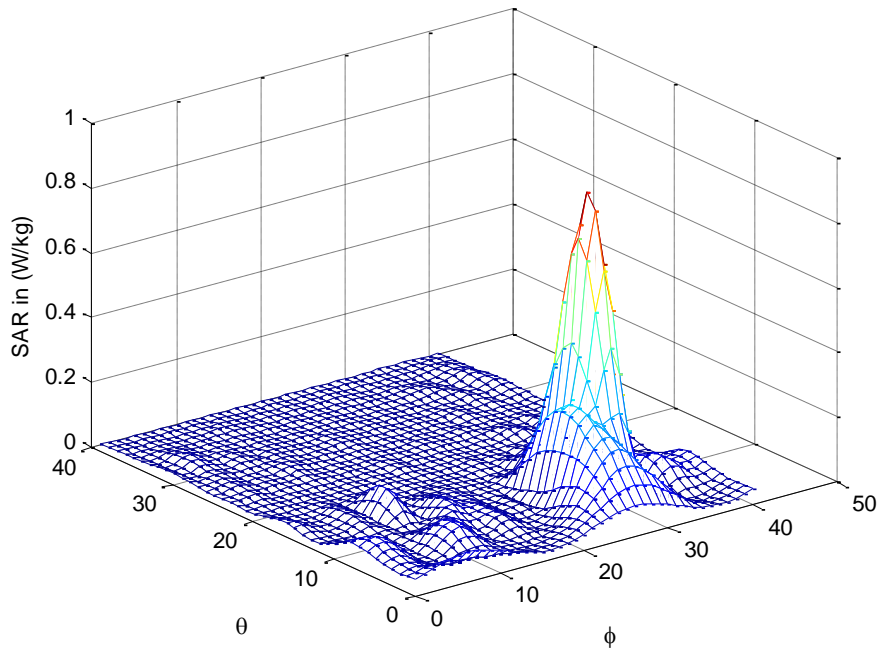


Fig. 3.46. SAR of the Skin for $\theta_o = \pi/4$ & $\phi_o = 3\pi/2$.

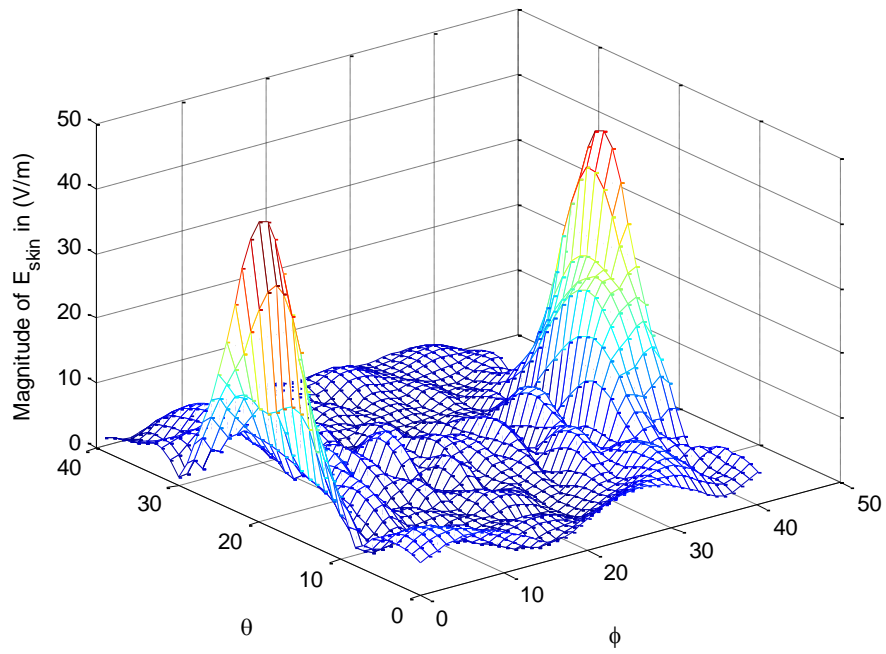


Fig. 3.47. Magnitude of Electric Field on the Skin for $\theta_o=\pi/2$ & $\varphi_o=0$.

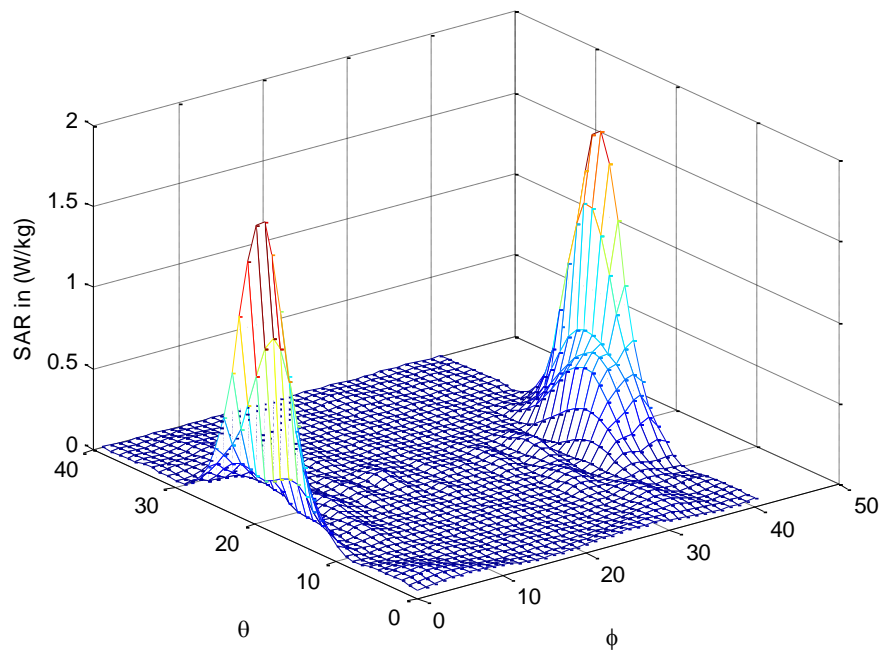


Fig. 3.48. SAR of the Skin for $\theta_o=\pi/2$ & $\varphi_o=0$.

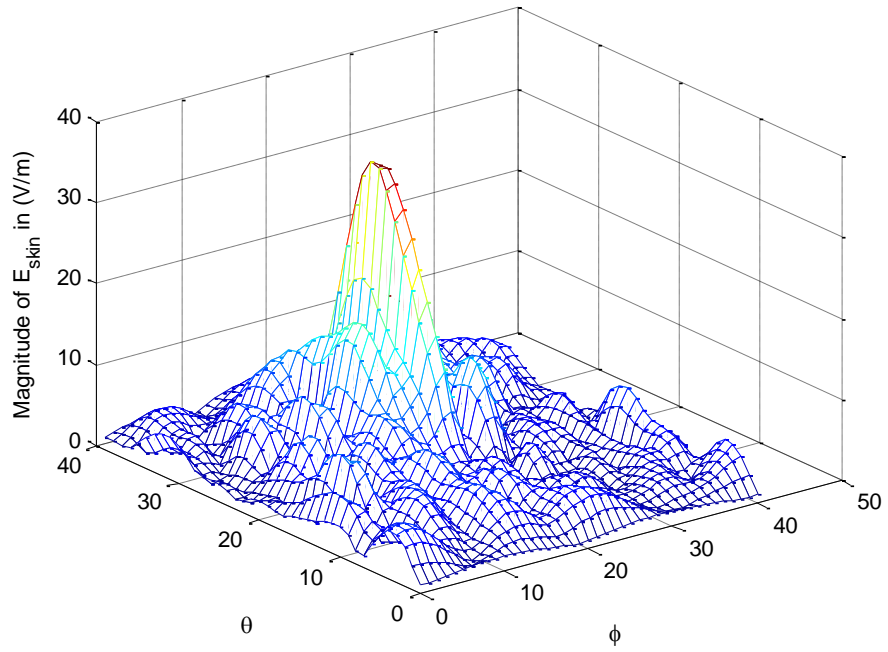


Fig. 3.49. Magnitude of Electric Field on the Skin for $\theta_o=2\pi/3$ & $\phi_o=\pi$.

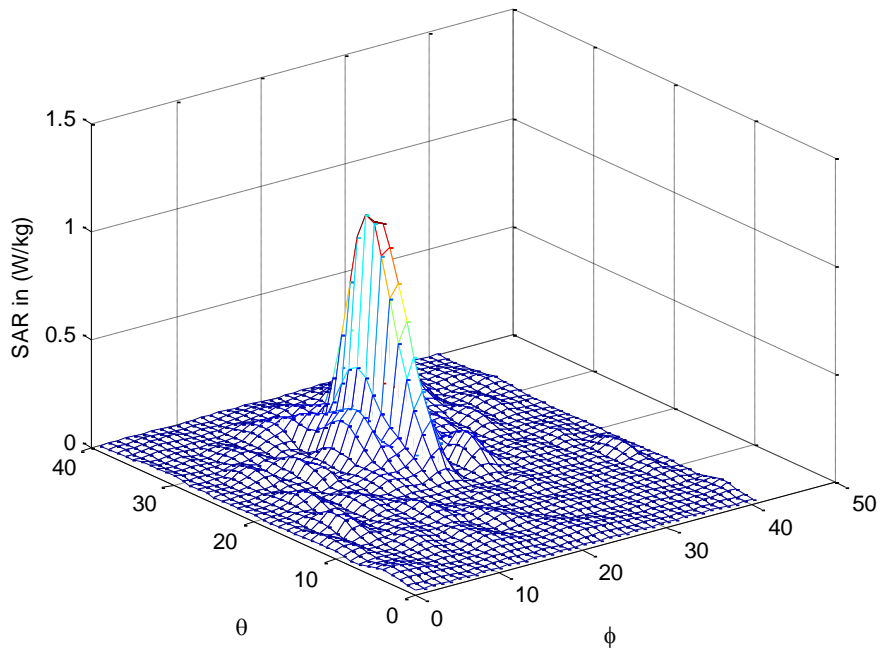


Fig. 3.50. SAR of the Skin for $\theta_o=2\pi/3$ & $\phi_o=\pi$.

It is clear from all the previous figures that the maximum value for the electric field, and thus the SAR, on the surface of the skin is always at the direction of transmission. The magnitude of the optimal currents were placed to insure that the antenna array will not give a maximum SAR reading that is greater than 2 W/kg. The level of SAR in all cases is less than 2 W/kg which implies that the array is safe for use regarding the international regulations for human exposure to RF radiation.

3.7 Reflection & Transmission Issues

Since the point of interest for either transmission or reception is in the brain (region (3)) then when electromagnetic fields penetrate through the layers, there are reflections and transmissions issues that must be considered. According to [1] and [53], when there is a field incident on a layer then part of that field will penetrate through, the *transmitted part*, and the other part will be reflected back to the original layer, the *reflected part*.

To quantify reflection and transmission, the concepts of the *reflection coefficient* (R) and the *transmission coefficient* (T) are used. In the case of the boundary-valued problem solved at the beginning of this chapter, these coefficients are defined using the following arguments. At the first interface ($r=b$), there is the boundary condition given by the following equation.

$$\begin{aligned} & \sum_{l=1}^{\infty} \sum_{m=-l}^l \{B_{lm} H_l^{(1)}(k_1 b) + C_{lm} H_l^{(2)}(k_1 b)\} \bar{r} \times \nabla Y_{lm}(\theta, \varphi) \\ & = \sum_{l=1}^{\infty} \sum_{m=-l}^l \{D_{lm} H_l^{(1)}(k_2 b) + E_{lm} H_l^{(2)}(k_2 b)\} \bar{r} \times \nabla Y_{lm}(\theta, \varphi) \end{aligned} \quad (3.126)$$

From (3.126) the reflection and the transmission coefficients can be obtained as:

$$\Gamma_{21} = \frac{\sum_{l=1}^{\infty} \sum_{m=-l}^l B_{lm} \left\{ \nabla \times \left[h_l^{(1)}(k_1 r) \bar{r} \times \nabla Y_{lm}(\theta, \varphi) \right] \right\} \Big|_{r=b}}{\sum_{l=1}^{\infty} \sum_{m=-l}^l C_{lm} \left\{ \nabla \times \left[h_l^{(2)}(k_1 r) \bar{r} \times \nabla Y_{lm}(\theta, \varphi) \right] \right\} \Big|_{r=b}} \quad (3.127)$$

$$T_{12} = \frac{\sum_{l=1}^{\infty} \sum_{m=-l}^l D_{lm} \left\{ \nabla \times \left[h_l^{(1)}(k_2 r) \bar{r} \times \nabla Y_{lm}(\theta, \varphi) \right] \right\} \Big|_{r=b}}{\sum_{l=1}^{\infty} \sum_{m=-l}^l C_{lm} \left\{ \nabla \times \left[h_l^{(2)}(k_1 r) \bar{r} \times \nabla Y_{lm}(\theta, \varphi) \right] \right\} \Big|_{r=b}} + \frac{\sum_{l=1}^{\infty} \sum_{m=-l}^l E_{lm} \left\{ \nabla \times \left[h_l^{(2)}(k_2 r) \bar{r} \times \nabla Y_{lm}(\theta, \varphi) \right] \right\} \Big|_{r=b}}{\sum_{l=1}^{\infty} \sum_{m=-l}^l C_{lm} \left\{ \nabla \times \left[h_l^{(2)}(k_1 r) \bar{r} \times \nabla Y_{lm}(\theta, \varphi) \right] \right\} \Big|_{r=b}} \quad (3.128)$$

Note that this is not a regular reflection/transmission problem. For example, in layer (1) there are two fields present. One field propagates towards the origin of the coordinate system (one with the C_{lm}), the other is propagating away from the origin (one with the B_{lm}). The reflection coefficient here is just a ratio between the ingoing and outgoing field (i.e. in some cases the Γ can be bigger than 1). Another remark is that the coefficients are given as a function of θ and φ and this can be interpreted as what happens to the field for a given surface. Similarly, the boundary condition at $r=a$ yields the following equation.

$$\begin{aligned} & \sum_{l=1}^{\infty} \sum_{m=-l}^l \{ D_{lm} H_l^{(1)}(k_2 a) + E_{lm} H_l^{(2)}(k_2 a) \} \bar{r} \times \nabla Y_{lm}(\theta, \varphi) \\ &= \sum_{l=1}^{\infty} \sum_{m=-l}^l F_{lm} J_l(k_3 a) \bar{r} \times \nabla Y_{lm}(\theta, \varphi) \end{aligned} \quad (3.129)$$

From (3.129) the reflection and the transmission coefficients can be obtained as:

$$\Gamma_{32} = \frac{\sum_{l=1}^{\infty} \sum_{m=-l}^l D_{lm} \left\{ \nabla \times \left[h_l^{(1)}(k_2 r) \bar{r} \times \nabla Y_{lm}(\theta, \varphi) \right] \right\} |_{r=a}}{\sum_{l=1}^{\infty} \sum_{m=-l}^l E_{lm} \left\{ \nabla \times \left[h_l^{(2)}(k_2 r) \bar{r} \times \nabla Y_{lm}(\theta, \varphi) \right] \right\} |_{r=a}} \quad (3.130)$$

$$T_{23} = \frac{\sum_{l=1}^{\infty} \sum_{m=-l}^l F_{lm} \left\{ \nabla \times \left[j_l(k_3 r) \bar{r} \times \nabla Y_{lm}(\theta, \varphi) \right] \right\} |_{r=a}}{\sum_{l=1}^{\infty} \sum_{m=-l}^l E_{lm} \left\{ \nabla \times \left[h_l^{(2)}(k_2 r) \bar{r} \times \nabla Y_{lm}(\theta, \varphi) \right] \right\} |_{r=a}} \quad (3.131)$$

Where the subscripts in the case of the reflection coefficient Γ_{ij} indicate the reflection of the field from layer i back to layer j , while for the transmission coefficient T_{ji} indicate the transmission of the field from layer j to layer i . Equations (3.126) through (3.131) give the transmission and reflection coefficients between all the layers except for the interface (0)-(1).

Figure 3.51 to Fig. 3.62 show the reflection and transmission coefficients for the skin-skull and the skull-brain interfaces for 3 different angles sets at $r_o=5cm$. The coefficients are plotted as a function of θ and φ showing how they vary on a spherical surface.

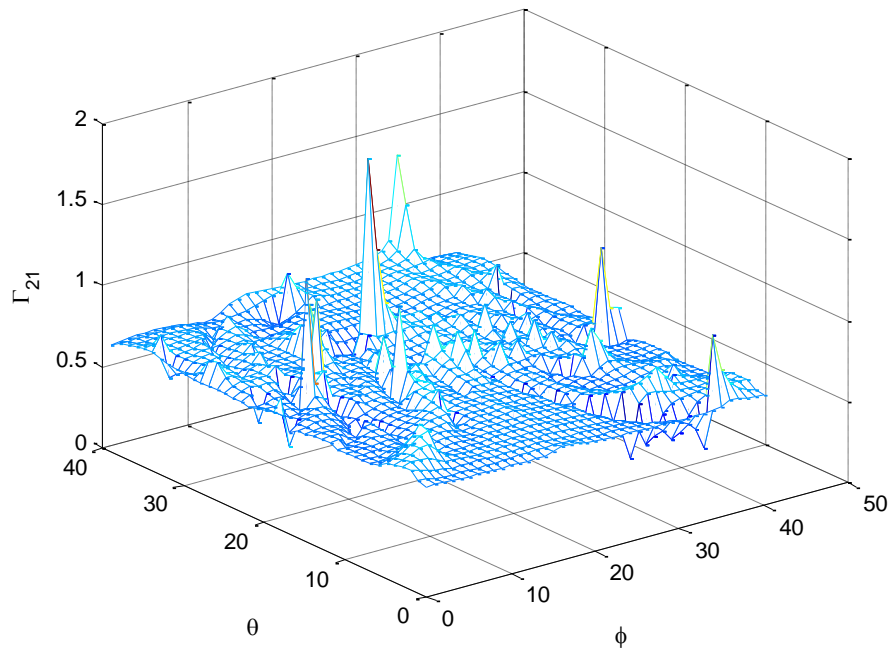


Fig. 3.51. Γ_{21} for the skin-skull interface for $\theta_o=\pi/4$ & $\varphi_o=\pi$.

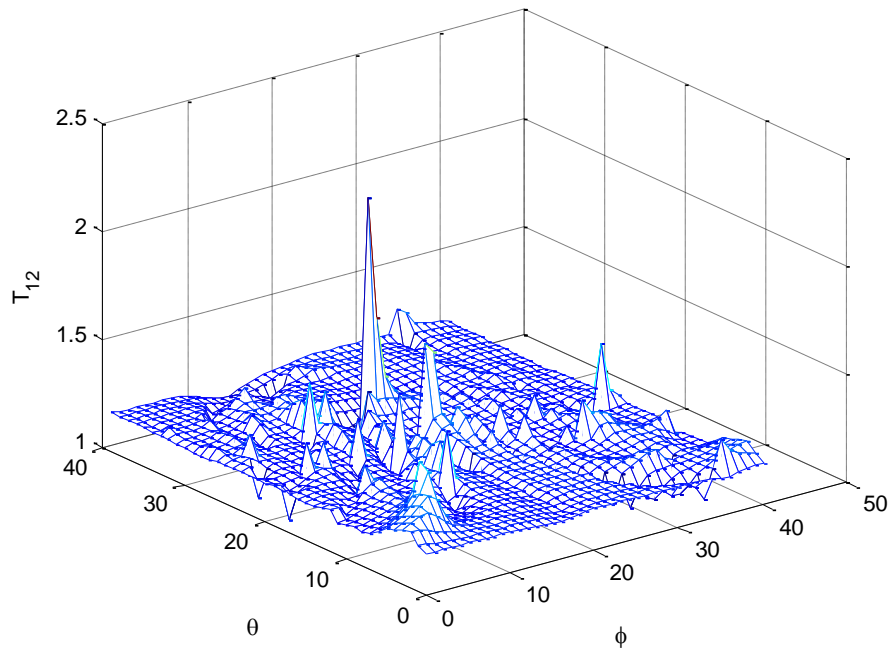


Fig. 3.52. T_{12} for the skin-skull interface for $\theta_o=\pi/4$ & $\varphi_o=\pi$.

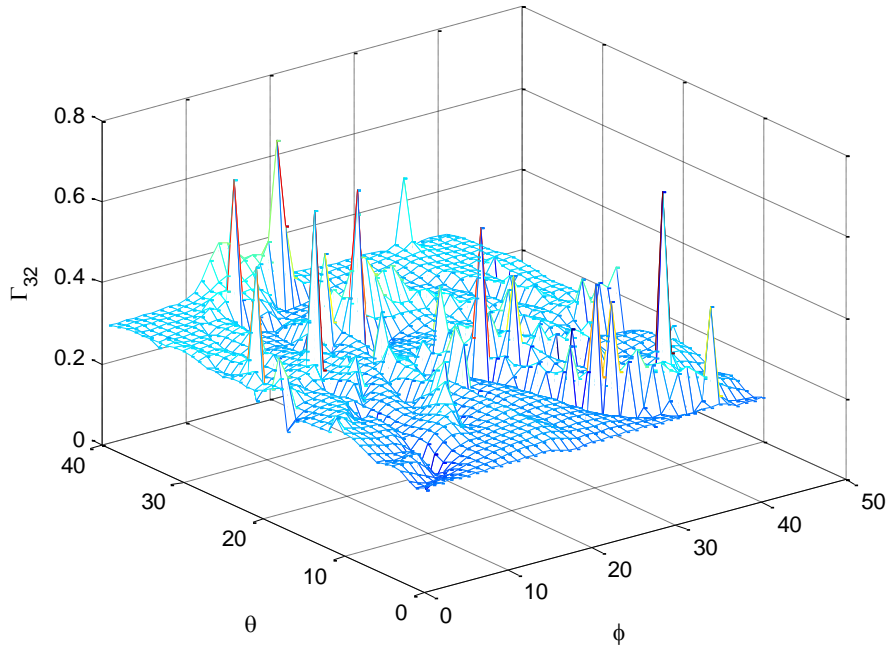


Fig. 3.53. Γ_{32} for the skull-brain interface for $\theta_o=\pi/4$ & $\varphi_o=\pi$.

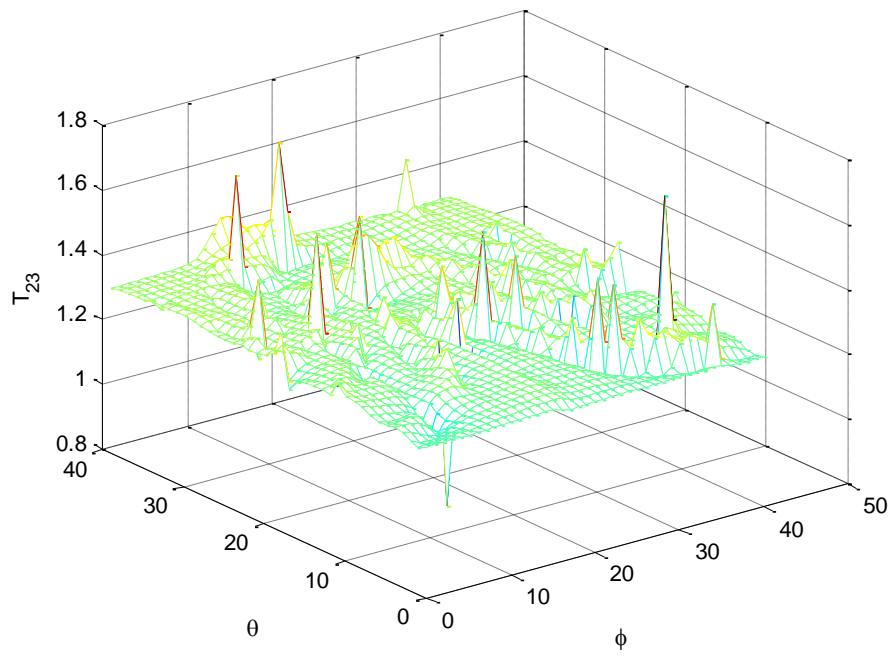


Fig. 3.54. T_{23} for the skull-brain interface for $\theta_o = \pi/4$ & $\varphi_o = \pi$.

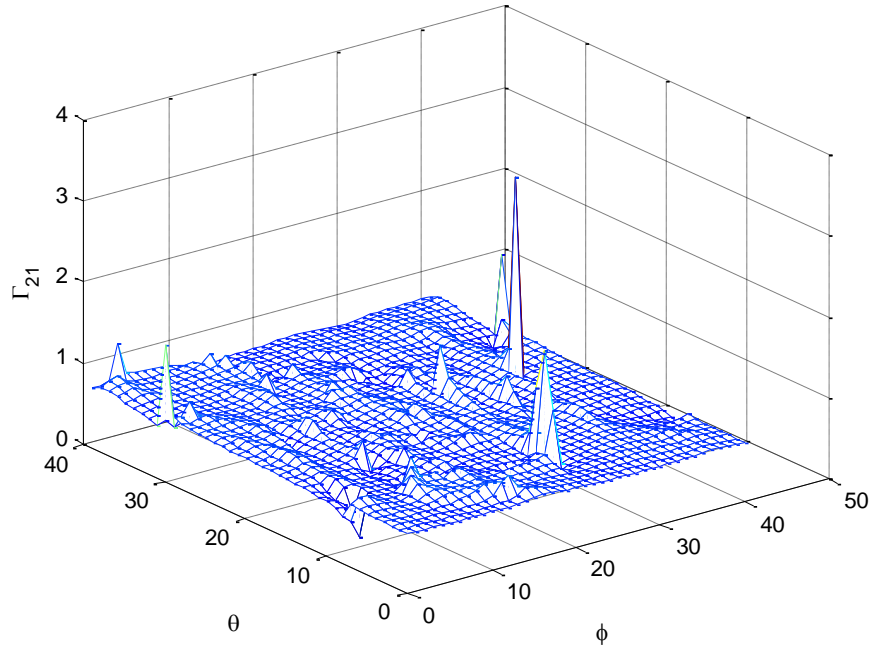


Fig. 3.55. T_{21} for the skin-skull interface for $\theta_o = \pi/2$ & $\varphi_o = 0$.

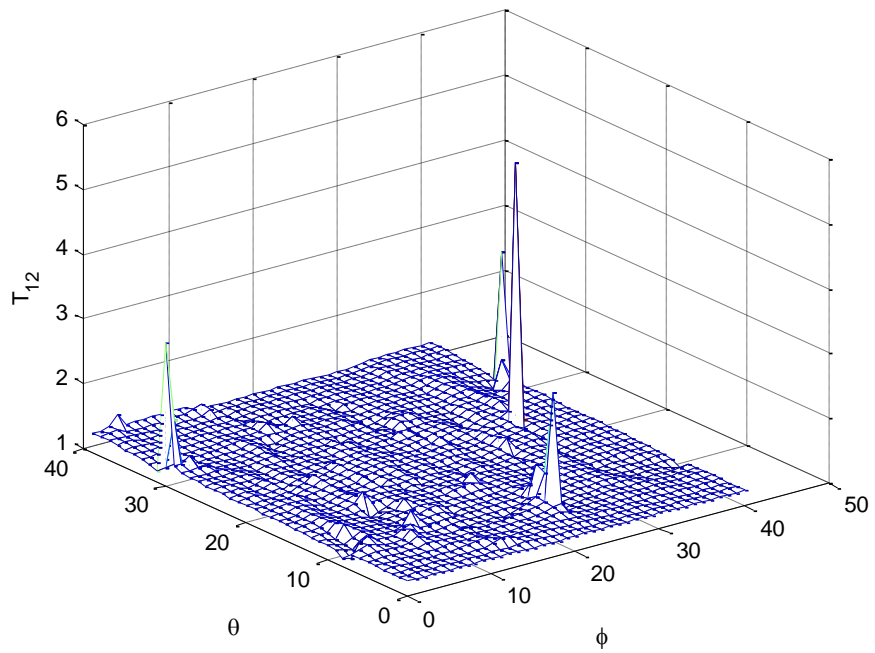


Fig. 3.56. T_{12} for the skin-skull interface for $\theta_o = \pi/2$ & $\varphi_o = 0$.

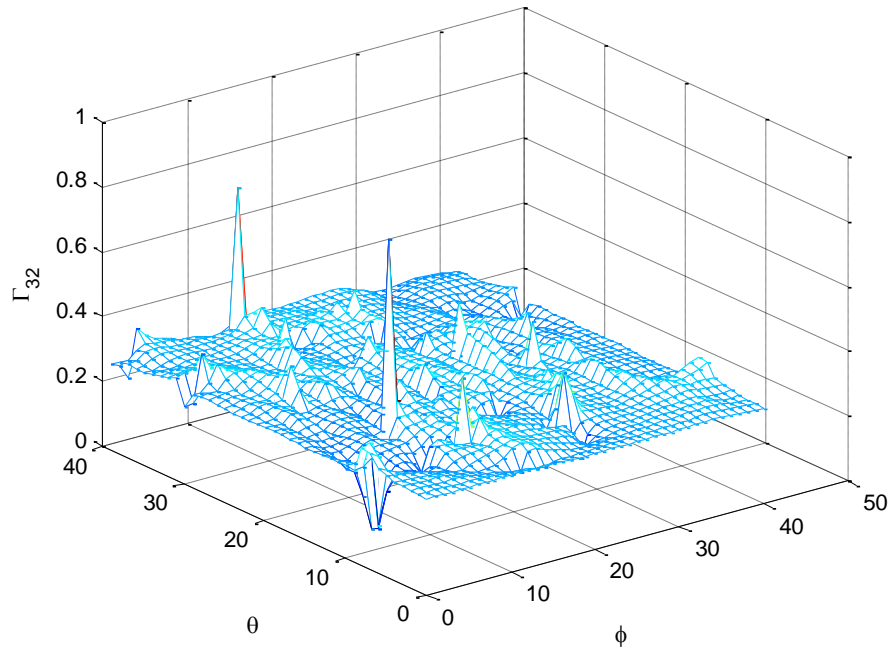


Fig. 3.57. Γ_{32} for the skull-brain interface for $\theta_o=\pi/2$ & $\varphi_o=0$.

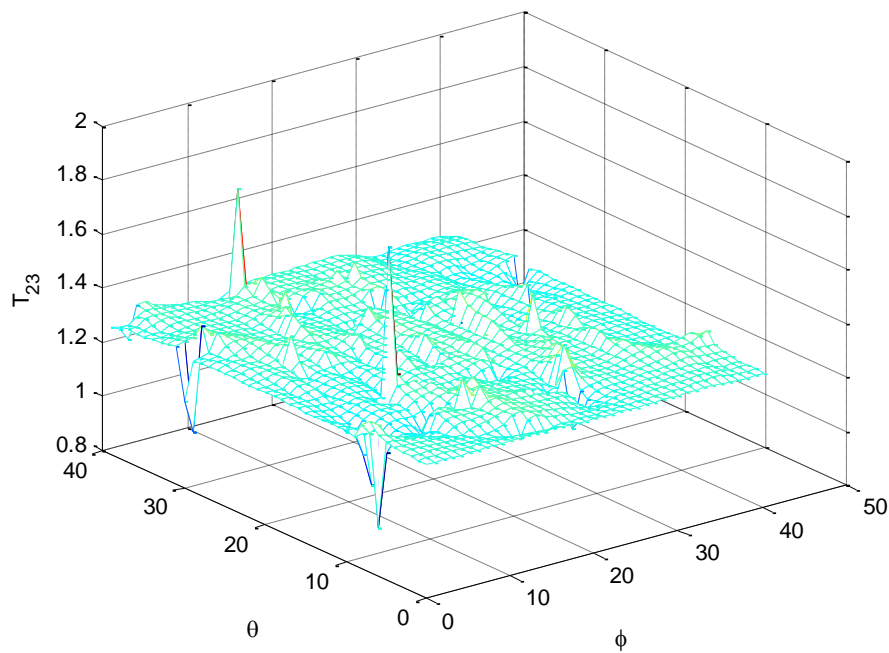


Fig. 3.58. T_{23} for the skull-brain interface for $\theta_o=\pi/2$ & $\varphi_o=0$.

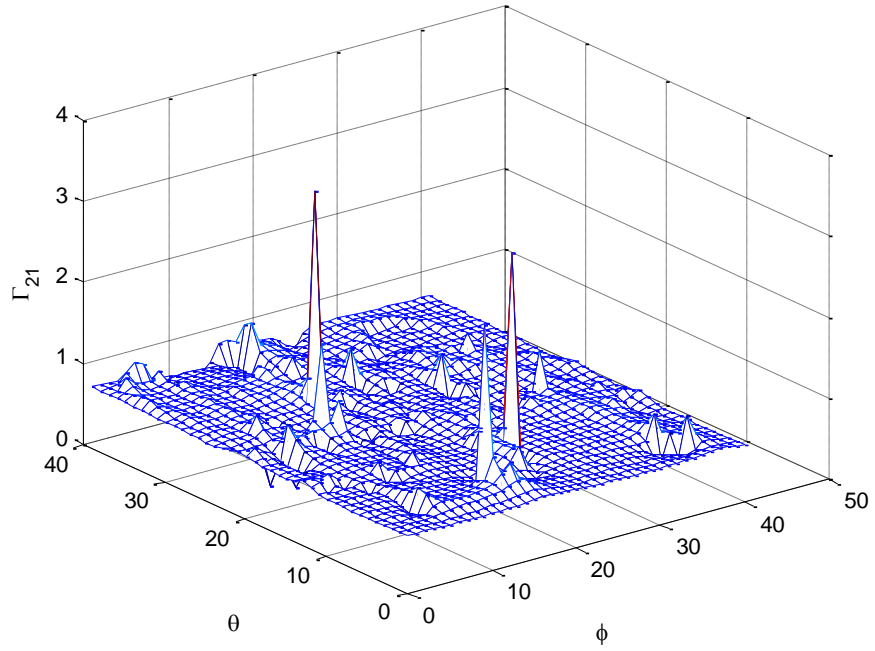


Fig. 3.59. Γ_{21} for the skin-skull interface for $\theta_o = \pi/4$ & $\phi_o = 3\pi/2$.

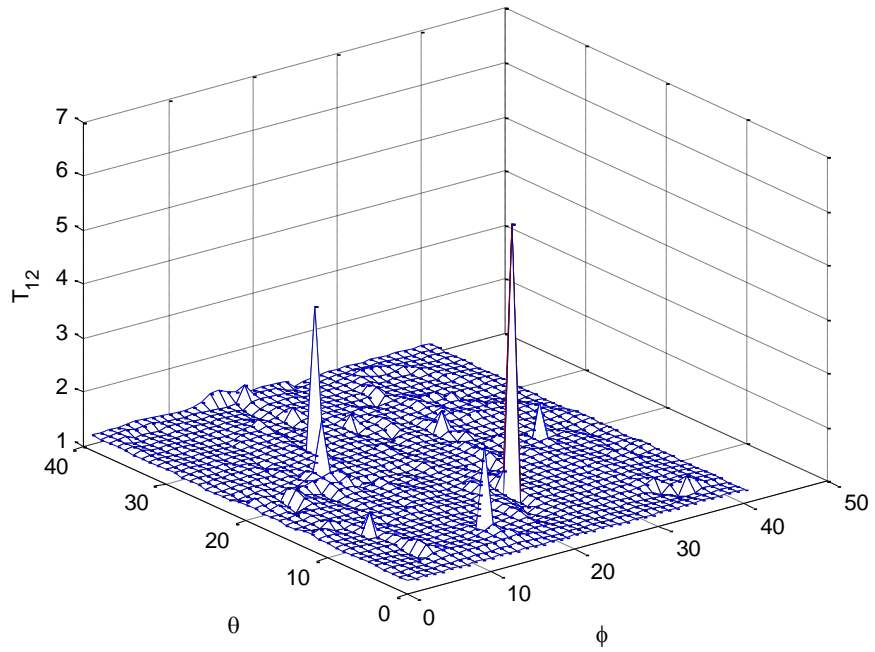


Fig. 3.60. T_{12} for the skin-skull interface for $\theta_o = \pi/4$ & $\phi_o = 3\pi/2$.

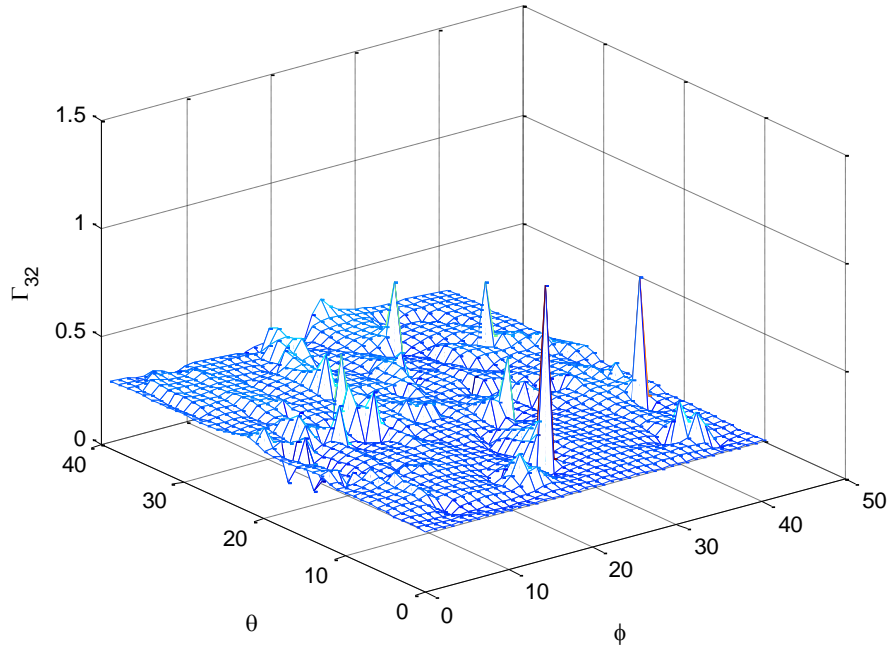


Fig. 3.61. Γ_{32} for the skull-brain interface for $\theta_o=\pi/4$ & $\phi_o=3\pi/2$.

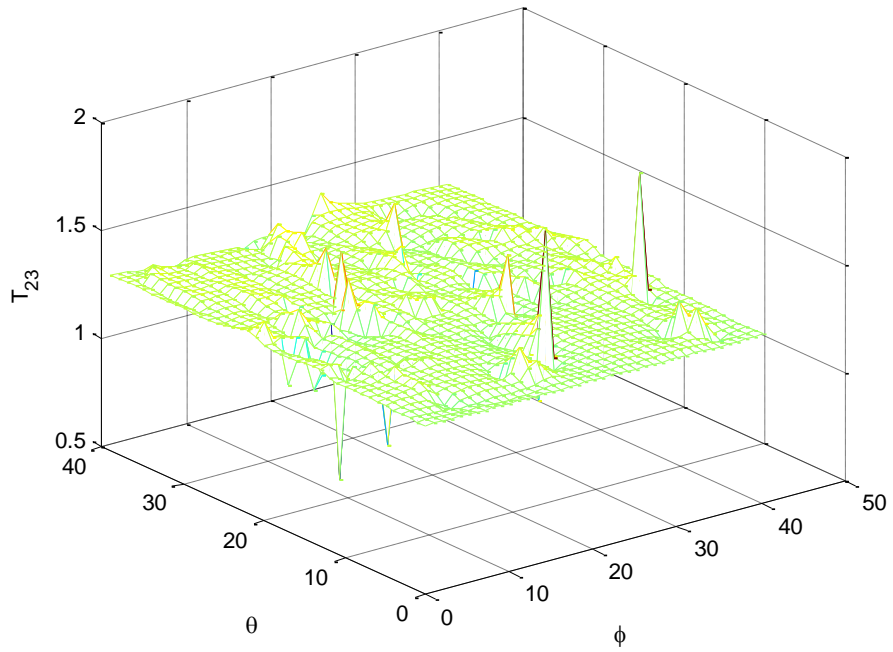


Fig. 3.62. T_{23} for the skull-brain interface for $\theta_o=\pi/4$ & $\phi_o=3\pi/2$.

3.8 Other RFID/IMD Applications

In this section we are going to discuss that the antenna array can be used for other RF applications. These applications can either be medical or non medical, but the main point is ability to control the direction of the power or field radiated in the direction that guarantees optimal power transfer efficiency between reader and tag. This is done by constructing the reader as an antenna array. Now since there are many applications, the geometry and the placement of the reader and tag are very important to know what kind of coordinate system to use. Instead of solving another boundary valued problem (for another coordinate system), the following general steps are given.

- 1- First the geometry and the coordinate system must be decided (in the case of the human head the obvious choice was the spherical coordinate), but in general it can be linear, cylindrical or spherical. For all coordinate systems the first step is to solve (3.2) for the appropriate coordinate system and in turn to get fields.
- 2- If there are multiple layers (especially for IMD where the tag is embedded inside the body) then boundary conditions must be imposed and solved to get the coefficients of the fields as done in Subsection 3.2.6.
- 3- When the coefficients are determined and the expressions of the fields are obtained the beamforming technique discussed in Subsection 3.3.2 can be used to sustain beamforming.

Chapter 4: Neural Networks

4.1 Introduction

In this chapter the beamforming technique is going to be carried out by the use of neural networks. Neural networks are excellent tools for approximating any given function of single or multivariable inputs and outputs. The essence of a neural network is in the mimicking of how the nervous system in our body processes information. The nervous system [48] is composed of millions of interconnected nerve cells where each will carry out a very simple task. Since in the interconnections between those cells are complex the result of these multi simple task accomplishments is the execution of a bigger more complicated task. In a similar sense, a neural network that is composed of a large number of interconnecting *neurons* does just that.

Each neuron (Fig. 4.1 [50], this figure gives an example of a scalar product neuron) is capable of communicating with its neighbors through weights and is capable of changing its present state depending on the signal it receives. All neurons can simultaneously change state while maintaining the global state or purpose of the network. All neurons are connected to each other in layers with the first layer being the input layer and the final layer being the output. Whatever is in between those two layers are called the *hidden* layers (Fig. 4.2). The objective of a neural network is, for a given set of inputs, it should give a set of desired or expected outputs. The weights (or *synaptic weights*) are updated using a certain *learning algorithm* until the *error*

between the actual output of the neural network and the *desired* output is reduced to an acceptable level (depending on the function being approximated).

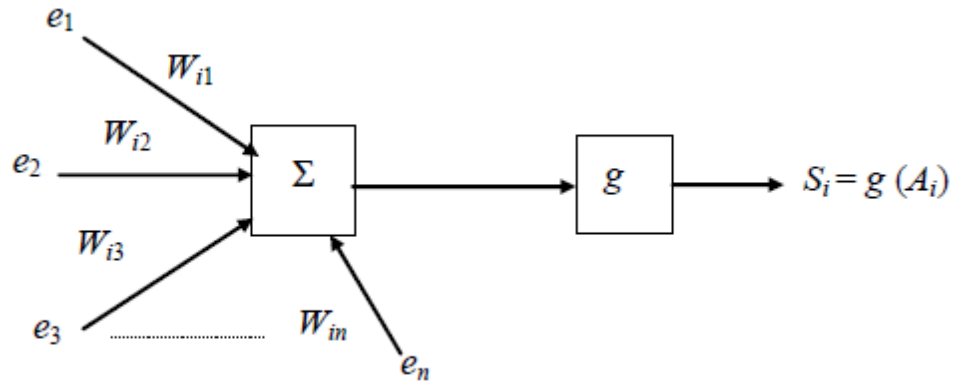


Fig. 4.1. A scalar product neuron ([50] Fig. 1, pp. 24).

From the Fig. 4.1 [50]:

$$A_i = \sum_{k=1}^n W_{ik} e_k \quad (4.1)$$

Where W_{ik} is called the synaptic weight of the k -th towards the i -th connection and e_i are the inputs. In scalar product neurons there are usually two consecutive mathematical steps: (1) A_i which is simply a linear transformation of the inputs with the synaptic weights and (2) g which is usually a nonlinear transformation function.

As mentioned earlier, the synaptic weights are updated or changed according to a certain *learning algorithm*. After each weight update, the output of the neural network is calculated, compared to the desired output to get the error. If the error is less than or equal to the desired then the learning stage of the network is over and it is ready to

be used as the desired function generator. If the error is still large then the weights are updated and the learning process starts all over again.

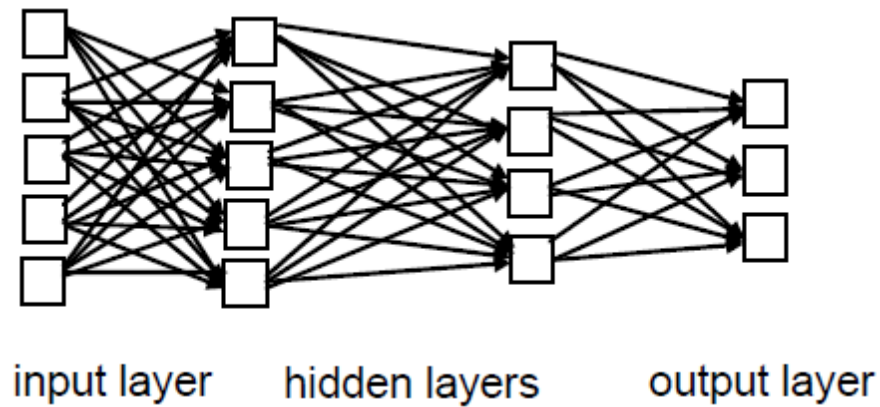


Fig. 4.2. Multi-layers networks ([50] Fig. 2, pp. 24).

4.2 Learning Algorithms

The theory of neural networks is a science or art of its own. There are a lot of learning algorithms that differ in complexity, size of the neural network (i.e. number of neurons needed) and number of learning steps or iterations needed to reach the optimal goal. The types of algorithms used go with the following types of networks:

- 1- Perceptron networks.
- 2- Back-propagation networks.
- 3- Recurrent networks.
- 4- Self-organizing networks.

In the thesis a *feed forward* back-propagation network is going to be used where the update of the synaptic weights is done by the *Levenberg-Marquardt* method [51].

Usually, what happens in the updating stage is that an error minimization scheme is taken which will allow the weights to be changed in such a way that will drive the error function to its minimum value. In other words, update the weights that will cause the gradient of the error function to go to zero (i.e. following the gradient to the steepest descent). Unfortunately, in some error functions the gradient may not descend quickly causing the number of iterations to be large and therefore the learning stage will take some time. To speed up the process of the descent, the first and second derivatives of the error function can be used.

4.3 Neural Network for Beamforming

As mentioned the objective of a neural network is execute a given function. This can be done by training the network with a series of input versus output scenarios. These input/output pairs make up the *training set* in which the network learns how to execute a given function. After the training is done and the error is reduced to an acceptable amount the neural network can be taken from the training phase and put into the operation phase. In the operation phase the neural network is capable of reproducing all the outputs for the inputs that were in the training set. Furthermore, the neural network should be able to approximate the outputs of inputs that were not given in the training set. This fact arises from the nonlinear transformation used in the neural network.

The neural network is going to be used here to approximate the function given in (3.86) which simply states the optimum current values to map the TE modes' coefficients (F_{lm}) of the H-field to the desired delta like H-field coefficients (\mathcal{E}_{lm}).

Since it is desired to beamform the main beam of the array in any desirable direction, then the training set used should cover all possible beam trajectories. The training set chosen here has a size of 70 input/output pairs. Rewriting (3.86) here:

$$\mathbf{I}_{opt} = (\mathbf{F}_{lm}^{M \times H} \mathbf{F}_{lm}^{M \times})^{-1} \mathbf{F}_{lm}^{M \times H} \mathbf{\Xi}_{lm}^V \quad (4.2)$$

Note that for the neural network, the input information is the desired direction of transmission given by the coefficients in the vector $\mathbf{\Xi}_{lm}^V$ while the output information is the current values, \mathbf{I}_{opt} , needed to get the desired beam shape. The neural network has to be trained to perform the transformation function $(\mathbf{F}_{lm}^{M \times H} \mathbf{F}_{lm}^{M \times})^{-1} \mathbf{F}_{lm}^{M \times H}$ on the input vector $\mathbf{\Xi}_{lm}^V$ to the output vector \mathbf{I}_{opt} for every possible pair of angles desired (θ_o, φ_o) .

For best error performance the neural network is divided into four small neural networks. Since the mapping involves complex numbers (\mathbf{I}_{opt} and $\mathbf{\Xi}_{lm}^V$ include magnitude and phase which can be expressed as a complex number) the mapping in (4.2) must be done for the real part and the imaginary part of the input/output separately. The reason that the real and imaginary parts are done separately is that for future work it is desired to implement the neural network using circuits and therefore the imaginary and real part must be separated. The other separation comes from the fact that it is difficult to have a good error performance when training the neural network for the entire training set for all 42 \mathbf{I}_{opt} outputs, so what is done here is that two neural networks (two for the real and two for the imaginary parts) are simulated which gives a total of four networks.

As mentioned earlier the input of the neural network is the vector $\bar{\mathcal{E}}_{lm}^V$. Since the double sum of the TE modes are taken up to $l=7$ then according to (3.87) there are 63 input elements for each $\bar{\mathcal{E}}_{lm}^V$, and of course the output is the vector I_{opt} which has 42 output elements. Best error performance the neural network will process the training set in the following manner:

- 1- *Network 1* will take care of the real part of equation (4.2) for 63 inputs versus the first 15 antenna elements (i.e. 15 outputs).
- 2- *Network 2* will take care of the real part of equation (4.2) for 63 inputs versus the other 27 antenna elements (i.e. 27 outputs).
- 3- *Network 3* will take care of the imaginary part of equation (4.2) for 63 inputs versus the first 15 antenna elements (i.e. 15 outputs).
- 4- *Network 4* will take care of the imaginary part of equation (4.2) for 63 inputs versus the other 27 antenna elements (i.e. 27 outputs).

Each network is constructed in the way shown in Fig. 4.3 [51]. Each neural network consists of 63 inputs placed in an input vector. Each element is then scaled by using the synaptic weights and added to each other with some bias coefficients (the exact interconnections are shown in Fig. 4.4). The first layer (*hidden layer*) contains the nonlinear function *tansig* (Fig. 4.5) which simply takes the hyperbolic tangent of its input function. The second layer (*output linear*) uses the function *purelin* (Fig. 4.6) which simply is a linear transformation of the output of the hidden layer. The synaptic weights and biases are updated by the *trainlm* training scheme which uses the *Levenberg-Marquardt* method. Networks 1 & 3 (real part mapping) have 30 *tansig* hidden neurons and 15 *purelin* output neurons each while Networks 2 & 4 (imaginary

part mapping) have 30 *tansig* hidden neurons and 27 *purelin* output neurons each. For each network a training set of 70 input/output pairs is used and the *trainlm* algorithm is followed until the *mean square error* (MSE) was reduced to an acceptable value.

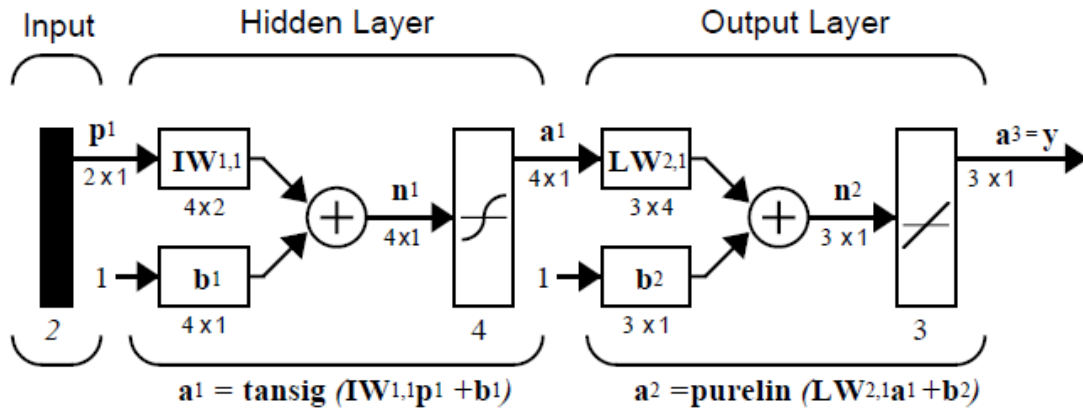


Fig. 4.3. The Neural Network Used for Beamforming ([51] pp. 3-6).

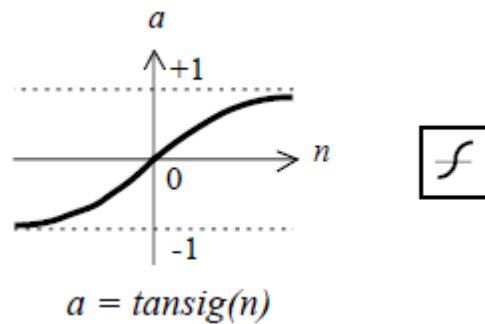


Fig. 4.4. Tan-sigmoid transfer function used in the hidden layer ([51] pp. 3-4).

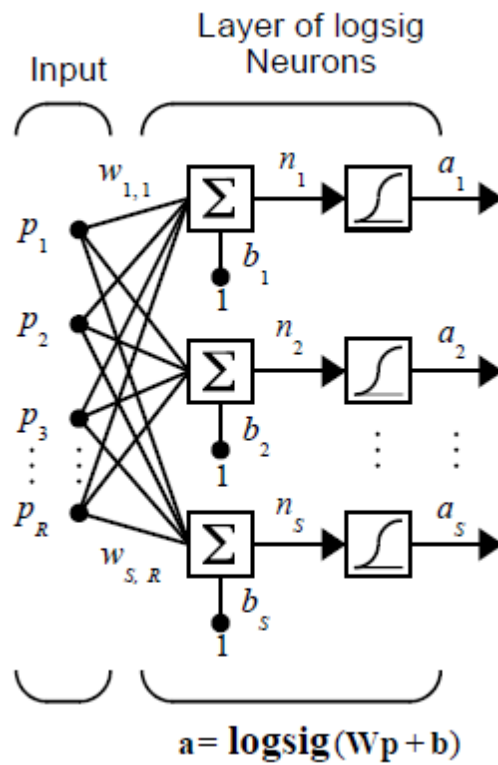


Fig. 4.5. Detailed interconnections for each layer. Note that here the *logsig* neuron is shown but in the thesis the *tansig* and the *purelin* neurons are used instead. This figure is only shown to illustrate what actually goes ([51] pp. 3-5).

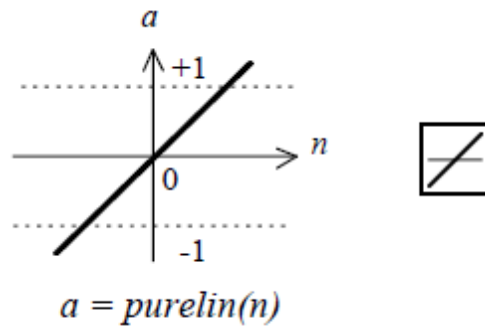


Fig. 4.6. Linear transfer function used in the output layer ([51] pp. 3-4).

Four separate training simulations were carried out for networks 1, 2, 3 & 4 respectively and the error performance for each were plotted and reported in the

upcoming figures. Table 4.1 shows the MSE for each network and the number of iterations or *epochs* needed to accomplish the MSE.

TABLE 4.1

Mean Square Error (MSE) versus the Number of Epochs for Each Neural Network.

	MSE	Epochs
Network 1	1.33×10^{-8}	84
Network 2	1.26×10^{-9}	394
Network 3	1.68×10^{-8}	1000
Network 4	4.85×10^{-8}	1000

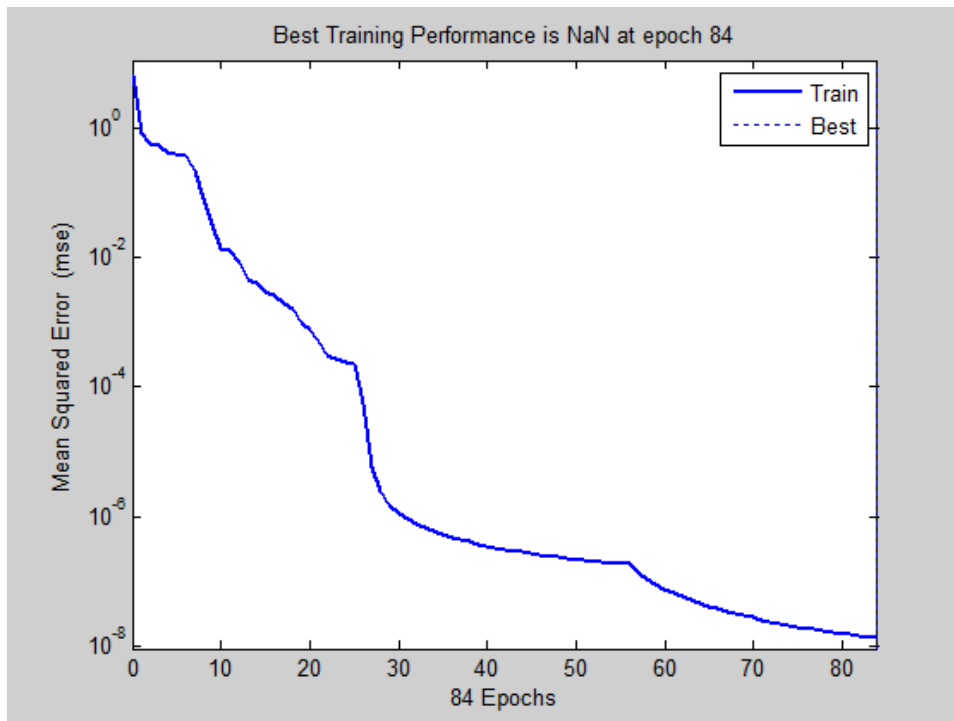


Fig. 4.7. MSE versus Epochs for Network 1.

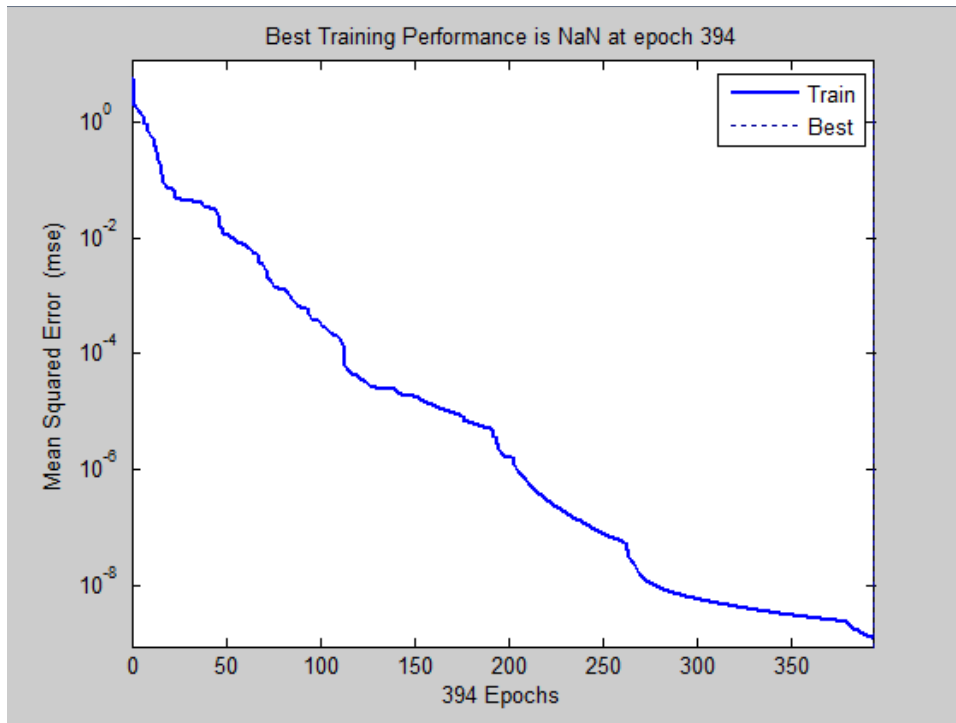


Fig. 4.8. MSE versus Epochs for Network 2.

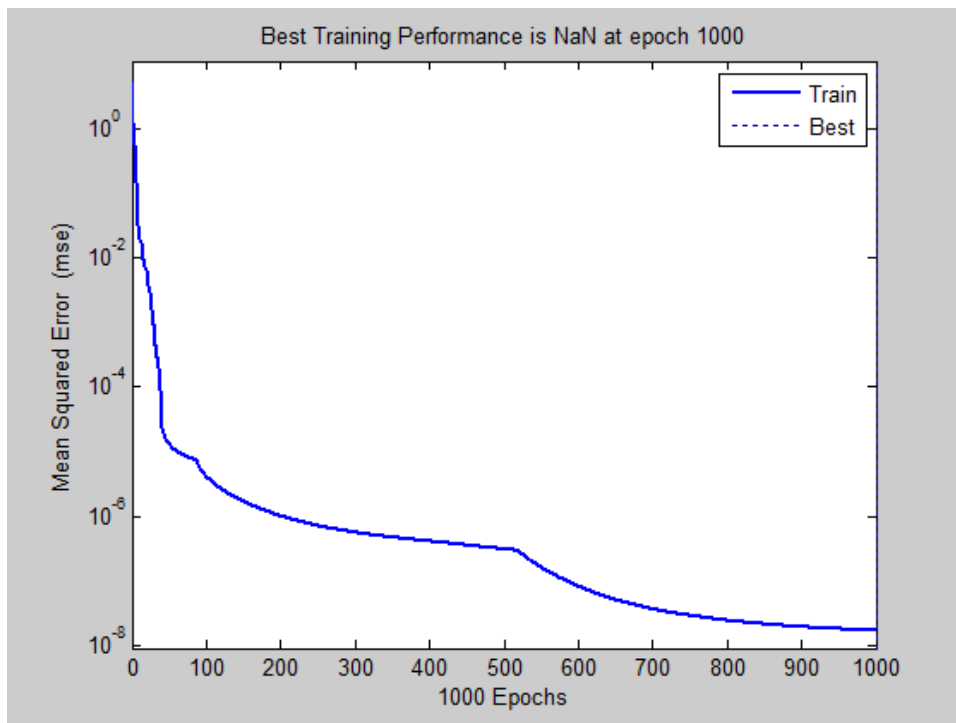


Fig. 4.9. MSE versus Epochs for Network 3.

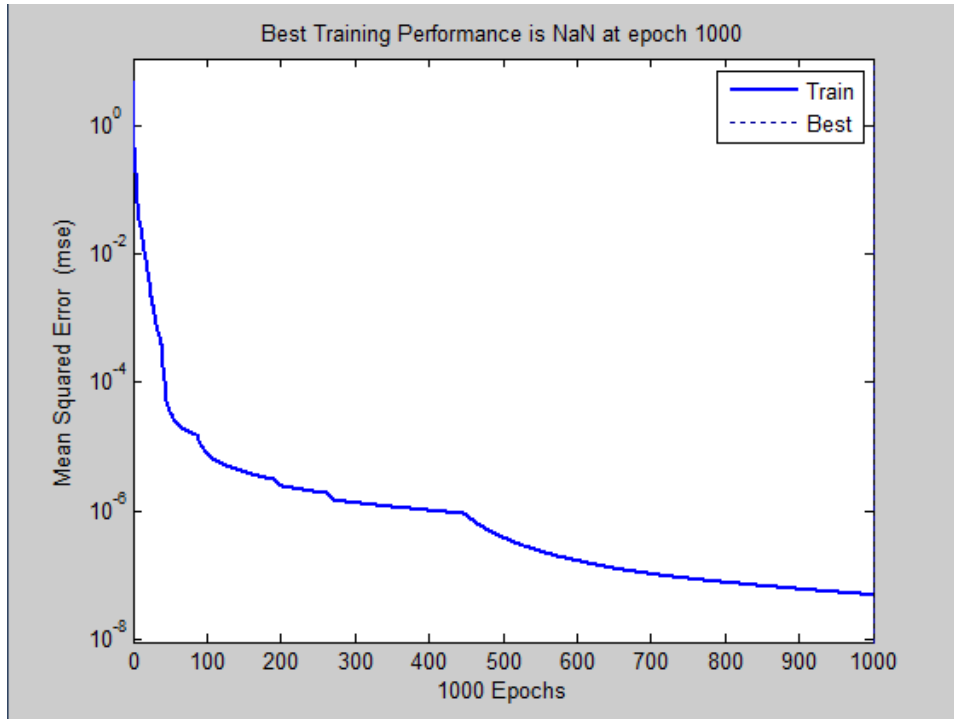


Fig. 4.10. MSE versus Epochs for Network 4.

After training all four networks, it was time to put them to the test to see if they perform the function they are intended to execute. The following figures give a comparison between the outputs of the simulated neural network response for, a specific input, against the actual output. The actual outputs are calculated exactly in MATLAB by simply using (4.2). The simulations were done for 4 different desirable angle sets.

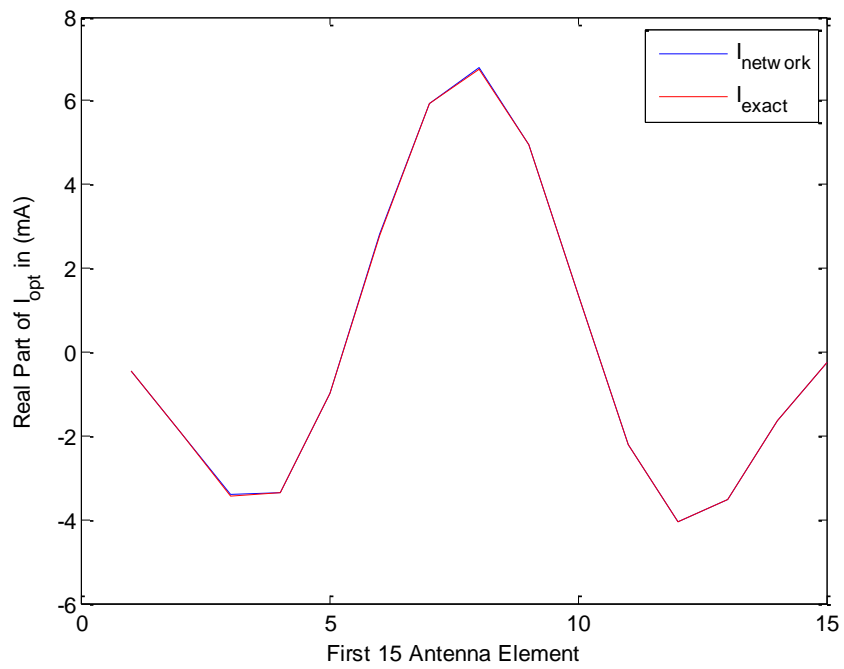


Fig. 4.11. Comparison of $Re\{I_{opt}\}$ for the first 15 elements between the neural network and the exact output for $\theta_o = \pi/6$ & $\varphi_o = 2\pi$.

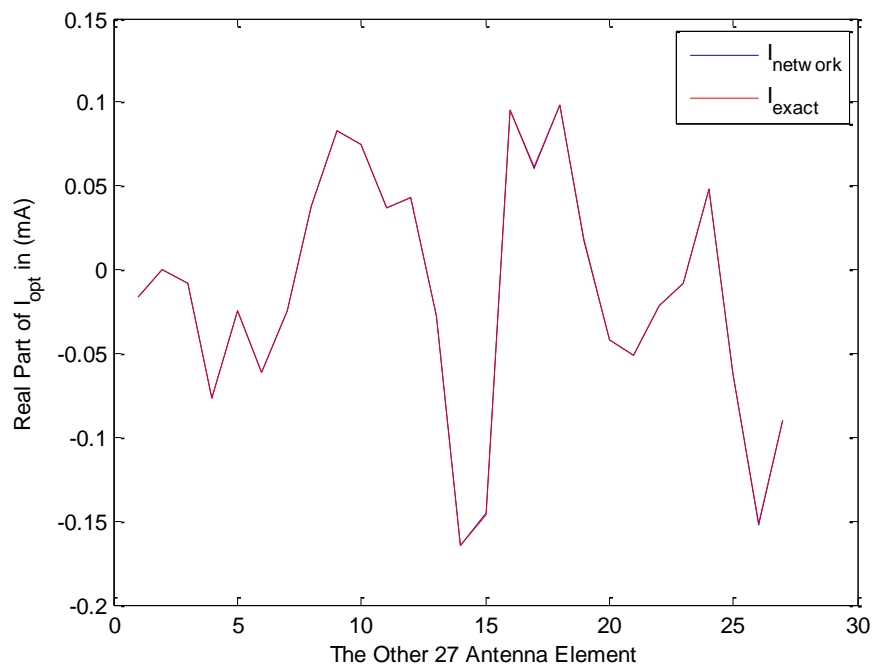


Fig. 4.12. Comparison of $Re\{I_{opt}\}$ for the other 27 elements between the neural network and the exact output for $\theta_o = \pi/6$ & $\varphi_o = 2\pi$.

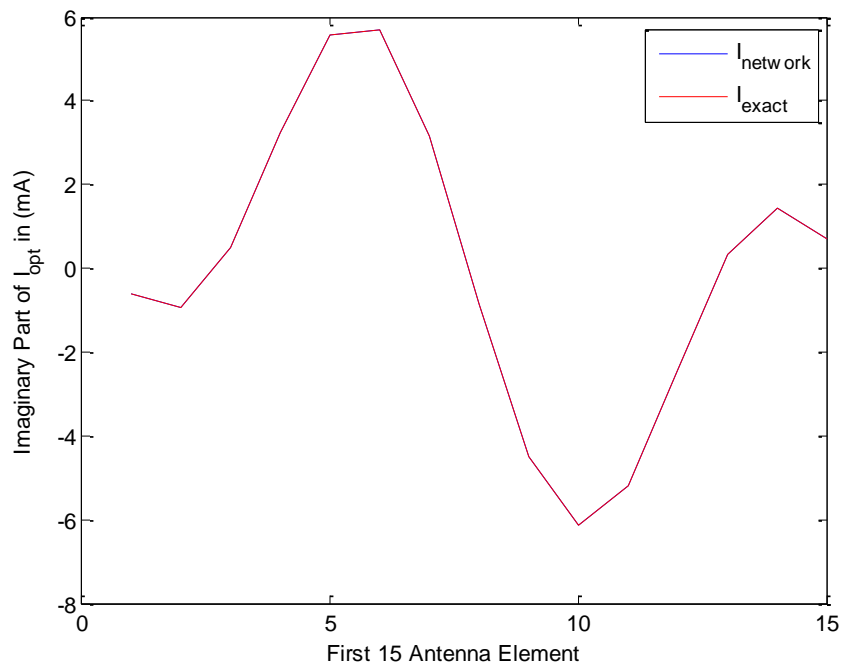


Fig. 4.13. Comparison of $Im\{I_{opt}\}$ for the first 15 elements between the neural network and the exact output for $\theta_o = \pi/6$ & $\varphi_o = 2\pi$.

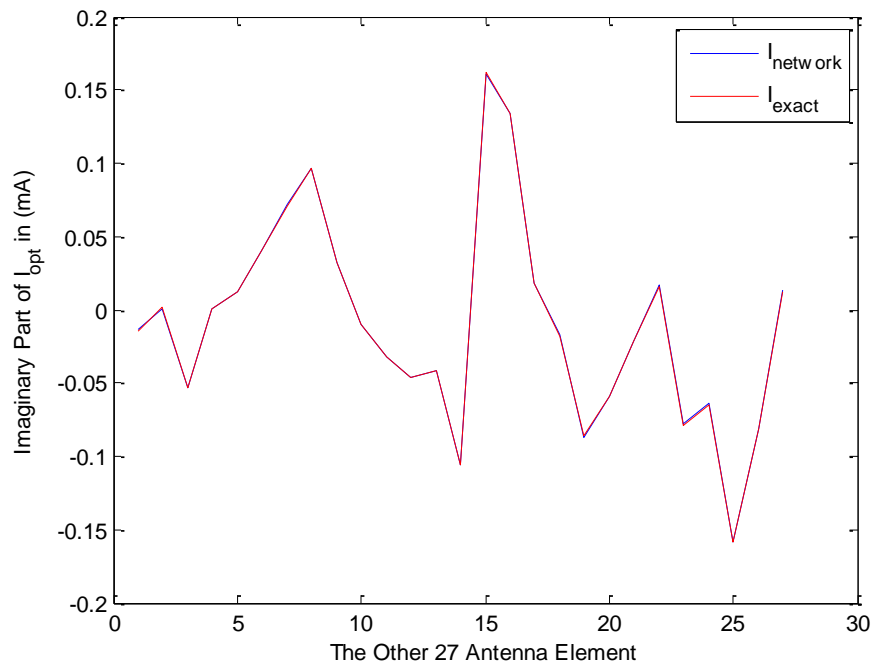


Fig. 4.14. Comparison of $Im\{I_{opt}\}$ for the other 27 elements between the neural network and the exact output for $\theta_o = \pi/6$ & $\varphi_o = 2\pi$.

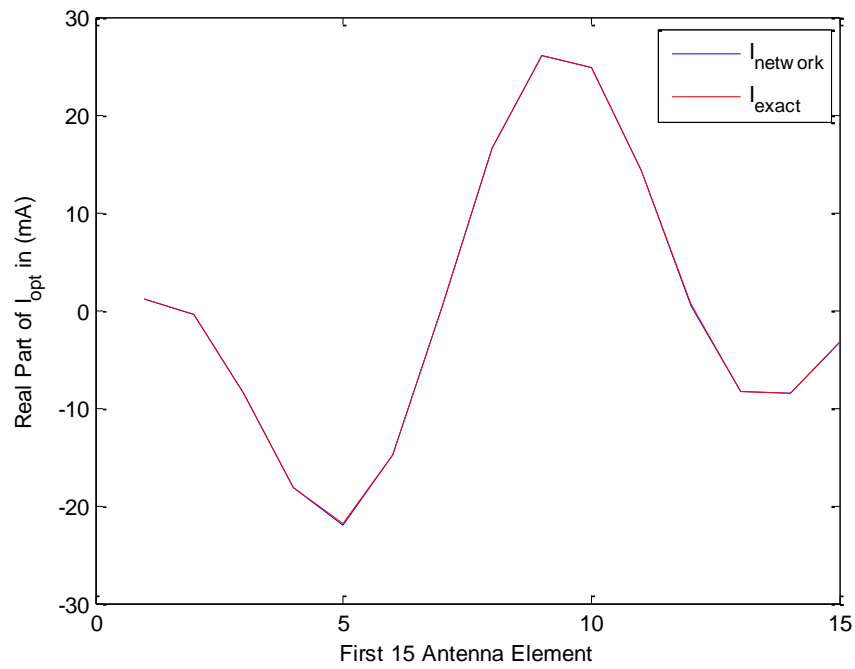


Fig. 4.15. Comparison of $Re\{I_{opt}\}$ for the first 15 elements between the neural network and the exact output for $\theta_o=\pi/2$ & $\varphi_o=2\pi$.

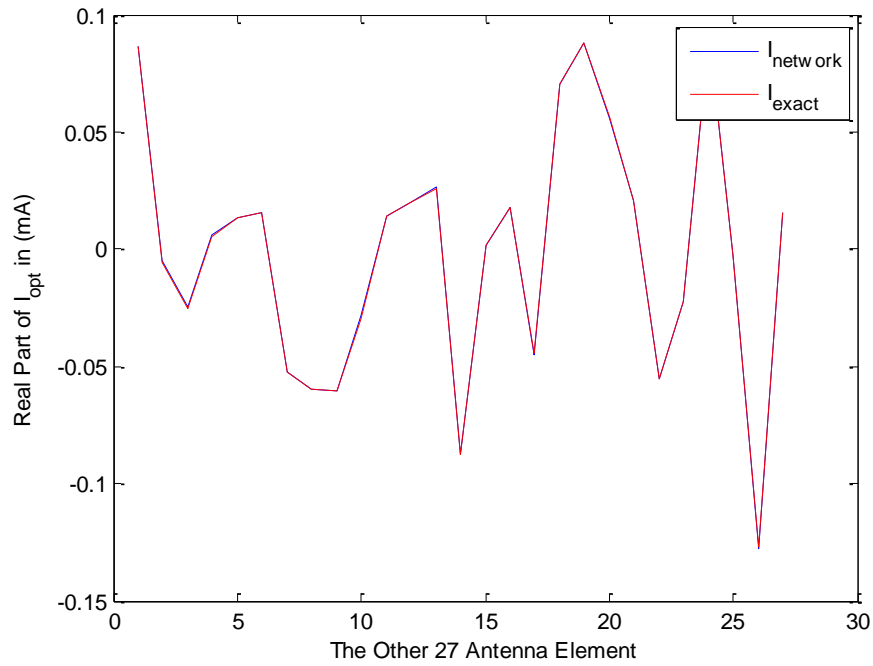


Fig. 4.16. Comparison of $Re\{I_{opt}\}$ for the other 27 elements between the neural network and the exact output for $\theta_o=\pi/2$ & $\varphi_o=2\pi$.

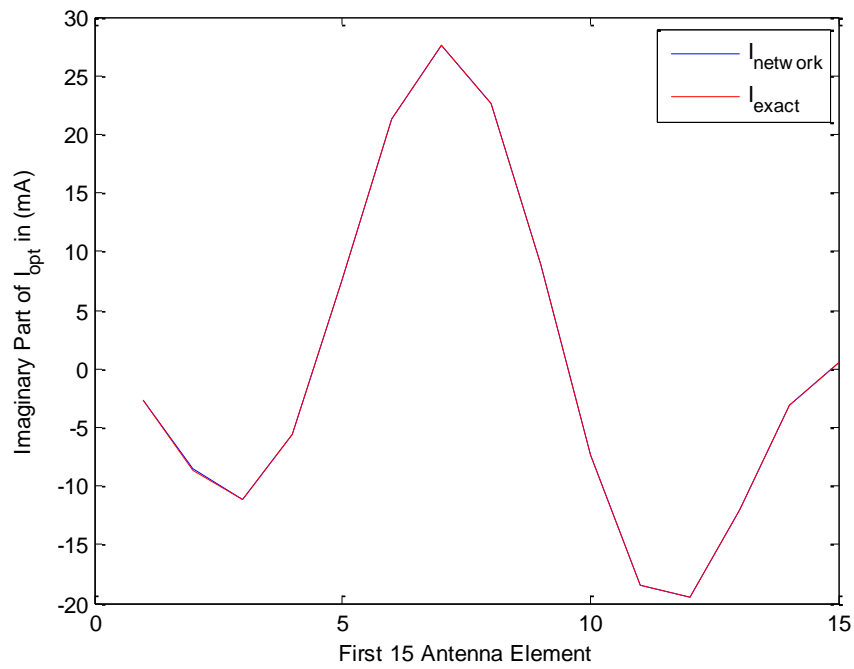


Fig. 4.17. Comparison of $Im\{I_{opt}\}$ for the first 15 elements between the neural network and the exact output for $\theta_o=\pi/2$ & $\varphi_o=2\pi$.

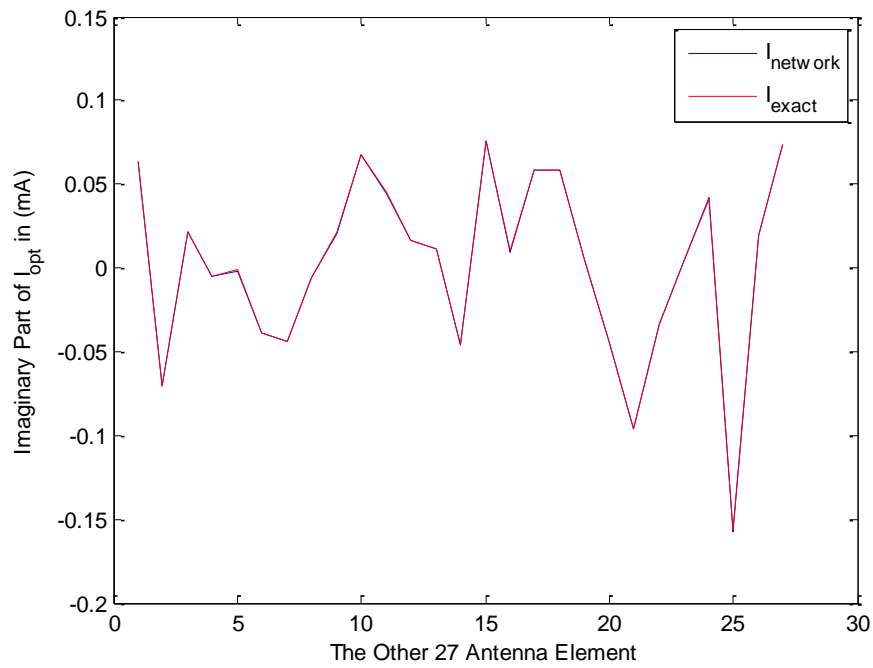


Fig. 4.18. Comparison of $Im\{I_{opt}\}$ for the other 27 elements between the neural network and the exact output for $\theta_o=\pi/2$ & $\varphi_o=2\pi$.

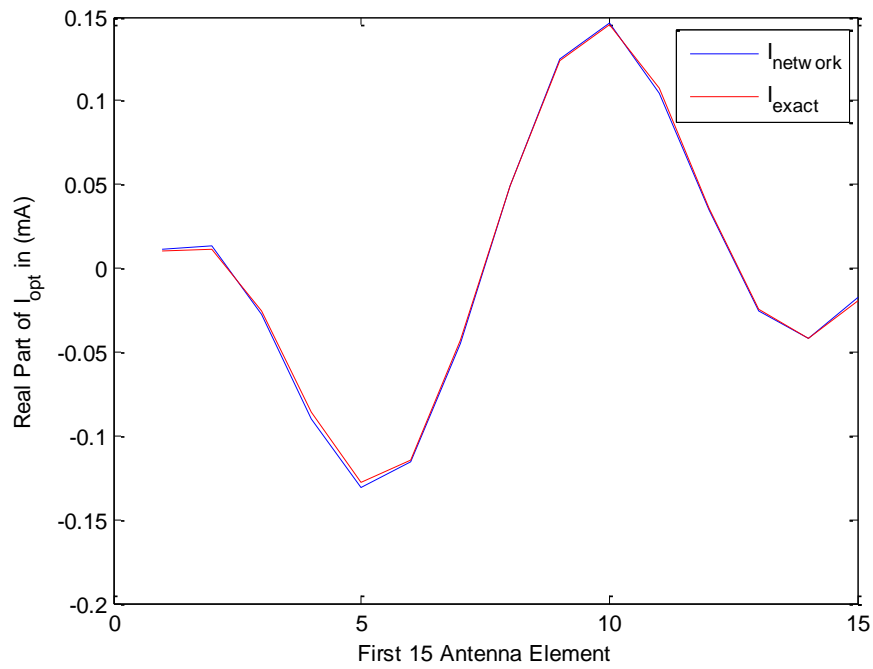


Fig. 4.19. Comparison of $Re\{I_{opt}\}$ for the first 15 elements between the neural network and the exact output for $\theta_o=0$ & $\varphi_o=0$.

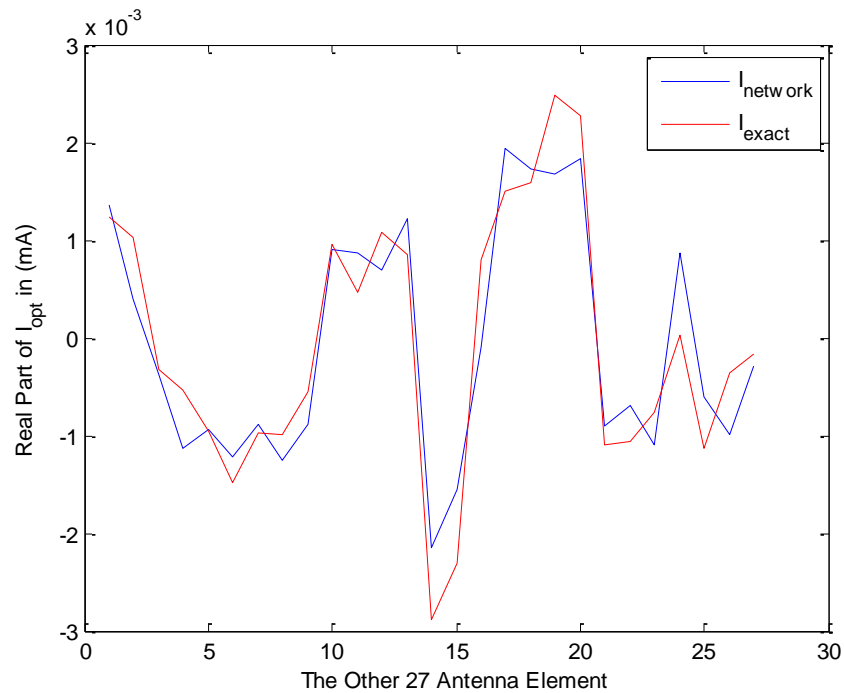


Fig. 4.20. Comparison of $Re\{I_{opt}\}$ for the other 27 elements between the neural network and the exact output for $\theta_o=0$ & $\varphi_o=0$.

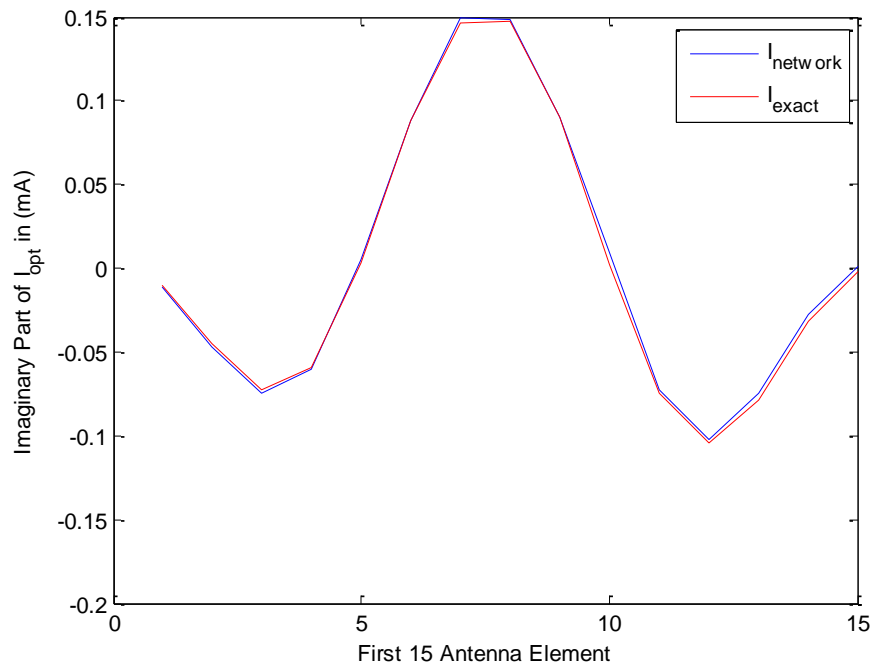


Fig. 4.21. Comparison of $Im\{I_{opt}\}$ for the first 15 elements between the neural network and the exact output for $\theta_o=0$ & $\varphi_o=0$.

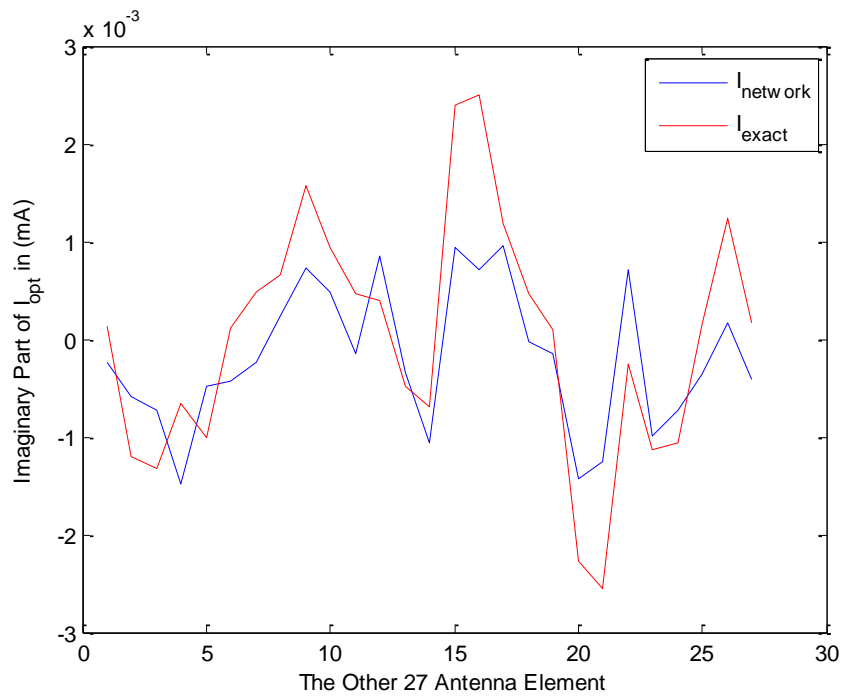


Fig. 4.22. Comparison of $Im\{I_{opt}\}$ for the other 27 elements between the neural network and the exact output for $\theta_o=0$ & $\varphi_o=0$.

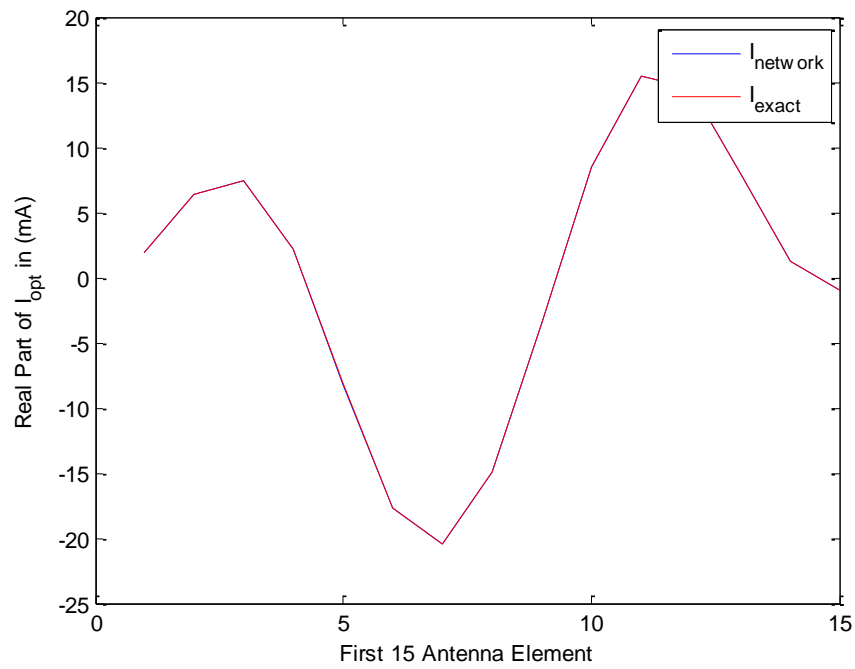


Fig. 4.23. Comparison of $Re\{I_{opt}\}$ for the first 15 elements between the neural network and the exact output for $\theta_o=5\pi/6$ & $\varphi_o=2\pi$.

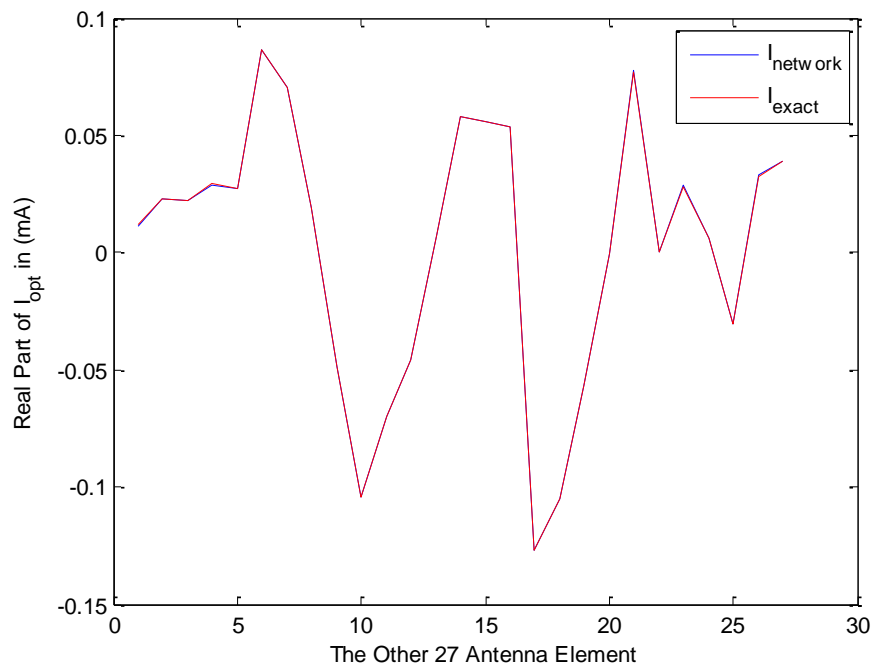


Fig. 4.24. Comparison of $Re\{I_{opt}\}$ for the other 27 elements between the neural network and the exact output for $\theta_o=5\pi/6$ & $\varphi_o=2\pi$.

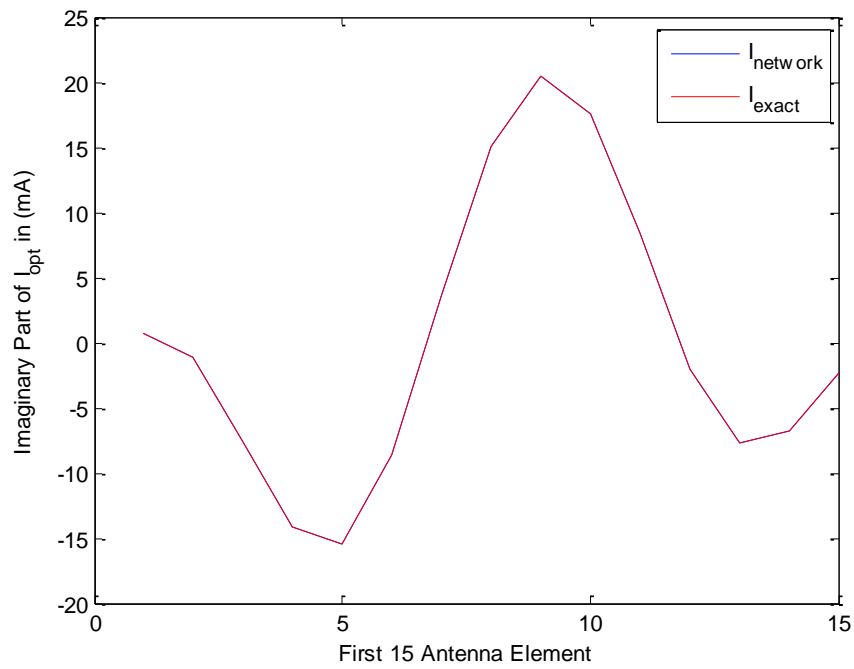


Fig. 4.25. Comparison of $Im\{I_{opt}\}$ for the first 15 elements between the neural network and the exact output for $\theta_o=5\pi/6$ & $\varphi_o=2\pi$.

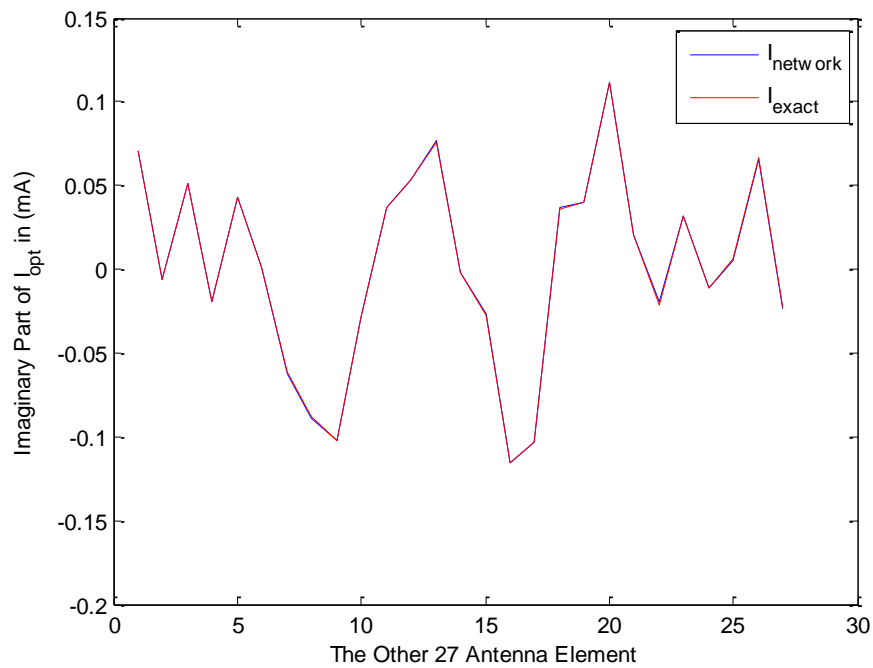


Fig. 4.26. Comparison of $Im\{I_{opt}\}$ for the other 27 elements between the neural network and the exact output for $\theta_o=5\pi/6$ & $\varphi_o=2\pi$.

From the figures it is clear how the neural network is capable of simulating the beamforming function of (4.2). Except for Fig. 4.19 to Fig. 4.22 where it is desired to direct the beam to the angle set $(0,0)$. At this angle set it is clear that the neural network fails to follow the actual output of (4.2). This means that the output of the neural network will cause incorrect magnetic field focusing which could harm the brain. More training is needed within the vicinity of this the angle set $(0,0)$ to improve the performance of the neural network.

Chapter 5: RF Electronics

5.1 RF Front-End

In this chapter the simulation of the RF transmitter and receiver is shown. A typical antenna array RF transmitter is shown in Fig. 5.1. An antenna array circuit with N elements consists of N oscillators, N phase shifters, N RF amplitude amplifiers and N power amplifiers. A typical antenna array RF receiver is shown in Fig. 5.2. It consists of N low noise amplifiers, N RF amplitude amplifiers, N phase shifters and an RF combiner or adder that sums up the signals from all the paths. In most RF application the receiver also mixers and local oscillators to downconvert the RF signal to the intermediate frequency (IF). In this case since the frequency of reception is only 500 kHz, downconversion is unnecessary. In both cases the control voltages on the phase shifters and the RF amplitude amplifiers (which make up the weight adjustment to the outgoing or incoming signal) are controlled by the beamforming or baseband circuit (*neural network* in the transmitter case).

The chapter will consider the theory and analysis of each component mentioned and that is found necessary for this specific application. First the transmitter circuit will be discussed which aims on the design of an antenna array with 42 elements capable of transmitting at 1.8 GHz. After that the antenna array receiver will be designed that is aimed on receiving signals at 500 kHz.

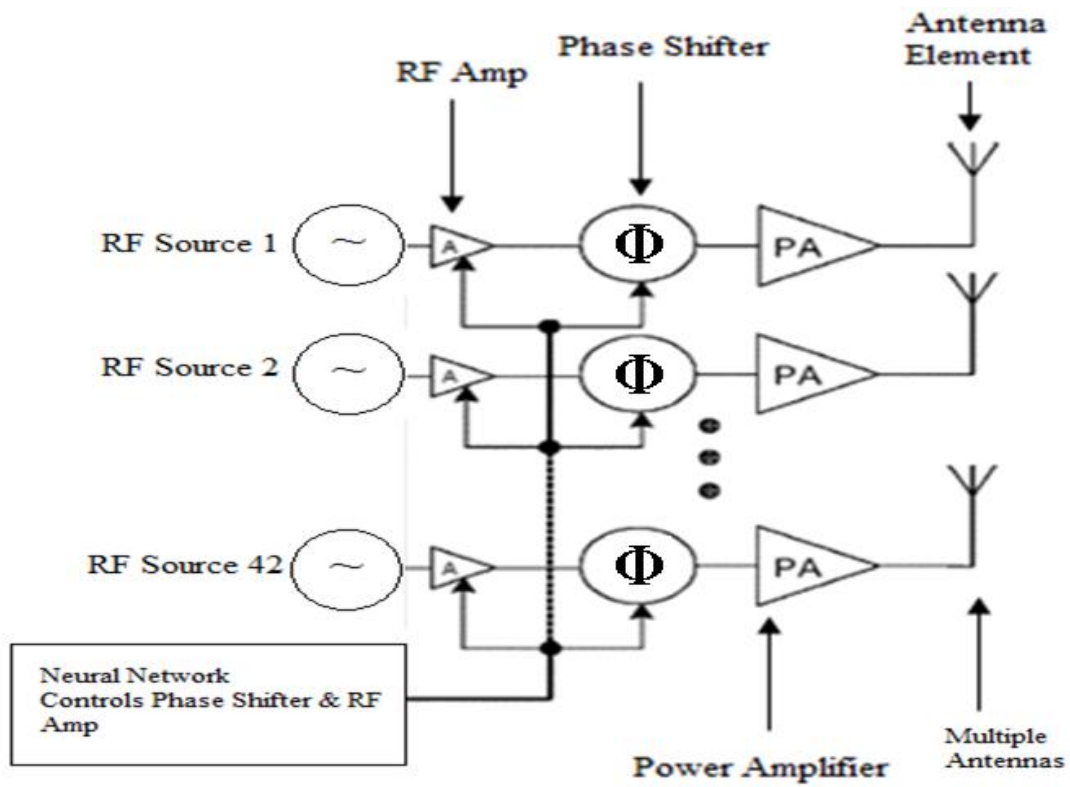


Fig. 5.1. A typical RF antenna array transmitter.

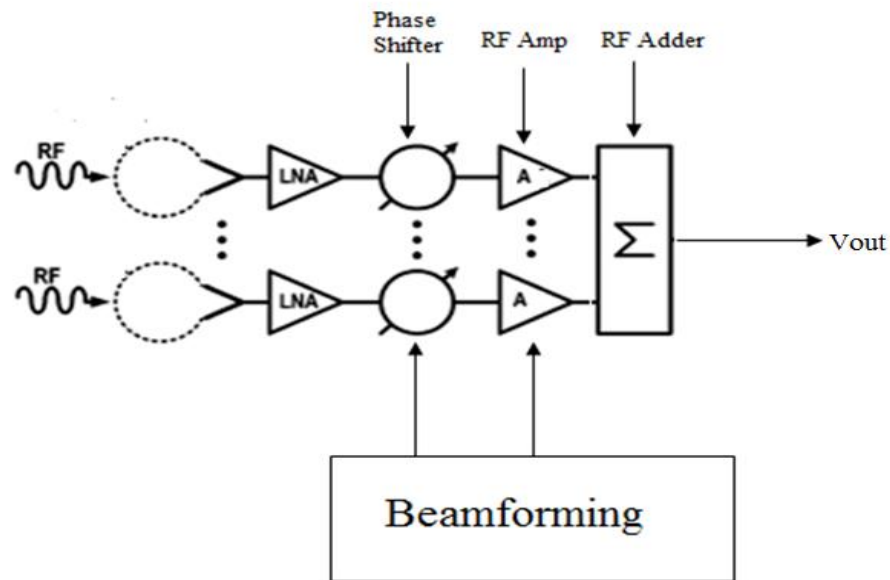


Fig. 5.2. A typical RF antenna array receiver.

5.2 RF Transmitter Circuit Components

5.2.1 Phase Shifter Design

A new phase shifter is designed in this thesis using the all-pass filter topology utilized in [30]. It is important to mention that the design strategy followed in [30] yielded phase shifting but not at high RF frequencies so therefore it was necessary to try and follow a different approach to sustain phase shifting at high frequencies (1 GHz and above). The phase shifter is utilized by using MOS technology with fixed valued capacitors and resistors. No inductors are needed which is a big advantage when considering the different issues in designing on chip inductors such as quality factor, losses and bandwidth associated with the inductor. Another advantage is that gain control through DACs is not needed which will lead to a great deal of simplification when considering circuit design. Phase shifting is accomplished in an analog manner by simply changing the bias gate voltage of a transistor (shown later).

5.2.1.1 Theory of the Phase Shifter

The main idea of this phase shifter was presented in [30] and it works by first considering the simple circuit in Fig. 5.3. The circuit shows a simple RC circuit in which the voltage v_x across the capacitor is given by equation (5.1) in the Laplace transform s -domain.

$$v_x(s) = \frac{v_{in}(s)}{1 + sRC} \quad (5.1)$$

Where v_{in} is the input signal, R is the resistance, $s=j\omega$ (ω frequency) and C is the capacitance.

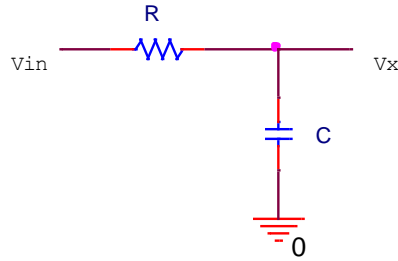


Fig. 5.3. RC Circuit to be used for the All-Pass Filter.

One can realize a first order all-pass filter if the following equation can be accomplished.

$$v_o(s) = 2v_x(s) - v_{in}(s) = \frac{1 - sRC}{1 + sRC} v_{in}(s) \quad (5.2)$$

Where v_o is the desired output voltage that will allow phase shifting. If (2) can be realized then the phase difference (Φ) between the output and input voltage signal is given by (5.3).

$$\Phi = -2 \tan^{-1}(\omega RC) \quad (5.3)$$

Phase shifting is achieved by varying the resistance, capacitance or both. It is clear from (5.3) that the maximum phase shift that can be achieved by this topology is 180° (theoretically), therefore to extend the shifting to 360° another equation should be realized.

$$v_o'(s) = v_{in}(s) - 2v_o(s) = \frac{sRC - 1}{sRC + 1} v_{in}(s) \quad (5.4)$$

$$\Phi' = -\pi - 2 \tan^{-1}(\omega RC)$$

From (5.4) it is clear how the other 180° phase shift can be obtained.

The approach taken in this paper is to try and select circuit topologies that are known to have high upper frequency values such as the common gate MOSFET since the gate-to-drain capacitance is shorted at one end in which case it will not cause feedback problems from output to input at high frequencies. The circuit topology used in this paper is shown in Fig. 5.4.

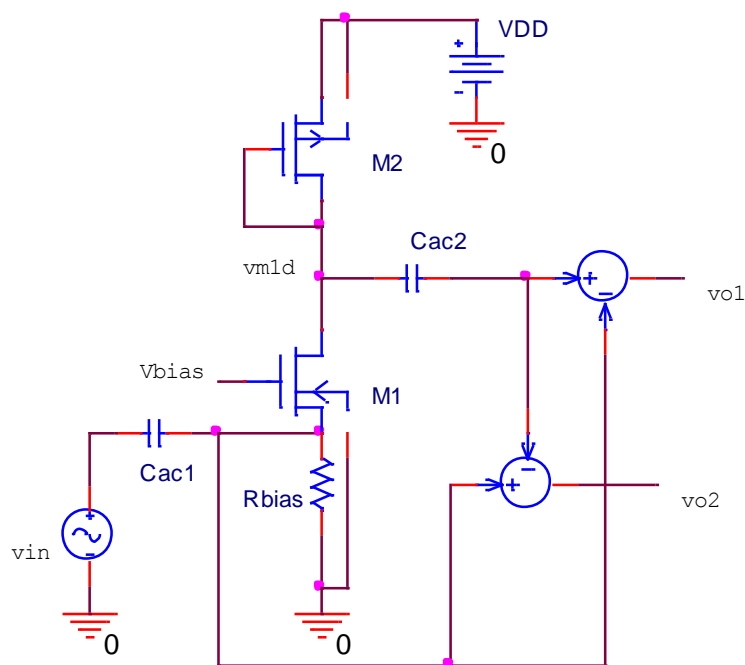


Fig. 5.4. Circuit Topology for the First Order All-Pass Filter.

As it can be seen M1 is an NMOS transistor connected in the common gate configuration (to improve performance at high frequencies) with the input small-signal connected to its source and output drain connected to a diode connected PMOS transistor M2. M2 is diode connected because it is desired to connect a load to M1 that gives a conductance equal to half the transconductance of M1.

When considering the small-signal model for transistors M1 and M2 and solving for the output voltage seen from the drain of M1, one can derive the following expression (Appendix D).

$$\frac{v_{m1d}}{v_{in}} = \frac{\frac{g_{m1} + g_{o1}}{g_{m2} + g_{o1} + g_{o2}}}{1 + \frac{s(C_{gd1} + C_{gs2})}{g_{m2} + g_{o1} + g_{o2}}} \approx \frac{\frac{g_{m1}}{g_{m2}}}{1 + \frac{s(C_{gd1} + C_{gs2})}{g_{m2}}} \quad (5.5)$$

Where v_{m1d} is the voltage at the drain of M1, g_{m1} and g_{m2} are the transconductances of M1 and M2, respectively, g_{o1} and g_{o2} are the Early conductances of M1 and M2, respectively, C_{gd1} is the gate-to-drain capacitance of M1 and C_{gs2} is the gate-to-source capacitance of M2. Note that in (5.5) it is assumed that $g_{m1} \gg g_{o1}$ and $g_{m2} \gg g_{o1} + g_{o2}$. By using two comparators or difference circuits the desired output voltages could be realized and are given by the following expressions.

$$\frac{v_{o1}}{v_{in}} = \alpha_1 \frac{\frac{g_{m1}}{g_{m2}} - \frac{s(C_{gd1} + C_{gs2})}{g_{m2}} - 1}{\frac{s(C_{gd1} + C_{gs2})}{g_{m2}} + 1} \quad (5.6)$$

$$\frac{v_{o2}}{v_{in}} = \alpha_2 \frac{\frac{s(C_{gd1} + C_{gs2})}{g_{m2}} + 1 - \frac{g_{m1}}{g_{m2}}}{\frac{s(C_{gd1} + C_{gs2})}{g_{m2}} + 1} \quad (5.7)$$

Where α_1 and α_2 are the small-signal voltage gains of the comparators circuits (see equation (5.14)). By setting $g_{m2} = g_{m1}/2$, two first order all-pass filters similar to those in (5.2) and (5.4) will be realized where input/output transfer functions and phase differences are given by (5.8) and (5.9).

$$\frac{v_{o1}}{v_{in}} = \alpha_1 \frac{1 - \frac{s 2(C_{gd1} + C_{gs2})}{g_{m1}}}{1 + \frac{s 2(C_{gd1} + C_{gs2})}{g_{m1}}} \quad (5.8)$$

$$\Phi_1 = -2 \tan^{-1} \left(\frac{2\omega(C_{gd1} + C_{gs2})}{g_{m1}} \right)$$

$$\frac{v_{o2}}{v_{in}} = -\frac{\alpha_2 v_{o1}}{\alpha_1 v_{in}} \quad (5.9)$$

$$\Phi_2 = -\pi - 2 \tan^{-1} \left(\frac{2\omega(C_{gd1} + C_{gs2})}{g_{m1}} \right)$$

Phase shifting is accomplished by varying V_{BIAS} of transistor M1 which in turn will vary g_{m1} and g_{m2} according to equation (5.10) as long as the dimension relationship between M1 and M2 in (5.11) is satisfied. Note that there are two regions of operation in which M1 and M2 simultaneously operate in and these are the saturation ($V_{BIAS} - R_{BIAS}I > V_{tl}$) and subthreshold ($V_{BIAS} - R_{BIAS}I < V_{tl}$), thus the two different equations for expressing g_m .

$$g_{m1}^{saturation} = k_n \left(\frac{W}{L} \right)_1 (V_{BIAS} - R_{BIAS}I - V_{t1}) \quad (5.10)$$

$$g_{m1}^{subthreshold} \approx \frac{I_o}{V_T} \exp \left(\frac{V_{BIAS} - R_{BIAS}I}{V_T} \right)$$

$$\left(\frac{W}{L} \right)_2 = \frac{1}{4} \frac{k_n}{k_p} \left(\frac{W}{L} \right)_1 = \frac{1}{4} \frac{\mu_n}{\mu_p} \left(\frac{W}{L} \right)_1 \quad (5.11)$$

Where V_{BIAS} is the gate voltage of M1, R_{BIAS} is the resistor connected to the source of M1 to allow a dc path to ground, I is the dc current running through the drain M1 and

M2, V_{tl} is the threshold voltage of M1, W is the MOSFET channel width, L is the MOSFET channel length, k_n and k_p are the PSPICE k_p parameters, μ_n and μ_p are the electron and hole mobilities respectively, I_o is the subthreshold saturation current and V_T is the thermal voltage. Note as long as (5.11) is satisfied g_{m2} is always going to be half of g_{m1} for all values of V_{BIAS} since M1 and M2 share the same bias current (I) and therefore only the design parameters are going to affect the relationship between g_{m1} and g_{m2} .

It is important to note that the capacitors C_{ac1} and C_{ac2} are both used for appropriate dc blocking such that the inputs to the comparators are only small signal so that the DC bias will not interfere with the biasing of the comparators. Also C_{ac1} will allow for correct dc biasing of the circuit of M1 and M2 without any interruption from the small-signal input signal v_{in} .

The comparator circuits are accomplished by using a differential-to-single ended amplifier with active PMOS current-mirror load like the one shown in Fig. 5.5 (Note that Fig. 5.5 only shows the two comparators used for the realization of the phase shifter, not the entire circuit. The inputs of the comparators are v_{m1d} and v_{in}). An additional advantage of using these amplifiers is that they can be designed to provide amplification in the output voltage with the desired phase shift. As it can be seen from Fig. 5.5, the differential inputs are applied to NMOS transistors M3, M4, M8 and M9 (which form the differential pair) and the output is taken from the drains of M4 and M9. Assuming that the differential pairs are perfectly matched and operate with equal dc currents, as do the current-mirror loads (M5, M6, M10 and M11), then the small-signal transconductances are $g_{m3}=g_{m4}=g_{m8}=g_{m9}=g_{m(dp)}$ ($g_{m(dp)}$ is defined as the

differential pair transconductance) and $g_{m5}=g_{m6}=g_{m10}=g_{m11}=g_{m(mir)}$ and the output current i_o is given by [54].

$$i_{out1} = g_{m(dp)}(v_{m1d} - v_{in}); i_{out2} = -i_{out1} \quad (5.12)$$

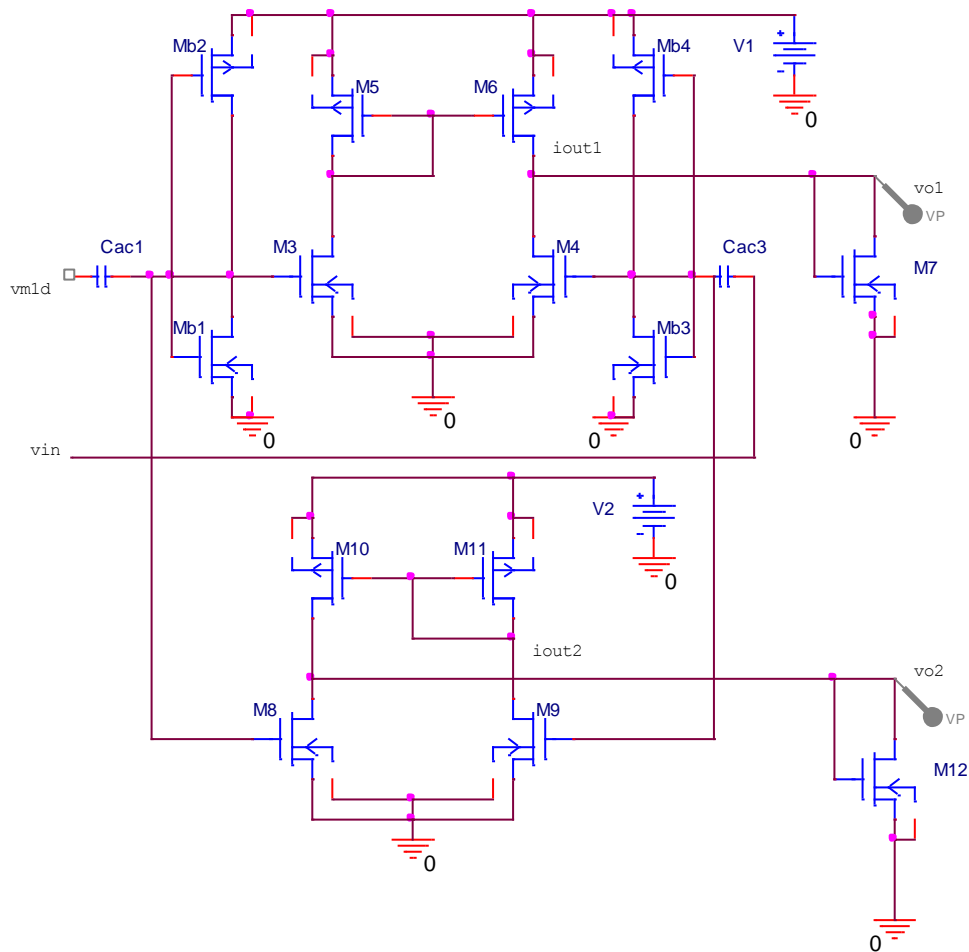


Fig. 5.5. The two differential-to-single ended amplifiers to realize the voltage differences needed.

Now depending on the designer's requirements, the output currents are going to be fed to the input stage of the next circuit component (in most cases a power amplifier). If a voltage amplification stage is necessary for some reason, then this can be provided by

selecting a high resistance load (R_o) into which all the output currents will sink into and so give the following output voltage (here only v_{o1} is considered).

$$v_{o1} = g_{m(dp)}(R_o \parallel r_{o4} \parallel r_{o6})(v_{m1d} - v_{in}) \quad (5.13)$$

Where r_{o4} , and r_{o6} are the Early resistances of transistors M4 and M6 respectively (a similar analysis can be made for v_{o2}). On the other hand, if an ideal first order all-pass filter response is needed (i.e. no voltage gain) then one can terminate the output of the amplifiers with diode-connected NMOS transistors (M7 and M12) and in this way the output voltages of the amplifier and the entire circuit are given by (5.14).

$$\begin{aligned} v_{o1} &= g_{m(dp)} \left(\frac{1}{g_{m7}} \right) \parallel r_{o4} \parallel r_{o6} (v_{m1d} - v_{in}) \\ &\approx \frac{g_{m(dp)}}{g_{m7}} (v_{m1d} - v_{in}) \approx (v_{m1d} - v_{in}) \\ v_{o2} &\approx \frac{g_{m(dp)}}{g_{m12}} (v_{in} - v_{m1d}) \approx (v_{in} - v_{m1d}) \end{aligned} \quad (5.14)$$

In theory, it is desired to set the transconductances of transistors M7 and M12 to be equal to those of M3, M4, M8 and M9. It was evident from the PSPICE simulation that under the prior conditions the voltage gain at 1GHz suffers a drop of around 3dB. Therefore, g_{m7} and g_{m12} were set smaller than those for M3, M4, M8 and M9 to compensate for this voltage gain drop. As it is clear from (5.14) that if $g_{m7,12} < g_{m(dp)}$ a voltage gain is sustained.

5.2.1.2 PSPICE Simulation Results

The phase shifter was designed and simulated in PSPICE using the AMI 0.5 μm technology. The voltage supply used was 3V and also the control voltage supplies for the comparators in Fig. 5.5 (V_1 and V_2). The transistor dimensions for M1 and M2 are (10 $\mu\text{m}/0.5\mu\text{m}$) and (7 $\mu\text{m}/0.5\mu\text{m}$). The transistors M3-M11 all have dimensions (1 $\mu\text{m}/0.5\mu\text{m}$) while the bias transistors Mb1-Mb4 have dimensions of (1 $\mu\text{m}/10\mu\text{m}$). The dc blocking capacitors C_{ac1} , C_{ac2} and C_{ac3} have values of 1 μF .

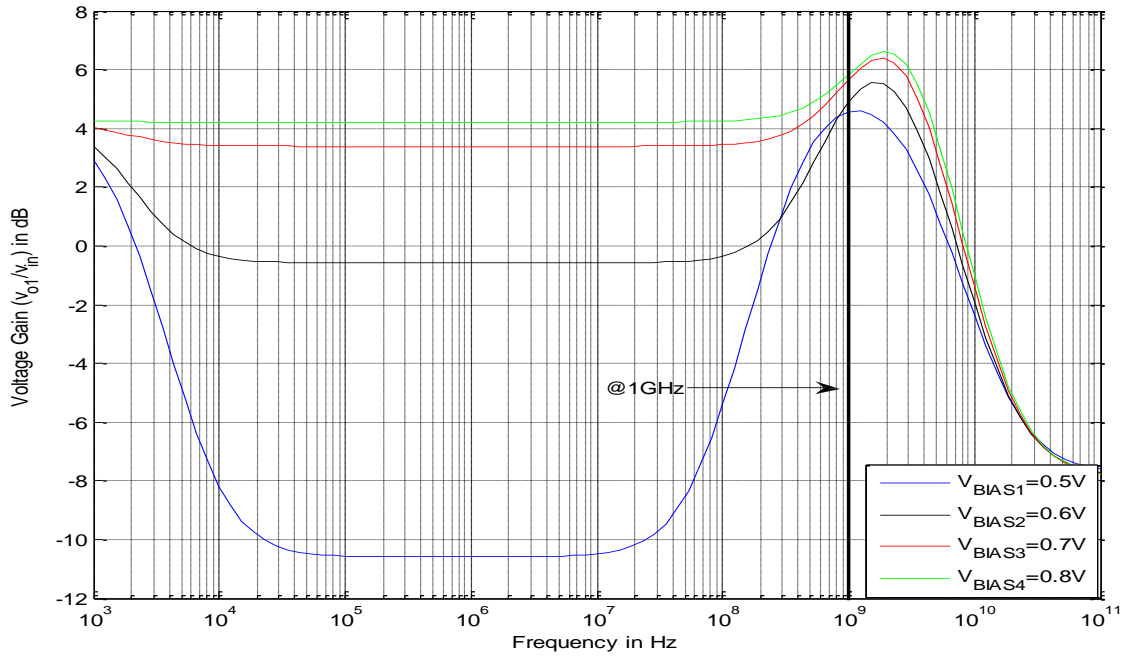


Fig. 5.6. Voltage Gain versus Frequency for v_{ol} .

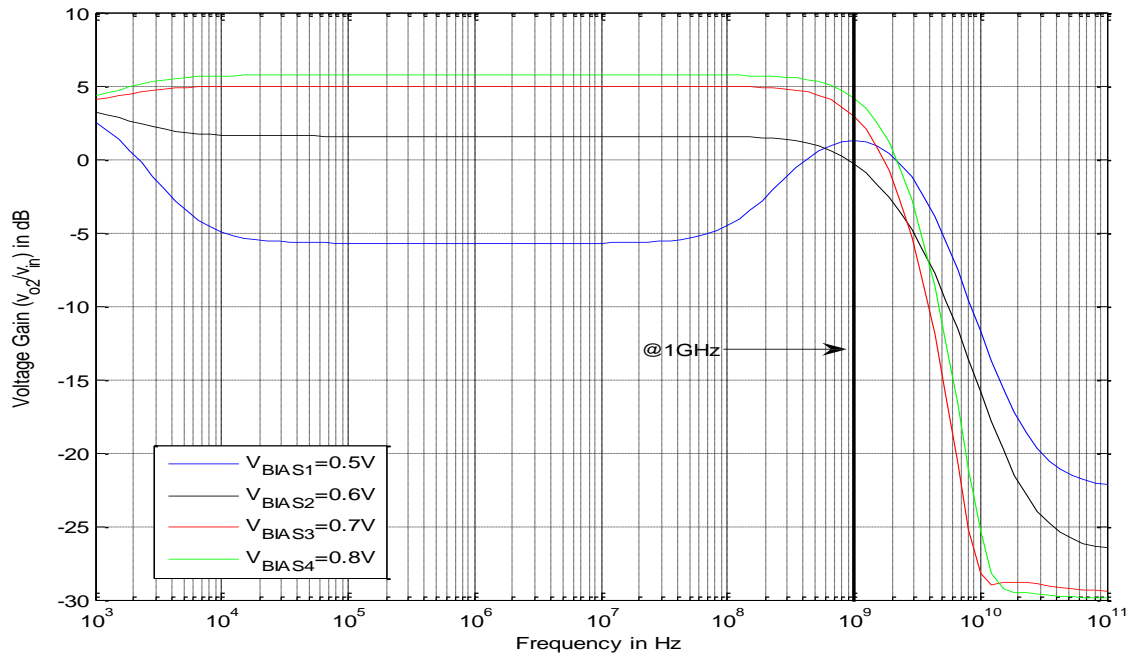


Fig. 5.7. Voltage Gain versus Frequency for v_{o2} .

Since the phase shifting is applied through the varying V_{BIAS} of transistor M1, the power consumption of the phase shifter will also vary with the desired phase shift. The maximum power consumption of the phase shifter when a phase shift from 0° to 180° is desired is $332\mu\text{W}$, on the other hand, when a phase shift between 180° to 360° is desired the consumption is $339\mu\text{W}$. So for a total of 42 phase shifters the maximum power dissipated will become $42 \times 339\mu\text{W} = 14.2\text{mW}$.

There were two phase shift ranges realized by the phase shifter and these were -93.4° to -174.6° ($\Delta\Phi_1 \approx 81.2^\circ$) and -231.4° to -363.0° ($\Delta\Phi_2 \approx 131.6^\circ$) (see Fig. 5.7). The voltage gain resulting from the phase shift for all cases was around 5dB at 1GHz.

Figures 5.6 and 5.7 show the voltage gain characteristics for v_{o1} and v_{o2} respectively. Figure 5.8 shows the phase characteristics for v_{o1} and v_{o2} . As it can be

seen from Figures 5.6 and 5.7, the voltage gain at dc is not 0 dB and this is because of the reason explained in the previous subsection. From Figure 5.8 it is clear how the phase shifter covers the two phase ranges $-93.4^\circ < \Phi_1 < -174.6^\circ$ and $-231.4^\circ < \Phi_2 < -363.0^\circ$ specified in the previous paragraph. Also an important remark is that for V_{BIAS} values of 0.5V and 0.6V there is a large phase change present since here M1 is in subthreshold and any change in V_{BIAS} will result in an exponential change in the transconductance g_{m1} , hence a larger phase change.

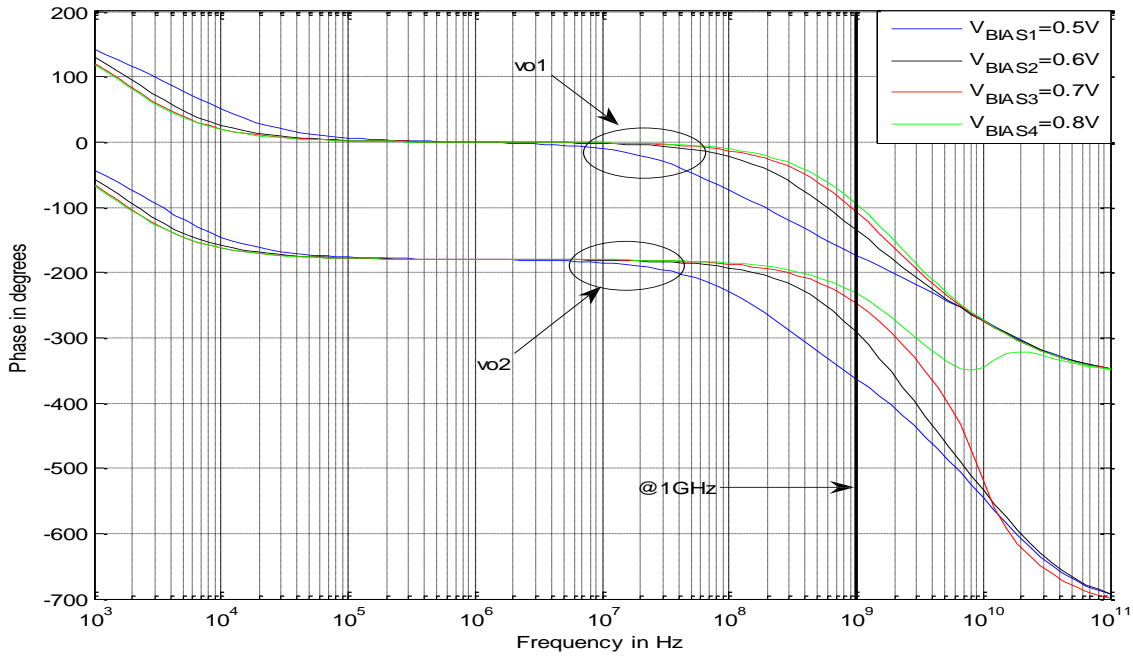


Fig. 5.8. Phase Response versus Frequency for v_{o1} & v_{o2} .

For V_{BIAS} values of 0.5V and 0.6V (subthreshold), there is a severe voltage gain drop in the frequency range $\sim 10^4$ Hz to 10^8 Hz and this is because the value of g_{m1} is small and therefore the Early conductances in (5) cannot be ignored anymore for that frequency range.

5.2.2 Antenna Element Impedance

Here the antenna is considered as an RF component in the circuit. To include the antenna in circuit design it is necessary to calculate its impedance at the frequency of operation (1.8 GHz in the transmitter case). Figure 5.9 shows the circuit model used for each antenna element in our array.

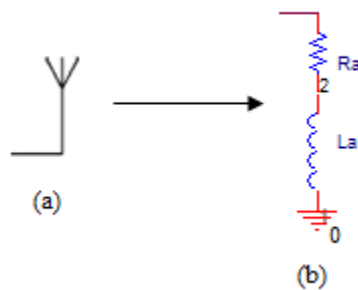


Fig. 5.9. (a) Symbolic representation of an antenna element & (b) Circuit model representation of an antenna element with inductive reactance.

As shown in Figure 5.9 the circuit model representation of an antenna element is a simple RL circuit. Knowing the values of the antenna resistance (R_a) and inductance (L_a) is essential when considering the design of the power amplifier (PA) and the low noise amplifier (LNA) for the transmitter and receiver respectively. From circuit theory the function of the PA is delivering power to the antenna with optimal power transfer efficiency (the transfer is related to the transfer of power from the RF circuitry to the antenna) and this can only be achieved by knowing the impedance of the antenna element being used.

To determine the impedance of the antenna element, the electric (E-field) and magnetic (H-field) field of the antenna element derived in Chapter 3 must be

considered. From Chapter 3 it was found that the E-field and H-field in region (0) at $r=c$ (free space) have the following expressions.

$$\vec{E}_0 = \frac{1}{c} \sum_{l=1}^{\infty} \sum_{m=-l}^l A_{lm} H_l^{(2)}(k_0 c) \vec{r} \times \nabla Y_{lm}(\theta, \varphi) \quad (5.15)$$

$$\vec{H}_0 = \frac{1}{j\omega\mu_0} \sum_{l=1}^{\infty} \sum_{m=-l}^l \nabla \times \left[\frac{1}{r} A_{lm} H_l^{(2)}(k_0 r) \vec{r} \times \nabla Y_{lm}(\theta, \varphi) \right] \Big|_{r=c} \quad (5.16)$$

According to [4], the complex power vector is given by the following equation.

$$\vec{S} = \frac{1}{2} \vec{E}_0 \times \vec{H}_0^* \quad (5.17)$$

The total radiated complex power S_{rad} is given by the following equation.

$$S_{rad} = \int_{\varphi=0}^{2\pi} \int_{\theta=0}^{\pi} \hat{r} \cdot \vec{S} \sin \theta d\theta d\varphi \quad (5.18)$$

Note that in (5.18) a dot product between the complex power and the radial unit vector is taken. This is because the cross product of (5.17) will only yield a radial component since the E-field and the H-field only have angular components and therefore their cross product is purely radial. Calculating the integral of (5.18) seems complicated, but actually it can be made very trivial by making use of the following identity.

$$\int_0^{2\pi} d\varphi \int_0^{\pi} \sin \theta d\theta [\vec{r} \times \nabla Y_{lm}^*(\theta, \varphi)] \cdot [\vec{r} \times \nabla Y_{lm}(\theta, \varphi)] = l(l+1) \delta_{ll} \delta_{mm} \quad (5.19)$$

where; $\delta_{ij} = \begin{cases} 1; i = j \\ 0; i \neq j \end{cases}$

Since the cross product $\vec{E}_0 \times \vec{H}_0^*$ has only a radial component, then taking the dot product with the radial unit vector will only result in (5.20).

$$\hat{r} \cdot \vec{S} = \frac{1}{j\omega\mu_0 c^2} \sum_{l=1}^{\infty} \sum_{m=-l}^l |A_{lm}|^2 H_l^{(2)}(k_0 c) H_l^{(2)*}(k_0 c) [\vec{r} \times \nabla Y_{lm}^*(\theta, \varphi)] \cdot [\vec{r} \times \nabla Y_{lm}(\theta, \varphi)] + M_{lm}(\theta, \varphi) \quad (5.20)$$

Where $M_{lm}(\theta, \varphi)$ is a double sum that contains all the coefficients with the mixed indices. Now applying (5.19) in (5.20) the following can be written.

$$\int_{\varphi=0}^{2\pi} \int_{\theta=0}^{\pi} M_{lm}(\theta, \varphi) \sin \theta d\theta d\varphi = 0 \quad (5.21)$$

$$S_{rad} = \frac{1}{j\omega\mu_0 c^2} \sum_{l=1}^{\infty} \sum_{m=-l}^l l(l+1) |A_{lm}|^2 H_l^{(2)}(k_0 c) H_l^{(2)*}(k_0 c) \quad (5.22)$$

When calculating the complex power, it is possible to look at the quantity in a different way, like in (5.23).

$$S_{rad} = \frac{1}{2} (R_a + jX_a) |I_a|^2 \quad (5.23)$$

Where R_a is the antenna resistance, X_a is the antenna reactance, j is the complex number $\sqrt{-1}$ and $|I_a|$ is the antenna current. By calculating (5.22) with MATLAB and matching it with (5.23) the antenna resistance was found to be $R_a = 122 \Omega$ and the reactance is $X_a = 472 \Omega$. Now since the reactance is positive this implies that it is an inductive reactance and the circuit model for the antenna is given by Figure 5.9(c).

The value of the inductance can be calculated by using (5.24).

$$L_a = \frac{X_a}{\omega_o} \quad (5.24)$$

Where ω_o is the frequency of operation By using (5.24) the value of the inductance $L_a=41.7 \text{ nH}$.

5.2.3 Power Amplifier (PA)

5.2.3.1 PA Theory

A power amplifier (PA) (Fig. 5.10) is the component in the RF transmitter that delivers the RF power to the load (i.e. antenna element) with maximum *power transfer efficiency*. According to [18] there are many PA topologies and the one chosen in this dissertation is the *Class E* PA since it can have a theoretical 100% power transfer efficiency. The disadvantages of using the class E PA is that it needs oversized devices (as will be shown later) to deliver a given amount of power to a load.

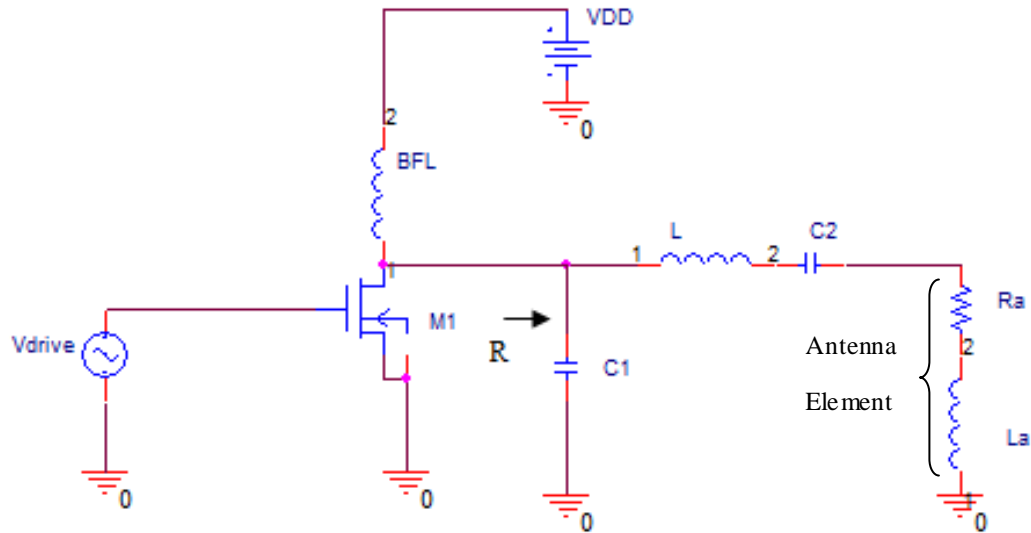


Fig. 5.10. Class E Power Amplifier (PA).

The main idea of the PA is that M1 acts as a switch. The class E PA uses a high order resonator circuit to shape the output voltage and current such that the power dissipation of the M1 is kept to a minimum. The *BFL* in Figure 5.10 is called the *big fat inductor* (also known as *RF choke*) and it is simply an inductor with a large inductance value to provide a DC path to the supply (V_{DD}) and also to approximate an open circuit at RF.

Contrary to the initial intuition that the power delivered to the load must be maximized, it is essential to maximize the power transfer efficiency instead. This is because if the regular theorem of having the output impedance of M1 equal to the complex conjugate to the impedance of the load, this implies that if it was intended to transmit 100 μW to the antenna then only 50% of that will be delivered which is very inefficient. The strategy of the design is based on the maximization of the power transfer efficiency and this is done by considering equation (5.25) [18].

$$P_o = \frac{2}{1 + \frac{\pi^2}{4}} \frac{V_{DD}^2}{R} \approx 0.577 \frac{V_{DD}^2}{R} \quad (5.25)$$

Where P_o is the maximum output power desired to be delivered, V_{DD} is the voltage supply and R is the required output resistance seen by the drain of M1 to guarantee maximum power delivery (R is indicated clearly in Figure 5.11). If it is desired to supply the antenna impedance an output power of 100 μW , then by using (5.25) the required equivalent resistance is $R=52 \text{ k}\Omega$. The next step is to solve for the unknown network values (L , C_1 & C_2) in Figure 5.11 to give the desired equivalent resistance R . The value of C_2 is set to cancel the effect of L_a (antenna element reactance) at resonance (@ 1.8 GHz), and therefore the value of C_2 is given by (5.26).

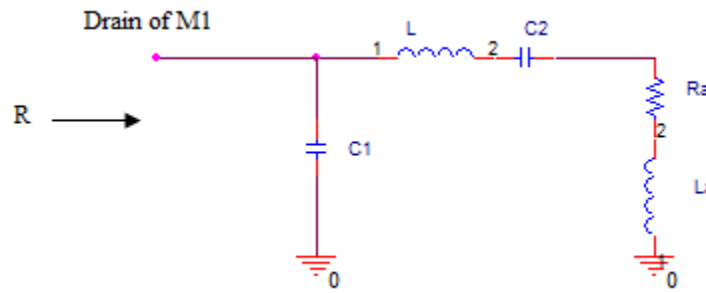


Fig. 5.11. Position of R .

$$C_2 = \frac{1}{\omega_o^2 L_a} \approx 0.1875 \text{ pF} \quad (5.26)$$

Since C_2 negates the effect of L_a , Figure 5.11 simplifies to Figure 5.12 at resonance.

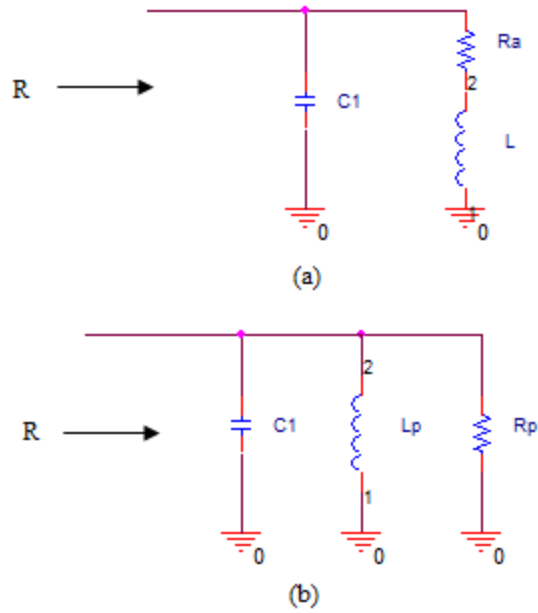


Fig. 5.12. (a) The simplified circuit, (b) The same circuit with the transformation of the RL series connection to an RL parallel connection.

From Figure 5.12(b) the equivalent parallel components R_p and L_p are given by the following equations (Appendix F).

$$R_p = \frac{R_a^2 + (\omega_o L)^2}{R_a} \quad (5.27)$$

$$\omega_o L_p = \frac{R_a^2 + (\omega_o L)^2}{\omega_o L} \quad (5.28)$$

From Figure 5.12(b) it is clear that C_1 must be set to cancel the reactance of (5.28) and R_p must be set equal to $R=52 \text{ k}\Omega$. From (5.27) $L=222 \text{ nH}$ and then from (5.28) $C_1=0.0351 \text{ pF}$.

5.2.3.2 PSPICE Simulation

The PA was designed and simulated in PSPICE using the AMI 0.5 μm technology. The voltage supply used was 3V and the BFL was set to 100 μH which will insure that it acts as an open circuit at resonance (i.e. $52 \text{ k}\Omega \ll \omega_o L_{BFL} = 1.16 \text{ M}\Omega \rightarrow L_{BFL} = 100 \mu\text{H}$). The transistor sizing for M1 is (1000 $\mu\text{m}/0.5\mu\text{m}$). By applying a sinusoidal RF source at the input (V_{drive}) with a frequency of 1.8 GHz the drain voltage and current of M1 are plotted and shown in Figure 5.13 and Figure 5.14.

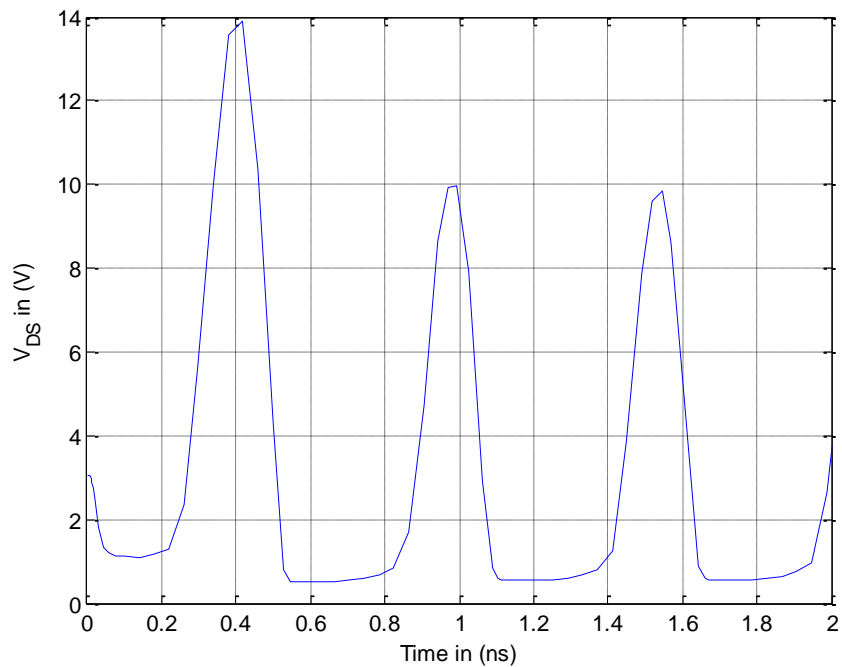


Fig. 5.13. V_{DS} time response of the PA.

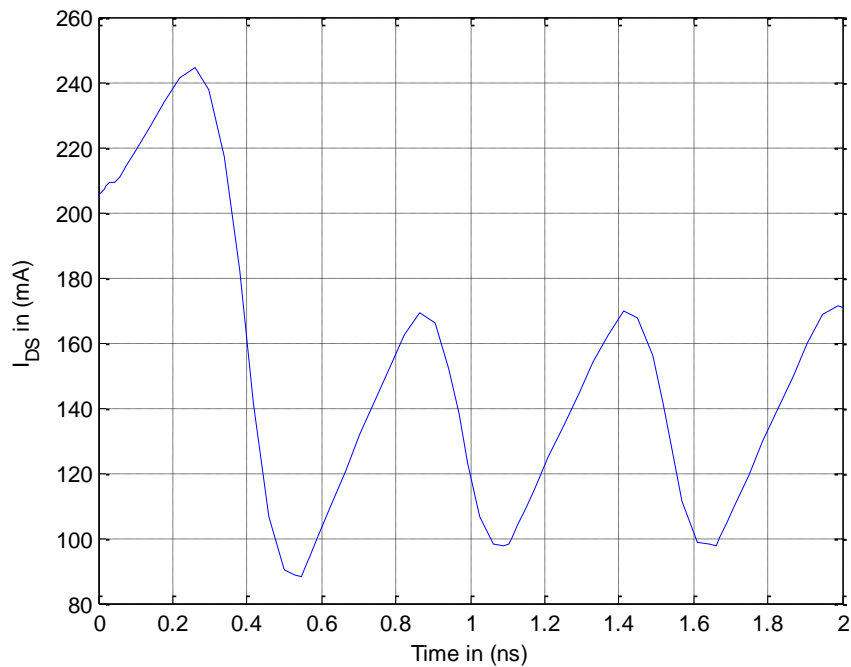


Fig. 5.14. I_{DS} time response of the PA.

Figure 5.15 shows how the normalized time response of the PA's drain voltage and current propagate with respect to each other. It can be seen from Figure 5.15 how the voltage and current responses are vital in determining the efficiency of the PA. As said before that M1 acts as a switch and it is clear from the figure that the maximum current and voltage values never coincide. Actually when considering each cycle, it can be seen that for the most part of the cycle the power dissipation is minimized since the current and voltage are almost out of phase and therefore their product ($P_{consumed} = V_{DS}I_{DS}$) which is the power consumed by M1 is kept to a minimum. The power consumption of the M1 was 22.7 pW and the power transfer efficiency was 90.9%.

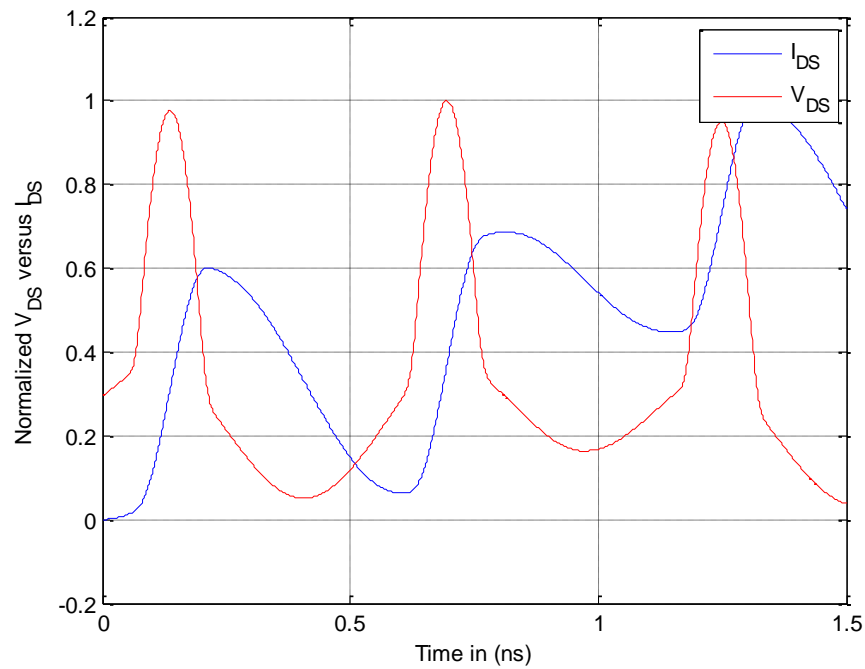


Fig. 5.15. The normalized drain voltage and current time responses.

5.2.4 RF Amplitude Amplifiers

The RF amplifiers are necessary to adjust the amplitude of the RF signal being transmitted according to the neural network. The RF amplifier and the phase shifter (Subsection 5.2.1) are used together as a weight adjuster for the RF signal to impose the desired amplitude and phase change necessary for beamforming. The amplifier used here is a tuned amplifier given in Figure 5.16. The tuned amplifier consists of a common source NMOS transistor M1 with its drain connected to the source of a common gate NMOS transistor M2. M1 provides the voltage gain while M2 enhances the frequency response of the amplifier by reducing the Miller Effect present in M1.

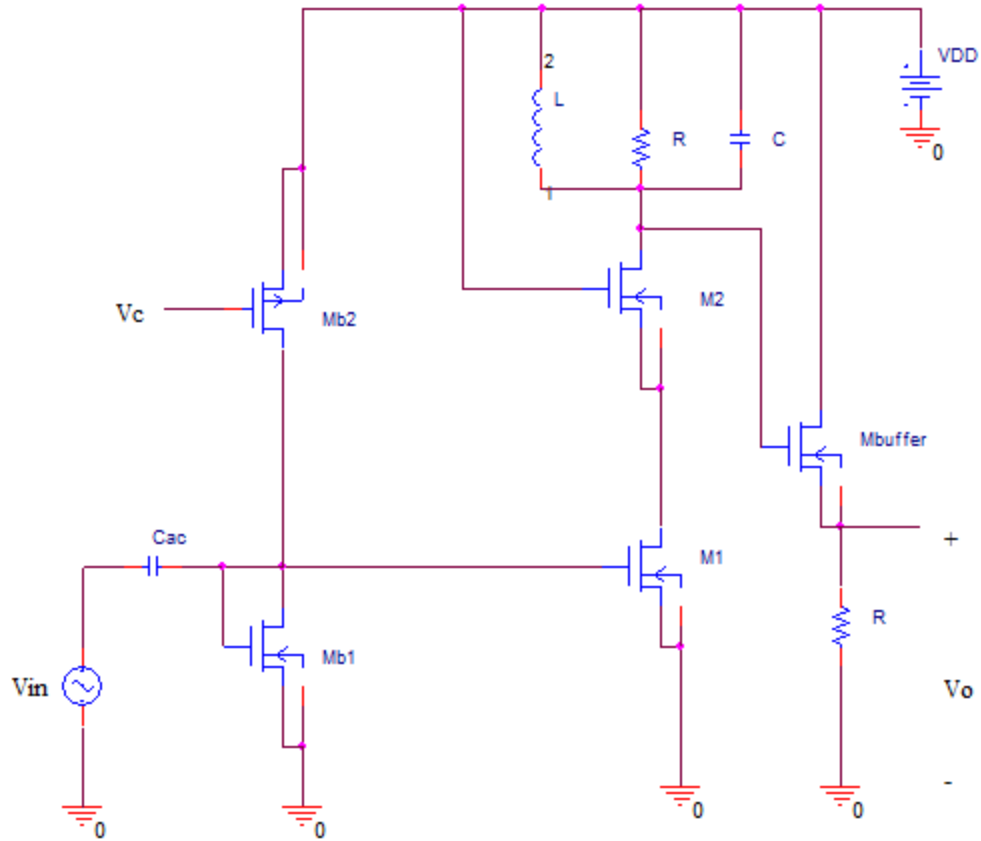


Fig. 5.16. Tuned RF amplifier.

The output of the amplifier is taken from the drain of M2 (D2) where it is also connected to an RLC resonator circuit. The RLC resonator is used to tune the output of the amplifier at the desired frequency (1.8 GHz). The tuning is done by the proper selection of inductance (L) and the capacitance (C). The frequency of is given by the following equation.

$$\omega_o = \frac{1}{\sqrt{LC}} \quad (5.29)$$

By setting the value of $L=5 \text{ nH}$, the capacitance $C=1.56 \text{ pF}$. According to RLC circuit theory the bandwidth (BW) of the resonator circuit is given by (5.30).

$$BW = \frac{1}{RC} \quad (5.30)$$

The value of R was selected to maintain a narrow bandwidth of about 100 MHz and this means that $R=6.41 \text{ k}\Omega$. The transistors M_{b1} and M_{b2} are simply two diode connected MOS transistors that are used to bias the gate of M_1 .

M_{Buffer} is a common drain transistor used to provide a high input resistance to the output of M_1 and a low output resistance to provide a proper loading condition for the input of the phase shifter. Recall that the input of the phase shifter (Fig. 5.4) is at the source of a transistor which means that the input resistance is in the order of $1/g_m$. To adapt to this very low input impedance M_{Buffer} is used. The output resistance of M_{Buffer} is around $1/g_{m\text{buffer}}$ and therefore by setting $g_{m\text{buffer}} \gg g_{m\text{phaseshifter}}$ then we will have proper loading condition. For example, if $g_{m\text{buffer}}=10g_{m\text{phaseshifter}}$ then 90% of the output voltage of the tuned amplifier will be dropped across the input of the phase shifter.

Gain control is accomplished by simply changing the control voltage (V_c) which is simply the gate voltage of M_{b2} . By considering the small signal analysis of the circuit at resonance, the gain of the amplifier is given by (5.31) (Appendix E).

$$A_v = \frac{-g_{m1}r_{o1}R(1+g_{m2}r_{o2})}{R+r_{o2}+r_{o1}(1+g_{m2}r_{o2})} \approx -g_{m1}R \quad (5.31)$$

Where g_{mi} is the transconductance of transistor i , r_{oi} is the Early resistance of transistor i and A_v is the gain.

The tuned amplifier was designed and simulated in PSPICE using the AMI 0.5 μm CMOS technology with a voltage supply of 3V. M1 and M2 had transistor dimensions of (1000 $\mu\text{m}/0.5\mu\text{m}$) while M_{b1} and M_{b2} had dimensions of (1 $\mu\text{m}/10\mu\text{m}$) and (1 $\mu\text{m}/5\mu\text{m}$) respectively. Figure 5.17 shows how gain control is achieved by varying the control voltage from 1.4 V to 2.3 V. It is also clear how the amplifier tunes the maximum voltage gain at 1.8 GHz for all values. The maximum power consumption of the amplifier is 75.5 mW with a gain of 43.8 dB.

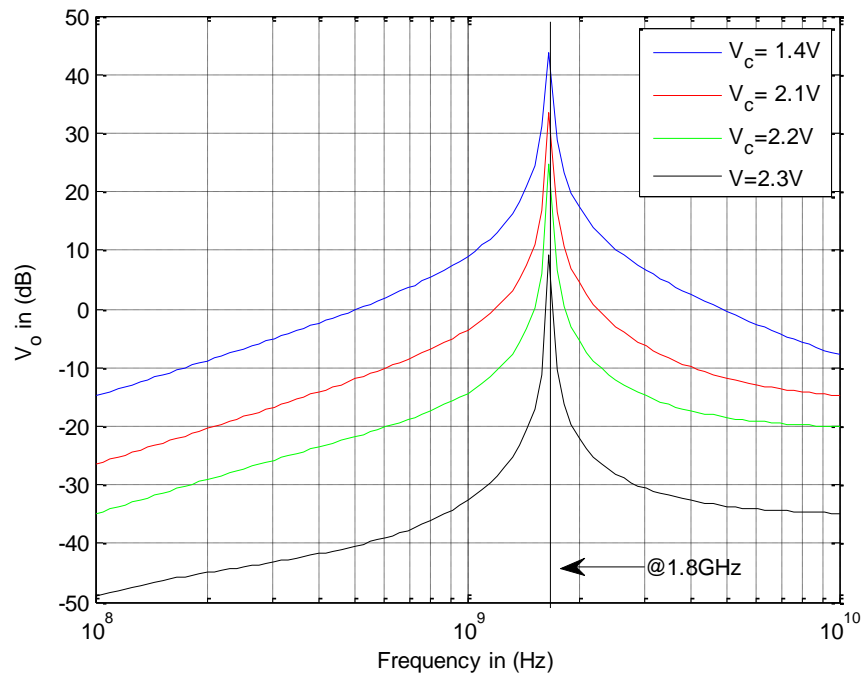


Fig. 5.17. Frequency response of the output voltage for several values of V_c .

5.3 RF Receiver Circuit Components

5.3.1 Low Noise Amplifier (LNA)

The LNA is the electronic circuit that receives the RF signal from the antenna element. The function of the LNA is to amplify the received signal without adding electronic noise to the signal. From the literature [31] the amplitude of the received potentials from the brain are in the μV -range. Here it is assumed that the LNA will receive an RF signal with a voltage amplitude of $10\ \mu\text{V}$. A typical LNA circuit is shown in Fig. 5.18.

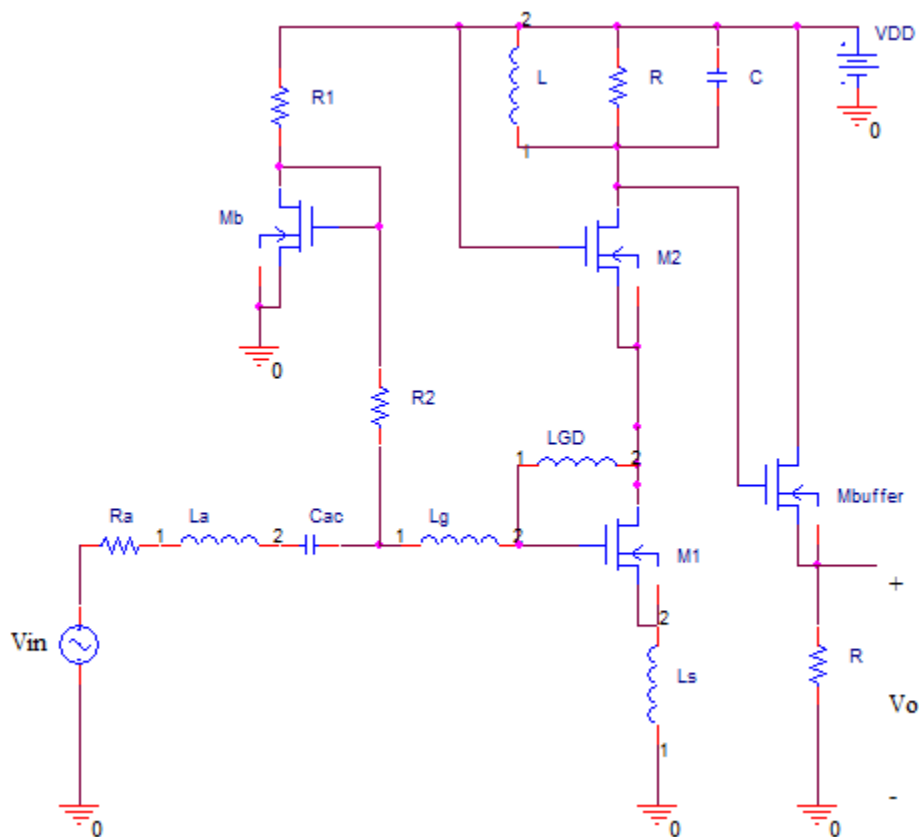


Fig. 5.18. LNA circuit.

The circuit consists of the RF input signal that is modeled as a sinusoidal voltage source V_{RF} and source impedance (Z_a) which consists of a resistance $R_a=122 \Omega$ and an inductive reactance with $L_a=41.7 nH$. The amplitude of the voltage source is taken to be $10 \mu V$ at a frequency of $500 kHz$. C_{ac} is a DC blocking capacitor that will insure correct biasing of the NMOS transistor M1 by using the biasing circuit that consists of M_b , R_1 and R_2 . The inductances L_g and L_s connected to M1 are used to provide impedance matching between the antenna element and the LNA. The inductance L_{gd} is placed to cancel the effect of C_{gdl} (gate-to-drain capacitance). Looking at the small signal model of M1 (Figure 5.19) the expressions for L_g and L_s can be derived. By applying simple KVL around the left loop one can come up with the following equation.

$$V_{in} = I_{in} \left(j\omega L_g + \frac{1}{j\omega C_{gs}} \right) + V_{s1} \quad (5.32)$$

Where C_{gs} is the gate-to-source capacitance of M1. The voltage V_{s1} can be expressed as:

$$V_{s1} = j\omega L_s \left(1 + \frac{g_{m1}}{j\omega C_{gs}} \right) I_{in} \quad (5.33)$$

Where g_{m1} is the transconductance of M1. By using (5.32) and (5.33), the input impedance of M1 can be written as:

$$Z_{in} = \frac{V_{in}}{I_{in}} = \frac{g_{m1} L_s}{C_{gs}} + j \left[\omega (L_g + L_s) - \frac{1}{\omega C_{gs}} \right] \quad (5.34)$$

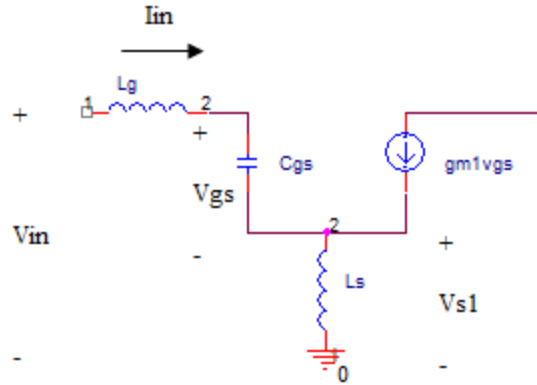


Fig. 5.19. Small signal model of M1.

For impedance matching, Z_{in} must be set equal to the complex conjugate of Z_a . This means that the following equations must hold.

$$R_a = \frac{g_{m1}L_s}{C_{gs}} \rightarrow L_s = \frac{R_a C_{gs}}{g_{m1}} \quad (5.35)$$

$$\left[\omega(L_g + L_s) - \frac{1}{\omega C_{gs}} \right] = -\omega L_a \rightarrow L_g = \frac{1}{\omega^2 C_{gs}} - L_s - L_a \quad (5.36)$$

The transistor M2 is cascoded on M1 to improve the high frequency performance of the LNA by reducing the Miller Effect. The RLC resonator circuit plays the same function as explained in Subsection 5.2.4. The output of the LNA is taken from the drain of M2. The output signal of the LNA is amplified with a voltage gain of A_v given by (5.31) (since the analysis is similar to that for the tuned amplifier at resonance).

The biasing circuitry in Fig. 5.18 is used to supply a DC voltage at the gate of M1 of around 1 V. The equation that governs the biasing circuit is given in (5.37).

$$V_{G1} = V_{DD} - \left(\frac{R_1 + R_2}{2} \right) \mu_n C_{ox} \left(\frac{W}{L} \right)_b (V_{GSb} - V_{tb})^2 \quad (5.37)$$

Where V_{G1} is the DC gate voltage for M1, R_1 and R_2 are the resistances shown in Fig. 5.18, μ_n is the electron mobility, C_{ox} is the oxide capacitance per unit area, $(W/L)_b$ is the transistor dimensions for M_b , V_{GSb} is the DC gate-to-source voltage and V_{tb} is the threshold voltage for M_b .

It is required that the amplitude of the output signal of the LNA is around 0.5mV-1mV since the next stage after the LNA would be the tuned RF amplifier (for reception) and it can handle any additional gain. This means that the gain required is 50-100 V/V and therefore from (5.31) the product $g_{m1}R$ can be set as desired. Following the same argument as in the RF tuned amplifier, the component values of the RLC circuit are given as: $L=10nH$, $C=10.1\mu F$ and $R=4k\Omega$. The value of the transconductance is calculated by using equation (5.38).

$$g_{m1} = \mu_n C_{ox} \left(\frac{W}{L} \right)_1 (V_{GS1} - V_{t1}) = \sqrt{2\mu_n C_{ox} \left(\frac{W}{L} \right)_1 I_{DS1}} \quad (5.38)$$

Where μ_n is the electron mobility, C_{ox} is the capacitance per unit area of the oxide layer, V_{GS1} is the DC gate-to-source voltage of M1, V_{t1} is the threshold voltage of M1 and I_{DS1} is the DC current of M1. To calculate the value of C_{gs} equation (5.39) is used.

$$C_{gs} = \frac{2}{3} C_{ox} W_1 L_1 = 13.3pF \quad (5.39)$$

From this the value of $L_s=16.2nH$ (using (5.35)) and from (5.36) $L_g=7.6mH$ (very large inductance). A remark that must be made is that the inductance L_{GD} was set to be $5/(\omega_o^2 C_{gs})$, thus $L_{GD}=38.1mH$.

M_{Buffer} is a common drain transistor used to provide a high input resistance to the output of M1 and a low output resistance to provide a proper loading condition for the input of the phase shifter. The same argument as the one used for the transmitter case is used here.

The LNA is simulated using PSPICE using the same CMOS technology as before. The transistor sizing is given as follows: M1 & M2 ($4000\mu\text{m}/2\mu\text{m}$); and M_b ($200\mu\text{m}/1\mu\text{m}$). The values for the bias resistance are as follows: $R_1=5k\Omega$ and $R_2=10k\Omega$. The frequency response of the LNA is plotted and shown in Fig. 5.20. It can be seen from the figure that the LNA achieves a gain of 34.1 dB ($\approx 50\text{V/V}$) at 500 kHz with a power consumption of 182 mW. This means that for the 42 antenna elements, the total power dissipated by the LNAs is 7.64 W.

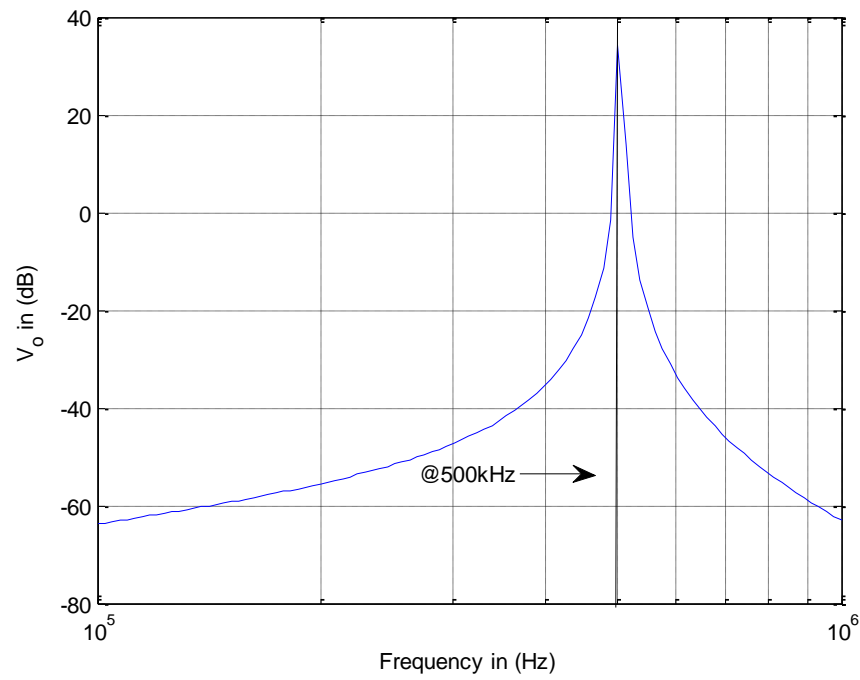


Fig. 5.20. Frequency response of LNA.

5.3.2 RF Adder

The RF adder shown in Figure 5.21 is capable of adding 5 different RF signals. After that, to successfully add all of the 42 signals the individual RF adders will be constructed as shown in Figure 5.22.

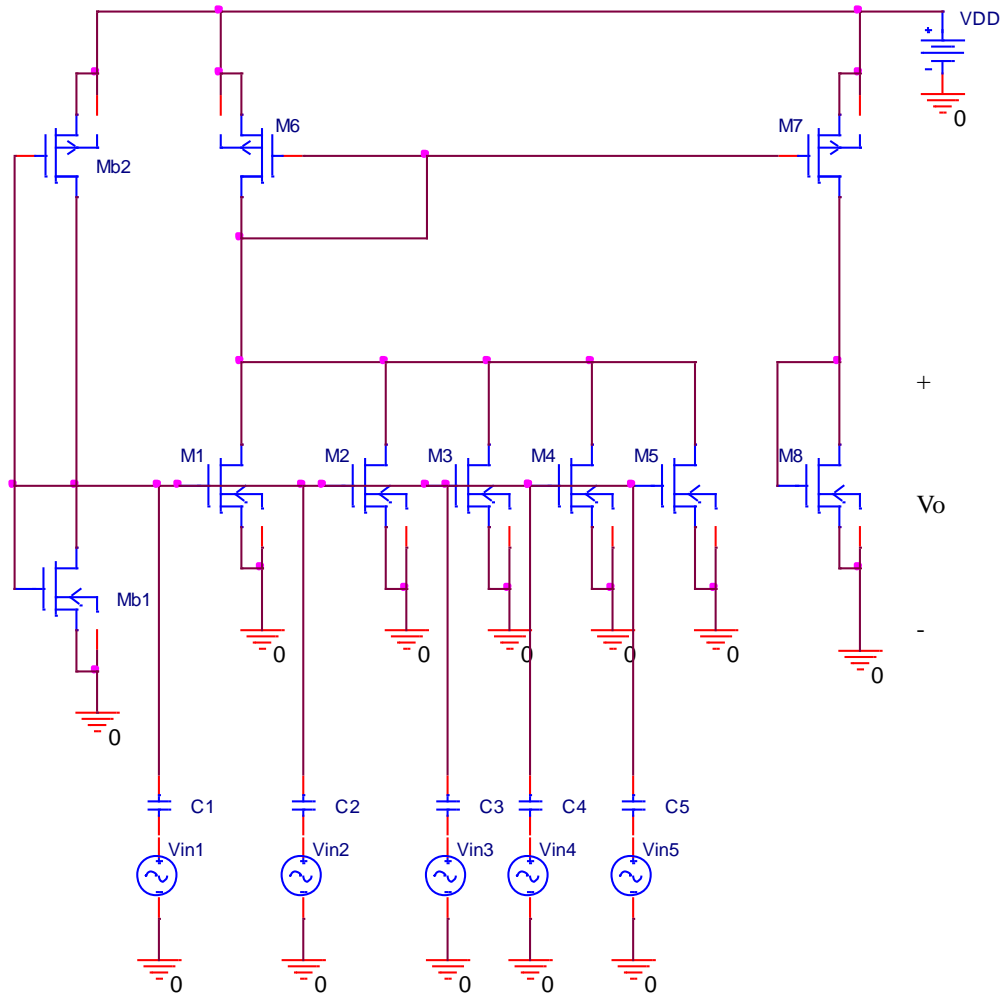


Fig. 5.22. RF adder capable of adding 5 RF signals.

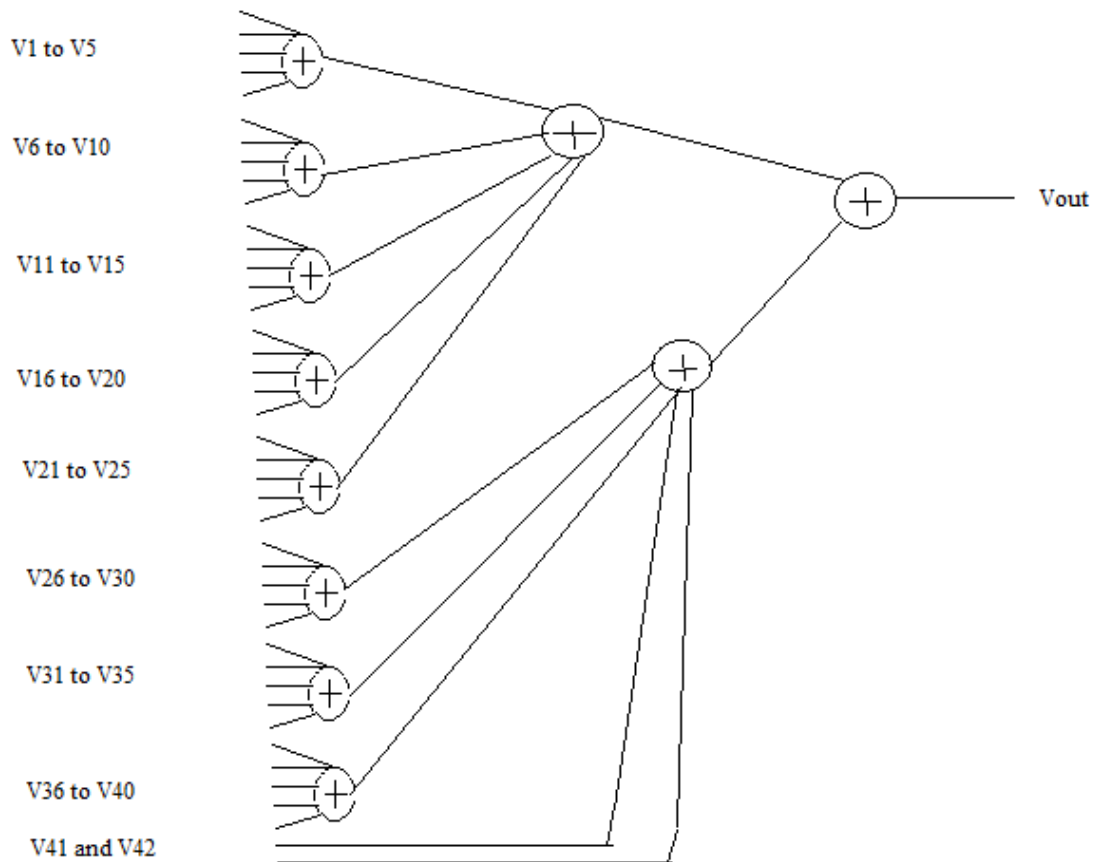


Fig. 5.23. Adder structure to combine all 42 signals.

It is clear from Figure 5.23, there are 10 adders that combine 5 signals simultaneously and one final adder that only adds two signals.

From Figure 5.22 the transistors M_{b1} and M_{b2} provide the necessary bias for the gates of transistors M1-M5. Transistors M1-M5 translate the small signal input voltages v_{in1} to v_{in5} to their corresponding small signal currents according to equation (5.40).

$$i_{mj} = g_{mj} v_{inj} \quad (5.40)$$

Where i_{mj} is the small signal current of the transistor Mj. The 5 currents are added and mirrored to the output stage by using the PMOS current mirror (M6 and M7). The output current i_{out} (5.41) is fed to an NMOS diode connected transistor (M8). The output voltage is given by (5.42).

$$i_{out} = g_{m1}v_{in1} + g_{m2}v_{in2} + g_{m3}v_{in3} + g_{m4}v_{in4} + g_{m5}v_{in5} \quad (5.41)$$

$$v_{out} = \frac{1}{g_{m8}}(g_{m1}v_{in1} + g_{m2}v_{in2} + g_{m3}v_{in3} + g_{m4}v_{in4} + g_{m5}v_{in5}) \quad (5.42)$$

By setting $g_{m1}=g_{m2}=g_{m3}=g_{m4}=g_{m5}=g_{m8}$ then the output voltage becomes:

$$v_{out} = v_{in1} + v_{in2} + v_{in3} + v_{in4} + v_{in5} \quad (5.43)$$

To satisfy the condition of the transconductances being equal, the (W/L) ratio of M8 must be set to be a fifth of that of M1-M5 because the DC current passing through M8 is 5 times larger than that of for M1-M5.

$$I_8 = 5I_{1,2,3,4,5} \quad (5.44)$$

$$\left(\frac{W}{L}\right)_8 I_8 = \left(\frac{W}{L}\right)_{1,2,3,4,5} I_{1,2,3,4,5} \rightarrow \left(\frac{W}{L}\right)_8 = \frac{1}{5} \left(\frac{W}{L}\right)_{1,2,3,4,5} \quad (5.45)$$

By using the AMI 0.5 μ m technology with a power supply voltage of 3V, the circuit of Figure 5.22 is simulated. The transistor sizing for M1-M7 is (5 μ m/0.5 μ m), M8 (1 μ m/0.5 μ m), M_{b1} (5 μ m/1 μ m) and M_{b2} (1 μ m/30 μ m). To test the RF combiner, 5 signals oscillating at 500 kHz with magnitudes 1 mV, 2 mV, 3 mV, 4 mV and 5 mV are applied to the gates of transistors M1-M5. The DC blocking capacitors used with

the signals all have a value of $1 \mu\text{F}$. The input and output signals are shown in Figure 5.24. It is clear from the figure that the RF adder works with a power dissipation of $417.7 \mu\text{W}$. This means that for the entire adder structure shown in Figure 5.23 the power consumption is $11 \times 417.7 \mu\text{W}$ which is 4.59 mW .

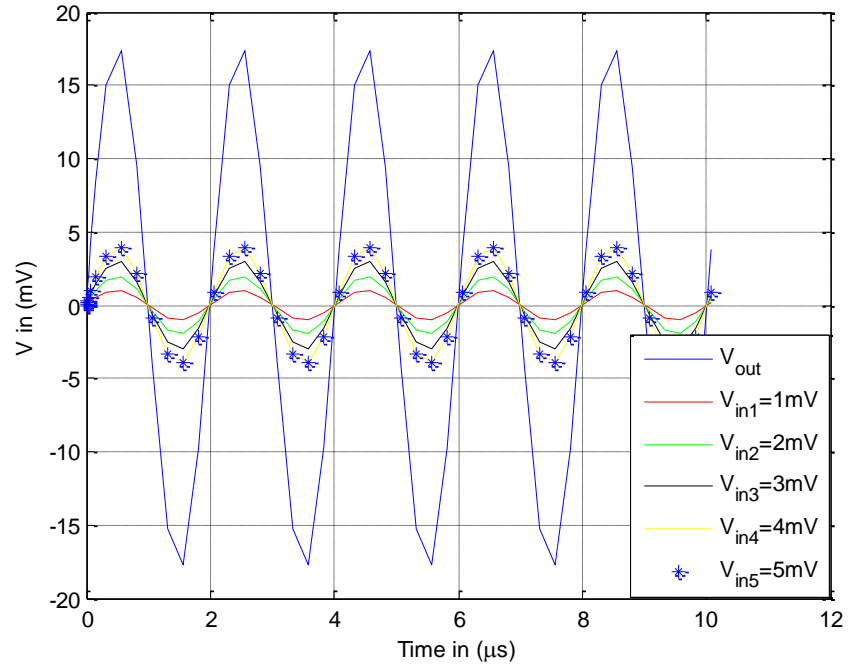


Fig. 5.24. Voltage time response, output versus input.

Chapter 6: Conclusion & Future Work

6.1 Conclusion

The advantages of using an antenna array is made possible in implantable microelectronic devices (IMD) applications where usually the point of observation of the transmitter is in close proximity to it such that neither the near field nor the far field approximations can be used. The antenna array problem is solved here as a boundary valued problem with the antenna elements introduced in the electromagnetic fields' boundary conditions.

A noninvasive technique, using a hemispherical antenna array, for focusing the magnetic field inside the human brain is developed for hyperthermia therapy and deep brain stimulation. The array might be a good alternative to alleviate the movement disorder symptoms of Parkinson's Disease. The human head is considered as a three layer hemisphere with each layer having its unique relative permittivity and permeability. The boundary valued problem is solved in spherical coordinates and the electromagnetic fields in all layers are derived and expressed in the most general form (i.e. no approximations made). A beamforming technique is developed that is capable of focusing the magnetic field anywhere inside the brain. The technique seeks to produce a delta-like magnetic field at the desired point which can replace having an electrode at that point. Since electromagnetic radiation is being generated, health issues must be addressed. In the thesis the electric field exposure is calculated and the

specific absorption rate (SAR), which is a safety measure, is calculated and kept within international standards.

To feed signals to the antenna array, an RF transmitter is designed and simulated in PSPICE using the AMI 0.5 μm CMOS technology with a 3V power supply used for all the transmitter components designed. For the transmitter the power amplifier, phase shifter and RF amplifier are designed. The power amplifier designed is a typical class E amplifier. The phase shifter used is custom designed and it uses the all-pass filter topology. The phase shifter and the RF amplifier are used to alter the magnitude and phase of the outgoing signal according to the beamforming scheme. The beamforming technique is accomplished through the use of a neural network.

Another application of the antenna array is its ability to be a receiver. Assuming that there is a brain wave generated within the brain, the equation for the induced currents on the antenna elements is derived and then a new beamforming technique is used to determine from where the brain wave signal was generated. The beamforming technique used is different from any other technique found in the literature. The technique used here is based on the orthogonality property of the TE and TM modes.

An antenna array receiver circuit is designed using the same CMOS technology as that for the transmitter. Component wise, the receiver consists of low noise amplifiers, phase shifters, RF amplifiers and an RF adder or combiner. The receiver is designed to receive signals at a frequency of 500 kHz. The phase shifter and the RF amplifier is the same to that used in the transmitter but tuned to 500 kHz of course. The RF adder is custom designed for this thesis.

The theory presented for the antenna theory can be used for other medical applications especially in IMDs. In IMD systems there is a reader and the tag and usually they both use inductive coils to send and receive data through a loosely coupled inductive link. The reader can be constructed as an antenna array to focus the transmitted power in the direction where optimal power transfer efficiency would be made possible. In this way misalignment issues that occur between the tag and the reader can be reduced.

6.2 Future Work

The antenna element structure used is very primitive and simple and was used only to demonstrate the new approach of the antenna theory. Other antenna geometries should be investigated and compared to find which shape and orientation best fits the application.

As seen in Chapter 3, there are reflection issues when considering the propagation of the electromagnetic fields through the layers of the head. A proper beamforming technique should be designed for the transmitter to allow it to beamform the magnetic field in the delta-like shape discussed in the thesis, but also be put under an additional constraint that will minimize the reflections that occur at the layer interfaces. The appropriate minimization function probably would be developed using Lagrangian multipliers and then the optimal current values calculated.

In Chapter 4 the neural network used is simulated through MATLAB. The actual circuit should be fabricated and tested to see if it matches the simulation. Since the

neural network is quite large (neuron wise) circuit implementation of the neurons should be done in the subthreshold region to reduce power consumption.

In Chapter 5 the entire RF transmitter/receiver components were simulated assuming that the electronics work in the saturation region. Future work will be focused on making the entire circuit in the subthreshold region to cut down on power consumption. Finally, the entire antenna array circuit should be fabricated and tested to extend the boundary from just the theoretical/simulation stage to the practical operating stage.

Appendix A

When applying the six boundary conditions for the three different interfaces mentioned in Chapter 3, the method or technique in which the coefficients were extracted was not explained thoroughly. That method was the orthogonality principle that was present because of the spherical harmonics. Considering equations (3.17) and (3.18) again the following two equations are written (which are just replicas of the prior).

$$\begin{aligned}
 & -\sum_{l=1}^{\infty} \sum_{m=-l}^l \{B_{lm}H_l^{(1)}(k_1c) + C_{lm}H_l^{(2)}(k_1c)\} \bar{r} \times \nabla Y_{lm}(\theta, \varphi) + \\
 & \frac{1}{j\omega\epsilon_1} \sum_{l=1}^{\infty} \sum_{m=-l}^l \nabla \times \left[\frac{1}{r} \{b_{lm}H_l^{(1)}(k_1r) + c_{lm}H_l^{(2)}(k_1r)\} \bar{r} \times \nabla Y_{lm}(\theta, \varphi) \right] \Big|_{r=c} \\
 & = -\sum_{l=1}^{\infty} \sum_{m=-l}^l A_{lm}H_l^{(2)}(k_0c) \bar{r} \times \nabla Y_{lm}(\theta, \varphi) + \\
 & \frac{1}{j\omega\epsilon_0} \sum_{l=1}^{\infty} \sum_{m=-l}^l \nabla \times \left[\frac{1}{r} a_{lm}H_l^{(2)}(k_0r) \bar{r} \times \nabla Y_{lm}(\theta, \varphi) \right] \Big|_{r=c}
 \end{aligned} \tag{A.1}$$

$$\begin{aligned}
 & \int_0^{2\pi} d\varphi \int_0^{\pi} \sin\theta d\theta [\bar{r} \times \nabla Y_{lm}^*(\theta, \varphi)] \cdot [\bar{r} \times \nabla Y_{lm}(\theta, \varphi)] = l(l+1)\delta_{ll}\delta_{mm} \\
 & [\bar{r} \times \nabla Y_{lm}^*(\theta, \varphi)] \cdot \nabla \times [g_l(kr)\bar{r} \times \nabla Y_{lm}(\theta, \varphi)] = 0
 \end{aligned} \tag{A.2}$$

$$\text{where; } \delta_{ij} = \begin{cases} 1; i = j \\ 0; i \neq j \end{cases}$$

The way to get the coefficients is accomplished by applying the concept of (A.2) in (A.1). First a dot product between the term $\bar{r} \times \nabla Y_{lm}^*(\theta, \varphi)$ and (A.1) is taken as shown in (A.3).

$$\begin{aligned}
& -\sum_{l=1}^{\infty} \sum_{m=-l}^l \{B_{lm}H_l^{(1)}(k_1c) + C_{lm}H_l^{(2)}(k_1c)\} \bar{r} \times \nabla Y_{lm}(\theta, \varphi) \cdot [\bar{r} \times \nabla Y_{l'm}^*(\theta, \varphi)] + \\
& \frac{1}{j\omega\epsilon_1} \sum_{l=1}^{\infty} \sum_{m=-l}^l \nabla \times \left[\frac{1}{r} \{b_{lm}H_l^{(1)}(k_1r) + c_{lm}H_l^{(2)}(k_1r)\} \bar{r} \times \nabla Y_{lm}(\theta, \varphi) \right] \Big|_{r=c} \cdot [\bar{r} \times \nabla Y_{l'm}^*(\theta, \varphi)] \\
& = -\sum_{l=1}^{\infty} \sum_{m=-l}^l A_{lm}H_l^{(2)}(k_0c) \bar{r} \times \nabla Y_{lm}(\theta, \varphi) \cdot [\bar{r} \times \nabla Y_{l'm}^*(\theta, \varphi)] + \\
& \frac{1}{j\omega\epsilon_0} \sum_{l=1}^{\infty} \sum_{m=-l}^l \nabla \times \left[\frac{1}{r} a_{lm}H_l^{(2)}(k_0r) \bar{r} \times \nabla Y_{lm}(\theta, \varphi) \right] \Big|_{r=c} \cdot [\bar{r} \times \nabla Y_{l'm}^*(\theta, \varphi)]
\end{aligned} \tag{A.3}$$

A direct result can be obtained from (A.3) by considering (A.2) and that is that the dot product of the orthogonal terms cancel out by nature, thus reducing (A.3) to (A.4).

$$\begin{aligned}
& -\sum_{l=1}^{\infty} \sum_{m=-l}^l \{B_{lm}H_l^{(1)}(k_1c) + C_{lm}H_l^{(2)}(k_1c)\} \bar{r} \times \nabla Y_{lm}(\theta, \varphi) \cdot [\bar{r} \times \nabla Y_{l'm}^*(\theta, \varphi)] + \\
& = -\sum_{l=1}^{\infty} \sum_{m=-l}^l A_{lm}H_l^{(2)}(k_0c) \bar{r} \times \nabla Y_{lm}(\theta, \varphi) \cdot [\bar{r} \times \nabla Y_{l'm}^*(\theta, \varphi)]
\end{aligned} \tag{A.4}$$

Now by taking a surface integral of both sides of (A.4), (A.5) can be written.

$$\begin{aligned}
& \int_0^{2\pi} d\varphi \int_0^{\pi} \sin\theta d\theta \left\{ \sum_{l=1}^{\infty} \sum_{m=-l}^l \{B_{lm}H_l^{(1)}(k_1c) + C_{lm}H_l^{(2)}(k_1c)\} \bar{r} \times \nabla Y_{lm}(\theta, \varphi) \cdot [\bar{r} \times \nabla Y_{l'm}^*(\theta, \varphi)] \right\} \\
& = \int_0^{2\pi} d\varphi \int_0^{\pi} \sin\theta d\theta \left\{ \sum_{l=1}^{\infty} \sum_{m=-l}^l A_{lm}H_l^{(2)}(k_0c) \bar{r} \times \nabla Y_{lm}(\theta, \varphi) \cdot [\bar{r} \times \nabla Y_{l'm}^*(\theta, \varphi)] \right\}
\end{aligned} \tag{A.5}$$

By using (A.2), (A.5) reduces to (A.6) for $l=l'$ and $m=m'$.

$$l(l+1)\{B_{lm}H_l^{(1)}(k_1c) + C_{lm}H_l^{(2)}(k_1c)\} = l(l+1)A_{lm}H_l^{(2)}(k_0c) \tag{A.6}$$

By cancelling the term $l(l+1)$ on both sides of (A.6), (A.6) becomes (A.7) which is the result shown in (3.19).

$$B_{lm}H_l^{(1)}(k_1c) + C_{lm}H_l^{(2)}(k_1c) = A_{lm}H_l^{(2)}(k_0c) \quad (\text{A.7})$$

To get the other set of coefficients from (A.1), the curl of both sides of (A.1) is taken first.

$$\begin{aligned} & -\sum_{l=1}^{\infty} \sum_{m=-l}^l \nabla \times \{B_{lm}H_l^{(1)}(k_1c) + C_{lm}H_l^{(2)}(k_1c)\} \bar{r} \times \nabla Y_{lm}(\theta, \varphi) + \\ & \frac{1}{j\omega\epsilon_1} \sum_{l=1}^{\infty} \sum_{m=-l}^l \nabla \times \nabla \times \left[\frac{1}{r} \{b_{lm}H_l^{(1)}(k_1r) + c_{lm}H_l^{(2)}(k_1r)\} \bar{r} \times \nabla Y_{lm}(\theta, \varphi) \right] \Big|_{r=c} \\ & = -\sum_{l=1}^{\infty} \sum_{m=-l}^l \nabla \times A_{lm}H_l^{(2)}(k_0c) \bar{r} \times \nabla Y_{lm}(\theta, \varphi) + \\ & \frac{1}{j\omega\epsilon_0} \sum_{l=1}^{\infty} \sum_{m=-l}^l \nabla \times \nabla \times \left[\frac{1}{r} a_{lm}H_l^{(2)}(k_0r) \bar{r} \times \nabla Y_{lm}(\theta, \varphi) \right] \Big|_{r=c} \end{aligned} \quad (\text{A.8})$$

By using the identity used in (3.21) which is expressed as (A.9), equation (A.8) can be transformed into (A.10).

$$\nabla \times \left\{ \nabla \times [g_l(kr) \hat{r} \times \nabla Y_{lm}(\theta, \varphi)] \Big|_{r=c} \right\} \Big|_{r=c} = -\frac{1}{c^2 k} [G_l'(kc) \bar{r} \times \nabla Y_{lm}(\theta, \varphi)] \quad (\text{A.9})$$

$$\begin{aligned} & -\sum_{l=1}^{\infty} \sum_{m=-l}^l \nabla \times \{B_{lm}H_l^{(1)}(k_1c) + C_{lm}H_l^{(2)}(k_1c)\} \bar{r} \times \nabla Y_{lm}(\theta, \varphi) + \\ & \frac{-1}{j\omega\epsilon_1 c^2 k_1} \sum_{l=1}^{\infty} \sum_{m=-l}^l \{b_{lm}H_l^{(1)}(k_1c) + c_{lm}H_l^{(2)}(k_1c)\} \bar{r} \times \nabla Y_{lm}(\theta, \varphi) \\ & = -\sum_{l=1}^{\infty} \sum_{m=-l}^l \nabla \times A_{lm}H_l^{(2)}(k_0c) \bar{r} \times \nabla Y_{lm}(\theta, \varphi) + \\ & \frac{-1}{j\omega\epsilon_0 c^2 k_0} \sum_{l=1}^{\infty} \sum_{m=-l}^l a_{lm}H_l^{(2)}(k_0c) \bar{r} \times \nabla Y_{lm}(\theta, \varphi) \end{aligned} \quad (\text{A.10})$$

It is clear that the purpose of taking the curl was to transform (A.1) to a form where the orthogonality principle can be applied to the TM set of coefficients. As before,

taking the dot product of the term $\bar{r} \times \nabla Y_{lm}^*(\theta, \varphi)$ with (A.10), (A.11) can be obtained with similar reasoning of simplification.

$$\begin{aligned} & \frac{1}{\varepsilon_1} \sum_{l=1}^{\infty} \sum_{m=-l}^l \{b_{lm} H_l^{(1)}(k_1 c) + c_{lm} H_l^{(2)}(k_1 c)\} \bar{r} \times \nabla Y_{lm}(\theta, \varphi) \cdot \left[\bar{r} \times \nabla Y_{lm}^*(\theta, \varphi) \right] \\ & = \frac{1}{\varepsilon_0} \sum_{l=1}^{\infty} \sum_{m=-l}^l a_{lm} H_l^{(2)}(k_0 c) \bar{r} \times \nabla Y_{lm}(\theta, \varphi) \cdot \left[\bar{r} \times \nabla Y_{lm}^*(\theta, \varphi) \right] \end{aligned} \quad (\text{A.11})$$

As done earlier, the surface integral can be taken for both sides of (A.11) and for the case where $l=l'$ and $m=m'$ the following can be written.

$$\frac{l(l+1)}{\varepsilon_1} \{b_{lm} H_l^{(1)}(k_1 c) + c_{lm} H_l^{(2)}(k_1 c)\} = \frac{l(l+1)}{\varepsilon_0} a_{lm} H_l^{(2)}(k_0 c) \quad (\text{A.12})$$

By simple cancellation and rearrangement of (A.12), (A.13) can be written which is the result of equation (3.22).

$$\frac{\varepsilon_1}{\varepsilon_0} a_{lm} H_l^{(2)}(k_0 c) = b_{lm} H_l^{(1)}(k_1 c) + c_{lm} H_l^{(2)}(k_1 c) \quad (\text{A.13})$$

The same technique was applied to get all of the coefficients for the remaining boundary conditions.

Appendix B

The boundary condition for the magnetic field at $r=c$ is a special case, since it is here where the effect of the antenna element's current density is introduced. As before to find the expressions for the coefficients involved the use of the orthogonality principle given in (A.2) is needed. In this special case the effect of this principle was imposed on the current density and two forms of this current density were derived. These were J_{TM} and J_{TE} given by equations (3.32) and (3.34) respectively. Here it will be shown how the equations are obtained by actually carrying out the integration of (3.32) and (3.34) as shown below.

$$J_{TM} = \int_{\theta} \int_{\varphi} [\bar{r} \times \nabla Y_{lm}^*(\theta, \varphi)] \cdot \bar{J}_i(\theta, \varphi) \sin \theta d\theta d\varphi \quad (\text{B.1})$$

$$J_{TE} = \int_{\theta} \int_{\varphi} [\bar{r} \times \nabla Y_{lm}^*(\theta, \varphi)] \cdot [\nabla \times \bar{J}_i(\theta, \varphi)] \sin \theta d\theta d\varphi \quad (\text{B.2})$$

Where the current density is given by (3.6) and shown here as (B.3).

$$\begin{aligned} \bar{J}_i(\theta, \varphi) = & \frac{I_i}{cL} [\hat{\theta} \delta(\theta - \theta_i) \{ \delta(\varphi - \varphi_i + \frac{\Delta\varphi}{2}) - \delta(\varphi - \varphi_i - \frac{\Delta\varphi}{2}) \} \\ & + \hat{\varphi} \delta(\varphi - \varphi_i) \{ \delta(\theta - \theta_i - \frac{\Delta\theta}{2}) - \delta(\theta - \theta_i + \frac{\Delta\theta}{2}) \}] \end{aligned} \quad (\text{B.3})$$

Before carrying out the integration it is important to note that the following term given by (B.4).

$$\bar{r} \times \nabla Y_{lm}^*(\theta, \varphi) = \hat{\varphi} \frac{\partial Y_{lm}^*(\theta, \varphi)}{\partial \theta} - \hat{\theta} \frac{1}{\sin \theta} \frac{\partial Y_{lm}^*(\theta, \varphi)}{\partial \varphi} \quad (\text{B.4})$$

Considering (B.1), the following can be written.

$$\begin{aligned}
J_{TM} &= \frac{I_i}{cL} \int_{\theta} \int_{\varphi} \frac{\partial Y_{lm}^*(\theta, \varphi)}{\partial \theta} \sin \theta \delta(\varphi - \varphi_i) \left\{ \delta\left(\theta - \theta_i - \frac{\Delta\theta}{2}\right) - \delta\left(\theta - \theta_i + \frac{\Delta\theta}{2}\right) \right\} d\theta d\varphi \\
&\quad - \frac{I_i}{cL} \int_{\theta} \int_{\varphi} \frac{\partial Y_{lm}^*(\theta, \varphi)}{\partial \varphi} \delta(\theta - \theta_i) \left\{ \delta\left(\varphi - \varphi_i + \frac{\Delta\varphi}{2}\right) - \delta\left(\varphi - \varphi_i - \frac{\Delta\varphi}{2}\right) \right\} d\theta d\varphi
\end{aligned} \tag{B.5}$$

By using the well known delta function integration property, the integration in (B.5) can be easily carried out.

$$\begin{aligned}
J_{TM} &= \frac{I_i}{cL} \left[\frac{\partial Y_{lm}^*\left(\theta_i + \frac{\Delta\theta}{2}, \varphi_i\right)}{\partial \theta} \sin\left(\theta_i + \frac{\Delta\theta}{2}\right) - \frac{\partial Y_{lm}^*\left(\theta_i - \frac{\Delta\theta}{2}, \varphi_i\right)}{\partial \theta} \sin\left(\theta_i - \frac{\Delta\theta}{2}\right) \right. \\
&\quad \left. - \frac{\partial Y_{lm}^*\left(\theta_i, \varphi_i - \frac{\Delta\varphi}{2}\right)}{\partial \varphi} + \frac{\partial Y_{lm}^*\left(\theta_i, \varphi_i + \frac{\Delta\varphi}{2}\right)}{\partial \varphi} \right]
\end{aligned} \tag{B.6}$$

Equation (B.6) can be further simplified by considering the last two terms.

$$-\frac{\partial Y_{lm}^*\left(\theta_i, \varphi_i - \frac{\Delta\varphi}{2}\right)}{\partial \varphi} + \frac{\partial Y_{lm}^*\left(\theta_i, \varphi_i + \frac{\Delta\varphi}{2}\right)}{\partial \varphi} = jmY_{lm}^*\left(\theta_i, \varphi_i - \frac{\Delta\varphi}{2}\right) - jmY_{lm}^*\left(\theta_i, \varphi_i + \frac{\Delta\varphi}{2}\right) \tag{B.7}$$

And it follows:

$$jmY_{lm}^*\left(\theta_i, \varphi_i - \frac{\Delta\varphi}{2}\right) - jmY_{lm}^*\left(\theta_i, \varphi_i + \frac{\Delta\varphi}{2}\right) = jmY_{lm}^*\left(\theta_i, \varphi_i\right) \left\{ e^{jm\frac{\Delta\varphi}{2}} - e^{-jm\frac{\Delta\varphi}{2}} \right\} \tag{B.8}$$

Finally:

$$\begin{aligned}
jmY_{lm}^*(\theta_i, \varphi_i) \left\{ e^{jm\frac{\Delta\varphi}{2}} - e^{-jm\frac{\Delta\varphi}{2}} \right\} &= -2mY_{lm}^*(\theta_i, \varphi_i) \left\{ \frac{e^{jm\frac{\Delta\varphi}{2}} - e^{-jm\frac{\Delta\varphi}{2}}}{j2} \right\} \\
&= -2mY_{lm}^*(\theta_i, \varphi_i) \sin\left(m\frac{\Delta\varphi}{2}\right)
\end{aligned} \tag{B.9}$$

So therefore the expression for J_{TM} is given by (B.10) which is the result shown in (3.32).

$$\begin{aligned}
J_{TM} = \frac{I_i}{cL} &\left[\frac{\partial Y_{lm}^*\left(\theta_i + \frac{\Delta\theta}{2}, \varphi_i\right)}{\partial\theta} \sin\left(\theta_i + \frac{\Delta\theta}{2}\right) - \frac{\partial Y_{lm}^*\left(\theta_i - \frac{\Delta\theta}{2}, \varphi_i\right)}{\partial\theta} \sin\left(\theta_i - \frac{\Delta\theta}{2}\right) \right. \\
&\left. - 2mY_{lm}^*(\theta_i, \varphi_i) \sin\left(m\frac{\Delta\varphi}{2}\right) \right] \tag{B.10}
\end{aligned}$$

To get the TE component of the current density, first the curl of the current density is taken.

$$\begin{aligned}
\nabla \times \bar{J}_i(\theta, \varphi) &= \frac{I_i}{c^2L} [\hat{\varphi}\delta(\theta - \theta_i) \{ \delta(\varphi - \varphi_i + \frac{\Delta\varphi}{2}) - \delta(\varphi - \varphi_i - \frac{\Delta\varphi}{2}) \} \\
&\quad - \hat{\theta}\delta(\varphi - \varphi_i) \{ \delta(\theta - \theta_i - \frac{\Delta\theta}{2}) - \delta(\theta - \theta_i + \frac{\Delta\theta}{2}) \}] \tag{B.11}
\end{aligned}$$

Now the integration of (B.2) can be taken.

$$\begin{aligned}
J_{TE} = \frac{I_i}{c^2L} &\left[jm(Y_{lm}^*\left(\theta_i - \frac{\Delta\theta}{2}, \varphi_i\right) - Y_{lm}^*\left(\theta_i + \frac{\Delta\theta}{2}, \varphi_i\right)) + \right. \\
&\left. \sin\theta_i \left\{ \frac{\partial Y_{lm}^*\left(\theta_i, \varphi_i - \frac{\Delta\varphi}{2}\right)}{\partial\theta} - \frac{\partial Y_{lm}^*\left(\theta_i, \varphi_i + \frac{\Delta\varphi}{2}\right)}{\partial\theta} \right\} \right] \tag{B.12}
\end{aligned}$$

By simplifying the last two terms as follows:

$$\begin{aligned}
& \sin \theta_i \left\{ \frac{\partial Y_{lm}^* \left(\theta_i, \varphi_i - \frac{\Delta \varphi}{2} \right)}{\partial \theta} - \frac{\partial Y_{lm}^* \left(\theta_i, \varphi_i + \frac{\Delta \varphi}{2} \right)}{\partial \theta} \right\} = \sin \theta_i \frac{\partial Y_{lm}^* (\theta_i, \varphi_i)}{\partial \theta} \left\{ e^{jm \frac{\Delta \varphi}{2}} - e^{-jm \frac{\Delta \varphi}{2}} \right\} \\
& = j2 \sin \theta_i \frac{\partial Y_{lm}^* (\theta_i, \varphi_i)}{\partial \theta} \left\{ \frac{e^{jm \frac{\Delta \varphi}{2}} - e^{-jm \frac{\Delta \varphi}{2}}}{j2} \right\} = j2 \sin \theta_i \frac{\partial Y_{lm}^* (\theta_i, \varphi_i)}{\partial \theta} \sin \left(m \frac{\Delta \varphi}{2} \right)
\end{aligned} \tag{B.13}$$

So therefore the expression for J_{TE} is given by (B.14) which is the result shown in (3.34).

$$J_{TE} = \frac{I_i}{c^2 L} \left[jm(Y_{lm}^* \left(\theta_i - \frac{\Delta \theta}{2}, \varphi_i \right) - Y_{lm}^* \left(\theta_i + \frac{\Delta \theta}{2}, \varphi_i \right)) + j2 \sin \theta_i \frac{\partial Y_{lm}^* (\theta_i, \varphi_i)}{\partial \theta} \sin \left(m \frac{\Delta \varphi}{2} \right) \right] \tag{B.14}$$

Appendix C

The beamforming technique presented in Subsection 3.3.2 uses the orthogonality principle to construct the desired magnetic field in the brain. The technique begins with the interest in constructing a magnetic field that has a delta-like behavior like the one shown in the following equation.

$$\vec{H}_{Desired} = \delta(r - r_o)\delta(\theta - \theta_o)\delta(\varphi - \varphi_o)(\hat{\theta} + \hat{\varphi}) \quad (C.1)$$

The theory of the beamforming begins with the argument of equating (C.1) to (C.2).

$$\begin{aligned} \vec{H}_{Desired} = & -k_3 \sum_{l=1}^{\infty} \sum_{m=-l}^l \Lambda_{lm} j_l(k_3 r) \vec{r} \times \nabla Y_{lm}(\theta, \varphi) \\ & - j \sqrt{\frac{\epsilon_3}{\mu_0}} \sum_{l=1}^{\infty} \sum_{m=-l}^l \Xi_{lm} \nabla \times [j_l(k_3 r) \vec{r} \times \nabla Y_{lm}(\theta, \varphi)] \end{aligned} \quad (C.2)$$

The expressions for the coefficients Λ_{lm} and Ξ_{lm} are given in equations (3.61) and (3.62) respectively without showing the full derivation. Here the full derivation is given for clarification. By equating (C.1) and (C.2) the following can be written.

$$\begin{aligned} & -k_3 \sum_{l=1}^{\infty} \sum_{m=-l}^l \Lambda_{lm} j_l(k_3 r) \vec{r} \times \nabla Y_{lm}(\theta, \varphi) \\ & - j \sqrt{\frac{\epsilon_3}{\mu_0}} \sum_{l=1}^{\infty} \sum_{m=-l}^l \Xi_{lm} \nabla \times [j_l(k_3 r) \vec{r} \times \nabla Y_{lm}(\theta, \varphi)] = \\ & \delta(r - r_o)\delta(\theta - \theta_o)\delta(\varphi - \varphi_o)(\hat{\theta} + \hat{\varphi}) \end{aligned} \quad (C.3)$$

By taking the dot product of both sides of (C.3) with the term $r^2 j_l'(k_3 r) \vec{r} \times \nabla Y_{lm}^*(\theta, \varphi)$ (C.3) can be simplified to the following equation.

$$\begin{aligned}
& -k_3 \sum_{l=1}^{\infty} \sum_{m=-l}^l \Lambda_{lm} j_l(k_3 r) \bar{r} \times \nabla Y_{lm}(\theta, \varphi) \cdot r^2 j_{l'}(k_3 r) [\bar{r} \times \nabla Y_{l'm'}^*(\theta, \varphi)] = \\
& \left\{ \delta(r-r_o) \delta(\theta-\theta_o) \delta(\varphi-\varphi_o) (\hat{\theta} + \hat{\varphi}) \right\} \cdot r^2 j_{l'}(k_3 r) [\bar{r} \times \nabla Y_{l'm'}^*(\theta, \varphi)]
\end{aligned} \tag{C.4}$$

By taking the volume integral of both sides the following equation can be written for the case $l=l'$ and $m=m'$.

$$\begin{aligned}
& -\frac{\pi l(l+1)}{2k_3} \Lambda_{lm} = \\
& \int_r \int_{\theta} \int_{\varphi} \delta(r-r_o) \delta(\theta-\theta_o) \delta(\varphi-\varphi_o) r^2 j_l(k_3 r) \left[\sin \theta \frac{\partial Y_{lm}^*(\theta, \varphi)}{\partial \theta} - \frac{\partial Y_{lm}^*(\theta, \varphi)}{\partial \varphi} \right] d\varphi d\theta dr
\end{aligned} \tag{C.5}$$

By carrying out the integration on the right hand side of (C.5) and rearranging the terms after integration, (C.6) can be written.

$$\Lambda_{lm} = \frac{-2r_o J_l(k_3 r_o)}{\pi l(l+1)} \left[\sin \theta_o \frac{\partial Y_{lm}^*(\theta_o, \varphi_o)}{\partial \theta} + jm Y_{lm}^*(\theta_o, \varphi_o) \right] \tag{C.6}$$

The other coefficient can be obtained by first applying the curl to both sides of equation (C.3).

$$\begin{aligned}
& -k_3 \sum_{l=1}^{\infty} \sum_{m=-l}^l \Lambda_{lm} j_l(k_3 r) \nabla \times \bar{r} \times \nabla Y_{lm}(\theta, \varphi) \\
& -j \sqrt{\frac{\epsilon_3}{\mu_0}} \sum_{l=1}^{\infty} \sum_{m=-l}^l \Xi_{lm} \nabla \times \nabla \times [j_l(k_3 r) \bar{r} \times \nabla Y_{lm}(\theta, \varphi)] = \\
& \nabla \times \left\{ \delta(r-r_o) \delta(\theta-\theta_o) \delta(\varphi-\varphi_o) (\hat{\theta} + \hat{\varphi}) \right\}
\end{aligned} \tag{C.7}$$

By simplifying (C.7), (C.8) can be written.

$$\begin{aligned}
& -k_3 \sum_{l=1}^{\infty} \sum_{m=-l}^l \Lambda_{lm} j_l(k_3 r) \nabla \times \vec{r} \times \nabla Y_{lm}(\theta, \varphi) \\
& + j \sqrt{\frac{\epsilon_3}{\mu_0}} \sum_{l=1}^{\infty} \sum_{m=-l}^l \Xi_{lm} J'_l(k_3 r) \vec{r} \times \nabla Y_{lm}(\theta, \varphi) = \\
& \delta(r - r_o) \delta(\theta - \theta_o) \delta(\varphi - \varphi_o) \left(-\hat{\theta} + \hat{\varphi} \right)
\end{aligned} \tag{C.8}$$

Before considering the volume integral like in the first case, we have to simplify the term $J'_l(k_3 r)$ by using the following equation.

$$\begin{aligned}
J'_l(k_3 r) &= \frac{d}{dr} [k_3 r j_l(k_3 r)] = k_3 [k_3 r j_{l-1}(k_3 r) - l j_l(k_3 r)] = k_3^2 \left[j_{l-1}(k_3 r) - l \frac{j_l(k_3 r)}{k_3 r} \right] \\
&= k_3^2 \left[j_{l-1}(k_3 r) - \frac{l}{2l+1} \{ j_{l-1}(k_3 r) + j_{l+1}(k_3 r) \} \right] = k_3^2 \left[\frac{l+1}{2l+1} j_{l-1}(k_3 r) - \frac{l}{2l+1} j_{l+1}(k_3 r) \right]
\end{aligned} \tag{C.9}$$

By taking the dot product of both sides of (C.9) with the term $r^2 j_{l-1}(k_3 r) \vec{r} \times \nabla Y_{lm}^*(\theta, \varphi)$ (C.9) can be simplified to the following equation.

$$\begin{aligned}
& j \sqrt{\frac{\epsilon_3}{\mu_0}} \sum_{l=1}^{\infty} \sum_{m=-l}^l \Xi_{lm} J'_l(k_3 r_o) \vec{r} \times \nabla Y_{lm}(\theta, \varphi) \cdot r^2 j_{l-1}(k_3 r) [\vec{r} \times \nabla Y_{lm}^*(\theta, \varphi)] = \\
& \left\{ \delta(r - r_o) \delta(\theta - \theta_o) \delta(\varphi - \varphi_o) \left(-\hat{\theta} + \hat{\varphi} \right) \right\} \cdot r^2 j_{l-1}(k_3 r) [\vec{r} \times \nabla Y_{lm}^*(\theta, \varphi)]
\end{aligned} \tag{C.10}$$

Now by taking the volume integral of both sides of (C.10) and making use of (C.9), the following equation can be written.

$$\begin{aligned}
& j \frac{\pi l(l+1)^2}{2(2l+1)} \sqrt{\frac{\epsilon_3}{\mu_0}} \Xi_{lm} = \\
& \int_r \int_\theta \int_\varphi \delta(r-r_o) \delta(\theta-\theta_o) \delta(\varphi-\varphi_o) r^2 j_{l-1}(k_3 r) \left[\sin \theta \frac{\partial Y_{lm}^*(\theta, \varphi)}{\partial \theta} + \frac{\partial Y_{lm}^*(\theta, \varphi)}{\partial \varphi} \right] d\varphi d\theta dr
\end{aligned} \tag{C.11}$$

By carrying out the integration and rearranging the terms in (C.11) the final expression for Ξ_{lm} can be expressed in (C.12) which is that in (3.63).

$$\Xi_{lm} = \frac{2r_o \sqrt{\mu_o} (2l+1) J_{l-1}(k_3 r_o)}{j\pi k_3 \sqrt{\epsilon_3} l(l+1)^2} \left[\sin \theta_o \frac{\partial Y_{lm}^*(\theta_o, \varphi_o)}{\partial \theta} - jm Y_{lm}^*(\theta_o, \varphi_o) \right] \tag{C.12}$$

Appendix D

In Chapter 5 the new phase shifter topology was given and explained. The small signal equations were given without explaining the derivation behind it. Consider the circuit in Figure D.1, which is the first part of the phase shifter (Figure 5.4).

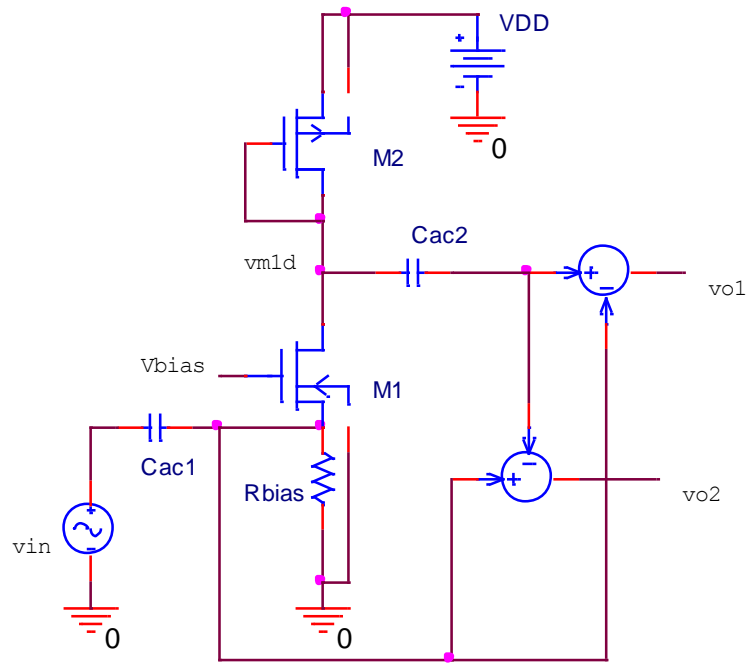


Fig. D.1. Circuit topology for the phase shifter given in Chapter 5.

The small signal circuit for Figure D.1 is given in Figure D.2.

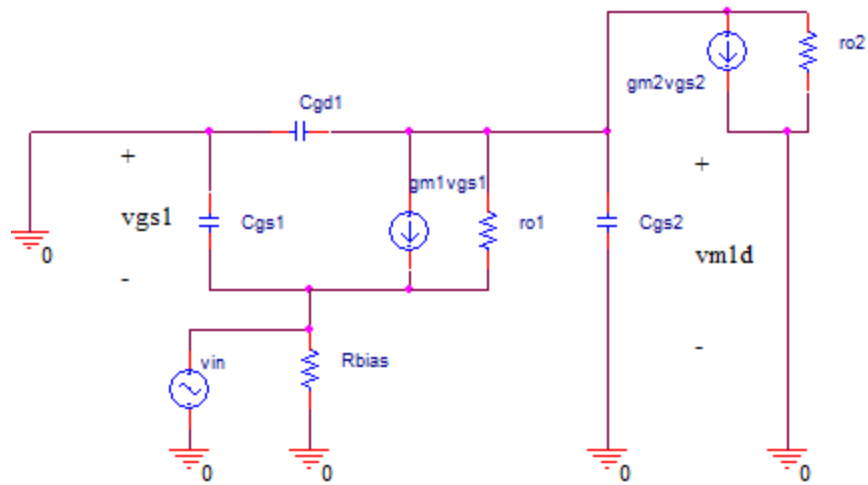


Fig. D.2. Small signal model of the phase shifter (excluding the difference circuits).

Figure D.2 can be simplified to Figure D.3.

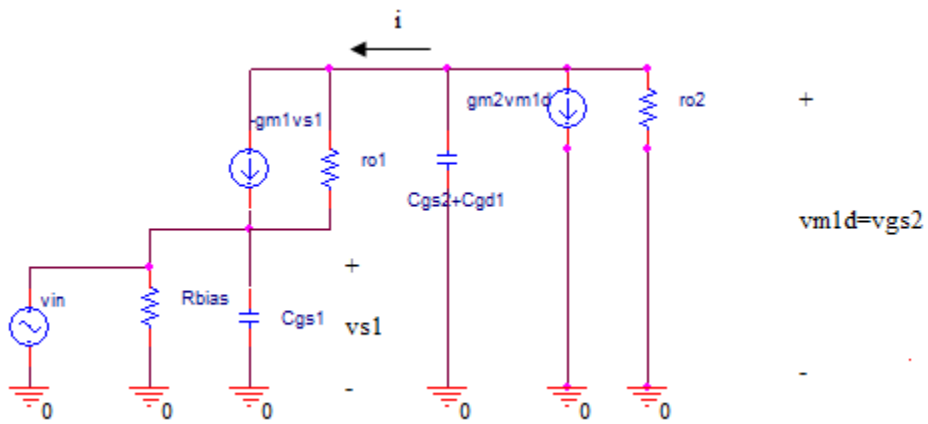


Fig. D.3. Simplified small signal circuit model.

By realizing that $v_{in} = v_{s1} = -v_{gs1}$ and $v_{m1d} = v_{gs2}$ then the equations for the current I shown in Figure D.3 can be written as:

$$i = -g_{m1}v_{in} + g_{o1}(v_{m1d} - v_{in}) \quad (D.1)$$

$$i = -s(C_{gd1} + C_{gs2})v_{m1d} - g_{m2}v_{m1d} - g_{o2}v_{m1d} \quad (D.2)$$

Equations (D.1) and (D.2) can be combined to eliminate i and get the following equation.

$$-g_{m1}v_{in} + g_{o1}(v_{m1d} - v_{in}) = -s(C_{gd1} + C_{gs2})v_{m1d} - g_{m2}v_{m1d} - g_{o2}v_{m1d} \quad (D.3)$$

By rearranging the terms and solving for v_{m1d}/v_{in} , equation (D.4) can be obtained (which is the result shown in equation (5.5)).

$$\frac{v_{m1d}}{v_{in}} = \frac{g_{m1} + g_{o1}}{1 + \frac{s(C_{gd1} + C_{gs2})}{g_{m2} + g_{o1} + g_{o2}}} \quad (D.4)$$

Appendix E

When designing the RF amplitude amplifier, the cascode configuration was used to achieve good high frequency performance by the alleviation of the Miller Effect caused by the gate-to-drain capacitance in the first stage transistor M1 (Figure E.1). The expression for the voltage was given without any detailed derivation, thus in this appendix the derivation is carried out in detail.

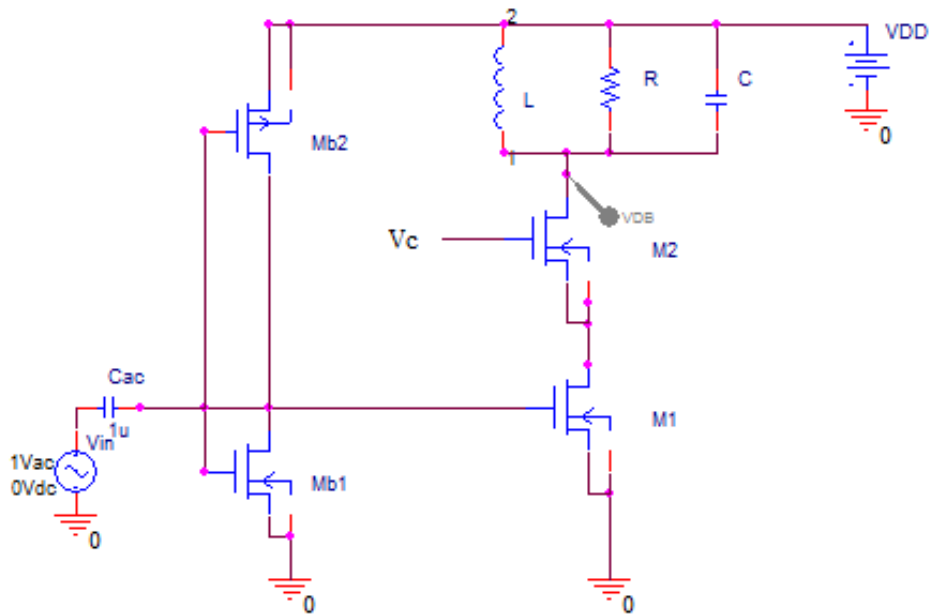


Fig. E. 1. RF tuned amplitude amplifier.

By considering the small signal model at resonance, the following circuit can be drawn for transistors M1 and M2 (note that M_{b1} and M_{b2} provide DC biasing do they are not included in the analysis).

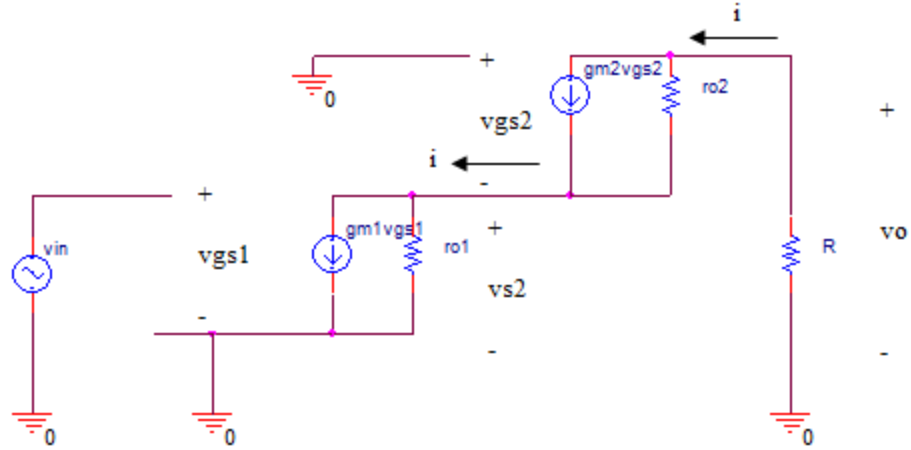


Fig. E.2. Small signal model of the RF amplitude at resonance.

By considering the fact that $v_{in}=v_{gs1}$ and $v_{gs2}=-v_{s2}$, the following equations can be written for the current i shown in Figure E.2.

$$i = g_{m1}v_{in} + \frac{v_{s2}}{r_{o1}} \quad (\text{E.1})$$

$$i = -g_{m2}v_{s2} + \frac{1}{r_{o2}}(v_o - v_{s2}) \quad (\text{E.2})$$

$$i = -\frac{v_o}{R} \quad (\text{E.3})$$

By solving (E.1) and (E.2), v_{s2} can be eliminated.

$$i = -g_{m2}r_{o1}(i - g_{m1}v_{in}) + \frac{v_o}{r_{o2}} - \frac{r_{o1}}{r_{o2}}(i - g_{m1}v_{in}) \quad (\text{E.4})$$

With some rearrangement of the variables (E.5) can be written.

$$i[r_{o2} + r_{o1}(1 + g_{m2}r_{o2})] = g_{m1}r_{o1}(1 + g_{m2}r_{o2})v_{in} + v_o \quad (\text{E.5})$$

By solving (E.3) and (E.5) together, the current i can be eliminated to get the voltage gain, which matches equation (5.31).

$$A_v = \frac{v_o}{v_{in}} = \frac{-g_{m1}r_{o1}R(1 + g_{m2}r_{o2})}{R + r_{o2} + r_{o1}(1 + g_{m2}r_{o2})} \quad (\text{E.6})$$

Appendix F

In this appendix the RL series to RL parallel transfer is derived in full.

Considering Fig. F.1, the RL series to the RL parallel transformation is considered.

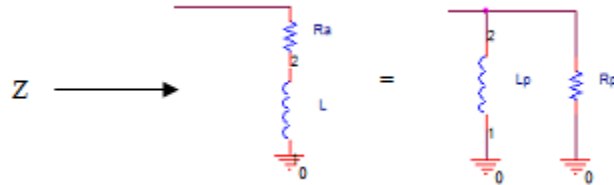


Fig. F.1. Series to Parallel Transformation.

The original impedance is given by (F.1).

$$Z = R_a + j\omega L \quad (\text{F.1})$$

It is desired to set the impedance of the parallel connection in Fig. F.1 to be Z of (F.1), which implies:

$$Z = \frac{j\omega L_p R_p}{R_p + j\omega L_p} = \frac{R_p (\omega L_p)^2 + R_p^2 j\omega L_p}{R_p^2 + (\omega L_p)^2} \quad (\text{F.2})$$

To equate (F.1) to (F.2), the following equations must be satisfied.

$$R_a = \frac{R_p (\omega L_p)^2}{R_p^2 + (\omega L_p)^2} \quad (\text{F.3})$$

$$\omega L = \frac{R_p^2 \omega L_p}{R_p^2 + (\omega L_p)^2} \quad (\text{F.4})$$

Note that here the unknowns are R_p and L_p . To solve for the unknowns, the following equation can be obtained from (F.3) and (F.4).

$$\frac{\omega L_p}{R_a} = \frac{R_p}{\omega L} \quad (\text{F.5})$$

By applying the result found in (F.5) in equation (F.3), the following equations can be derived.

$$R_p = \frac{R_a^2 + (\omega L)^2}{R_a} \quad (\text{F.6})$$

$$\omega L_p = \frac{R_a^2 + (\omega L)^2}{\omega L} \quad (\text{F.7})$$

(F.6) and (F.7) matches equations (5.27) and (5.28), respectively.

Bibliography

- [1] J. Jackson, "Classical Electrodynamics," Third Edition, Wiley, 1998.
- [2] B. Ford, "Deep Brain Stimulation for Parkinson's Disease," *Parkinson's Disease Foundation*, 2002.
- [3] R. E. Collin, "Antennas and Radiowave Propagation," International Edition, McGraw-Hill, 1985.
- [4] J. Sahalos, "Orthogonal Methods for Array Synthesis: Theory and the ORAMA Computer Tool," Wiley, 2006.
- [5] S. J. Orfanidis, "Electromagnetic Waves and Antennas," November 2002, Chapter 16, pp.634-657.
- [6] F. Gross, "Smart Antennas for Wireless Communications," McGraw-Hill, 2005.
- [7] B. Allen, M. Ghavami, "Adaptive Array Systems", Wiley, 2005.
- [8] H. H. Chen, S. C. Chan, Z. G. Zhang & K. L. Ho, "Adaptive Beamforming and Recursive DOA Estimation Using Frequency-Invariant Uniform Concentric Spherical Spheres," *IEEE Transactions on Circuit and Systems*, Vol. 55, No. 10, November 2008, pp: 3077-3089.
- [9] T. Svantesson, M. Wennstrom, "High Resolution Direction Finding Using a Switched Parasitic Antenna,"
<http://www.signal.uu.se/Publications/pdf/c0111.pdf>.

- [10] S. Caylar, G. Dural, K. Leblebicioglu, "Neural Network Method for Direction of Arrival Estimation with Uniform Cylindrical Microstrip Patch Array," *IET Microwaves, Antennas & Propagation*, 2008.
- [11] M. Amin, A. Rahman, S. Bin-Mahbub, K. Ahmed & Z. Chowdhury, "Estimation of Direction of Arrival (DOA) Using Real-Time Array Signal Processing," *5th International Conference on Electrical and Computer Engineering ICECE 2008*, 20-22 December 2008, Dhaka, Bangladesh, pp: 422-427.
- [12] V. I. Vasylyshyn, "Antenna Array Signal Processing with High-Resolution By Modified Beamsearch MUSIC Algorithm," *International Conference on Antenna Theory and Techniques*, 17-21 September, 2007, Sevastopol, Ukraine pp. 455-457.
- [13] A. Zooghy, C. G. Christodoulou & M. Georgiopoulos, "A Neural Network-Based Smart Antenna for Multiple Source Tracking," *IEEE Transaction on Antennas and Propagation*, Vol. 48, No. 5, May 2000, pp: 768-776.
- [14] M. Sarevska, B. Milovanovic & Z. StankoviC, "Alternative Signal Detection For Neural Network-Based Smart Antenna," *7th Seminar on Neural Network Applications in Electrical Engineering, Neural-2004*, September 23.25.2004, pp: 85-89.
- [15] M. Sarevska & A. Salem, "Antenna Array Beamforming using Neural Network," *World Academy of Science, Engineering and Technology* 24 2006, pp: 115-119.

- [16] R. Want, "An Introduction to RFID Technology," *IEEE CS and IEEE ComSoc*, 2006.
- [17] N. Rueangsi, and A. Thanachayanont, "Coil Design for Optimum Operating Range of Magnetically-Coupled RFID System," *IEEE ISCIT*, pp. 1199-1202, 2006.
- [18] T. H. Lee, "The Design of CMOS Radio-Frequency Integrated Circuits," Second Edition, Cambridge, 2006.
- [19] S. Atluri & M. Ghovanloo, "Incorporating Back Telemetry in a Full-Wave CMOS Rectifier for RFID and Biomedical Applications," *IEEE*, 2007.
- [20] K. Fotopoulou & B. Flynn, "Optimum Antenna Coil Structure for Inductive Powering of Passive RFID Tags," *IEEE International Conference in RFID*, pp: 71-77, March 2007.
- [21] C. Zierhofer, and E. Hochmair, "High-Efficiency Coupling-Insensitive Transcutaneous Power and Data Transmission Via an Inductive Link," *IEEE Trans. Biomed. Eng.*, Vol. 37, pp. 716-722, July 1990.
- [22] M. Baker, and R. Sarpeshkar, "Feedback Analysis and Design of RF Power Links for Low-Power Bionic Systems," *IEEE Transactions on Biomedical Engineering*, Vol. 1, pp. 28-38, March 2007.
- [23] G. Wang, W. Liu, M. Sivaprakasam & G. Kendir, "Design and Analysis of an Adaptive Transcutaneous Power Telemetry for Biomedical Implants," *IEEE Transactions Circuits and Systems-I*, Vol. 52, pp.2109-2117, October 2007.

- [24] M. Abdalla, K. Phang, and G. V. Eleftheriades, "A Bi-Directional Electronically Tunable CMOS Phase Shifter Using the High-Pass Topology," 1-4244-0688-9/07, 2007, IEEE Xplore.
- [25] M. Ahmadi, L. Chen, N. Fayyaz, S. Safavi-Naeini, and D. Banbury, "A Novel CMOS Integrated Smart Antenna Transceiver," 0-7803-9412-7/06, 2006, IEEE Xplore.
- [26] K. Koh, and G. Rebeiz, "An X- and Ku-Band 8-Element Phased-Array Receiver in 0.18- μm SiGe BiCMOS Technology," *IEEE Transactions of Solid-State Circuits*, Vol. 43, No. 6, pp. 1360-1371, June 2008.
- [27] T. Yu, and G. Rebeiz, "A 22-24 GHz 4-Element CMOS Phased Array With On-Chip Coupling Characterization," *IEEE Transactions of Solid-State Circuits*, Vol. 43, No. 9, pp. 2134-2143, September 2008.
- [28] S. Jeon, Y. Wang, H. Wang, F. Bohn, A. Natarajan, A. Babakhani & A. Hajimiri, "A Scalable 6-to-18 GHz Concurrent Dual-Band Quad-Beam Phased-Array Receiver in CMOS," *IEEE Journal of Solid-State Circuits*, Vol. 43, No. 12, December 2008, pp: 2660-2673.
- [29] H. Krishnaswamy, and H. Hashemi, "A Variable-Phase Ring Oscillator and PLL Architecture for Integrated Phase Array Transceivers," *IEEE Transactions of Solid-State Circuits*, Vol. 43, No. 11, pp. 2446-2463, November 2008.
- [30] B. J. Maundy & P. Aronhime, "A Novel First-Order All- Pass Filter," *International Journal of Electronics*, Vol. 89, No. 9, pp. 739 – 743, 2002.

- [31] F. Klostermann, J. Vesper, G. Curio, "Identification of Target Areas for Deep Brain Stimulation in Human Basal Ganglia Substructures Based on Median Nerve Sensory Evoked Potential Criteria," *J Neurol Neurosurg Psychiatry*, 2003;74: pp: 1031–1035.
- [32] M. Titcombe, L. Glass, D. Guehl & A. Beuter, "Dynamics of Parkinsonian Tremor during Deep Brain Stimulation," *Chaos*, Vol. 11, No. 4, December 2001, pp: 766-773.
- [33] L. Garcia, G. D'Alessandro, B. Bioulac & C. Hammond, "High-frequency Stimulation in Parkinson's disease: more or less?," *Trends in Neurosciences*, Vol. 28, No. 4, April 2005, pp: 209-216.
- [34] Wikipedia, "Thalamus," <http://en.wikipedia.org/wiki/Thalamus>.
- [35] M. Ali & S. Ray, "SAR Distributions in a Spherical Inhomogeneous Human Head Model Exposed to Electromagnetic Field for 500 MHz – 3 GHz Using FDTD method," *NCC 2009*, January 16-18, IIT Guwahati, pp: 64-67.
- [36] R. F. Harrington, "Time-Harmonic Electromagnetic Fields," *IEEE Press Series on Electromagnetic Wave Theory* 2001, Chapter 6, p: 264-269.
- [37] M. J. Schroeder, A. Sadasiva & R. M. Nelson, "An Analysis on the Role of Water Content and State on Effective Permittivity Using Mixing Formulas," *Journal of Biomechanics, Biomedical and Biophysical Engineering*, Vol. 2, Issue. 1, 2008, pp: 1-11.

- [38] H. P. Partal, J. R. Mautz, and E. Arvas, "Radiation from a Circular Loop in the Presence of a Spherically Symmetric Conducting or Dielectric Objects," *IEEE Transactions on Antenna and Propagation*, Vol. 48, No. 10, pp: 1646-1652, October 2000.
- [39] L. A. Costa, O. M. C. Pereira-Filho & F. J. S. Moreira, "Analysis of Spherical-Rectangular Microstrip Antennas," <http://www.cpdee.ufmg.br/~fernando/artigos/imoc05c.pdf>.
- [40] J. Ashkenazy, S. Shtrikman & D. Treves, "Electric Surface Current Model for the Analysis of Microstrip Antennas on Cylindrical Bodies," *IEEE Transactions on Antennas and Propagation*, Vol. AP-33, No. 3, March 1985, pp: 295-300.
- [41] K. M. Luk & W. Y. Tam, "Patch antennas on a spherical body," *IEE Proceedings-H*, Vol. 138, No. 1, February 1991, pp: 103-108.
- [42] B. Ke & A. A. Kishk, "Analysis of spherical circular microstrip antennas," *IEE Proceedings-H*. Vol. 138, No. 6. December 1991, pp: 542-547.
- [43] "Chapter 6: Harmonic Expansion of Electromagnetic Fields," <http://physics.usask.ca/~hirose/p812/notes/Ch6.pdf>.
- [44] Z. Li, R. Duraiswami, "Flexible and Optimal Design of Spherical Microphone Arrays for Beamforming," *IEEE Transactions on Speech & Audio Processing*, Vol. 15, No. 2, pp: 702-714, Feb. 2007.
- [45] I. Marinova & V. Mateev, "Electromagnetic Field Modeling in Human Tissue," *World Academy of Science, Engineering and Technology* 64 2010, pp: 298-303.

- [46] A. I. Sabbah & N. I. Dib, "SAR and Temperature Elevation in a Multi-Layered Human Head Model Due to an Obliquely Incident Plane Wave," *Progress In Electromagnetics Research M*, Vol. 13, pp: 95-108, 2010.
- [47] S. Khalatbari, D. Sardari, A. A. Mirzaee & H. A. Sadafi, "Calculating SAR in Two Models of the Human Head Exposed to Mobile Phones Radiations at 900 and 1800MHz," *Progress In Electromagnetics Research Symposium 2006*, Cambridge, USA, March, pp: 26-29.
- [48] R. Rojas, "Neural Networks: A Systematic Introduction," Springer-Verlag, Berlin, 1996.
- [49] B. Krose & P. V. D. Smagt, "An Introduction to Neural Networks," Eighth Edition, November 1996.
- [50] L. Merad, F. T. Bendimerad, S. M. Meriah & S. A. Djennas, "Neural Networks for Synthesis and Optimization of Antenna Arrays," *Radioengineering*, Vol. 16, No. 1, April 2007, pp: 23-30.
- [51] M. H. Beale, M. T. Hagan & H. B. Demuth, "Neural Network Toolbox™ 7," MATLAB User's Guide.
- [52] C. Lu, A. H. Pham & D. Livezey, "On the Feasibility of CMOS Multiband Phase Shifters for Multiple-Antenna Transmitters," *IEEE Microwave and Wireless Components Letters*, Vol. 16, No. 5, May 2006, pp: 255-257.
- [53] L. C. Shen, J. A. Kong, "Applied Electromagnetism," Third Edition, PWS Publishing Company, 1995.

- [54] Gray and Meyer, "Analysis And Design Of Analog Integrated Circuits," Fourth Edition, Wiley, 2001.
- [55] P. E. Allen & D. R. Holberg, "CMOS Analog Circuit Design," Second Edition, Oxford University Press, 2002.
- [56] B. Razavi, "RF Microelectronics," Prentice Hall PTR, 1998.
- [57] A. Sedra & K. C. Smith, "Microelectronic Circuits," Fourth Edition, Oxford University Press, 1998.
- [58] L. Li, M. Leong, P. Kooi & T. Yeo, "Exact Solutions of Electromagnetic Fields in Both Near and Far Zones Radiated by Thin Circular-Loop Antennas: A General Representation," *IEEE Transactions on Antennas and Propagation*, Vol. 45, No. 12, December 1997, pp: 1741-1748.
- [59] Thomas B. A. & G. A. Desjardins, "Electromagnetic Field Penetration into a Spherical Cavity," *IEEE Transactions on Electromagnetic Compatibility*, Vol. EMC-16, No. 4, November 1974, pp: 205-208.
- [60] R. H. MacPhie & K. Wu, "A Plane Wave Expansion of Spherical Wave Functions for Modal Analysis of Guided Wave Structures and Scatterers," *IEEE Transactions on Antennas and Propagation*, Vol. 51, No. 10, October 2003, pp: 2801-2805.
- [61] M. Safar & R. W. Newcomb, "Design of a Hemispherical Antenna Array for Magnetic Field Control in the Brain," *LISSA 2011 Conference*.

- [62] E. Zastrow, S. Hagness, B. Veen & J. Medow, "Time-Multiplexed Beamforming for Non-invasive Microwave Hyperthermia Treatment," *IEEE Transaction on Microwave Engineering*, December 2010.
- [63] M. Suzuki, K. Kato, T. Hirashima, Y. Shindo, T. Uzuka, H. Takahashi & Y. Fujii, "Heating Properties of the Re-entrant Type Cavity Applicator for Brain Tumor with Several Resonant Frequencies," *31st Annual International Conference of the IEEE EMBS Minneapolis*, Minnesota, USA, September 2-6, 2009.
- [64] M. Suzuki, K. Kato, T. Hirashima, N. Mimito, Y. Shindo, S. Ono, T. Tsuchiya, M. Kubo, T. Uzuka, H. Takahashi & Y. Fujii, "SAR Analysis of a Re-entrant Cavity Applicator for Brain Tumor Hyperthermia Treatment with a 3-D Anatomical Human Head Model." *32nd Annual International Conference of the IEEE EMBS Buenos Aires*, Argentina, August 31-September 4, 2010.
- [65] A. Fenn, V. Sathiaselan, G. King & P. Stauffer, "Improved Localization of Energy Deposition in Adaptive Phased-Array Hyperthermia Treatment of Cancer," *The Lincoln Laboratory Journal*, Vol. 9, No. 2, 1996, pp: 187-195.

